Microstructure evolution in Nb alloyed Esshete 1250 creep resistant austenitic stainless steel.

Wong, Chia Yuin

Microstructure Evolution in Nb Alloyed Esshete 1250 Creep Resistant Austenitic Stainless Steel

Chia Yuin Wong

Doctor of Philosophy (PhD) Thesis

Submitted to the Swansea University in fulfilment of the requirements for the Degree of Doctor of Philosophy.

2008

Academic Supervisor: Dr. G. Fourlaris
Materials Research Centre
School of Engineering
Swansea University

ProQuest LLC.
789 East Eisenhower Parkway
P.O. Box 1346
Ann Arbor, MI 48106 – 1346

Declaration

This work has not previously been accepted in substance for any degree and is not being concurrently submitted in candidature for any degree.

Signed : _____(Candidate)

Date : 14/11/2008

STATEMENT 1

This thesis is the result of my own investigations, except where otherwise stated. Where correction services have been used, the extent and nature of the correction is clearly marked in a footnote(s).

Other sources are acknowledged by footnotes giving explicit references. A bibliography is appended.

Signed : _____(Candidate)

Date : 14/11/2008

STATEMENT 2

I hereby give consent for my thesis, if accepted, to be available for photocopying and for inter-library loan, and for the title and summary to be made available to outside organisations.

Signed : _____(Candidate)

Date : 14/11/2008.

CONTENTS

Chapter 3

Chapter 4

Chapter 5

Chapter 6

Chapter 7

Acknowledgement

The author would like to thank her research supervisors, Dr. G. Fourlaris for his constructive suggestions and opinions throughout the course of the research. In addition, the help from Mr. P. Davies during electron microanalysis is very much appreciated. The author would also like to thank her family and friends who have been supportive throughout. Sponsorship from Niobium Products GmbH from Germany is greatly appreciated. The provision of creep samples by Mr. Mike Spindler of British Energy is gratefully appreciated.

Abstract

The microstructure evolution of a commercial grade creep-resistant austenitic steel, namely Esshete 1250, was investigated under different creep temperature and stress conditions, with an overall aim of exploring the micorstructural relationship to creep rupture during high temperature application. Creep tests data was supplied by British Energy on temperatures varied from 550°C to 700°C for periods of up to 17 years.

The literature review includes the study of various creep resistant alloys and a detailed investigation on the precipitation reactions that take place in creep resistant steels. Moreover, the strengthening mechanisms in order to obtain suitable creep resistance properties for engineering materials for high temperature applications is also reviewed.

Long term creep deformation for Esshete 1250 creep resistant steel is reviewed in Chapter 2. The tensile properties of Esshete 1250 parent material and weld material are included in this Chapter as well. Qualitative and quantitative metallography techniques are reviewed in order to provide the required background information for the interpretation of obtained microstructure.

The experimental study involved hardness testing and scanning electron microscopy examination. The size, distribution of MX precipitates was analysed with electron microscopy techniques together with Optilab analysis, while metallographic grain evolution measurements in creep exposed samples was also carried out.

As part of this study, the grain size evolution and precipitate size evolution of Esshete 1250 creep resistant steel are obtained. Attention then is given to the volume fraction, size and distribution of MX (Nb-rich) particles. It is concluded that MX precipitation is the key factor that influences the creep resistance of Esshete 1250 under service conditions, while grain size is additional to the effect of MX precipitation in solution and is of secondary importance. The obtained results can be implemented into other creep alloy design, helping to meet the challenge of developing high temperature alloy systems for greater sustainability.

List of tables

List of Figures

Figure 92: Secondary electron micrographs and associated EDX spot microanalysis traces in Esshete 1250 parent sample creep tested for 3489h at 575°C.

CHAPTER 1

1.0 INTRODUCTION

The environmental impact and economic factors have focused our attention on the development of high efficiency and low emission energy systems. The challenge for the power generation industry thus is to increase efficiency while at the same time reducing operating costs. The material used in the power generation industry hence must not only increase thermal efficiency but also reduce maintenance costs. Thus, worldwide research and development on construction materials has never decelerated and advanced alloy steels have been developed for higher temperature applications [1-8].

Construction materials for the components of a power plant such as steam generators, turbine rotors, superheater tube/pipe require operating at high temperatures, under significant stresses. Failures and fractures of materials under these aggressive environments is usually the performance limiting factor and are of primary concern to the material designer. For this reason, the components and structures need to be designed on the basis that excessive creep distortion or creep failure must not occur within the expected operating life. Creep resistance thus, is an essential mechanical property of a material that requires operating continuously at severe engineering environments.

Creep resistant alloys are used in applications appropriate to the different requirements of corrosion resistance and creep resistance properties. The common commercial materials used for high temperature components in power plant consist of ferritic/martensitic and austenitic alloys. Ferritic/martensitic creep resistant steels developed are aimed for use in thick section pipes and headers. The evolution of these steels has been reviewed by Masuyama [1]. For example ferritic/martensitic materials

such as HCM12 and NF616 are used especially in thick sections and places that are prone to thermal fatigue due to their better resistance for thermal shocks. The benefits of the austenitic materials are high creep strength and low oxidation rates, for example in superheaters tubes or pipes, where alloy such as Esshete 1250, NF709, TP347H and others are employed [2, 9-10]. Chemical specification and maximum service temperature for examples of creep resistant alloy stated are shown in Table 1.

Table 1: Examples of creep resistant alloy steel used for high temperature components in power plants [1, 4, 9-10].

ASME Specifications	Composition	Component	Max. temperature (°C) at 32.5MPa
Ferritic / Martensitic alloys			
HCM2S	0.01C-2.25Cr-0.03Mo-1.6W-V-Nb-N-B	Furnace panels	625
HCM12	0.1C-12cr-1Mo-1W-V-Nb-N	Furnace panels	625
NF616	0.1C-9Cr-0.5Mo-1.8W-V-Nb-N-B	Thick section boiler component	610
HCM12A	0.1C-11Cr-0.5Mo-1.8W-1Cu-V-Nb-N-B	Thick section boiler component	610
Austenitic alloys			
TP347HFG	18Cr-10Ni-1Nb	Superheaters headers, tubes and pipes	~620
Esshete 1250	0.016/0.15C-14/16Cr-9/11Ni-0.8/1.2Mo-0.72/1.25Nb-N-B	Superheaters tubes and pipes	~620
Super 304H	18Cr-9Ni-0.4nb-Cu-N	Superheaters tubes to resist H_2S and S attack	~625
NF709	20Cr-25Ni-1.5Mo-0.25Nb-0.05Ti-N	Superheaters tubes and pipes	~630
Nickel based alloys			
Inconel 617	22Cr-54Ni-0.4Si-0.4Mn-8.5Mo-2.5Co-Al	Superheaters	~700
Inconel 740	0.03C-0.5Si-0.3Mn-0.5Mo-1.8Ti-2.0Nb-0.9Al-25Cr-20Co-0.7Fe-Ni	Superheaters	~720

The austenitic stainless steel (16-18% Cr, 8-12% Ni) have found numerous applications in various fields of industry, particularly in equipment for power plants and petrochemical industry as well as in the manufacture of critical units in the aviation, railway, automotive and chemical industries. As a part of the effort to improve the efficiency of power generation industry, much research focuses on improving the creep strength of the austenitic creep resistant alloys. The material studied, named Esshete 1250, is nominally a 16Cr-10Ni precipitation strengthened austenitic stainless steel with improved creep rupture strength and corrosion resistance at elevated temperatures. This creep resistant austenitic grade is a stabilised stainless steel, which guarantees that formation of chromium carbide ($Cr_{23}C_6$) particles does not occur to avoid sensitisation. Precipitation strengthening is attributes primarily to the presence of finely dispersed niobium carbide (NbC) particles (Figure 1). Esshete 1250 with a rupture strength at 600°C nearly double than that of AISI 316 grade austenitic stainless steel was found to offer major improvements over the 300 series stainless steel. [8] Due to its suitability for demanding conditions in superheater and reheater units in coal-fired power generation, its specification is now the standard construction material in the UK power stations.

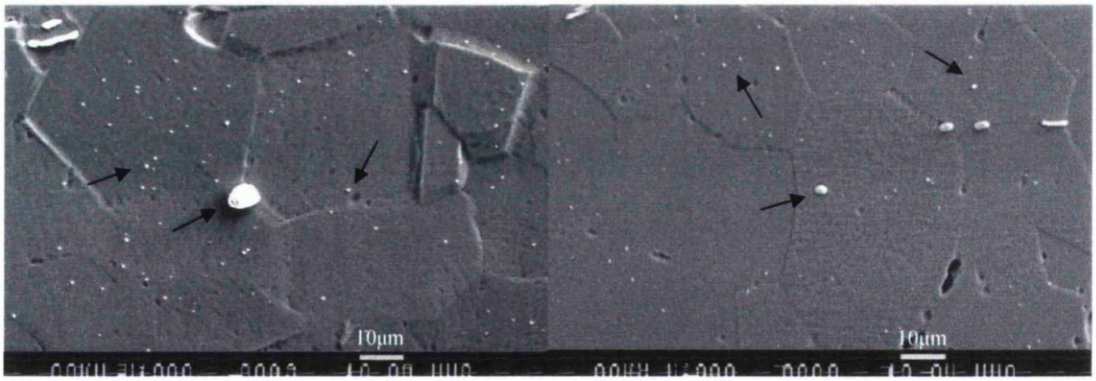

Figure 1: (a) As-received Esshete 1250 and (b) Esshete 1250 aged for 2790h at 550°C. Arrows show precipitates of niobium carbide (NbC) in Esshete 1250 alloy.

The material studied was provided by British Energy (Gloucester). The creep testing on Esshete 1250 has been initiated by British Energy associated with ERA technology in order to develop a new creep deformation model. Although the creep test programme is currently in progress, some data had been produced and they are sufficient for primary and secondary creep behaviour analysis. The dataset provided

contains creep data acquired at stresses ranging from 70 to 420MPa and temperatures from 550°C to 700°C. However, analysis of creep data and creep deformation model is not part of the present study. This thesis presents the microstructural analysis related to creep deformation for Esshete 1250 under various stresses and temperatures condition.

The alloy design methodology used to modify the creep resistant steels for improved high temperature mechanical properties has been explored. [6, 11-13] The fracture mechanisms, microstructure property relationships and the damage evaluation have been extensively studied under creep or creep fatigue conditions in creep resistant alloys such as NF616 ferritic alloy, NF709 austenitic alloy and so on [13-20]. No current microstructural study exists for creep deformed Esshete 1250 austenitic alloy. For this reason, the microstructural study on Esshete 1250 steel after long term creep exposure and the effect of Nb additions on creep strength were investigated. By tracking the changes in chemistry and long term (for example 100,000 hours) creep strength at high temperatures, let say 650°C, some major metallurgical changes and alloy effects are observed. The effect of grain size on creep resistant properties is complex and depends quite fundamentally on the creep conditions and the predominant creep mechanism involved. Precipitate hardening plays an important role in creep resistant steels [17, 20-23]. Several theories have been presented to explain the presence of fine carbides precipitates in the microstructure of creep resistant steels [22, 24-26]. Nevertheless, more detailed analytical electron microscopy data is still needed to clarify the mechanistic behaviour in creep resistant alloy.

1.1 Aims of the project

The metallurgical characterisation of creep resistant alloys and the investigation of creep failure and fracture failure analysis require a detailed knowledge of the microstructure. Therefore, the preparation and investigation of micro sections of creep resistant alloy for examination under electron microscope is extremely important. Also, knowledge of the microstructure to be expected for a given type of creep resistant alloy is necessary to allow correct interpretation.

The microstructure stability of creep resistant steels during exposure to high temperature conditions is mainly affected by the precipitated particles. Therefore, the present work has been carried out to elucidate the effect of size and distribution of precipitate in order to facilitate the microstructural study on niobium added creep resistant austenitic steel. The aim is to obtain more detailed analytical electron microscopy data on the Esshete 1250 Nb alloyed creep resistant steel in various high temperature conditions as well as to clarify grain growth inhibition and the attendant control of the microstructure of creep resistant steel.

As part of this research, creep exposed Esshete 1250 Nb alloyed austenitic creep resistant steel was investigated under different creep exposure temperatures and stress conditions, with an overall aim of exploring the effect niobium additions have for microstructure stability at high temperature applications. In particular, this research has the following specific objectives:

- To study the grain coarsening characteristics of creep exposed Esshete 1250 austenitic stainless steel.
- To clarify the effect of alloying elements, in specific niobium on the creep resistant steel studied, as well as, the attendant control of its mechanical properties.
- To characterise the mechanical properties and obtained microstructures in Nb alloyed creep resistant austenitic grades.

CHAPTER 2

2.0 LITERATURE REVIEW

Creep-resistant steels are widely used in the petroleum, chemical and power generation industries. These steels must be reliable over very long periods of time at high temperatures and in severe environments. Therefore, understanding and improving long-term creep strength is essential for the safe operation of plant and equipment.

The basic principles of alloy design for creep resistance are well established by experience. This chapter includes an overview of the creep resistant alloy design methodology in order to discover current trends of creep resistant materials. Attempt has been made to give an account of microstructures and deformation mechanisms where appropriate, as well as information on structural characteristics been included. However, presentation of data has been limited to providing an illustration of critical properties for selected materials. Creep deformation and tensile properties of the material studied, i.e. Esshete 1250 austenitic creep resistant steel, used as a superheater boiler tube in power plants is also included in this chapter.

Quantitative metallography is used to explore the microstructure of the creep resistant steel of the present study. The manual quantitative metallography is sometimes difficult, tedious and time-consuming especially when the microstructure is complicated or of a fine scale. To solve these problems, computer assisted quantitative analysis is explored. Therefore, computer aided analysis on the qualitative and quantitative metallography used for the present research is reviewed in this chapter.

2.1 Design and development of creep resistant steels

The desire for increased efficiency has led eventually to the development and improvement of numerous heat resistant alloyed steels for different parts and components structures in power plants. The end of useful service life of high-temperature components in the power generation industry (the superheater and reheater tubes and headers, for example) is usually a failure by creep or stress-rupture mechanism. The root cause may not be the elevated temperature employed, as fuel-ash corrosion or erosion may reduce the wall thickness so that the onset of creep and creep failures occur sooner than expected. Owing to the severe environment and elevated temperature application, the construction material must be corrosion resistant in addition to creep resistant. Therefore, most of the Fe-Cr and Fe-Cr-Ni alloys are suitable candidates for high temperature components. In this section a brief review of the current status of creep resistant alloys is presented. The aim is to give an overview of the advantages and limitations of the various classes of materials with the emphasis on current and potential applications.

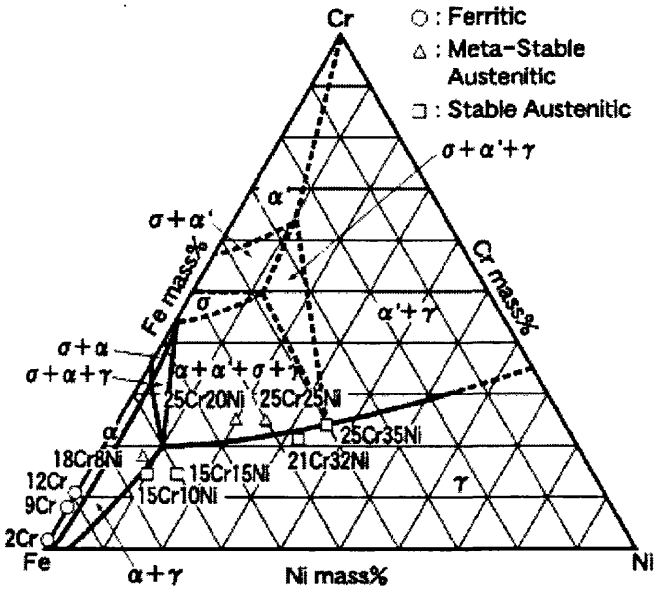

Figure 2: Chemical composition of creep resistant steels in the Fe-Cr-Ni ternary phase diagram at 800°C. [1]

Creep resistant steels are a class of alloys, which have been designed to resist deformation during service at elevated temperatures (more than 480°C). There exists a large variety of creep resistant steels used according to their specification. They are generally classified into ferritic steels and austenitic steels, and further sub-divided into low chromium alloy, martensitic, austenitic, and nickel based alloys. [10] The review of each classes of alloy will be presented. Figure 2 shows the chemical composition of typical creep resistant steels used under high temperatures and stresses in the Fe-Cr-Ni ternary phase diagram.

Generally, austenitic grades are used in situations that require good oxidation resistance and good creep strength for example, in superheater and reheater tubing. However, the drawback is the lower thermal fatigue resistance of these materials. [14] The ferritic grades are used for higher creep strength applications such as thick section pipes and headers due to their better resistance for thermal shocks [3, 10]. Ferritic steels include CrMo low alloy steels and 9-12% Cr martensitic steels. Austenitic steels include 15-18%Cr-8-10%Ni steels, 25%Cr-20%Ni steels of the AISI300 series, high nickel alloys such as 21%Cr-32%Ni steels (Alloy 800H). Figure 3 presents the concept of alloy design and modification for various existing steels specifications to improve their creep resistance.

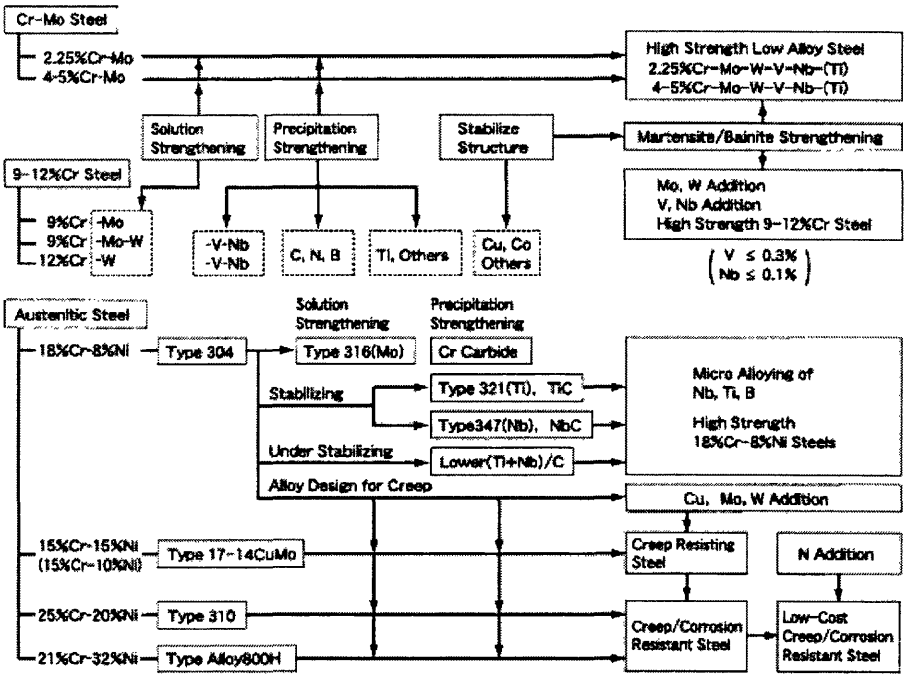

Figure 3: General concept of alloy design for creep resistant steels. [1]

2.1.1 Ferritic steels

Considerable work is being devoted to design stronger ferritic alloys for use at higher temperature application. Ferritic steels are essentially alloys of Fe-Cr providing an attractive level of high temperature strength at a low cost. There are numerous ferritic creep resistant steels ranging from Cr-Mo steels, Cr-Mo-V steels and 9-12 wt.% Cr steels. The characteristics of ferritic alloy steel are:

· Good tensile strength (120 MPa) at temperatures up to 450 °C

· Creep strength at temperatures up to 550 °C

· Excellent weldability with no requirement for post-weld heat treatment

· Resistance to steam oxidation

· Resistance to low NOx corrosion usually by weld overlay or spray coatings.

The following gives a short introduction to the different ferritic steels used in industry.

CrMo Low Alloy Steels (1-3% Cr)

Specifically, these are tubing alloys particularly for the cooler sections of superheaters and reheaters and also for the waterwalls in the temperature range where mild steel becomes too weak in creep. Alloys of this type are sometimes used in thick-section components such as headers and steam pipes. The composition of a selection of available alloys is given in Table 2.

Table 2: Composition of low alloy 1-3% Cr steels.[2, 10]

Alloy		Composition, wt%													
		C	Mn	P	S	Si	Cr	Mo	V	N	Nb	W	B ppm	Al	Ti
Grade 11	Min	0.05	0.3			0.5	1.0	0.44							
	Max	0.15	0.6	0.025	0.025	1.0	1.5	0.65							
Grade 22	Min	0.05	0.3				1.9	0.05							
	Max	0.15	0.6	0.025	0.025	0.5	2.6	1.13							
Grade 23	Min	0.04	0.1				1.9	0.05	0.2		0.02	1.45	5		
	Max	0.1	0.6	0.03	0.01	0.5	2.6	0.3	0.3	0.03	0.08	1.75	6	0.03	
Grade 24	Min	0.05	0.3			0.15	2.2	0.9	0.2				15		0.05
	Max	0.10	0.7	0.02	0.01	0.45	2.6	1.10	0.3	0.012			70	0.02	0.10
1CrMoV		0.25	0.8	0.01	0.02	0.2	1.0	1.0	0.3	0.004				0.01	

The basic microstructure is bainitic with creep strength enhanced by the formation of (usually) chromium carbides. Little development of these alloys was carried out until the advent of Grade 23, which is a modified 2Cr1Mo steel that, it is claimed, does not require post-weld heat treatment [24]. The improvements have been achieved through

the addition of tungsten and boron whilst reducing the carbon content. A further recent development has been Grade 24, where the microstructure has been further refined by modification of the vanadium, niobium, titanium, boron, tungsten and molybdenum levels. This steel has superior long-term creep properties to Grade 23.

9-12% Cr Martensitic Steels

These steels are used in both boilers and in steam turbines for many components such as pipes, headers, rotors, casings and chests with a current maximum operating temperature of ~620°C. Due to these alloys having lower coefficients of thermal expansion and higher thermal conductivities than austenitic steels, they should therefore be more resistant to thermal cycling [10, 14, 34]. The martensitic steels hold the key to high efficiency low cost power plant due to the fact that they are considerably cheaper than austenitic materials [2]. In steam turbines, alloys of this type are used for rotors and blading but also in cast form for steam chests and valve bodies. The evolution of these steels has been thoroughly reviewed by Masuyama [2]. Specific alloys in this class include Grade 9, Grade 91, E911, Grade 92, HT 9, Tempaloy F12M, HCM12 and etc. The chemical compositions are given in Table 3.

Table 3: Composition of 9-12% Cr martensitic steels. [2, 10, 14]

Alloy	Composition, wt%									
	C	Mn	Si	Cr	Mo	V	N	W	B	Other
Grade 9	0.12	0.45	0.6	9	1					
E911	0.12	0.51	0.2	9	0.94	0.2	0.06	0.9		0.25 Ni
Tempaloy F12M				12	0.7			0.7		
Grade 91	0.1	0.45	0.4	9	1	0.2	0.049			0.8 Ni
Grade 92	0.07	0.45	0.06	9	0.5	0.2	0.06	1.8	0.004	
HCM12	0.1	0.55	0.3	12	1	0.25	0.03	1.0		
Grade 122	0.11	0.6	0.1	12	0.4	0.2	0.06	2.0	0.003	1.0 Cu
TAF	0.18			10.5	1.5	0.2	0.1		0.04	0.05 Ni
TB12	0.08	0.5	0.05	12	0.5	0.2	0.05	1.8	0.3	0.1 Ni
NF12	0.08	0.5	0.2	11	0.2	0.2	0.05	2.6	0.004	2.5 Cu
SAVE12	0.1	0.2	0.25	10		0.2	0.05	3.0		3.0 Co, 0.1 Nd
X20CrMoV121	0.20	1.0	0.5	12	1.0	0.3				0.6 Ni
X12CrMoVNbN101	0.12			10	1.5	0.2	0.05			
X12CrMoWVNbN1011	0.12			10	1.0	0.2	0.05	1.0		
X18CrMoVNbB91	0.18			9	1.5	0.25	0.02		0.01	

Tempering of some of the ferritic grade such as 12 wt.% Cr steel with sufficient carbon will result into a martensitic steels (Figure 4a). The resulting microstructure for these

tempered martensite materials is that creep resistance is imparted by controlled precipitation of carbides and nitrides (Figure 4b).

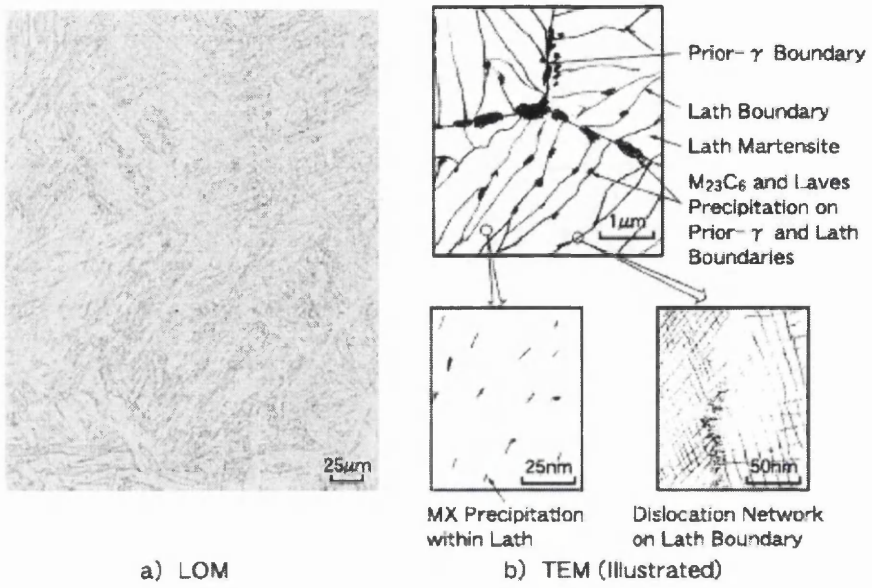

Figure 4: Typical microstructure of tempered martenstitc 9-12% Cr steel.

The characteristics of martensitic alloy steel are:

· Creep strength and long-term structural stability at the operating temperature

· Ac1 temperature consistent with relatively high tempering temperature

· Good weldability with low susceptibility to type IV cracking

· Resistance to steam oxidation

· Low-cost relative to austenitic materials

· Good performance under cyclic and variable load conditions

Figure 5 shows the development progress of ferritic steel used for boilers. Conventional 9% Cr steels are used for temperatures up to ~565 °C. Modified 9% Cr steels by adding alloying elements such as Mo, Nb, V and C allow this grade to withstand higher temperatures of ~593° [13-15, 21]. However, when the temperature exceeds 600°C, the 9% Cr steels become limited by oxidation resistance and 12 % Cr steels or austenitic grade have to be used. Past alloy development programmes have concentrated on improving the creep properties of 9-12% Cr steels. From the baseline

properties of Grade 91, improvements in creep resistance have been made which resulted in alloys such as Grade 92, E911, Grade 122 and TAF.

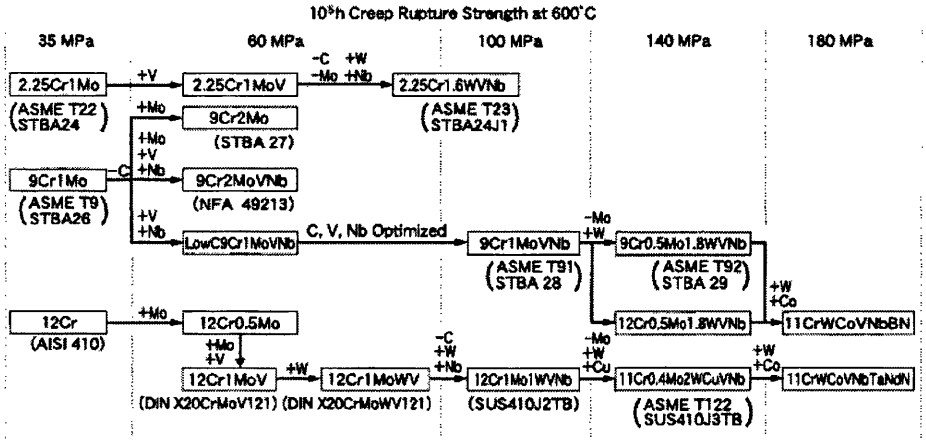

Figure 5: Development progress of ferritic steels for boiler. [1]

Work carried out in Japanese and European programmes has resulted in the improved 9% and 12% Cr alloys that can be used for thick-section components intended for use in the operating range 565-620°C. Materials such as Grade 92 and Grade 122 are also likely to be used in sub-end supercritical units where their higher strengths will allow the use of thinner sections, thereby reducing the threat of fatigue due to thermal cycling. The reduction in weight brought about by thinner walls also has the effect of reducing stresses at the boiler and turbine connections, as well as on the structural steel work, all of which contributes to increased life of components and reduced costs. [16, 23, 32]

2.1.2 Austenitic Steels

Austenitic steels are essentially alloys of Fe-Cr-Ni, which are suitable candidate materials when oxidation resistance and corrosion become important, in addition to creep strength. These stainless steel grades are more expensive than ferritic steels and have higher coefficients of thermal expansion and relatively poor thermal conductivity. [14, 34] Consequently, applications for austenitic steels are restricted to higher temperature boiler tubes, for example the superheater and reheater tubing and to the

specific situations where severe corrosion conditions are expected in power plant structures.

Austenitic steels can be classified into two categories: those contain less than 20wt%Cr and those containing more than 20wt%Cr. These are basically austenitic stainless steel grades originated from the AISI 300 series developed according to their intended service conditions. Austenitic stainless steel grades such as 316, 321, 347, and Esshete 1250 are most commonly used for heat resistant applications. [8, 10] These steels fall into the classification of having less than 20wt%Cr. Some of the alloys contain more than 20wt%Cr for example, 310 and NF709 offering the potential for elevated temperature (more than 650°C) creep resistant applications.

Research and development carried out in 1970's to early 1980's aimed at improving the conventional 18Cr-8Ni alloys, which were originally developed as corrosion resistant materials for chemical use, mainly with respect to their creep strength. Table 4 presents the chemical composition of a selection of austenitic steels.

Table 4: Composition of austenitic steels [2, 10, 14].

Alloy	Composition, wt%											Other
	C	Mn Max	P max	S max	Si max	Cr	Mo	N	Nb	Ni	B	
AISI 302	0.15	2	0.045	0.03	1	18				9		
AISI 304	0.08	2	0.045	0.03	1	18				8		
AISI 321	0.08	2	0.045	0.03	1	17				11		0.15 Ti
AISI 347	0.08	2	0.045	0.03	1	17				11		0.8 Nb+Ta
AISI 316	0.08	2	0.045	0.03	1	17	2.5			12		
AISI 309	0.2	2	0.045	0.03	1	23				14		
AISI 310	0.25	2	0.045	0.03	1.5	24				19		
ASME TP347HFG	0.08	1.6			0.6	18			0.8	10		
Tempaloy A-1	0.12	1.6			0.6	18			0.1	10		0.08 Ti
Tempaloy A-3	0.05	1.5			0.4	22		0.15	0.7	15	0.002	
Super304H	0.1	0.8			0.2	18		0.1	0.4	9		3.0 Cu
HR3C	0.06	1.2			0.4	25		0.2	0.45	20		
HR6W	0.10	2.0	0.03	0.03	1.0	23			0.4 max	40		6.0 W, 0.2 max Ti
NF709	0.15	1			0.5	20	1.5		0.2	25		0.1 Ti
Esshete 1250	0.09	6	0.03	0.003	0.6	15	1	0.04		10	0.004	0.02 Al, 0.9 Nb, 0.25 V, 0.14 Cu

Austenitic stainless steels such as Esshete 1250 with the approximate composition of 16wt% chromium, 10wt% nickel and additions of niobium are one of the heat resisting

steels with high creep strength for use as superheater boiler tube material in the UK power stations. It is one of the higher alloyed steels found to have resulted in a major improvement over the 300 series stainless steels, as far as creep resistance is concerned. From 1980's to the early 1990's, improvements were made on the creep strength of conventional 20-25Cr alloys, which have superior oxidation and corrosion resistance than lower chromium (18-20Cr) austenitic alloys. Masuyama has presented a comprehensive review of historical evolution of power plant heat resistant steels [1]. According to this review, research during the last decade has generally focussed on developing cost effective high strength ferritic steels capable for operating in conditions up to 620°C instead of austenitic steels. However, there is still a place for austenitic steels which are primarily used in the finishing stages of superheater or reheater tubing, where oxidation resistance and fireside creep characteristics become important. Therefore, there has been a considerable development with respect to austenitic stainless steels. Oak National laboratory have developed some improved grade to 347 [47]. European work had also modified Esshete 1250 to develop higher creep resistant steel grades (Figure 6).

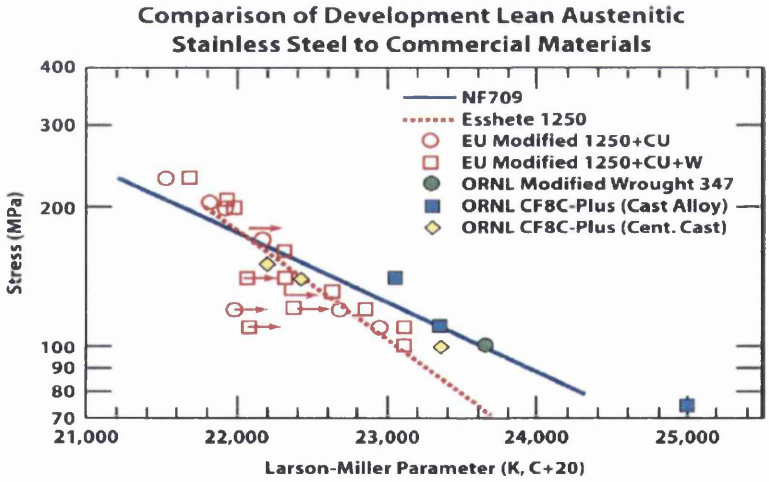

Figure 6: Plots of Larson-Miller Parameter (LMP) versus test stress for commercial grade of NF709 and Esshete 1250 stainless alloy together with new developed steels grade. [47]

Nickel based steels

Nickel based alloys are vitally important to the power generation industry because of their ability to withstand a variety of severe operating conditions involving severe corrosion environments, elevated temperatures (>700°C), high stresses (>450MPa), and combinations of these conditions. Nickel and nickel based alloys have many applications, most of which are geared to resistance to corrosion and/or heat. Examples include aircraft gas turbines, steam turbine power plants, turbochargers and valves in reciprocating engines and etc. Iron-base alloys are less expensive, in general, than the nickel-base alloys. The strength at temperature and durability of iron base alloys is, of course, lower than that of the nickel-base alloys. For this reason, nickel based alloys are used for extremely high temperature with severe corrosion conditions, let's say beyond 700°C [10]. The earliest precipitate hardening nickel based alloy, Nimonic 80 was developed in the UK in 1941. This nickel based alloy with 2.25%wt Ti and 1% Al forms the $Ni_3(Al,Ti)$ precipitates. Al has been found to be detrimental for hot corrosion resistance and when combined with Ti, the result is slightly beneficial. There have been improvements over the years to modify this alloy by additions of microalloying elements such as Mo, Co, B etc. Considerable effort has been expended to develop nickel based alloys with improved hot corrosion resistance. The effect of chromium is dominant in establishing hot corrosion resistance and at least 15%wt Cr is needed to produce reasonable good resistance at elevated temperature. [10] The chemical composition of some Ni based alloys is presented in Table 5. The characteristics of nickel based alloy steel are:

- High creep strength at temperatures up to 1150°C and long-term structural stability at operating temperature
- Good weldability
- Good performance under cyclic and variable load conditions
- Adherent oxide layer for good oxidation resistance, resistance to hot salt corrosion and steam oxidation.

Table 5: Chemical composition of Ni Based alloys. [2]

Alloy	Composition, wt%											Other
	C	Mn	Si	Cr	Mo	Fe	Co	Al	W	B	Ti	
IN617	0.07	0.5	0.5	22	9		12.5	1				
Haynes 230	0.10	0.5	0.4	22	2	3	5	0.3	14	0.015		0.02La
Haynes 242	0.03	0.8	0.8	8	25	2	2.5	0.5		0.006		0.5 Cu
C263	0.06	0.6	0.4	20	5.8	0.7	20	0.45			2.125	

2.2 Chemical composition and microalloying elements

Creep resistant alloys used for high temperature applications can have a wide range of compositions. Microalloying elements are used to modify the steel for improved mechanical properties. We know that creep resistant steels are corrosion resistant as well, thus these alloys must have sufficient chromium content to protect against the corrosive effects of exposure to oxygen. The role of alloying elements are summarised as follows.

Chromium (Cr) is present at amounts of at least 10.5%wt to improve susceptibility to oxidation and heat resistance at high temperatures. However, Cr promotes grain growth, so it is rarely used as an alloying element on its own. Nickel (Ni) is present to limit grain growth at sustained high temperatures of exposure [10]. Moreover, it is also an austenite stabiliser, which allows austenitic structures to be stable at all temperatures. Manganese (Mn) is introduced as a substitute for Ni during its shortages in the global market and for economical reasons. In addition, it is also used to increase solubility of nitrogen (N) in austenite. N can increase creep life in alloyed steel by acting like carbon (C) to precipitate the stable form of titanium (Ti) or niobium (Nb) nitrides. Both of these alloying elements: Mn and N, stabilise the austenite matrix and provide increased strength and strain hardening behaviour [14].

Stabilising agents such as Nb, Ti and vanadium (V) are added to improve creep properties by precipitating fine MX carbides/nitrides or carbonitrides intragranularly [17, 22, 41, 42]. For example, addition of small amounts of Nb raises the high temperature strength due to the fact that Nb does not easily to dissolve at high temperatures [43, 44]. Optimum C content is considered to be between 0.05 to 0.10%wt in order to satisfy high temperature strength, good weldability and formability which required for creep resistant steels [43].

It is well known that Nb added to a wide range of steels to improve processing, microstructure and mechanical properties, therefore performance. Meyer outlined the

historical developments of Nb as a microalloying element in his paper [44]. Nb has a low affinity to oxygen but a high affinity for carbon and nitrogen that could form face centered cubic compounds (NbX) which are especially favoured in steels. The sufficient solubility in austenite and the potential of precipitation in austenite and ferrite make it unique, and is regarded as one of the most effective microalloying elements in alloy steels. The special effects Nb has are improvements in mechanical properties that could be achieved even with extremely low concentrations of 1 niobium atom in 10,000 iron atoms. [43]

Molybdenum (Mo) is also an important element that determines the high temperature strength of creep resistant steels especially in ferritic grades. It is a ferrite stabiliser and enhances solution hardening and precipitation hardening by carbides. The addition of 2-5% of Copper (Cu) has long been known to improve the creep properties of stainless steels. [10, 45] Addition of aluminium (Al) has long been a goal of austenitic alloys to improve high temperature oxidation resistance. Tungsten (W) is a new alloying element added to improve creep strength by solid solution strengthening or by stabilisation of the $M_{23}C_6$ carbides. Boron (B) is considered as a 'surface active element' that may retard the coarsening of grain boundary of $M_{23}C_6$ carbides in ferritic steels and refine carbide structures in austenitic steels. [21]

The additional use of metallic alloying elements, primarily as a result of their influence on the phase transformation in steel, provide an even greater control over microstructure, with consequent benefits in the mechanical properties of the steel. For the design of creep resistant alloys, heat treatment with the aim of adjusting the microstructure and the effect of alloying elements induce a change in creep resistant steel microstructure before and after service conditions. Moreover, changes are inevitable over the long term service so that there must be sufficient solid solution strengthening to ensure long term creep resistance. Alloying elements greatly improve creep strength of steels, however the proportion of each element that has to be added must be chosen, in such a way as to maximise the strengthening effect and avoid precipitation of detrimental phases such as sigma phase, Laves phase and other intermetallic phases.

2.3 Structure of creep resistant steels

It is worth noting at this point that all metals are crystalline in structure. In practice, they are composed of many grains and these are typically the principal feature of the alloy microstructure which influences the properties of the material. The general concept for developing a creep resistant steel with good high temperature strength is to produce a target service microstructure consisting of a high strength matrix phase with a fine dispersion of stable precipitates which are resistant to coarsening. Hence, creep resistant alloyed steels are mostly two phase alloys in which the principal phase (matrix) is predominant and the precipitated phase is in the form of a secondary phase.

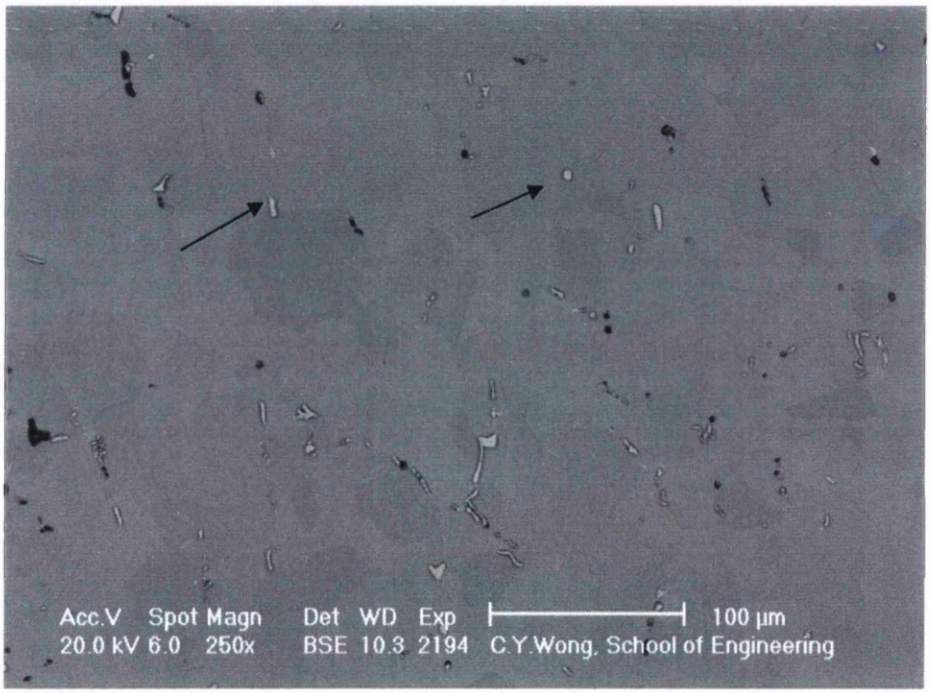

Figure 7: Backscattered scanning electron micrograph of Esshete 1250 austenitic creep resistant steel.

The microstructure of an austenitic creep resistant steel is illustrated in Figure 7. Its austenitic matrix contains some precipitation of carbides. The structure is typical of alloy metals in the annealed condition. It is built up of a number of crystals of the same composition, given the name austenite in metallography. The addition of niobium to the austenitic steel results in precipitation of alloy carbides, which are the bright contrast particles pointed by arrows in Figure 7.

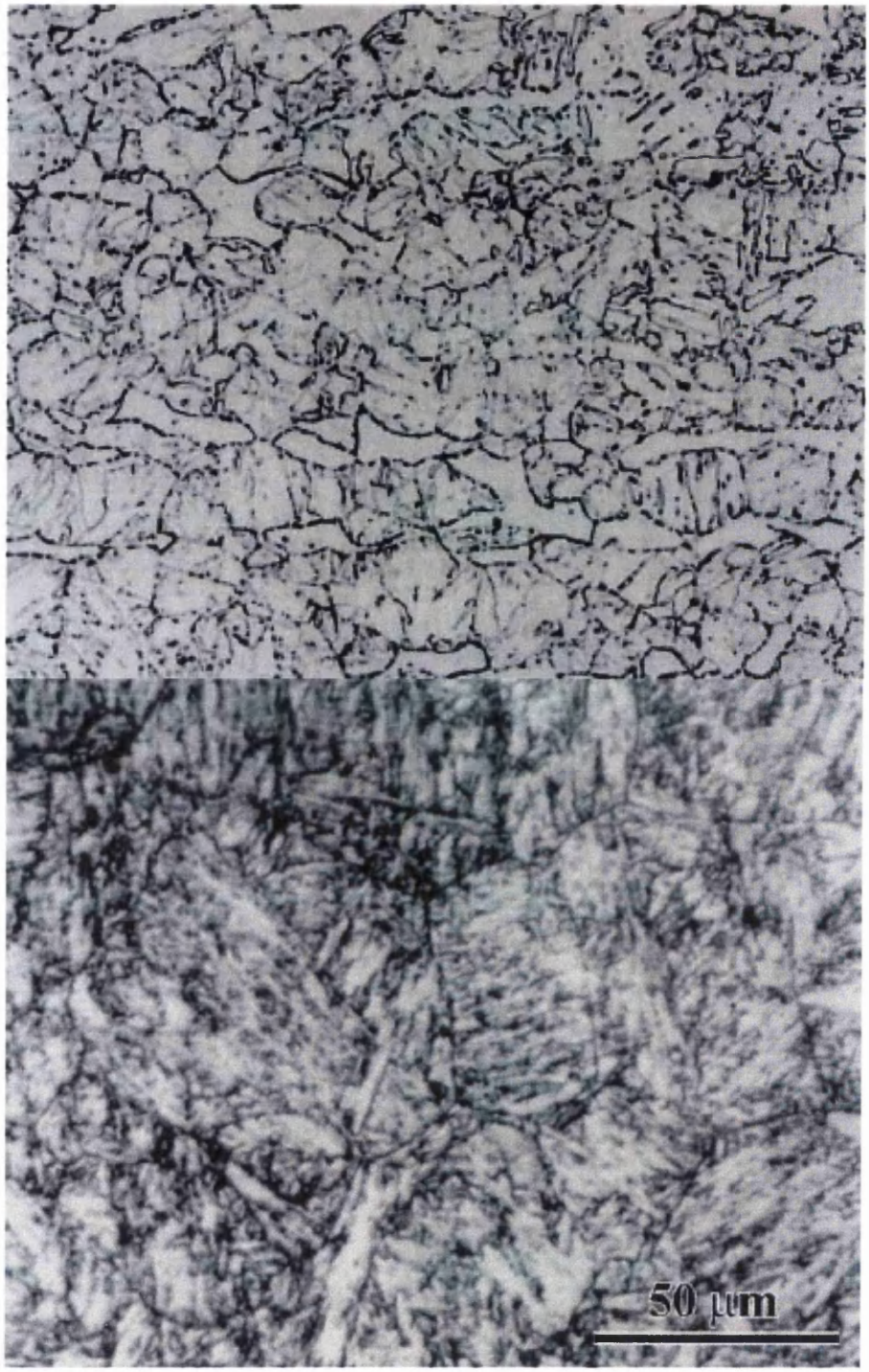

Figure 8: (a) Typical optical micrograph of 12Cr–2W–Cu–V–Nb steels. [71] and (b) Typical optical micrograph of high Cr ferritic steel. [23]

The vast majority of the 9-12% creep resistant steels have bainitic or martensitic microstructures in the normalised condition (Figure 8) [39-41]. After normalising, the

steels are tempered at high temperatures to produce a 'stable' microstructure consisting of a variety of alloy carbides in a ferritic matrix. For austenitic creep resistant steels, the primary precipitation of alloy carbides is known to be preventing sensitisation. However, the occurrence of finely dispersion MX carbides particle contributes to creep strength. The known precipitates in most families of creep resistant steels will be discussed at a later section (2.6.2). These precipitates determine the microstructure of creep resistant steels and are crucial in the development of creep strength.

Creep strength being dependent on the stability of the microstructure. The microstructural stability of creep resistant steels at high temperatures is of some concern and has been the subject of a number of investigations [20-21, 39, 45 46]. Creep resistant alloys must have a stable microstructure which contains fine alloy carbides to resist dislocations motion. It is widely accepted that creep resistant steel have been developed by increasing the strength via solid solution strengthening and precipitate strengthening. Sourmail had made a detailed review on precipitation strengthening in creep resistant austenitic steels [42]. Hald and Korcakova had investigated the long term stability of precipitate particles and their influence on creep stability of 9-12% Cr steels [21].

2.4 Strengthening mechanisms in creep resistant steels

Alloy steels cover a wide range of the strength spectrum from low yield stress levels (around 200 MPa) to very high levels (approaching 2000 MPa). These mechanical properties are usually achieved by the combined use of several strengthening mechanisms, and in such circumstances it is often difficult to quantify the different contributions to the strength. Like other metals, creep resistant steel can be strengthened by several basic mechanisms, the most important of which are:

- Strengthening by grain size control
- Solid solution strengthening by interstitial and substitutional atoms
- Strengthening by second phase precipitates

2.4.1 Strengthening by grain size control

Firstly, we should note that all metals and alloys are crystalline. All the metal atoms sit in a regular crystal lattice and a bulk alloy consists of many grains which are oriented in different directions. The smaller the size of the grains in the alloy, the higher is the alloy strength. This is strengthening by grain size control as expressed in the Hall-Petch equation where the flow strength is inversely proportional to the square root of the grain diameter (*Equation 1*):

$$\sigma = \sigma_0 + k/\sqrt{d} \qquad \text{(Equation 1) [47]}$$

where σ_0 and k are constants, d is the mean grain size. The grain size dependence is related to the length of a slip band and that the maximum slip band length is determined by the grain size. The reason for this great increase in strength is that grain boundaries act as barriers to dislocation movement at lower temperatures. Grain

refinement is the only way to simultaneously improve strength and toughness of the steel at room temperature. The refinement of the grain size of ferrite provides one of the most important strengthening routes in the heat treatment of steels. The grain size effect on the yield stress can therefore be explained by assuming that a dislocation source operates within a crystal causing dislocations to move and eventually to pile up at the grain boundary. The pile-up causes a stress to be generated in the adjacent grain, which, when it reaches a critical value, operates a new source in that grain. In this way, the yielding process is propagated from grain to grain. The grain size determines the distance dislocations have to move to form grain boundary pile-ups, and thus the number of dislocations involved. With large grain sizes, the pile-ups will contain larger numbers of dislocations, which will in turn cause higher stress concentrations in neighbouring grains. In practical terms, the finer the grain size, the higher the resulting yield stress and, as a result, in modern steel working much attention is paid to the final ferrite grain size.

Fine second phase particles have long been known to limit grain growth by pinning the grain boundaries. The interaction of second phase particles with grain boundaries exert a retarding force therefore, it is important to understand the interrelationship. Zener [60] proposed that the driving pressure of grain growth due to the curvature of the grain boundary would be counter by a pinning pressure exerted by the particles on the boundary. The relationship in the original analysis proposed by Zener does not give information about the actual process of grain growth, the growth rate or size distribution of grains. However, it has played an essential role in the subsequent development of theories concerning annealing phenomena in particle containing materials.

Grain growth occurs in polycrystalline arrays so as to reduce the total grain boundary energy. This motion could be inhibited by second phase particles. As we know that grain boundaries are defect sites which favour precipitation, thus second phase precipitates on grain boundaries might have an important effect on grain growth. The drag on the boundary due to an array of insoluble, incoherent spherical particles is because the grain boundary area decreases when a boundary intersects the particle (Figure 9). Therefore, to move away from the particle requires the creation of new

surface. The net drag force on a boundary of energy γ per unit area due to a particle of radius *r* is given by the Zener Drag effect (Figure 10).

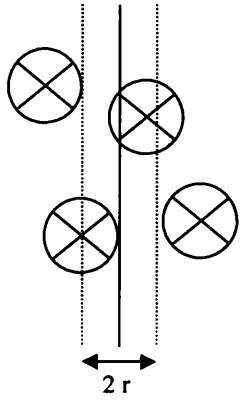

Figure 9: Grain boundary motion across second phase particles. [56]

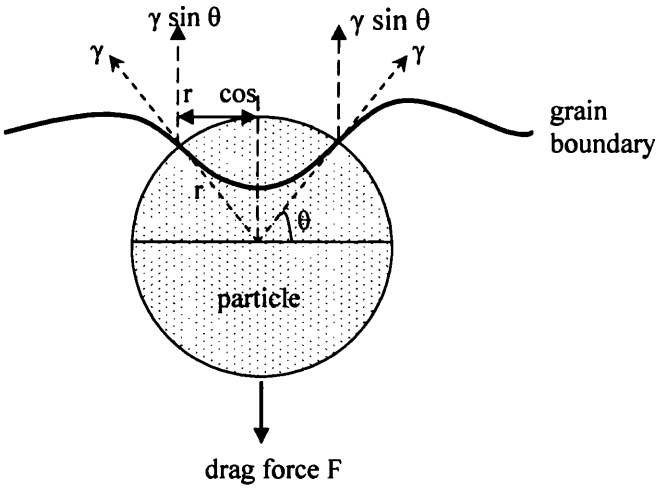

Figure 10: Zener Drag effect. [60]

C.S. Smith outlined the fundamental principles of grain growth based on the Zener equation [74]. In general consideration for the drag force exerted by a single particle, the interaction of a boundary of a specific energy, γ with a spherical particle of radius, *r* which has an incoherent interface is illustrated in *Figure 10*. If the boundary meets the particle at an angle *θ*, as shown in *Figure 10*, since *γ sin {θ}* = force per unit length, the restraining force on the boundary would be:

$$F = \gamma \sin\{\theta\} \times 2\pi r\{\theta\}$$ *(Equation 2) [59]*

Where γ = specific energy (J/m^2)

θ = angle (°)

r = radius of the spherical particle (nm)

In order to obtain the maximum restraining effect, at $\theta = 45^o$,

$$F_{max} = \gamma \pi r \qquad \textit{(Equation 3) [59]}$$

Having considered the pinning force from a single particle, suppose now we need to consider that there is a random array of spherical particles of volume fraction, f with the number of particles per unit volume, N given by:

$$N = \frac{f}{\frac{4}{3}\pi r^3} \qquad \textit{(Equation 4) [59]}$$

Where f = volume fraction of random array of particles

N = number of particles per unit volume

r = spherical particles radius (nm)

Only those particles within a distance $\pm r$ can intersect a plane. The number of particles intersected by a plane of area $1\mu m^2$ will therefore be:

$$n = 2rN = \frac{3f}{2\pi r^2} \qquad \textit{(Equation 5) [59]}$$

From equations 3 and 5, the drag pressure, P is then often expressed as:

$$P = F_{max} n = \frac{3\gamma f}{2r} \qquad \textit{(Equation 6) [59]}$$

P, as given by equation 6, is commonly known as the Zener pinning pressure. This may be a significant pressure if the particles are fine [52, 56].

Austenite grain size exerts a major influence on the microstructure and properties of subsequent transformation products. Grain growth in austenite and ferrite is limited by particle pinning and by solute segregation at grain boundaries. Particle

pining of grain boundaries is vital in controlling the grain size during high temperature processing of austenite for example, carbonitride formation in HSLA steels and AlN in Al killed plain carbon steels. In either case, the grain size is much lower than in the absence of precipitated particles. Many experimental and theoretical studies of grain growth have been performed over the years. A paper by Militzer and et al. illustrates some important characteristics of austenite grain growth in commercial Al-killed plain carbon steel [75]. It relates theoretical predictions to experiments on commercial alloys. P was used as a fitting parameter accounting for both particle pinning and solute drag to force agreement between theory and experiment. P was found to be linear in temperature and time dependent in the higher carbon steels but showed more complex behaviour in low carbon steels. Hillert [76] made an elegant analysis of grain growth and according to the statistical treatment derived from his work, a particle size distribution in grain growth similar to that for diffusion controlled particle coarsening. His work also included the effects of second phase particles in the evolution of the grain size distribution and found that a steady state particle size distribution was unattainable in the presence of particle pinning.

The most promising development in the understanding of grain growth is provided by computer simulation. Modelling and numerical simulation of kinetics grain growth was facilitated by greater algorithm sophistication and computing power. Krill and Chen had work on the grain size analysis of 304 austentic stainless steel. [77] They claim that their model is in better agreement with Hillert. A statistical theory of grain growth claimed to be more rigorous than earlier efforts was developed by Abbruzzese and Lucke [56]. Their prediction of the effects of pinning on grain growth is different from Hillert work. The particle pinning term was left as a parameter and this pinning term was used as a parameter in data filling for later works.

For creep resistant steels used at high temperature, the grain size effect is not a significant strengthening mechanism. The most distinctive aspect of strengthening of creep resistant steel is the role of the solutes atoms such as Nb, Ti, V, Mo, C and N. These elements also play a vital part in interacting with dislocations.

2.4.2 Solid solution strengthening

In creep resistant alloys, carbon or nitrogen atoms can diffuse into the matrix to form interstitial solid solution. As atoms of different metals are of a different size, their inclusion in the lattice leads to a distortion of the lattice and the crystal planes become less smooth. Since deformation of the crystal takes place by the sliding of crystal planes over each other, any distortion of the lattice by atoms of other metals will increase the force necessary to slip the planes over each other. This is known as solid solution strengthening. C and N are added to alloy as a solid solution strengthening element in a non stabilised grades but mainly by precipitation strengthening when Nb, Ti or V are present.

In practical terms, the contribution to strength from solid solution effects is superimposed on hardening from other sources, e.g. grain size and dispersions. Also there exists a strengthening increment, like that due to grain size, which need not adversely affect ductility. In engineering alloyed steels, solid solution strengthening is far from negligible factor in the overall strength, where it is achieved by a number of familiar alloying elements, e.g. manganese, silicon, nickel, molybdenum, several of which are frequently present in a particular steel and are additive in their effect. These alloying elements are usually added for other reasons, e.g. Silicon (Si) to achieve deoxidation, Mn to combine with sulphur (S) or Mo to promote hardenability. Therefore, the solid solution hardening contribution can be viewed as a useful bonus.

2.4.3 Strengthening by second phase precipitates

It is known that second phase particles can exert a strong pinning effect on boundaries, with the pinning pressure being determined primarily by the size, volume fraction, interface and distribution of the particles [52-55]. Since the size, distribution and volume fraction of second phase particles in an alloy are affected by composition and thermomechanical processing, second phase particles may be used to control the microstructure. As in many steels, precipitation of fine particles can control the grain size via a pinning effect during the recrystallisation of the steel, alternatively, it could also strengthen creep resistant steels by hindering dislocation motions [22, 46, 51]. A

two phase structure is normally stronger than a single phase structure. The degree of strengthening depends on the relative sizes of the different phases and their distribution. The presence of hard, small particles of a second phase at grain boundaries and within the grains impedes the passage of dislocations through the crystal lattice and a higher force or stress is needed to deform the metal or alloy. This mode of strengthening is called dispersion hardening and is particularly effective at high temperatures. Nb alloyed creep resistant steels are two-phase alloys in which the principal phase (matrix) is predominant and the precipitated phase is in the form of a secondary phase. The formation of fine dispersions of precipitates of second phase can be controlled by heat treatment known as ageing. The smaller the particles or precipitates and the more of them present, the greater the degree of strengthening. The deformation of creep resistant alloy takes place via slip in the matrix. When mobile dislocations encounter the precipitated phase, these small, hard, not very ductile secondary phase particles become difficult obstacles to dislocation movement: the force produced along the dislocation line may be enough to shear the small precipitate particle, or the precipitate may be bypassed by the dislocations. Thus, considerable strengthening can be obtained by relatively small volume fractions of particles provided they are very fine in size and well dispersed. This fact gives us a clue to the design of microalloyed creep resistant steels, since it is unlikely that significant strengthening of creep resistant steel can be achieved from just control of grain size or solid solution strengthening. The use of small fractions of fine carbide particles to provide dispersion hardening of creep resistant steels is reported in the literature [21, 23, 52]. The philosophy of creep resistant alloy development is to increase the volume fraction of strengthening precipitates by replacing alloy carbides with other more stable carbides/nitrides for example, NbC and TiN precipitates, while at the same time, releasing chromium to the matrix to offer enhanced corrosion resistance.

The precipitation of fine particles is an essential way to control the microstructure and properties of creep resistant steels. During high temperature exposure at which grain growth occurs, the second phase particles may not be stable. Particle coarsening is one of the most important degradation processes for creep resistant steels. The growth process of precipitate which follows after the nucleation stage is considered to begin when the second phase has reached appreciable size and the degree of supersaturation of the matrix has become very slight [59, 60].

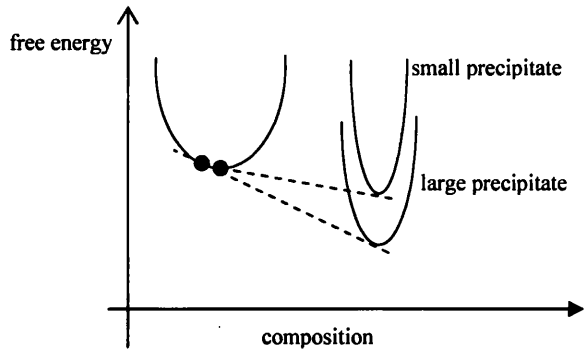

Figure 11: Coarsening of precipitates [56].

The microstructure of creep resistant steels is always unstable since the total free energy is not at a minimum. Therefore, a high density of small precipitated particles will tend to coarsen to a lower density of larger particles with a smaller total interfacial area. Coarsening is driven by surface energy. The surface to volume ratio for a spherical particle is $3 / r$, where r is the particle radius. The particle therefore has an extra energy of $3\ \sigma / r$ where σ is the interfacial energy per unit area. It follows that (*Figure 11*) the equilibrium compositions will be altered so that there will be a diffusion flux from the small to the large particles, leading to coarsening [38]. Lifshitz and Sloyzov have outlined the principles of second phase particle coarsening kinetics [53]. Particle coarsening is observed to follow this well known Ostwald ripening equation:

$$r^3 - r_0^3 = \frac{8\sigma VDtC^s}{9RT} \qquad \textit{(Equation 7)} \quad [53]$$

Where r = particle radius at time t

r_0 = particle radius at time 0

σ = interfacial energy (grain boundary energy=800.10^{-7} J/cm)

V = molar volume of precipitate

D = diffusivity of solute in matrix

t = time for particle coarsening

C^s = concentration of saturated solution

R = universal gas constant (8.31 J/mol-K)

T = absolute temperature (K)

From Equation 7, the mean radius cubed varies as time, as opposed to the radius squared in growth calculations. Coarsening is thus a much slower process than precipitate growth, as is reasonable in that growth of one particle only occurs by cannibalising other particles. The key material variables of precipitate coarsening are solubility and diffusion coefficient. An alloy system of sparingly soluble particles made of a slow diffusing solute will be stable against coarsening. Second phase particles of interest in alloyed steels are largely carbides, nitrides, carbonitrides, oxides and sulphides rather than solid solutions. At least two diffusivities and two concentrations are involved in determining the coarsening behaviour. This coarsening phenomenon is undesirable due to causing degradation of creep resistant properties at elevated temperatures and also leading to loss of grain boundary pinning effect, which strengthens the steel during creep deformation. To minimise coarsening, it is necessary to reduce the interfacial energy, so that to minimise the diffusion coefficient and to minimise the solubility of solute in the matrix, hence diffusion gradients would be small. The influence of chemical composition on coarsening rate also is essential to the understanding of long term microstructure stability.

Most of the creep resistant alloys are strength at elevated temperatures is due to their dislocations dissociated by climb into configurations which cannot glide. The mechanisms, which are employed to enhance creep strength, are broadly the same as those used to improve ordinary temperature strength, i.e. solution hardening, precipitate strengthening and dispersion hardening. In this context, the difference between one creep resisting material with another depends on the relative persistence of strengthening mechanisms with increase of temperature.

2.5 Precipitates in creep resistant steels

Precipitation in creep resistant steel is more complex due to it occurring during high temperature service exposure. Lots of precipitates could form and some of them can be used to design the engineered microstructure for creep resistance. In contrast, others precipitate which may occur could lead to deterioration of the microstructure at severe engineering environment. Consequently, the microstructural design concept for creep resistant alloys also includes controlling precipitation along grain boundaries and eliminating deleterious aging induced phases such as sigma and Laves phases.

This section is a review of common precipitates in high alloyed steels. Precipitate phases are important for both strengthening and for grain size control in ferrite and austenite. Creep resistant steels contain several precipitate types, which form either during the final heat treatment or during subsequent creep exposure of the steel. Prediction of long term stability of precipitated particles and their influence on creep stability of creep resistant steels has to rely on the volume fraction and mean particle sizes and evolution of these parameters as functions of temperature, time, and stress [21, 52, 58]. Carbides, nitrides/carbonitrides and intermetallic phases are the common types of precipitates frequently appearing in creep resistant steels. [17, 21, 22, 42, 61] Carbides are mainly MC, M_6C, M_7C_3 and $M_{23}C_6$. Nitrides/carbonitrides are MN, M_2N, M(CN) and M_2NC. Intermetallic phases include sigma (σ), chi (χ), and Laves (η) phases.

The formation of carbide particles occurs when strong carbide forming elements are present in alloyed steels. MC precipitates have a face center cubic (fcc) structure and often form on dislocation sites within the matrix, on stacking faults, on twin or grain boundaries. After sufficient ageing, they have either spherical or cuboidal shape, e.g. NbC is spheroidal in shape. Small MC particles may have a strong effect on the microstructure of creep resistant steels. They could strengthen the steel by pinning dislocations and inhibit grain growth during exposure to elevated temperatures. MC precipitates are very stable and easily form just below the solidification temperature. They are not easily dissolved during heat treatment and thus restrict grain growth. M_6C was known as η-carbide with a fcc structure which only forms after long ageing time.

It is rarely documented but has been reported to be Mo [39, 40] rich or Nb rich [63, 64]. $M_{23}C_6$ particles have a fcc structure forming during tempering and located on grain boundaries and sub-boundaries (Figure 12(a)). This carbides form during low temperature heat treatments and also in the service temperature. They precipitate in the grain boundaries. Cr, Fe, Mo and W are significantly soluble in this carbide [40, 42, 65].

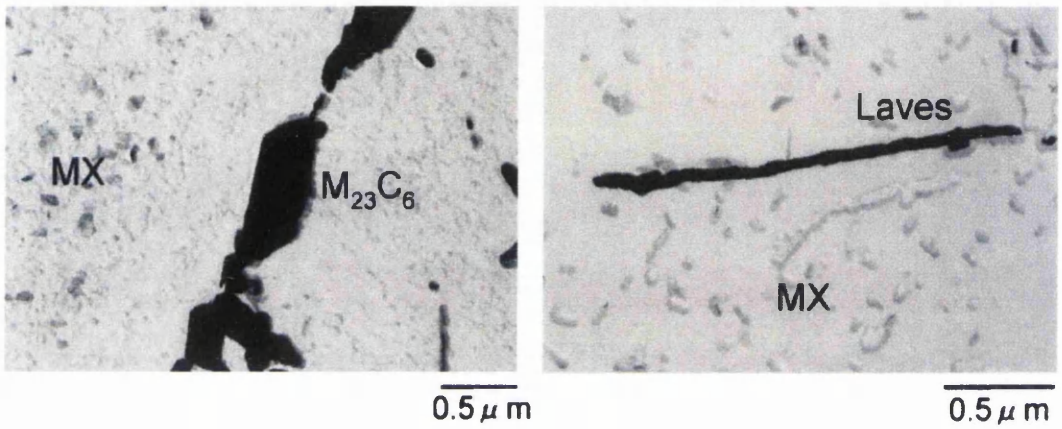

Figure 12: TEM images from extracted replica of 12Cr–2W–Cu–V–Nb steels showing the morphology of (a) MX, $M_{23}C_6$ (before creep exposed) and (b) Laves phase (after 3yrs creep exposed). [71]

Nitrides such as MN with fcc structure are found in alloyed steels such as in austenitic stainless steels 316 and 321, the form of MN is either the stable NbN or the TiN and tend to suppress formation of $Cr_{23}C_6$. [66] (Figure 13) VN is also found in alloyed steels and it is claimed to have significant contribution to creep strength (Figure 12 (a)) [71]. Carbonitrides such as Nb(CN) and V(CN), also have an fcc structure and found to increase creep strength when they are finely distributed in the matrix of alloyed steels [26-67].

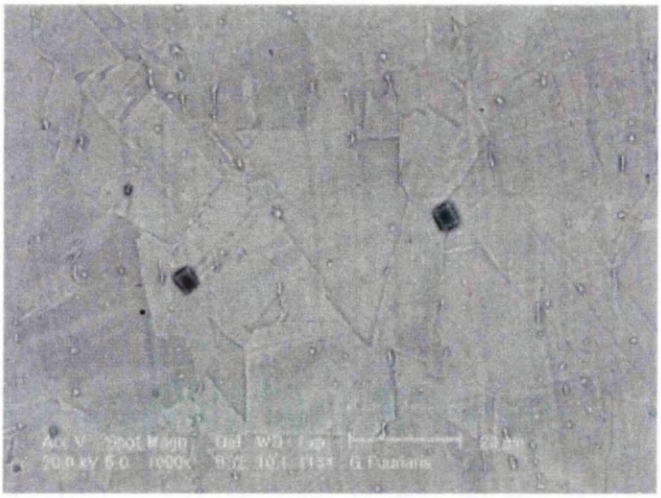

Figure 13: SEM backscattered micrograph of 321H austenitic stainless steel showing TiN precipitates at grain boundaries following solution treatment at 1100°C for 30 mins.

For creep resistance, Nb is added for two main purposes, first, to stabilise the steel and prevent sensitisation and weld line intergranular corrosion. Second to form stable finely dispersed carbides. Keown and Pickering had summarised the role of Nb in stainless steel with major emphasis on the physical metallurgy [43]. NbC and NbN are commonly found in stainless steels. NbC is being more soluble than NbN in austenite. [43] NbC forms during solidification as eutectic with austenite in spheroidal form whilst, NbN largely forms directly from the melt as small cuboids. Despite their main function to prevent sensitisation, primary NbC and NbN found to be controlling the grain growth during recrystalisation, whilst secondary dispersed NbC are known to enhance the creep strength of alloy steels. There is also evidence that Nb(CN) is formed due to nitrogen filling the interstitial vacancies into NbC lattice. [26, 41, 42] These MX precipitates can be found to increase creep strength in martensitic creep resistant steels [23].

Nb can also form some intermetallic compounds in creep resistant alloys and most of them could deteriorate the properties of the steel. One of the particular examples is sigma phase which is generally based on the complex cubic structure of FeCr. In addition, alloys containing Ti and Mo also form sigma phase. Another common intermetallic compound which forms in both ferritic and austenitic steels

containing Nb is Laves phase. This phase is isomorphous with close packed hexagonal (hcp) structure and normally forms with higher Nb contents [64].

Sigma phase is an undesirable precipitate which can appear in several binary, tertiary and quarternary system such as Fe-Cr, Fe-Mo, Fe-V, Fe-Mn, Fe-Cr-Ni, Fe-Cr-Mo, Fe-Cr-Mn and Fe-Cr-Ni-Mo. Its precipitation is very frequent in stainless steels and will occur in the austenitic, ferritic and also duplex structure. Figure 14 show sigma phase in austenitic stainless steel after long term creep exposure. Sigma phase has very low carbon and nitrogen solubility, hence carbide and nitride precipitation should happen before sigma precipitation and sigma phase is incoherent with austenite and its nucleation is difficult. Preferential nucleation of these phases is on grain boundaries and especially at triple points [68, 69]. The precipitation of this phase not only causes loss in ductility and toughness of the steel but also reduces its corrosion resistance by removing chromium and molybdenum form the austenitic matrix [65].

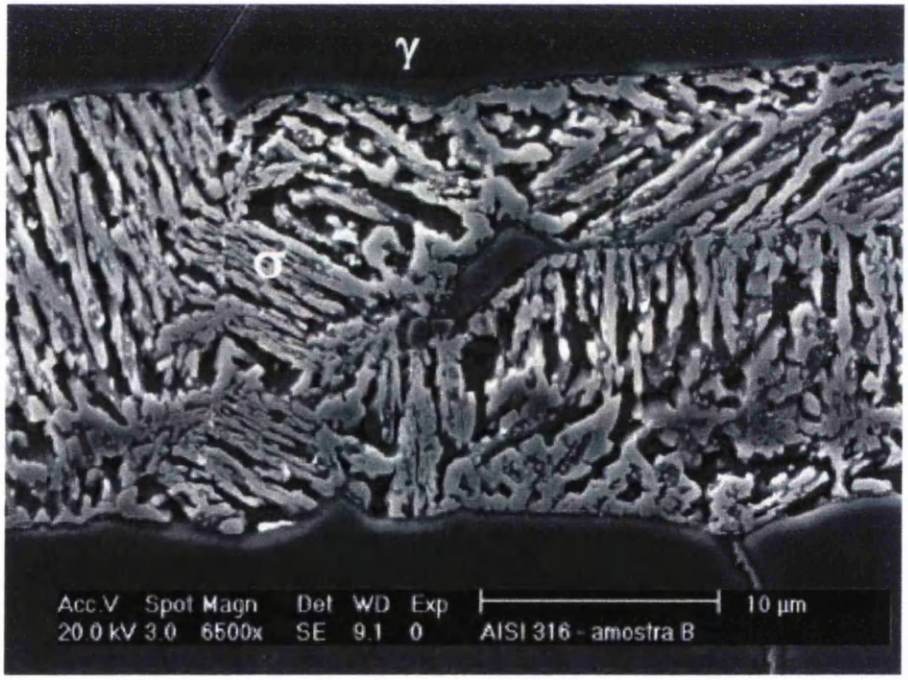

Figure 14: Sigma phase precipitation inside ferrite of creep exposed sample of 316L austenitic steel at 550°C for 85 000h (150MPa) etched with V2A Beize. [68]

Laves phase (Fe_2M) is an intermetallic compound forming in W and Mo containing steels with a tetragonal close packed (TCP) structure, e.g. Fe_2W or Fe_2Mo. It is not present after tempering, but precipitates on grain boundaries and sub-

boundaries during creep testing (Figure 12b) [70, 71]. This phase is hard and brittle and its formation causes loss of toughness. However, it is suggested that fine precipitation of $Fe_2(W,Mo)$ Laves phase improves creep resistance in ferritic steels under service conditions [71].

2.6 The phenomenology and mechanism of creep

When considering the resistance of materials to deformation and failure over long-term periods under stress conditions at high temperatures, particular attention must be given to creep resistance. Creep is a time dependent deformation resulting from an externally applied load (stress) to a material over a period of time. At temperature greater than 0.4 of the melting temperature, T_m (in degrees Kelvin), material will slowly deform under loads which would not cause any plastic deformation at room temperature. Deformation under certain conditions will, if allowed, culminate in rupture. Because an increase in either stress or temperature can reduce the time to rupture, attention must be given to both factors during investigation of a failure by a stress-rupture mechanism. The end of useful service life of the high-temperature components such as boiler (the superheater and reheater tubes and headers, for example) is usually a failure by a creep or stress-rupture mechanism. This can occur particularly by two mechanisms: short-term overheating and high temperature creep. Overheating causes by a single incident or a small number of incidents, exposes the tube steel to an excessively high temperature (hundreds of degrees above normal) to the point where deformation or yielding takes place. It results from abnormal conditions such as loss of coolant flow, internal oxide layer or flame incidence. The second is either called long term or extended overheating failure, which results from a relatively continuous extended period of slight overheating, stress, or the accumulation from several periods of excessive overheating. The root cause may not be elevated temperature, as fuel-ash corrosion or erosion may reduce the wall thickness so that the onset of creep and creep failures occur sooner than expected.

However, regardless of the cause, failure will exhibit the characteristics of a creep or stress rupture. Indeed, the standards for creep deformation at high-temperature provide design limitations for allowable stresses for all alloys used in the creep range. One of the criteria used in the determination of these allowable stresses is 1% creep deformation, in 100,000 hours of service. Thus, the standard recognises that over the operating life, some creep deformation is likely. Creep failures do display some deformation or tube swelling in the immediate region of the rupture.

There is a general agreement that creep is a thermally activated process. To understand creep, the establishment of a function ε (t) at a constant temperature and stress is desired and a determination of the dependence of this function on temperature, stress, composition, microstructure and environment is required. The strain instead of depending only on the stress, also depends on temperature, T and time, t,

$$\dot{\varepsilon} = f(\sigma, t, T)$$

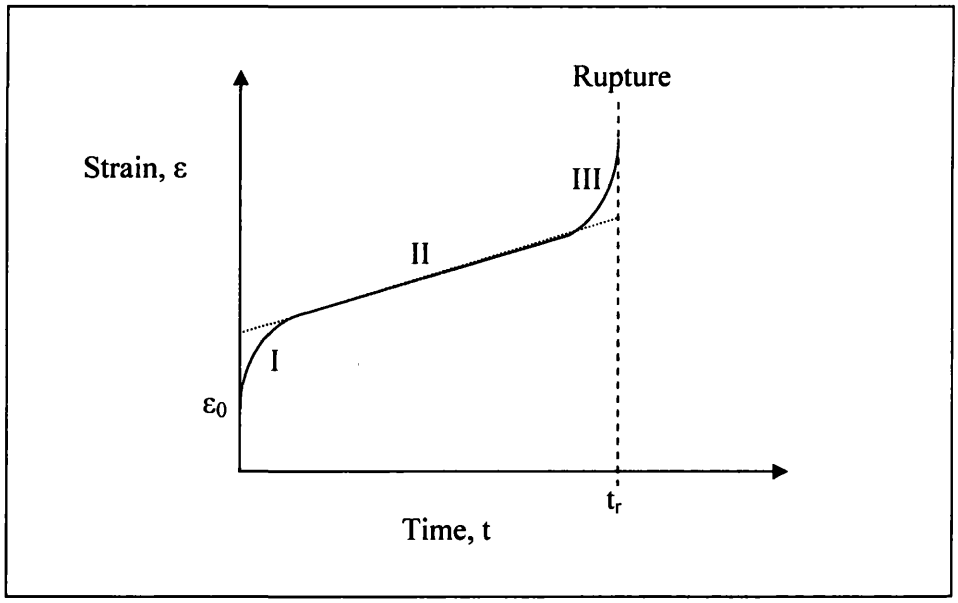

Figure 15: Typical creep strain versus time curve. [27]

According to the conventional creep curve (*Figure 15*), creep deformation processes are made up of three main stages, viz: primary (I), secondary (II) and tertiary (III) states. Primary (transient) creep is an initial period of decreasing strain rate. The primary creep state implies a strong dependence on the thermal and mechanical pre-

treatment of the material. The secondary creep state is the area of engineering interest, where creep rate is almost constant. The portion in stage II is nearly linear and predictable. Depending on the load or stress, the time can be very long; two years in a test and several decades in service. The tertiary state (III) is beyond the constant-creep-rate or linear region, shows a rapidly increasing creep rate which culminates in failure. Even under constant-load test conditions, the effective stress may actually increase due to the damage that forms within the microstructure. An engineering part should spend the majority of its life in the steady state (secondary) range since once the tertiary state is entered, creep strain accelerates rapidly to rupture.

Neubauer and Wedel [2] were first to publish the relationship of creep-life consumption of plant components to cavitation. Based on observations on steam pipes in German power plants, they estimated the approximate time interval required for the damage to evolve from one stage to the next under typical plant conditions. They characterized cavity evolution in steels at four stages and formulated recommendations corresponding to A, B, C, D – i.e., isolated cavities, oriented cavities, linked cavities (microcracks) and macrocracks as shown in Figure 16.

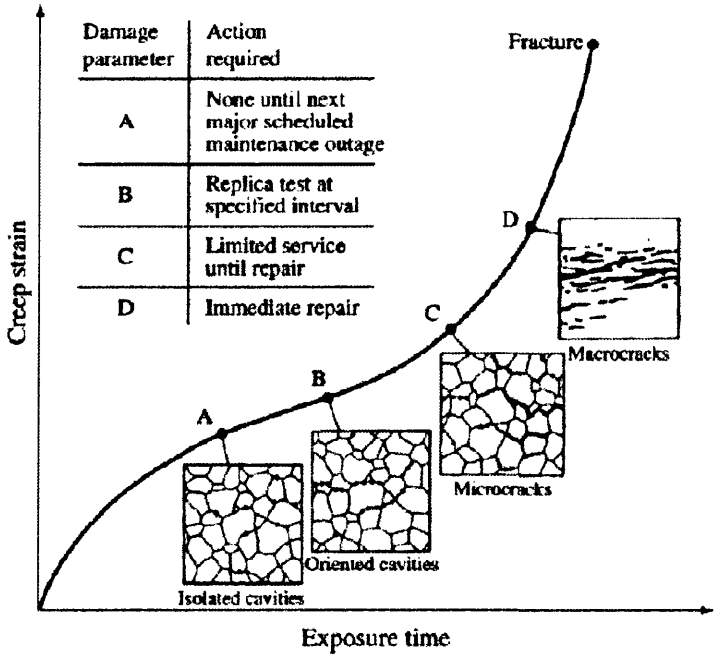

Figure 16: Creep life assessment based on cavity classification.[87]

They established that there was no microstructural evidence of creep damage during the primary state. The first microstructural evidence of damage appears as individual voids or pores somewhere along the secondary state (linear portion). The location of these first voids or holes varies, often noted at the junction of three or more grains, occasionally at nonmetallic inclusions. These individual voids grow and link to form cracks several grains long, and finally failure occurs.

Ashby summarised various deformation mechanisms and proposed the creep deformation map, which is a schematic tool for different creep-controlling deformation mechanism regimes in stress-temperature space. [27] This creep deformation mechanism map representing the regions of temperature and stress in which different creep mechanisms dominate at secondary (steady state) creep only. For any specified creep conditions, the contribution of each creep mechanism to the overall creep rate is calculated from the appropriate constitutive equation relating stress, temperature and strain rate for each process. The advantage of deformation maps in alloy design is that maps provide the essential information of which type of creep operates at the stress and temperature of service and therefore which strengthening methods can be chosen between. However, the vast amount of information which is needed to compile this creep deformation map is usually derived from many different sources and the disadvantage is, the data may often not be available for a given material.

At high temperatures ($T>0.4T_m$) creep deformation is believed to be diffusion controlled. There are two different mechanisms that can control the deformation of materials at high temperatures ($T>0.4T_m$, where T_m is the melting point): (i) diffusion-controlled dislocation creep and (ii) grain boundary diffusion creep [6]. The former is controlled by the non-conservative motion of dislocations involving vacancy diffusion or by cross slip. Vacancies can diffuse either by pipe diffusion (along dislocations) at intermediate temperatures or by bulk diffusion at high temperatures [29]. The later is deformation of polycrsytals occuring at lower stress conditions due to vacancy diffusion through the lattice and along grain boundaries at elevated temperatures [29]. The creep rate of diffusion creep is proportional to the applied stress and decreases when grain size is increased [29]. The grain size effect is plausible when diffusion creep is operative.

Though the conventional creep curve provides a basic understanding of creep mechanisms, creep deformation processes are more complicated especially in multi component alloy steels [6, 12, 13, 28]. Extensive research has been conducted on the atomistic creep equations based on different rate controlling processes. Although transient and steady state creep usually occur together during creep at high temperatures, the transient creep has limited effect on the microstructure. A steady state creep equation is commonly used in the analysis of creep deformation of materials under elevated temperature service. For this purpose, the main objective is to provide an assessment on microstructural evolution during high temperature creep deformation in Esshete 1250 steel and the factors affecting the steady state creep. Due to the contribution of the steady state creep to the total creep deformation, a review of classical theory of steady state creep will be presented.

In order to study the creep behaviour of a metal, creep testing must be carried out in order to obtained creep data for a specific steel studied. In creep testing a constant load is applied to a specimen and the specimen's elongation, or strain, is measured. This strain is plotted against time to form a creep curve. This curve usually contains three regimes, after the initial elastic strain. (See Figure 15) The first is primary creep where the strain rate, $d\varepsilon/dt$, is initially rapid and then decreases with time. Then the specimen enters into secondary creep, or steady-state creep, in which the creep rate is constant. This constant creep rate is called the steady-state creep rate, ε_{ss}, or minimum creep rate, ε_{min}, since it is the slowest creep rate during the test. Finally, the specimen enters into tertiary creep, in which the creep rate continuously increases until the specimen breaks. This event is called creep rupture or creep fracture, and is measured by the time to fracture, t_f. Some steels do not exhibit a well-defined secondary creep state. Instead, the primary creep passes directly into tertiary creep. The point at which this change occurs is the slowest creep rate. Although accurately called ε_{min}, it is frequently called ε_{ss}, in conformity to the more commonly observed creep behaviour in designing components that operate at high temperatures, two items must be considered. First, excess creep deformation must be prevented because this will lead to interference between components. And second, the component must not be allowed to fail by creep rupture.

In designing against creep deformation ε_{min} or ε_{ss}, is commonly used. Primary creep may be included with the initial elastic strain or treated as a function of time. Tertiary creep is usually not considered since failure by excessive elongation usually occurs prior to tertiary creep. To study creep deformation, creep rate, ε_{ss} is the most common approach. The stress dependence of ε_{ss}, at a constant temperature is usually given by a power-law relationship,

$$\dot{\varepsilon}_{ss} = B\sigma^n \qquad \textit{(Equation 8)} \text{ [27]}$$

where n is a material constant called the creep exponent and B is a function of temperature. When plotted on log-log coordinates, the data falls along a straight line whose slope is given by n.

The temperature dependence of ε_{ss} at a constant stress is usually given by an Arrhenius rate equation,

$$\dot{\varepsilon}_{ss} = C\exp\left(\frac{-Q}{RT}\right) \qquad \textit{(Equation 9)} \text{ [27]}$$

where C is a function of stress, Q is the activation energy for creep, R is the universal gas constant and T is in degrees Kelvin. Note that as the temperature increases, the rate increases exponentially. The value of Q is found by plotting the natural logarithm of ε_{ss} versus. 1/T. The data should fall along a straight line of slope -Q/R.

The general relationship between ε ss, σ and T can be expressed as

$$\dot{\varepsilon}_{ss} = A\sigma^n \exp\left(\frac{-Q}{RT}\right) \qquad \textit{(Equation 10)} \text{ [27]}$$

where A, n and Q are material constants that vary from material to material, and have to be found experimentally. In addition to controlling excess elongation at high temperatures, it is necessary to prevent creep rupture. To do this, plots of σ vs. log t_f or log σ vs. log t_f are constructed at various temperatures. These plots may or may not yield a linear relationship between the variables.

This steady state power law equation is a basis for creep deformation data analysis. The equation is often further modified, which appropriate to the modelling of creep deformation data, on the basis of the shape of creep deformation curve. Esshete

1250 austenitic steel exhibits a sharp change in the curvature as the material moved towards the end of primary creep. [28]. Power law equation is not sufficient to model the creep curve hence, Mike [28] suggested an exponential form of equation used by White for 316 stainless steel is more appropriate for the modelling. Therefore, attempts had been made to model the behaviour of Esshete 1250 austentic creep resistant steel using equation from White:

$$\varepsilon = \{\varepsilon_{fp}(1-\exp(-rt^{\mu}))\} + \{\dot{\varepsilon}_s t\} \qquad \textit{(Equation 11)} \text{ [28]}$$

Where ε = creep strain (in absolute units)

ε_{fp} = strain at the end of primary creep (in absolute units)

t = time (h)

$\dot{\varepsilon}_s$ = minimum creep strain rate (1/h)

r, μ = constants

Significant research efforts have been carried out on the prediction of creep deformation, i.e. the strain and rupture life [13, 28, 30, 31]. In order to control excess creep deformation at high temperatures, it is necessary to predict the creep in order to prevent rupture. Thus, plots of σ vs. log t_f or log σ vs. log t_f are constructed at various temperatures. These plots are adequate if the design life is within the range of the experimental data. However, many design lives are much longer than this range. Therefore, 10 to 30 years are common design life for modelling of creep rupture life. However, if time to obtain experimental data is too long for starting the design of component, some means of extrapolating the data to long lives is necessary. A common method of doing this is the use of time-temperature parameters which relate the stress and temperature to the time to failure. The most widely used parameter is the Larson-Miller parameter,

$$\text{L-M Parameter} = T\,[C' + \log t_f] \qquad \textit{(Equation 12)} \text{ [85]}$$

where C' is a constant. C' is approximately equal to 20 when the temperature is expressed in degrees Kelvin and the time is expressed in hours. This parameter is plotted against the stress to obtain a master curve of the creep rupture behaviour. By knowing the L-M Parameter for a given stress it is possible to determine the time to

failure at a given temperature. By running experiments at the design stress, but at a higher temperature, creep rupture will occur in a reasonable length of time, and the L-M Parameter can be found by using Equation 12.

2.7 Creep deformation of Esshete 1250

The creep deformation model is found to be related to the plant operation temperature (550°C and 575°C). Creep testing was conducted on the specimens extracted from the thick section (67.5mm) of unused boiler tube material (Esshete 1250) called 'Spare Spine', which was supplied in the solution heat-treated condition. Details of the chemical composition are given in Chapter 3, Table 8. This section gives an overview of creep deformation modelling on Esshete 1250 austenitic creep resistant steel. Standard creep specimens with a 28mm gauge length and a 5.64mm diameter were extracted from the Spare Spine material. The creep tests were carried out to BS EN 10291:2000 at Bodycote Material Testing Ltd, Newcastle. Additional tests data have also been obtained from Inco and at ERA Technology. [88]

Table 6: Values of the Constants in the Exponential Model (Equation 11). [88]

Constant	Value	
r	$\exp[\min(-0.52995, -4.6317 + 0.01375\sigma_{True})]$	
μ	0.62823	
A	133.89	
σ_i	$\sigma_{True} > 190$MPa	$\sigma_i = \frac{1730.8\varepsilon_{IPS}}{1.6}$
	$\sigma_{True} \leq 190$MPa	$\sigma_i = 0$
P	-23577.55	
m	2.873	
B	283612.77	
Q	-43359.25	
n	3.995	

The primary and secondary creep deformation behaviour of Esshete 1250 parent metal has been modelled using an exponential-type equation. [28] The resulting model has been shown to provide satisfactory predictions of the creep behaviour of this

material, especially at the temperatures relevant to plant operation (550°C and 575°C). [88]

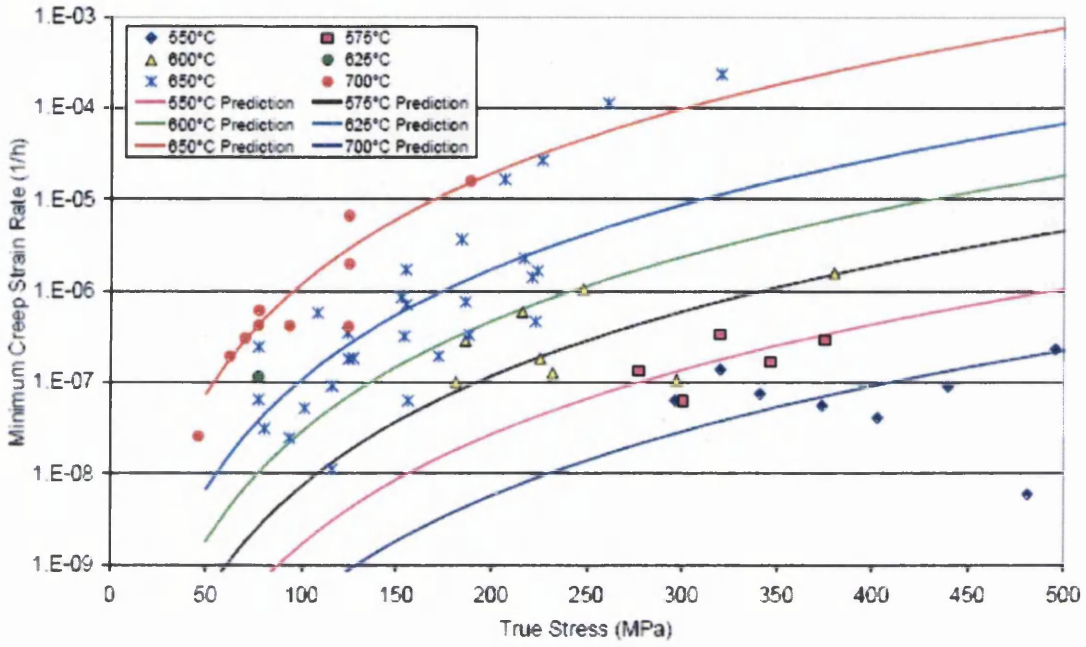

Figure 17: The minimum creep strain rate for each test with creep model prediction. [88]

The secondary creep deformation behaviour of Esshete 1250 parent metal has been modelled using an exponential-type equation (Figure 17). The resulting model has been shown to provide satisfactory predictions of the creep behaviour of this material, especially at the temperatures relevant to plant operation (550°C and 575°C).

A creep deformation graph is constructed for material studied using the Larson parameter in chapter 4. The main target is to have a clear image of microstructure observed related to the creep deformation. It does not construct with enough creep data therefore, it is not sufficient for creep analysis or modelling. However, it is sufficient to provide an interpretation of microstructural changes during creep deformation.

No discussion was carried out on the data fitting of the creep deformation modelling. However, more details in creep deformation, rupture and ductility of Esshete 1250 can be found in the paper by Spindler [28].

3.3 Tensile properties of Esshete 1250

The tensile properties for Esshete 1250 that are presented are specifically intended to be used for pipes for the main boiler spines at Heysham I/Hartlepool power station. The tensile data was come from the construction records and from tests on the 'spare spine' which is the material studied. The data were obtained from a number of sources according to British Energy. However, due to the nature of the limited material from the 'spare spine' provided by British Energy, no tensile data could be carried out during the present research project. The tensile testing data of Esshete 1250 steel were obtained from British Energy will be presented in this section for reference purposes. More detailed information can be obtained from the engineering report of British Energy Structural Integrity Group [89]. These tests were reported to have been conducted in accordance with BS EN10002-1:1990 and BS EN10002-1:2001 for the room temperature tests, and in accordance with BS EN10002-5:1992 for the elevated temperature tests. Figures 18 and 19 give an overview on tensile properties on the Esshete 1250 austenitic creep resistant steel. The temperatures of interest for engineering assessments of the steel span a wide range from room temperature to temperatures experienced during welding. Thus, data for the widest range of temperatures were analysed. It can be noted that the proof stress data from the spare spines material compare reasonably well with the data from ERA Technology and from Corus (Figures 1b and 1c). However, the ultimate tensile strength is lower than the data from ERA Technology and Corus (Figure 1d).

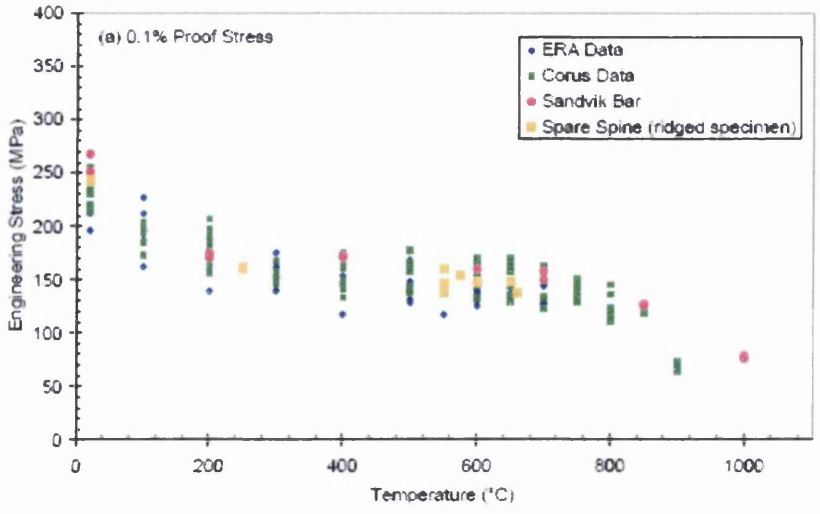

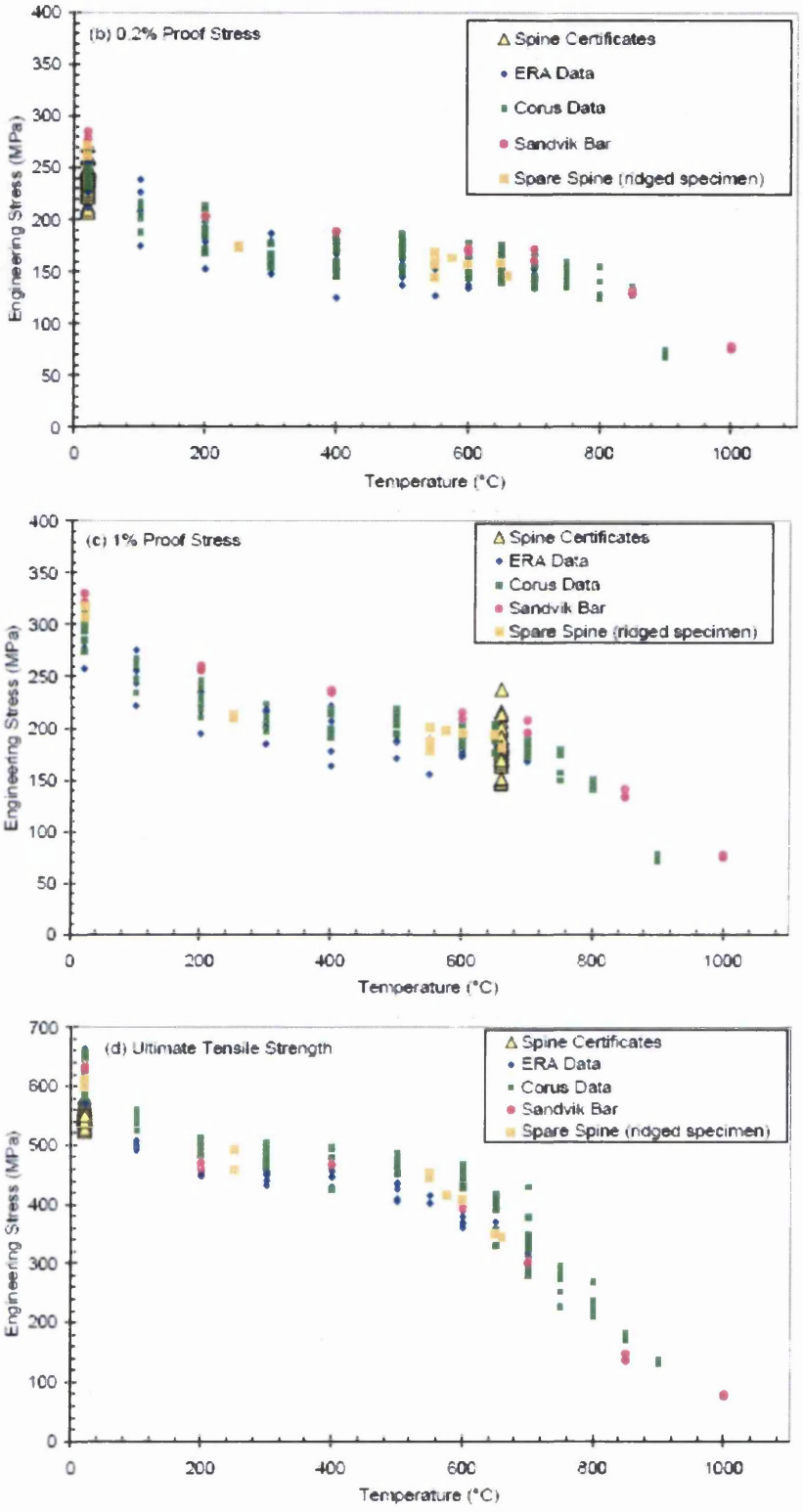

Figure 18: Tensile Properties of Esshete 1250 Parent Steel. [89]

According to the engineering report provided, the room temperature tests provided from ERA technology and Corus were conducted at the same relatively slow strain rate that was used for the elevated temperature tests. However, the room temperature tests

on the 'Spare Spine' and 'Sandvik bar' materials were conducted at significantly higher strain rates. The elevated temperature tests on 'Spare Spine' material were conducted at the same strain rate throughout the test. Thus, the UTS values were determined at the same relatively slow strain rate that was used for the proof stress measurements. In all the other tests the testing rate was significantly higher for the determination of UTS.

The elevated temperature tensile properties of the Esshete 1250 can be calculated by multiplying the room temperature mean and lower 95% confidence interval data from the analysis of construction records by fits to the normalised data. In this way predictions of tensile properties are possible at temperatures for which the construction records contain no data. The details of calculation can be referred on the engineering report from British Energy [89]

The mean and lower 95% predictions are compared in Figure 19. It can be seen from Figures 19a and 19b that the 0.2% and 1% proof stresses of the tensile data from various sources are reasonably well predicted. Figure 19c shows that the predicted elevated temperature UTS for boiler spine underestimates the strength of the multi-cast data from Corus and ERA Technology. This is because of the difference between the construction record data and the multi-cast data from Corus and ERA Technology, which may be due to the testing rate. [89] It is suggested that the differences between the values are due to testing practice and not to differences between the materials. [89]

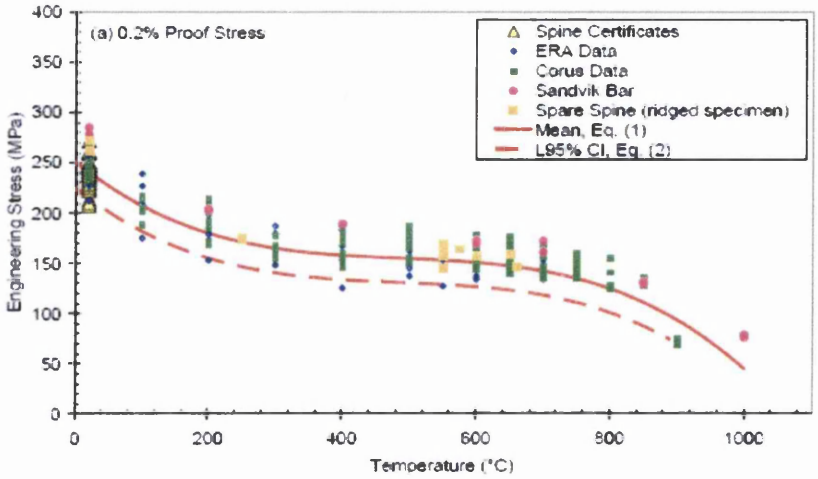

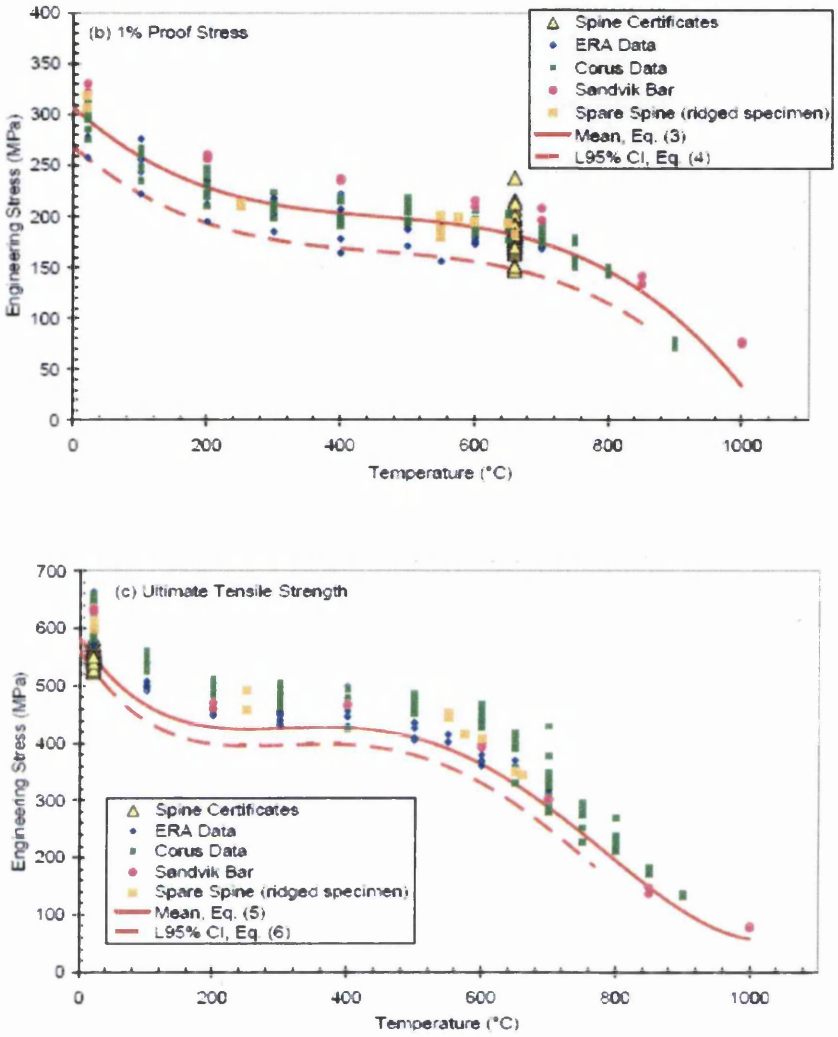

Figure 19: Tensile Properties of Esshete 1250 Parent Steel, showing the Predicted Elevated Temperature Properties of Boiler Spine Material. [89]

2.9 Qualitative and quantitative metallography

To reveal the structure properties relationship of a material, quantitative metallography plays an important role to provide an interpretation of physical properties and behaviour characteristic of material. This will eventually lead to material design with predetermined combinations of properties. Thus, to obtain a valid characterisation of the microstructure, the procedures of quantitative measurement must be well planned. Computer-aided microscopy is primarily concerned with the extraction of useful information and data from an image. The ability to record patterns collected from an optical or scanning electron microscope require carefully sample preparation. This section is concern about characterisation of microstructure of alloyed steel at both the qualitative and quantitative level. Microstructural characterisation requires a systematic approach on the material's variability, the specimen preparation and the test method. Thus, the review is about commonly used methods of quantitative metallography and methods used to identify microstructural features of alloy steel.

2.9.1 Specimen and Metallographic Preparation

Metals being opaque to light can be examined using reflected light on a two dimensional plane section from the three dimensional object. The sectioning plane will cut through the grains or particles anywhere between their major diameter and the apex of a corner. This will result a structure appear with variable size and shape regardless of the uniformity of the three dimensional size of the features. Alloyed steel structures are always in polycrystalline form and in order to reveal the microstructure, it has to be polished and etched so that the features may be visible using an optical microscope or electron microscope.

Sectioning of steel specimens is usually using a cutting tool such as a band saw or power hacksaw. However, a steel grade which is softer requires abrasive cutting wheels to prevent substantial deformation on the specimen. ASM Handbook Volume 9 gives details information for sectioning specimens for various materials.

Mounting of specimen is to facilitate metallography grinding and polishing process. Cold setting epoxy and bakelite is common mount for alloyed steel. 'Mounting of specimens' in ASM Handbook Volume 9 give details on mounting materials and problems associated with various mounting methods.

Grinding of specimen is performed using P120, P250, P320 and P600 grit silicon carbide papers. This procedure usually carried out by hand and specimen should be rotated 45° to 90° between each step. Polishing of specimen followed after grinding usually start with rough polish state using 6μm diamond paste then follow with finer polish state using 1μm diamond paste. Both polishing procedures were done on napless, low-nap or medium nap cloths with the aid of lubricant extender to reduce drag. Polishing can be carried out by hand or machine. Pressure should be moderate and firm and a wheel speed of ~150rpm is usually adequate. 'Grinding, Abrasion, and Polishing' in ASM Handbook Volume 9 give more detail information on the procedures.

Etching is always required to examine the microstructure. Problems may occur when obtaining the microstructure image and this is not the question of optics but selective etching. The sample must not be over etched, sometimes samples do not require etching. This is because some features may be too sensitive and may easily pit by even a weak etchant. There is vast variety of etchants used to reveal the microstructures of steel. Most etchants ingredients are dissolved in water, methanol or ethanol or mixture of these solvents. Specimens are always immersed into the etchant for a period of time. Carefully selection of the etchant type and the time for etching is required and depend on the material for examination. Electrolytic etching is also popular for uniformly etched results. Sometimes it depends on what feature of the microstructure you are after in order to choose the suitable etchant. For example, some of the etchants give significant result in revealing the grain boundaries and some preferentially reveal the precipitation in the steels. More details on methods of etching are presented in ASM Handbook Volume 9.

2.9.2 Microscopic examination

Microstructural characterisation is achieved by allowing some form of probe to interact with a carefully prepared sample. The most common used of probes is visible light from optical microscopy and high energy electron beam from electron microscopy. Once the probe has interacted with the sample, the scattered signal is collected and processed into a form where it can be interpreted, either qualitatively or quantitatively. The collected data are read out, processed and recorded. Two-dimensional images are obtained from microscopy and the results then have to be interpreted.

Every technology has its limitations, and methods of microstructural characterisation should be chosen according to the information required. Table 7 gives information on the limitation of each microscopic technique. Optical microscopy using reflected or transmitted light to obtain information on microstructure has limited application due to the resolution limit of about 0.3μm. Therefore, electron microscopy is available for over 40 years for higher resolutions (in nanoscale) of microstructures. Common electron microscopes available are such as the Scanning electron microscope (SEM) and Transmission electron microscope (TEM), which are widely used for microstructure characterisation. This research work is based on the surface imaging of creep resistant alloy thus SEM was chosen due to it is use primarily for the study of surface topography of solid materials.

Table 7: The limitation of resolution for various microscopy techniques. [90]

TECHNIQUE	LIMITS	RESOLUTION
eye	retina	70 μm
optical microscope	diffraction of light	0.3 μm
scanning electron microscope	diffraction of electrons	0.003 μm
transmission electron microscope	diffraction of electrons	0.0001 μm
field ion microscope	atomic size	0.0003 μm

Scanning Electron Microscope permits a depth of field far greater than optical or transmission electron microscope. The resolution of the scanning electron microscope is about 0.3μm (Table 7), approximately two orders of magnitude greater than the optical microscope and one order of magnitude less than the transmission electron microscope. Thus, SEM bridges the gap between the other two techniques. Moreover, elemental analysis is available if SEM and TEM are equipped with appropriate detector (EDX, WDX). [90]

Samples for SEM must be solid materials and the minimum size is 0.1 mm while maximum size depends on the machine. The samples must be conductive or coated with thin conductive layer. A schematic illustration of SEM equipment is presented in Figure 20.

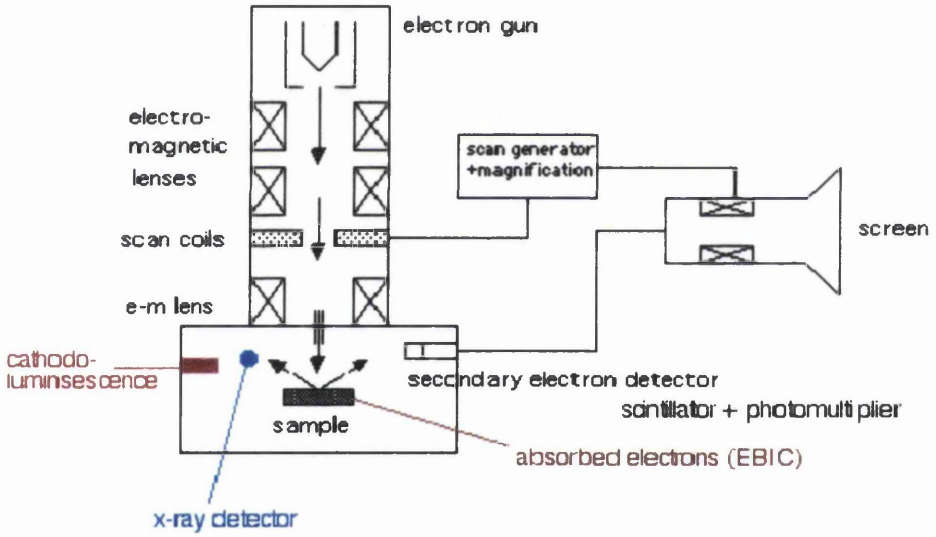

Figure 20: Schematic diagram of typical SEM. [90]

An electron beam passing through an evacuated column is focused by electromagnetic lenses onto the specimen surface. The beam is then raster over the specimen in synchronism with the beam of a cathode ray tube display screen. Inelastically scattered secondary electrons are emitted from the sample surface and collected by a scintillator. Electron interactions with materials do not travel very far, on average, into materials. Electrons incident on a material may scatter back or knock out other electrons (Figure 21). In this way the secondary electron emission from the sample is used to form an image on the display screen. [90]

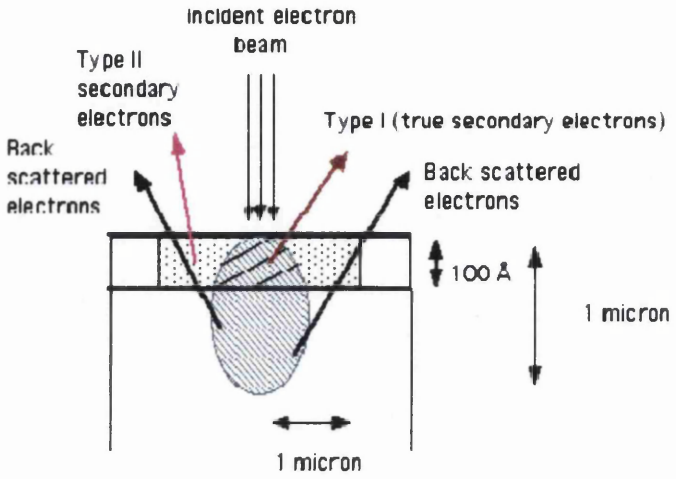

Figure 21: Schematic diagram of a scanning electron beam incident on a solid sample. [90]

A Camera is provided to record the images on the display screen. Differences in secondary emission result from changes in surface topography. If backscattered (elastically) electrons are collected to form the image, contrast results from compositional differences will be obtained. The number of secondary electrons produced is relatively insensitive to atomic number of the atoms in the material. The number of backscattered electrons, however, is sensitive to the atomic number of the material. [90] The sensitivity of electrons is given in Figure 22.

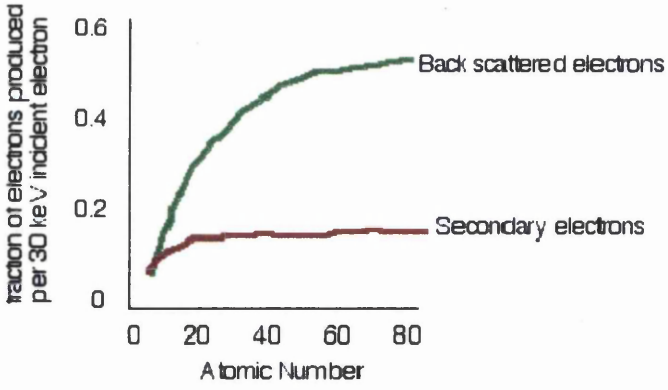

Figure 22: the surface varies with the incident electron energy. [90]

Figures 7 and 14 show backscattered electron image and secondary electron image respectively of an austenitic stainless steel. The lower men atomic number phases appear darker. The precipitate particles are in contrast from the austenite matrix.

2.9.3 Elemental analysis

Modern equipment for microstructural characterisation often combines several techniques on one platform, so the limitations of a specific technique do not always mean that we have to prepare different samples or search for another piece of equipment. Energy Dispersive X-ray Analysis (EDX) is used for elemental analysis of regions of micron dimensions and usually attaches to a SEM or a TEM. The proportion of the X-rays emitted under electron excitation together with the corresponding energy losses in the primary electron beam are the characteristics of the chemical composition of a solid sample. These characteristic X-rays may be selected from the observed spectrum of emitted electromagnetic radiation according to their energy or wavelength, and the signal distribution from the sample can be displayed in an elemental map to provide qualitative and quantitative information on the morphological relationship between the microstructure and the chemical composition. [90]

The detection of characteristic X-Rays can be done by either using Energy-Dispersive Spectrometry (EDS) or Wavelength Dispersive Spectrometry (WDS). Sample is most solids (non-conducting sample must be coated with conducting layer). Electron beam excites X-rays which have energies characteristic of the element. Quantitative analysis is then possible with the aid of computer. [90]

In the EDS, the pulse height recorded for an incident photon by a detector is directly proportional to the energy of the photon responsible for the pulse. The detectors used for this purpose are lithium drifted silicon (Si(Li)), solid state detector. An incident photon absorbed by the silicon crystal creates ionisation events in the active thickness of the detector. The total charge developed is proportional to the incident photon energy and is detected as a current pulse that is shaped, digitised and counted in a multi-channel analyser. [90]

For WDS, a series of bent single crystals of different lattice spacing cover the range of wavelength that are of interest. The wavelengths within the range of each spectrometer crystal are scanned by rotating the crystal to scan the Bragg angle 2θ and synchronously moving the detector while keeping the position of the bent crystal fixed.

An argon gas proportional counter can be used to collect the photons elected by the diffracting crystal. These gas counters have sufficient energy discrimination to ensure that second and higher order reflections (wavelengths that are multiples of that selected) are rejected. At the same time, the width of the current pulse generated by a photon in the gas proportional counter is much narrower than can be achieved in the Si(Li) solid state detectors. Therefore, the 'dead time' of the gas proportional counter is not a limitation on the counting rate. [90]

There are two problems associated with EDS compared to WDS system. The first is the relatively poor energy resolution. EDS with a typical resolution of 150eV can lead to peak overlap while WDS system has better energy resolution providing better resolution of peaks, by at least an order of magnitude, especially for the detection of long wavelength, low energy radiation. The second problem is with low energy (long wavelength) photon detection that requires either a windowless detector or a detector protected from the rest of the system by only very thin and fragile window. Care is thus needed to ensure the detector retains its long wavelength sensitivity and is not degraded nor contaminated in the vacuum environment of the microscope. As all solid state detectors are cooled by liquid nitrogen, so that detector is often the coldest region in the system. Cryogenic condensation of contamination on the surface of the detector is then a serious life limiting concern. However, the only advantage of EDS is WDS have a slow speed of collection data mode compared to EDS.

2.9.4 Computer Aided Image Analysis

Manual stereological methods and conventional image analyzer are sometimes difficult and time-consuming to obtain the informative data for some complicated microstructures in metals. To solve these problems, a computer assisted quantitative analysis is explored. Computer aided image analysis is used to rapidly and accurately count, measure and classify quantitatively features of microstructure such as particles, grain size or other structural elements. [91] Image manipulation is an essential element of image analysis in terms of how the visual representation of the image can be made

more appealing and more understandable to the human eye. Modern digital image analyser used computer to process digital images with a range of software (e.g. Optilab) to enhance the measurement accuracy. The basic operations of an image analysis system are presented below.

1. A digital image input - this can be obtained from a camera mounted on optical microscope or using a recorded electron microscopy image (micrograph). The electronic signal of micrograph is stored in the computer as an array of numbers.
2. Grey level image - due to computer can read only binary (black and white) image, micrograph images must be saved in greyscale for image analysis.
3. Segmentation of binary image - all computers use binary images as the basic form for measuring structural details. The segmentation process is essential to ensure quantitative measurement since it requires quantitatively locating boundaries of interest and forming a binary image of the different structural features that are to be analysed.
4. Parameters selection - with the aid of computer software, most parameter can be measure for example, object area, the mean intercept perpendicular, diameter, and so forth.
5. Measurement of parameters selected - this can be performed automatically since computer aided image analysis considered a distribution of dimensions, having the statistically measured mean and standard deviation.
6. Storing data and output - data can be output directly for later statistical evaluation and analysis using software programs such as Excel.

The limitation is since feature discrimination is based on grey level contrast or edges in the image, it is imperative to choose an imaging mode that allows the feature of interest to be differentiated from the remainder of the field. Furthermore, only two dimensional features are measured. Volumetric information of the feature of interest can be obtained only by assuming a specific geometry. [91]

2.9.5 Measurement of parameters and data analysis

The two parameters that are widely measured are grain size and particle size. Measurement of the grain size of metals is one of the oldest but most important method as grain size influences many properties. The measurement of grain size can be done manually or by computer aided image analysis. The average grain size of a specimen with a single distribution of grain diameters can be estimated by chart comparison method or measured by intercept methods [90]. However, specimen with more complex grain size distribution or non equiaxed shapes are more difficult to analyse. With the aid of computer image analysis software e.g. Optilab, the grain area is easily obtained from a planimetric section. However, the ASTM standards E112, E1181 and British standard only covers measurement of specimens with manually method. [82]

The volume fraction of a constituent is an important measurement for microstructure features. The most efficient approach for manual determination of the volume fraction is the point count method developed about 70 years ago, independently by Thomson and Glagolev [90]. In this method, a grid with a number of systematically spaced test points is placed over the microstructure image (micrograph). The points lying over the constituent of interest are counted and divided by the total number of grid points to obtain a point fraction. Points lying on the interface are counted as ½. This process is repeated for a number of randomly chosen fields. The mean and standard deviation of the field values of the point fraction are determined. ASTM E652 provides details on this method. [82]

The measurements of quantitative metallography are mostly statistical in nature. Data presentation is usually in the form of distribution and cumulative curves for the parameters. The measured values of any parameter will be distributed about a statistical mean or average value and the width of this distribution can be defined and measured to describe the spread of the measure values in terms of a 'statistical error'. Moreover, any statistical function that is derived from data related to frequency of observation can also be interpreted as a probability distribution. The probability

distribution or so called frequency function determines the probability that a microstructural parameter will have any given value. [90-91]

To access the precision of a measurement, the mean and the standard deviation of the field or individual feature measurements are calculated. For most measurements, the distribution of the frequency of the individual measurements is Gaussian. From the standard deviation and the number of measurements, 95% confidence limit can be calculated. The 95% confidence limit is then divided by mean and then expressed as a percentage to obtain the % relative accuracy. The mean, standard deviation, 95% confidence limit and % relative accuracy provide the foundation for data analysis.

CHAPTER 3

3.0 EXPERIMENTAL PROCEDURES

Metallographic studies were carried out on the Esshete 1250 alloyed steel, which was in the as received, thermally aged weld specimen, and creep exposed conditions for durations up to 17 years. Analytical electron microscopy studies were carried out on each steel using SEM. MTDATA calculations were performed to predict the phases forming, under equilibrium conditions, using the TCFE database. This section consists of experimental work procedures and the techniques used for quantitative analysis. The experimental procedure is illustrated in Figure 23.

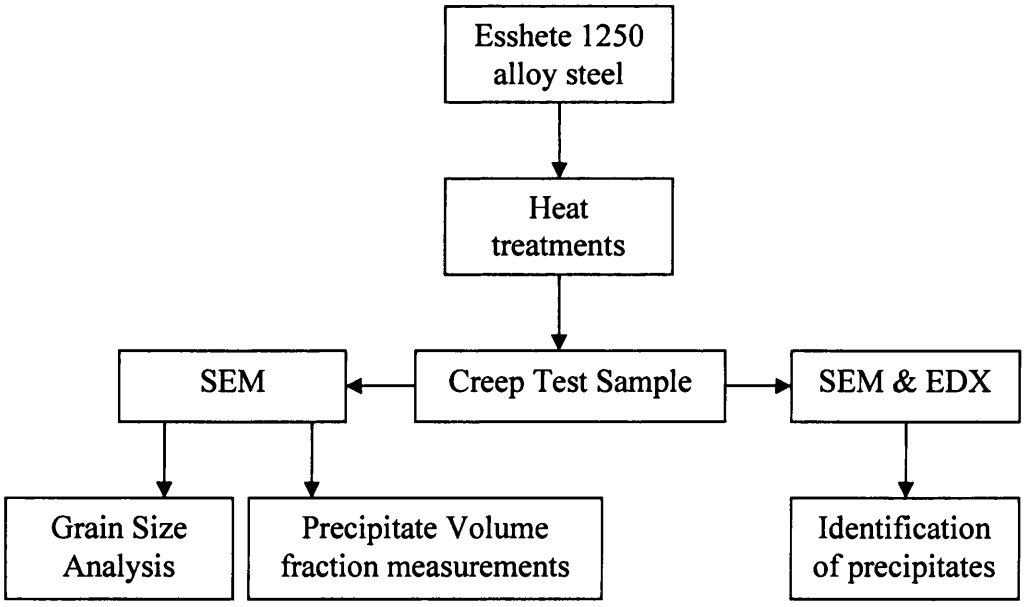

Figure 23: Schematic diagram of experimental procedures.

3.1 Material for Investigation

The material for investigation is Esshete 1250 austenitic stainless steel used for the main boiler superheater tube at Heysham I/Hartlepool power station in UK. Material for this research work was kindly supplied by British Energy (Gloucester) [79]. The chemical composition for the material investigated was derived from analysis of product form and is given in Table 8.

Table 8: Chemical compositions for material investigated (wt%).[79]

Element	British standard specification	Esshete 1250 (E1250)	BH-E1250
C	0.15max	0.10	0.11
Si	0.2-1.0	0.51	0.40
Mn	5.5-7.0	6.7	5.75
P	0.04max	0.02	0.023
S	0.03max	0.008	0.018
Cr	14.0-16.0	14.9	15.50
Mo	0.8-1.2	1.21	1.01
Ni	9.0-11.0	10.3	9.55
Al	-	<0.005	-
Co	0.10max	0.039	-
Nb	0.75-1.25	0.74	1.05
Ti	-	0.008	-
V	0.15-0.40	0.30	0.24
B	0.003-0.009	0.005	0.0066
W	-	0.03	-
N	-	0.05	-
Fe	Bal.	65.075	66.3424
Form and dimensions (mm)		67.5mm thick pipe and 603mm O.D.	Bar, Dia:21mm
Solution treatment	1050°C - 1150°C	1080°C for 45mins (WC)	1050°C for 30mins (AC)

The specimens received for microstructure examination are as follows:

1. Esshete 1250 in the as received condition (Parent).

This is the Esshete 1250 austenitic stainless steel for boiler tubing in Heysham I/Hartlepool power station. The as-received Esshete 1250, which referred as parent material, comes from an unused 67.5mm thick pipe and 603mm O.D. and was nominally solution treated at 1080°C for 45mins, followed by quenching in water. The as-received material was cut into samples of 20mm x 13mm with a thickness of 3mm and referred as 'parent' coupon in this study.

2. Creep exposed Esshete 1250 parent samples (E1250), Figure 24.

This material was the 'parent' following creep exposure. Standard creep specimens with a 28mm gauge length and a 5.64mm diameter were extracted from the parent material. Uniaxial creep testing was carried out at Bodycote Material Testing Ltd, Newcastle according to BS EN 10291:2000 standard. The creep test conditions are given in Table 9. [79]

3. Creep exposed Esshete 1250 samples (BH-E1250), Figure 25.

The material for investigation was also Esshete 1250 austenitic steel taken from a different cast (referred as BH) bar with diameter measurement of 21mm, solution treated at 1050°C for 30mins and then air cooled to room temperature. The BH-E1250 specimens were creep tested by ERA Technology and the conditions are presented in Table 10. [79]

Table 9: Creep test condition of Esshete 1250 parent samples. [79]

Specimen ID	Temperature (°C)	Stress (MPa)	Duration (h)	Reduction of Area (%)
P3-MZM	550	360	7132	22.6
P8-MZL	550	380	4944	24.5
P2-MZK	550	400	2792	24.7
P7-MZJ	550	420	1301	29.5
P4-MZO	575	320	3490	21
P10-MZP	575	340	2035	24

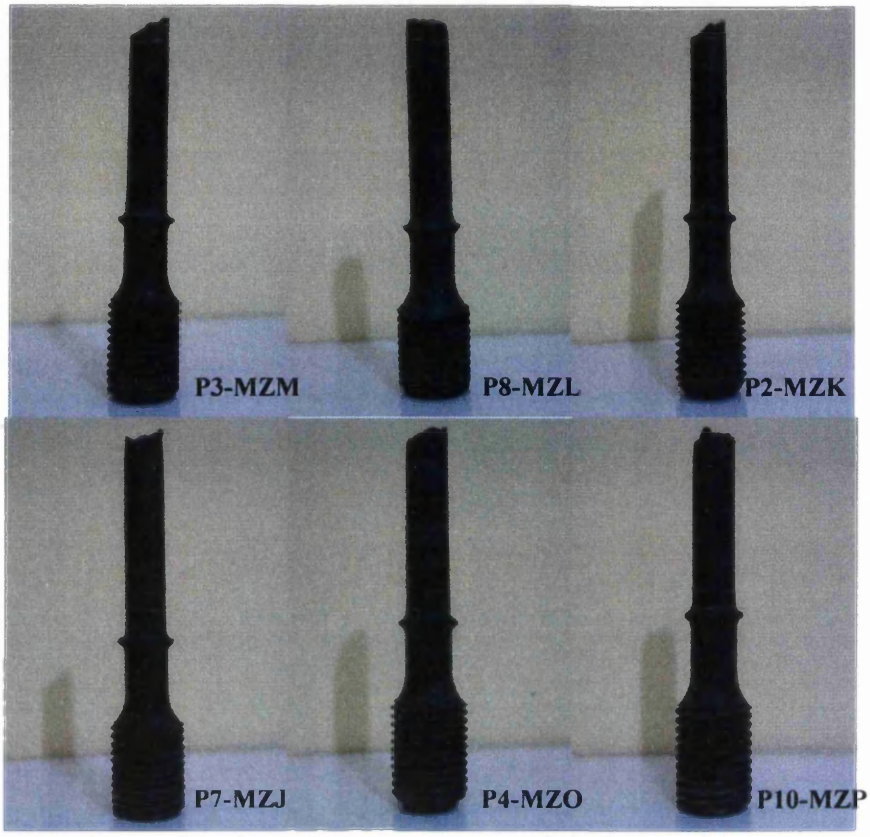

Figure 24: Photo taken from the 6 creep exposed Esshete 1250 parent samples.

Table 10: Creep test condition for 12 BH-E1250 samples. [79]

Specimen ID	Temperature (°C)	Stress (MPa)	Duration (h)	Reduction of Area (%)
BH24	550	402	5527	22
BH28	550	263	82138	10
BH7	600	309	1180	16
BH6	600	263	6951	19
BH10	600	232	153491	20
BH11	650	263	258	45
BH4	650	232	3521	47
BH2	650	185	29398	57
BH27	650	116	77896	61
BH16	700	247	36	57
BH9	700	108	7077	71
BH22	700	70	48370	61

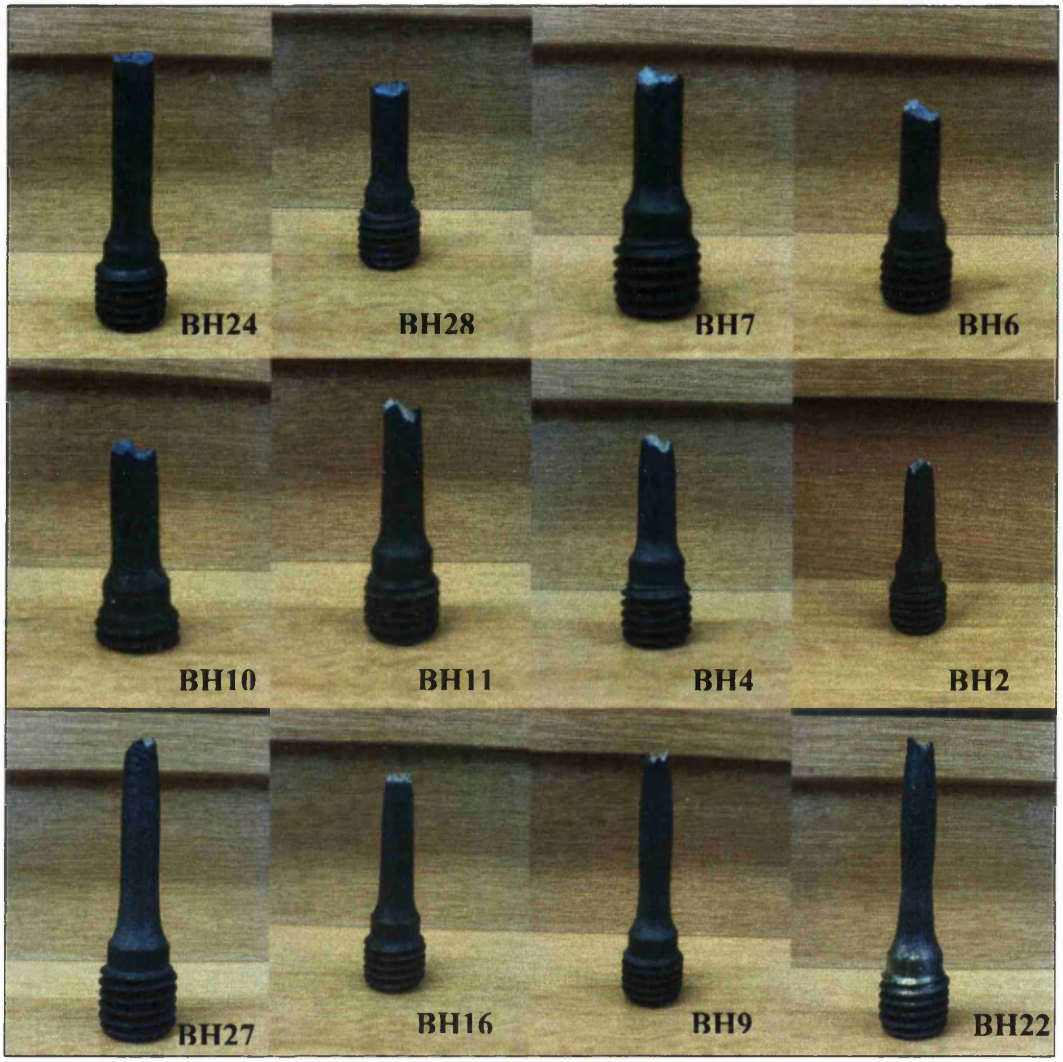

Figure 25: Photos taken from the 12 creep exposed Esshete 1250 specimens.

The creep exposed specimens, which were examined using SEM during this investigation came from the grip area and gauge area of the exposed creep test pieces. The samples for microscopic studies were taken according to the description provided in Figure 26. 7-8mm away from the end of the grip area from each of the test pieces was cut off, and 2-3mm away from the fracture area was also cut off for each specimen to facilitate SEM examination. Samples were etched with oxalic acid aqueous solution and imaged perpendicular to the long axis of the initial creep exposed specimen. Metallographic samples taken from the grip area of the creep test specimens were considered statically aged (stress-free) while the gauge area was considered creep deformed. Qualitative and quantitative analysis were obtained from both areas.

General information and characterisation of microstructures was obtained using Optical microscopy and SEM. Grain size and precipitate size was measured from SEM micrographs using Optilab Image Analysis software. The composition of the precipitates was identified using Energy Dispersive X-ray analysis.

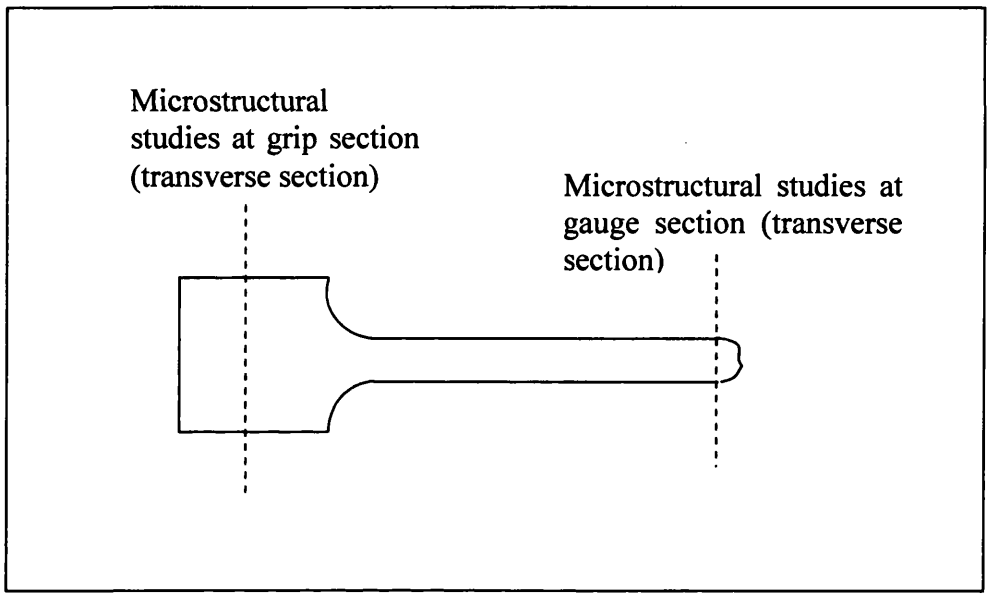

Figure 26: Sectioning of samples form the creep specimens.

3.2 Metallography

3.2.1 Sampling and mounting

The purpose of sampling and mounting is to produce a specific sample that can be handled and prepared for examination under electron microscope. Cutting an appropriate piece for metallography preparation was done by Struers Accutom 50 cutting machine using a fine SiC wheel. Handling of small samples for grinding and polishing requires embedding them in resin. A polyester casting resin (Kleer-Set Type FF) is used.

3.2.2 Grinding and polishing

The purpose of grinding and polishing is to prepare a suitable flat and scratch free surface for examination that is free from the deformation induced in the surface layer by cutting and grinding. Thus, the deformation induced at each grinding stage must be removed by the next less severe grinding or polishing step until it is completely removed at the final polishing stage. For grinding, water is used as a cooling and lubricating agent. The grinding process is performed by hand. Grinding is beginning with the coarsest abrasive silicon carbide (SiC) paper. The sample is ground in one direction until all imperfections are removed and the surface is covered with a uniform pattern of scratches. Then the sample is turned 90° and after washing, ground with the next finer grade of Si-C paper until no scratches form the previous grade is visible. This procedure is followed through the range of Si-C papers up to the finest grade (1000 grit) of grinding paper. Polishing by standardised metallographic techniques using a lubricant to 1μm diamond paste finish is the following procedure after grinding.

3.2.3 Etching

Etching the surface is done to reveal the microstructure of the alloy. Etching for stainless alloy can be difficult due to the 'stainless' character. The metallographic specimens were electrolytically etched by using 10w.o.% of dilute aqueous oxalic acid at 2V for 30s and also 50w.o.% of dilute KOH solution at 2V for 3s. Both etchants were chosen according to

the ASM Stainless Steel handbook [14]. After comparison of these two etchants, the first etchant was chosen for this study due to its good performance in revealing carbides and grain boundaries.

3.3 Quantitative microscopy and image analysis

3.3.1 Optical microscope examination

The specimen for optical microscope examination were mounted with polyester casting resin and ground with silicon carbide paper and then polished to 1 μm diamond paste finish. Electrolytic etching done by solution of 10% oxalic acid in distilled water at 2V attacks the precipitates and grain boundaries after about 30s. Using KOH solution however, give satisfying results (2V for 3s) revealed grain boundaries but not precipitates. Optical microscope gives a general impression of the coarse precipitates over the austenitic matrix on grain boundaries, intergranular and twin boundary.

3.3.2 Scanning electron microscope (SEM) examination

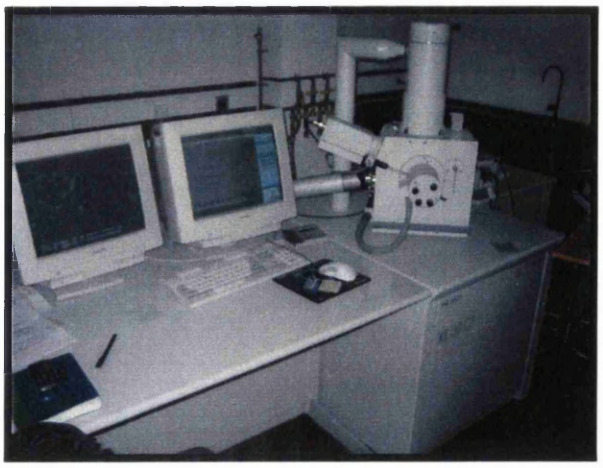

Analytical electron microscopy was carried out using a Phillips XL-30 Scanning Scanning Electron Microscope (SEM) unit fitted with a back-scattered detector operated at 20kV. Secondary electron backscatter images were recorded using an accelerated voltage of 20kV

and a 10-15mm working distance. Backscattered electrons (BSE) were detected and used for imaging. Backscattered images provide atomic number contrast information.

3.3.3 Energy dispersive X-ray spectroscopy (EDX) analysis

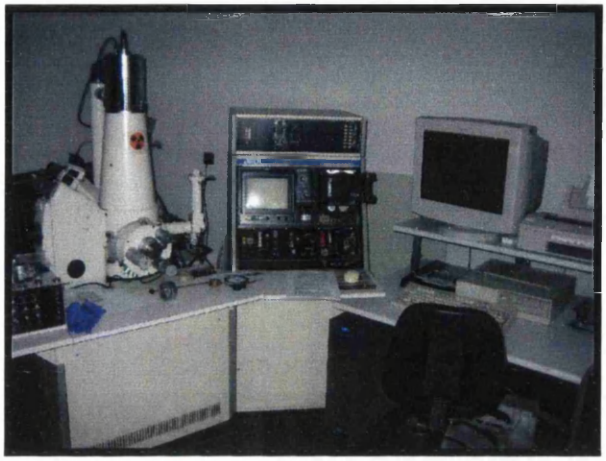

Elemental Analysis was carried out using a Jeol JSM-35C fitted with a Link-Isis Energy Dispersive unit (EDX) operated at 20kV. To perform EDX analysis in the SEM, the specimen was tilted to 45°. The real time was set at 120s and the dead time was kept below 20%. In EDX (Energy dispersive X-ray analysis), the characteristic X-rays emitted by the different atoms as consequence of their excitation under the electron beam are used to identify them.

3.3.4 Quantitative measurements

A computer-aided image analysis program, Optilab, has been employed to analyse recorder electron micrographs. Optilab is used to obtain quantitative microscopic information of grain size, size and distribution of precipitate. Quantitative analysis results obtained are presented in graphs in the experimental results (Chapter 4) of the thesis.

Grain size measurements

Measurements of grain size in the as received E1250 sample were carried out using the chart comparison method according to the ASTM E112 standard. [82] The images at

magnification of 100x are compared to a set of standard micrograpghs of a known grain size. These standards charts are available in the ASTM E112 standard. This is a fast method but not as accurate as other measurement methods. However, due to the fine grain size and complex grain size distributions, Optilab image analysis was used for grain size measurements on the rest of the samples.

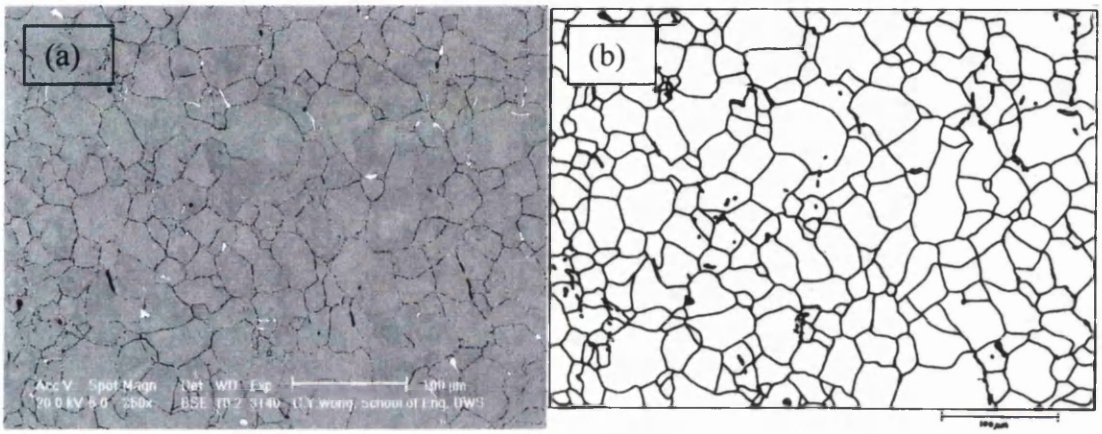

Figure 27: (a) SEM backscattered micrograph used for grain size measurement and (b) Tracing of grain size and scanning of the image in black and white.

The SEM electron micrographs were used for tracing the grain size on a tracing paper and then scanned into a digital black and white image. (Figure 27) The scanned image with black and white format was the binary image used in the Optilab image analysis program. Grain area was obtained in μm^2. Arithmetic mean of the data was used to analysis the evolution of grain size in every sample. There were 37 samples in total that were analysed for grain size measurements. The measurements were done on the both static aged area (grip area) and creep exposed (gauge area) of all specimens.

Precipitate size measurement

The precipitate size measurement was performed on unetched SEM backscattered electron micrographs. The measurements were done on both static aged area (grip area) and creep deformed (gauge area) of all specimens. Figure 28 shows SEM backscattered electron micrograph used for precipitate size measurement in the unetched condition. The precipitate particles give bright contrast and are in binary scale therefore suitable for use in the Optilab.

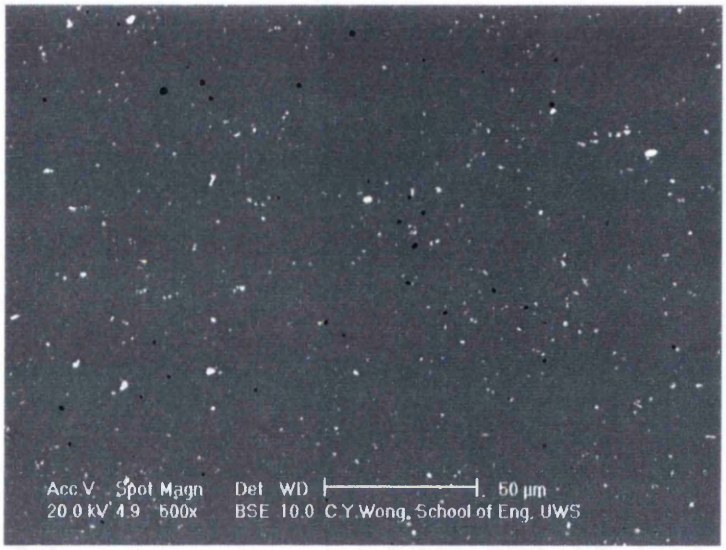

Figure 28: SEM backscattered electron micrograph used for precipitate size measurement.

The size measurement was in μm^2 and the arithmetic mean was obtained. Volume fraction of precipitate from planar section was measured using point counting method on the micrograph according to ASTM E 562 standard. [82] A grid with a number of systematically spaced test points is placed over the microstructure. The points lying over the constituent of interest are counted and divided by the total number of grid points to obtain a point fraction. Mean point fraction, $\overline{P_p}$ of second phase particle in planar section was the volume fraction calculated. This point counting method is generally the most efficient method used for obtaining volume fraction of second phase particles. [82]

3.4 Mechanical testing - Hardness testing

Vickers hardness measurements using a load of 10kg were employed to obtain hardness profiles in various aged and creep exposed conditions. 10 readings were collected for each sample tested. The test was carried out according to the British Standard BS 3S 500:1996. [92]

3.5 MTDATA calculations

MTDATA was used for studying and predicting the formation of various phases and formation of precipitates, under equilibrium conditions, on Esshete 1250 niobium alloyed creep resistant steel. Modelling of long term microstructural stability should include predictions of phase stability as a function of chemical composition, temperature and stress. The development of databases and software enables calculation of thermodynamic equilibria in multicomponent systems which allow predictions of phase stability for alloyed steels. MTDATA is a powerful phase equilibrium software developed by the National Physical Laboratory. [78] The basis for the calculations presented in this work is the TCAB database and the computer programs MTDATA.

MTDATA calculates equilibria system using a robust true Gibbs energy minimisation procedure, which requires no initial estimate of the equilibrium state. The basis behind the calculations made by this software product is the thermodynamic properties for various competing phases modelled as a function of temperature and composition. The used of MTDATA thermodynamic calculations in this work is to:

(i) Reducing the complexity of experimental investigations
(ii) Allows determination of phases occurred at the concerned temperature
(iii) Supports experimental procedures by identifying important phase prediction.

CHAPTER 4

4.0 EVOLUTION OF MICROSTRUCTURE UNDER STATIC AGING

Esshete 1250 austenitic steel is currently set as a standard material for superheater tubing in UK power plant. The study on microstructural evolution is to ensure that the secondary phases formed would not detrimental to creep strength and also would not invalidate the extrapolations of creep test data. Two grades of Esshete 1250 were provided by British Energy. The compositions and heat treatment information are given in Table 8.

4.1 Prediction of the phases present in Esshete 1250 and Esshete 1250-BH using MTDATA

MTDATA was used to predict equilibrium phases occurred in Esshete 1250 austenitic steel. This helps to confirm the secondary phases present during ageing and during high temperature exposure. Figure 29 shows predicted equilibrium phases calculated by MTDATA for E1250 parent steel. Precipitate of MX at the solution treatment temperature at 1080° was predicted. No sigma phase was predicted at the temperature above 700°C. These results are in agreement with SEM observations. Relatively large precipitates (mean size of 15.61μm^2) are found in E1250 as received (parent) sample. The precipitates are residual precipitates which are not dissolved during solution treatment.

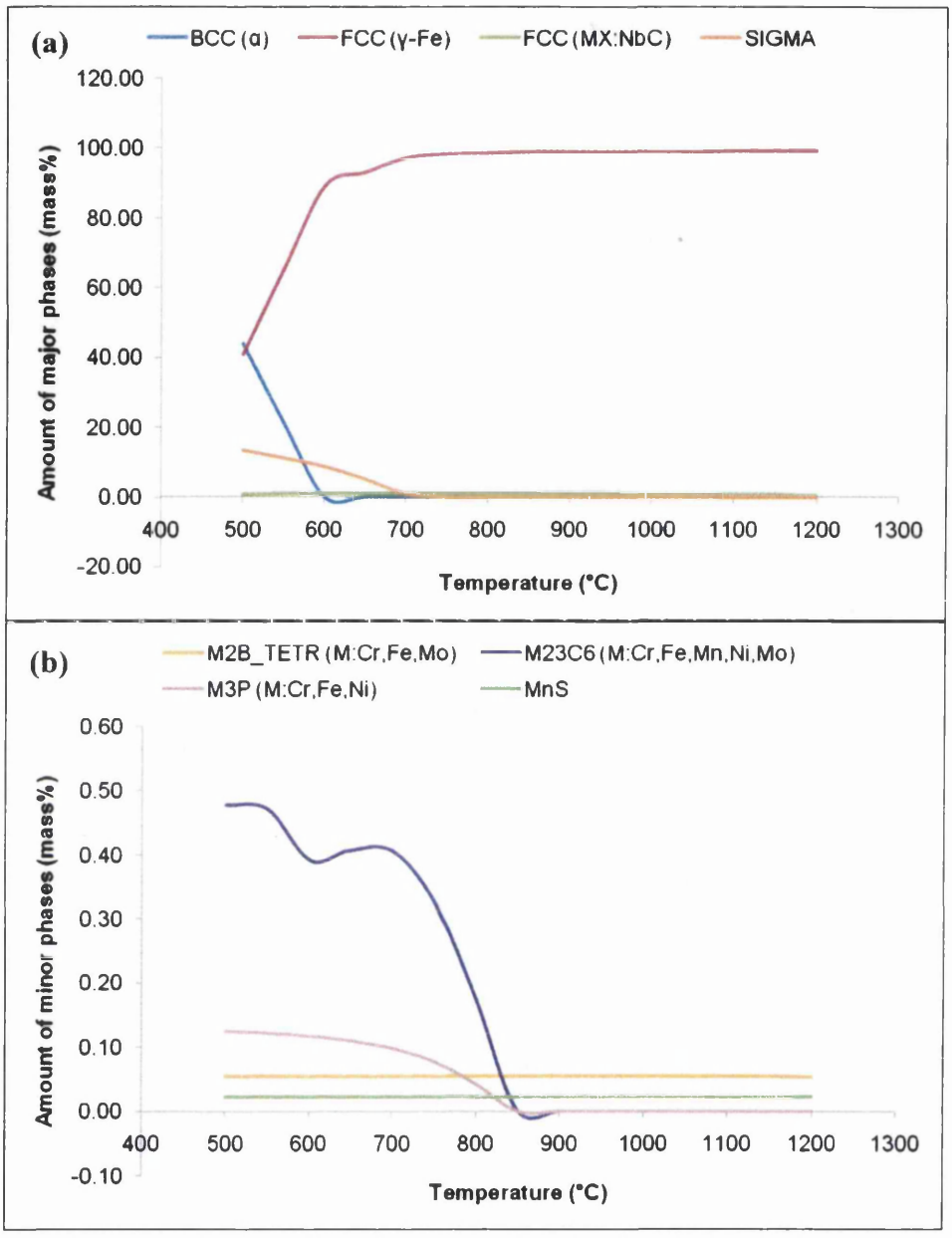

Figure 29: MTDATA thermodynamic prediction of phases expected to be present (under equilibrium conditions) in E1250 parent material (a) major phases (b) minor phases.

MX particles and sigma phase were found to be the major precipitation phase in the temperature range of 500°C to 700°C. However, precipitation of sigma phase was predicted to decrease when temperature is increased. Precipitation of the MX phase is stable over the temperature range. SEM observation shows stable MX precipitate over the austenite matrix during static aging at a temperature of 550°C and 575°C. However, No sigma phase was detected after long term aging. $M_{23}C_6$ carbide was predicted to be a minor constituent (>0.5%) in the steel at a temperature of 500°C to 800°C. The amount

predicted is very low concentration and decrease significantly with the increase in temperature. It however, not appeared in the E1250 as received condition and after long term aging at temperatures of 550°C and 575°C under SEM observation.

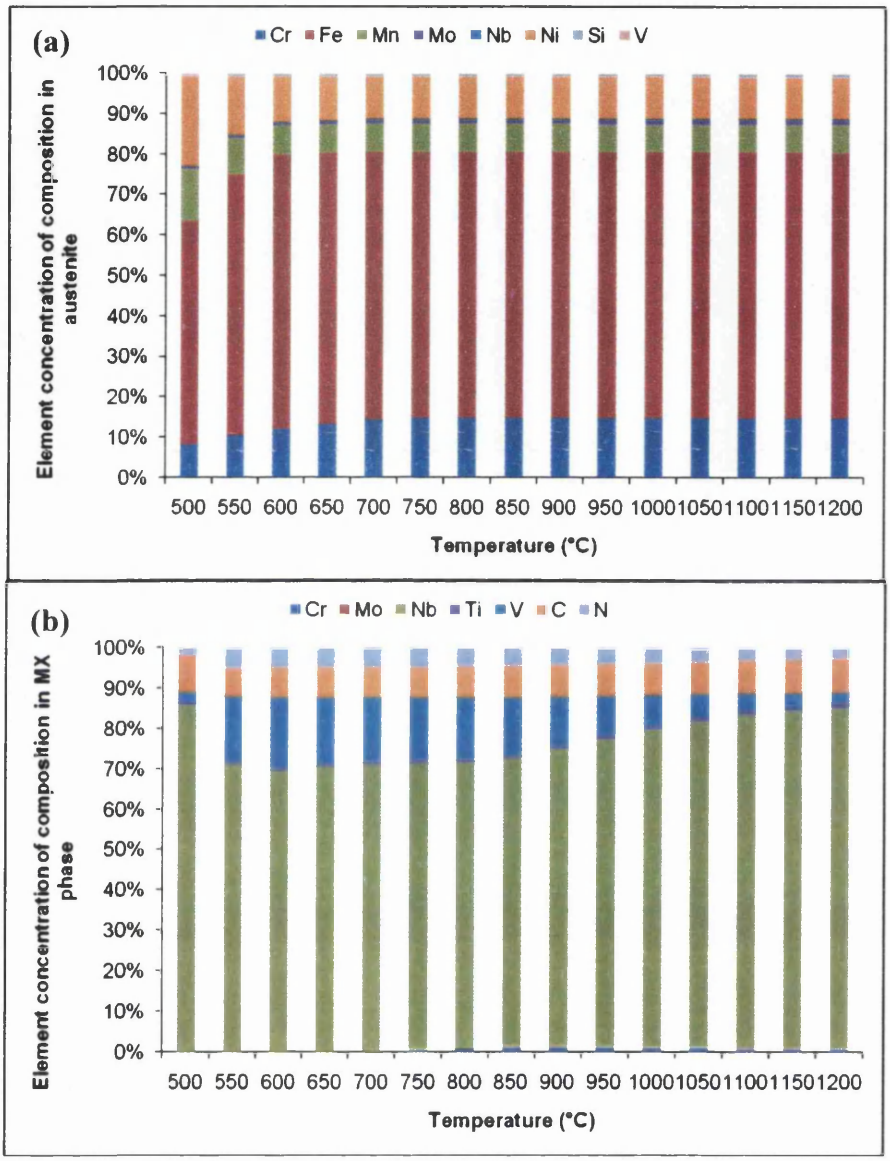

Figure 30: Calculated elemental concentration in (a) austenite and (b) MX phases for the Esshete 1250 parent material.

Figure 30 shows equilibrium chemical compositions of austenite and MX precipitate. Cr and Fe increase as the temperature increases in austenite. Mn and Ni are predicted to decrease as the temperature increases. There is a little change in composition of sigma phase in the temperature range of 550°C to 700°C. The amount of Nb increases with the increase of temperature in the MX phase. The amount of V is predicted to decrease in MX

phase as the temperature increases. Fe and W in $M_{23}C_6$ increase as the temperature increases, while Cr and Mo in $M_{23}C_6$ decrease as the temperature increases.

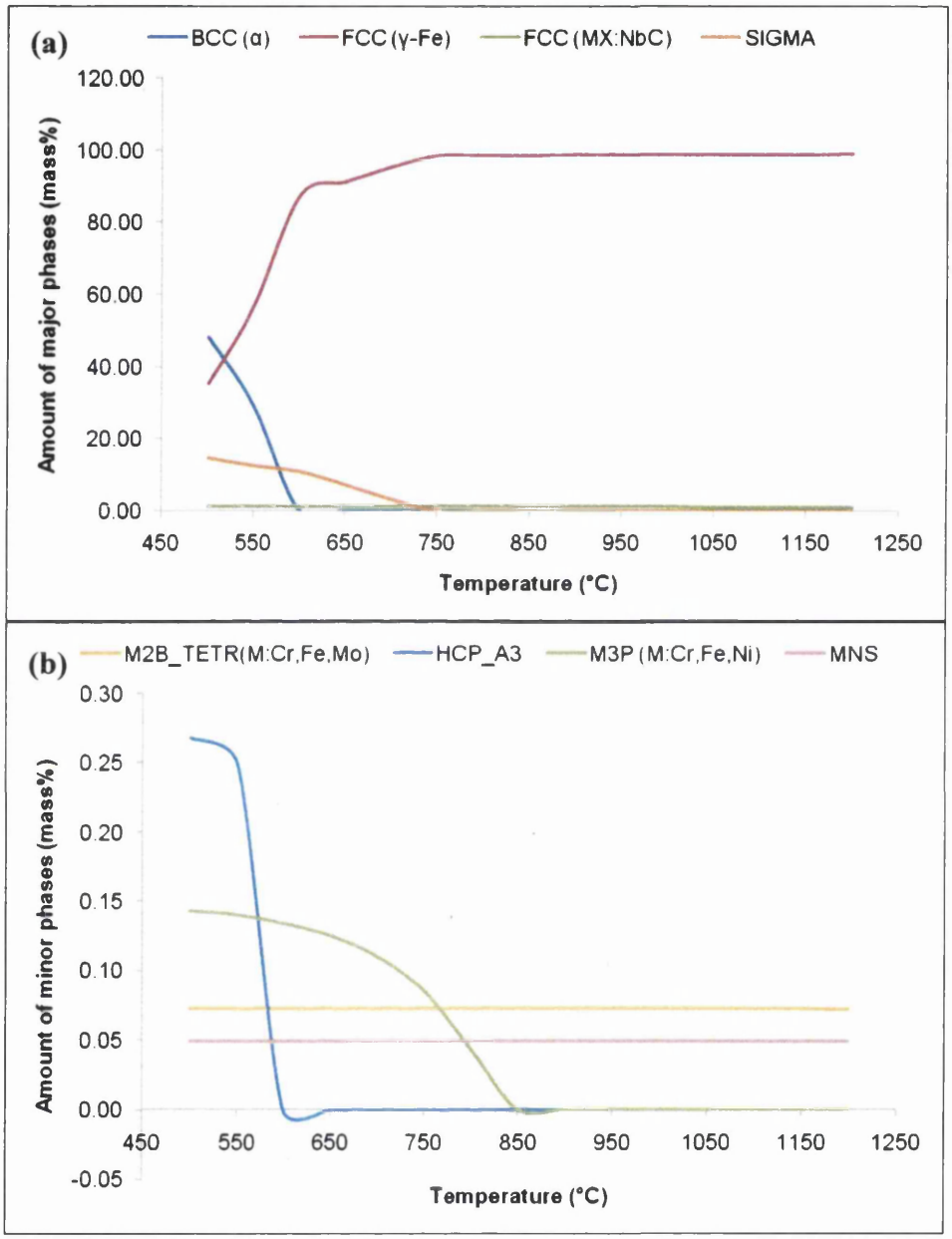

Figure 31: MTDATA thermodynamic prediction of various phases expected to be present (under equilibrium condition) in BH-E1250 material, (a) major phases (b) minor phases.

It is difficult to make meaningful prediction for the parent material of E1250-BH as the material is come with creep exposed conditions. Therefore, no SEM information could be obtained from the 'parent' of this material. However, solution treatment was known be treated at a temperature of 1050°C followed by air cooled. According to the MTDATA prediction, major phases predicted to occur are austenite, sigma phase and MX

phase. The predicted phases occur in E1250-BH by MTDATA calculation are not much different than those of the E1250 parent (Figure 31). SEM observation on statically aged samples at the temperatures of 550°C, 600°C, 650°C and 700°C show relatively coarse second phase precipitates and finely dispersed secondary precipitate distributed over austenite matrix. (Appendix-Figures 81-84) However, sigma phase was not found to appear during long term aging.

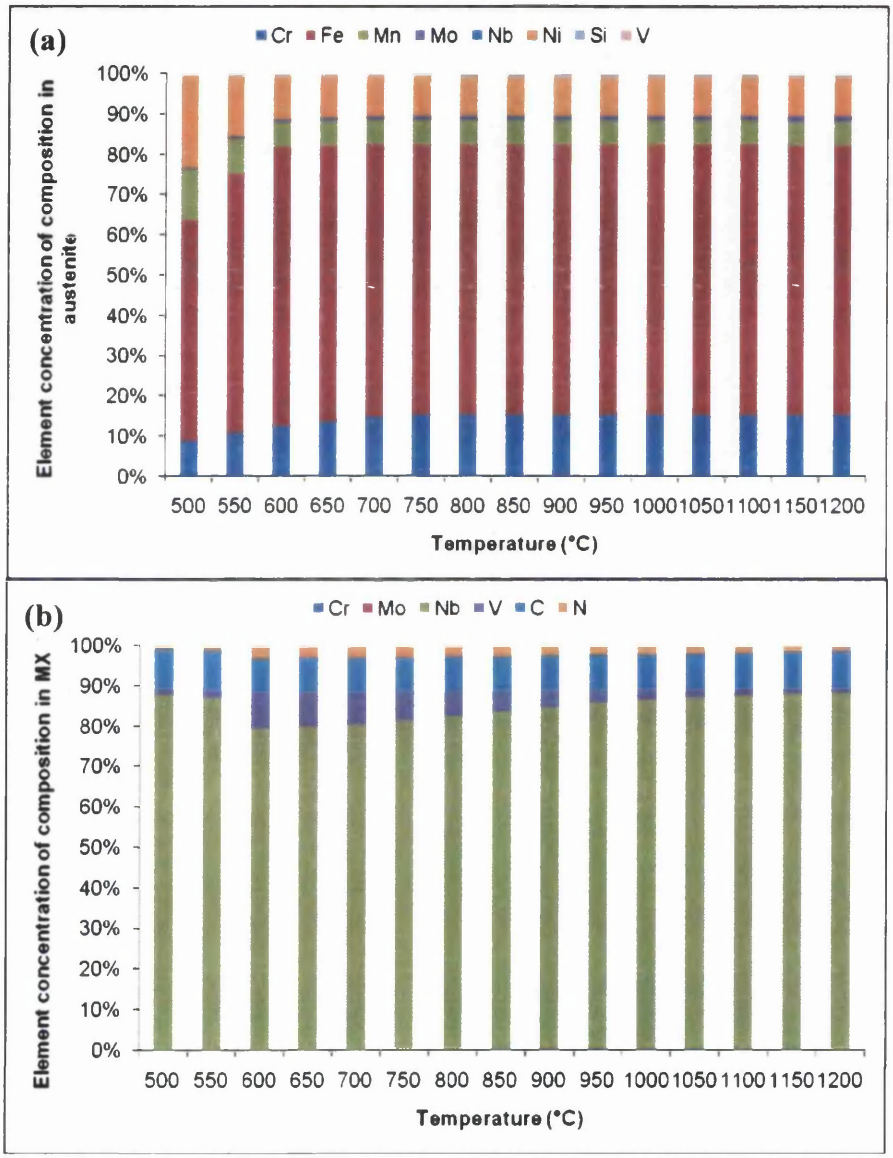

Figure 32: Calculated elemental concentration for (a) austenite and (b) MX phases in E1250-BH steel in various temperatures.

Figure 32 presents the MTDATA calculations of the composition concentration within γ-Fe and MX phase. According to MTDATA calculations, under equilibrium

conditions, the amount of Fe increases in solution until approximately 600°C, while it stabilises when 700°C is exceeded as predicted in E1250 parent. During heating at temperatures of 400-600°C, the compositions of Ni and Mn decrease in solution. The composition of Cr increases in solution until 750°C, while it remains steady when this temperature is exceeded. The amount of other alloying elements such as Mo, Si and V is very small as indicated. The result on the composition of MX precipitates shows a decrease of Nb while the amount of V increases in solution. This prediction also shows Nb increasing with temperature rise and thus reducing the amount of V in solution. HCP phase is predicted to be rich in V, Nb, N and Cr. However, its occurrence is predicted to disappear at temperatures higher than 600°C.

MTDATA calculations suggest that under equilibrium conditions, MX precipitates in E1250-BH steel are mainly niobium rich carbides. (Figure 32b) Such a composition remains very stable for all temperatures modelled (within the 500-1200°C range). This is in agreement with the SEM observation on statically aged samples.

4.2 Identifying MX precipitate with SEM and EDX

The experimental methods are described in detail in Chapter 3. Efforts have been made on the etching of Esshete 1250 steel with two different kinds of etchants. Some of the previous work on etching stainless steels has been performed using KOH solution. [8, 25, 68-69] Therefore, the first attempt to etch the Esshete 1250 samples was using the 56w.o.% KOH aqueous solution. The technique chosen was electrolytic etch providing uniformly etch results according to the ASM Stainless Steel Speciality handbook [8]. The second attempt was using 10w.o% dilute aqueous oxalic acid solution. Both etchants will be evaluated under the consideration that they should work for scanning electron microscopy and for manual point counting as well as digital image analysis. The results of etching were presented in Figure 33.

The use of KOH solution reveals clear grain boundaries but severe pitting of precipitates from the austenite matrix. No σ-phase was found to appear in the steel. However, oxalic acid solution gives more adequate etching to reveal both grain boundaries and precipitates in the austenite matrix. Therefore, oxalic acid solution was chosen as the preferred etchant for Esshete 1250 steel during this work. This etchant though is very sensitive to the choice of current and etching time. All the specimens studied were etched at 2V for 30s-60s in 10w.o.% dilute aqueous oxalic acid solution.

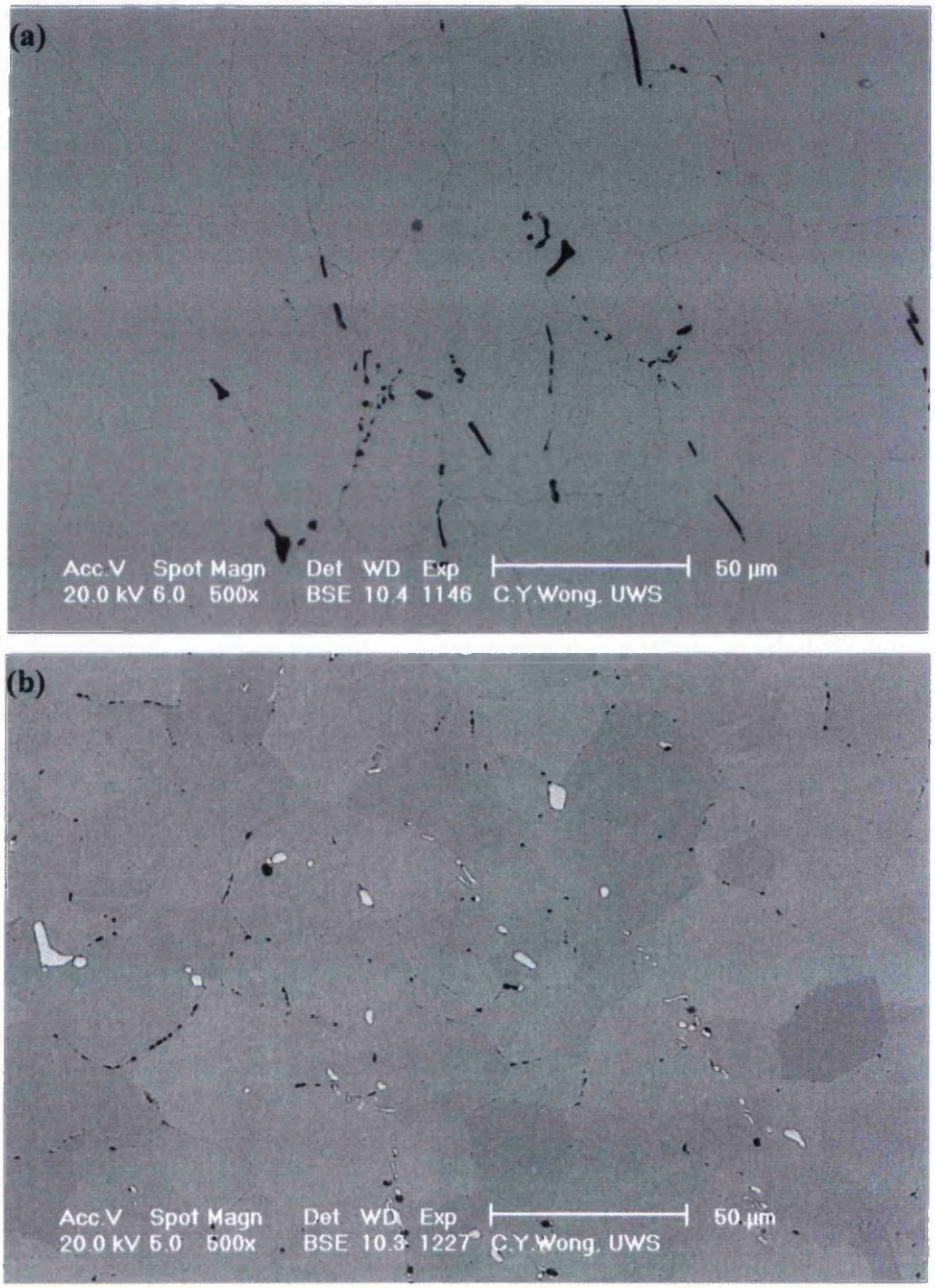

Figure 33: SEM backscattered micrographs of Esshete 1250 parent using (a) KOH solution and (b) oxalic acid solution, electrolytically etched at 2V dc for 30s.

The use of backscattered electron micrographs on polished samples is a reliable technique, and this was done on the Esshete 1250 steel with good results. Figure 34 show the SEM secondary and backscattered micrographs of the microstructure of Esshete 1250 parent steel.

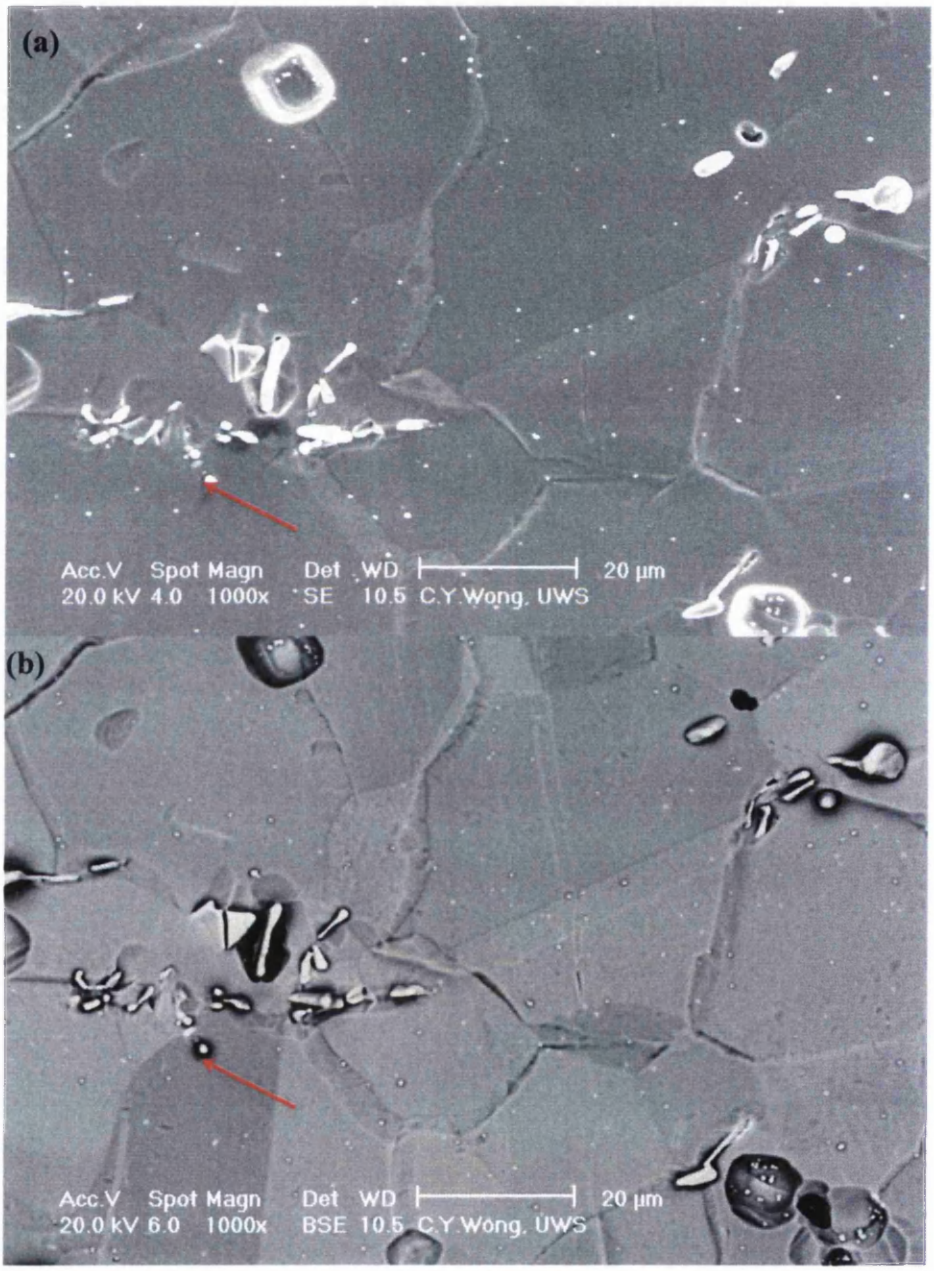

Figure 34: SEM micrographs of as received Esshete 1250 steel using (a) secondary electron and (b) backscattered electron.

SEM studies indicated that in the Esshete 1250 austenitic stainless steel contained an extensive precipitation of irregular shaped particles at austenite grain boundaries and within the matrix. Since SEM and MTDATA suggested that it is high probability that MX

precipitate is rich in Niobium (Nb), it was necessary to characterise these secondary phase. EDX microanalysis is therefore, used to investigate the nature of these precipitates and their composition

The microstructure in the as received E1250 contained coarse and fine second phase particles. The coarse particles are precipitates that do not dissolved during the solution treatment. EDX microanalysis has been performed on these secondary phase precipitates to obtain their quantitative composition. The results obtained indicate that the particles were rich in Nb (Figure 35). These secondary phases are also found in statically aged samples. The EDX spectra results of the elemental analysis are shown in Figures 90-95 in Appendix. Most of the investigations have focused on the coarse irregular precipitates and finely distribute spherical precipitates. The EDX spectra revealed the presence of a substantial amount of Nb, giving a composition closer to the expected NbX phase.

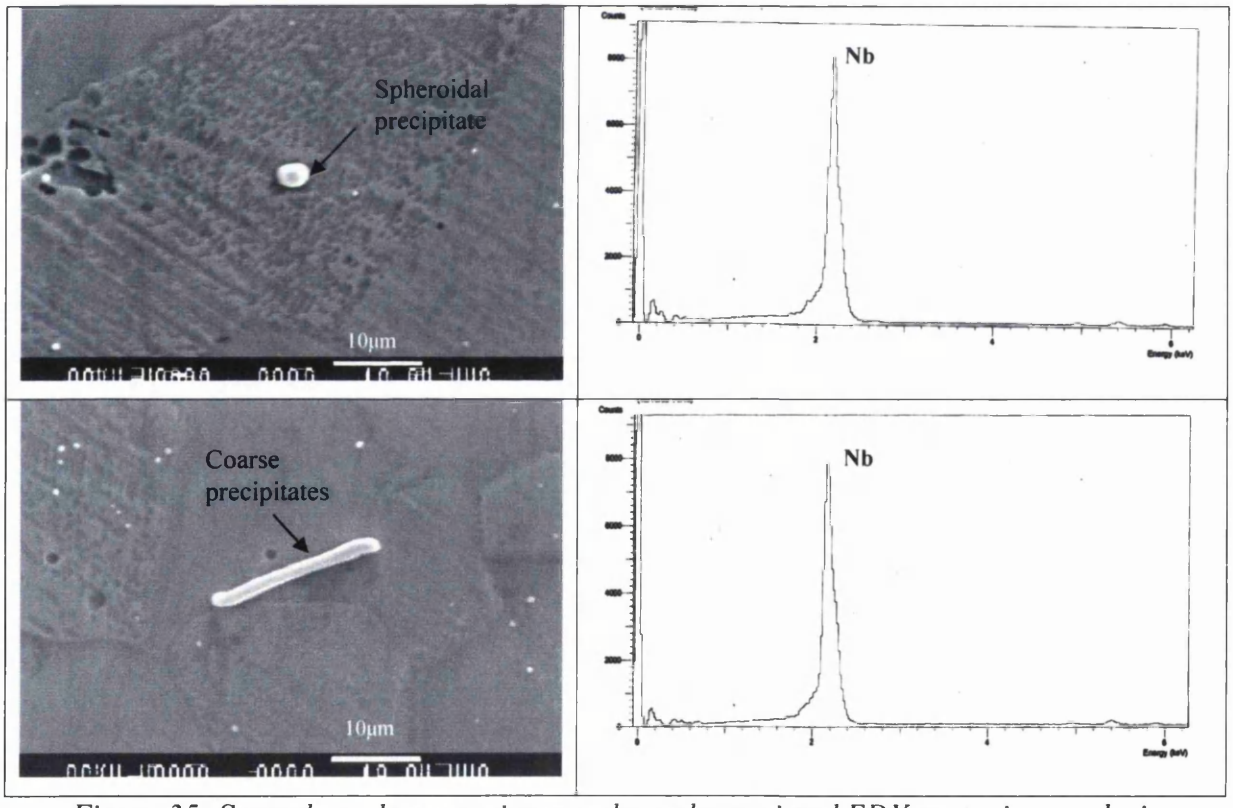

Figure 35: Secondary electron micrographs and associated EDX spot microanalysis traces of the as received E1250 parent material.

EDX microanalysis was carried out to perform the elemental analysis of precipitate species. This work is to confirm the main chemical element present in the majority of the

precipitates. Therefore, it is only an indication of the main element present and not the quantity or amount of a specific chemical element present in the analysed area.

4.3 Particle Size Analysis

The contrast from MX precipitate using backscattered electrons in stainless steel with Nb is very strong on a polished sample. (Figure 34b) So it is almost desirable to avoid etching for volume fraction and precipitate size calculation work, as underestimation of the size and distribution of particles is an apparent risk. Figure 36(a) show the SEM micrographs employed for precipitate size and volume fraction calculations. SEM samples for particle size analysis were unetched due to the severe pitting caused to an etched sample resulting in 'drop out' of second phase precipitates.

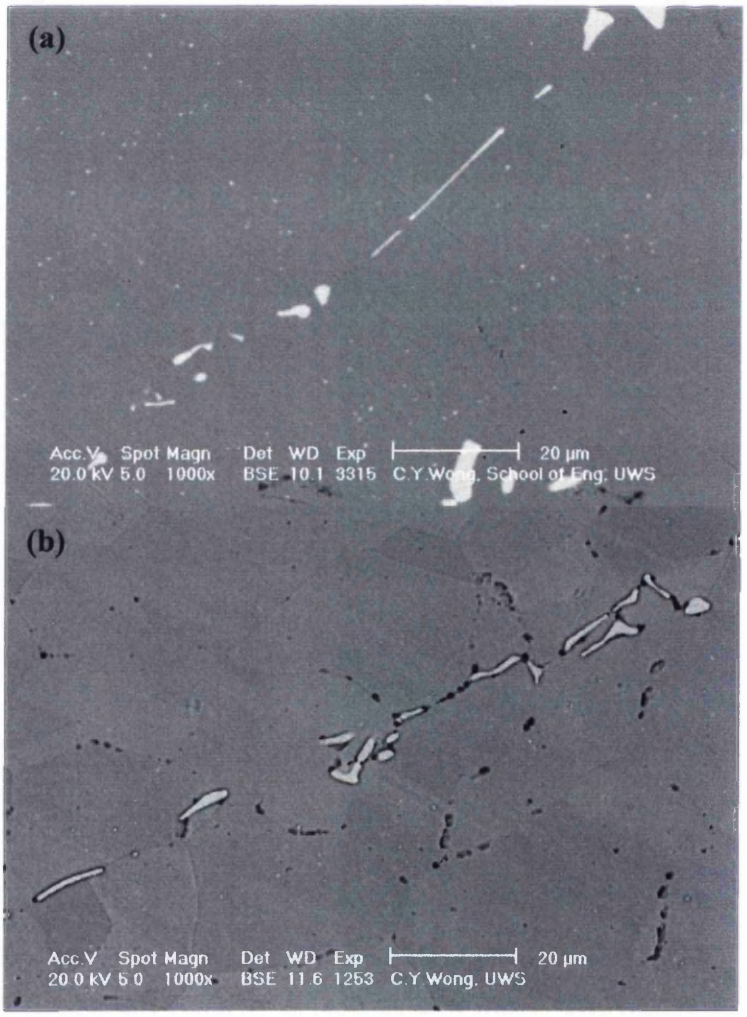

Figure 36: SEM micrographs used for image analysis and manual point counting of volume fraction. (a) un-etched condition, (b) etched with oxalic acid solution.

SEM backscatters electron micrographs give a perfect contrast of the MX precipitate thus facilitating digital image analysis (Figure 36). Therefore, both manual point counting and digital image analysis are possible. The precipitate size of MX particles is obtained from areas corresponding to statically aged samples and also on creep exposed areas. The error bar used is the standard error of the mean calculated from the standard deviation and mean of precipitate sizes measured in each sample. Distribution graphs of each size group are tabulated to facilitate interpretation of precipitate size evolution.

4.3.1 Particle size measurement in E1250 steel

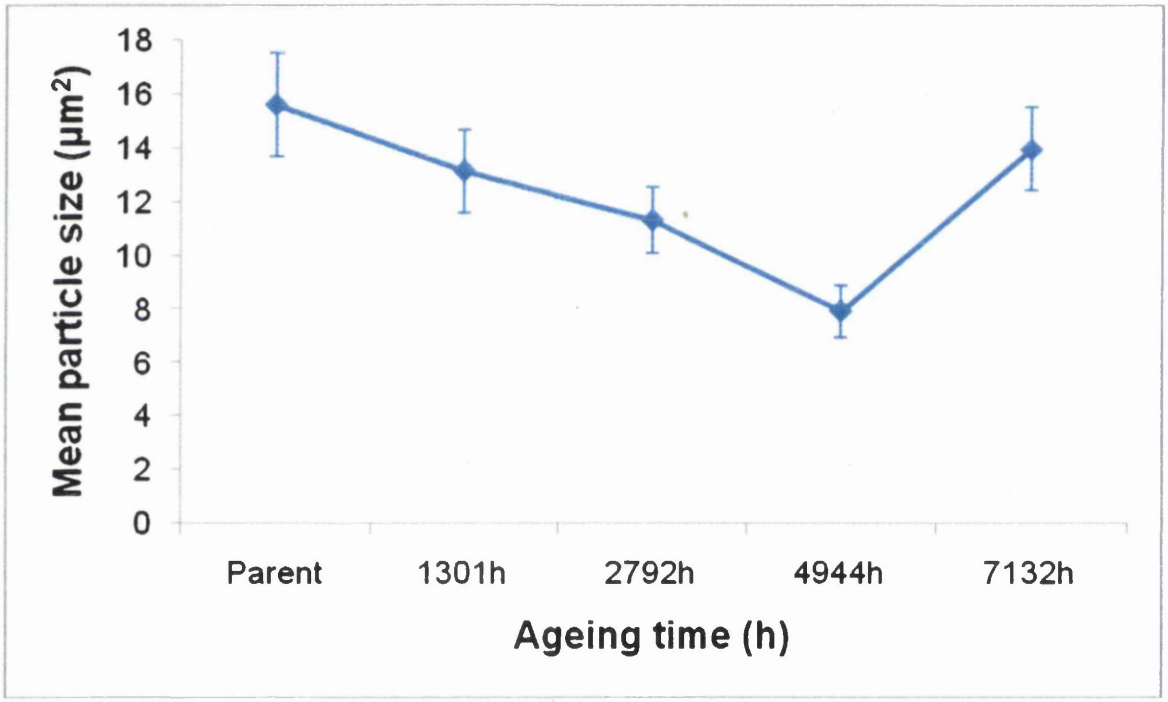

Figure 37: Change of MX particle mean size of E1250 steel during ageing at 550°C.

The evolution of average MX particle size for E1250 steel aged at 550°C is presented in Figure 37. It is found that the mean particle size decreases after prolonged ageing until 4944h. The mean particle size increases after extended ageing for 7132h. The distribution of MX particle size is presented in Figure 38. Relative frequency on the size group of 5.00-5.99 μm^2 is high in the E1250 parent specimens, specimens aged at 1301h and 2792h. However, prolonged aged specimens for 4944h exhibit a realtive high amount of MX particles that are in the finest group size (<4.99μm^2). Precipitate size decreases up to long ageing times of 4944h. After prolonged ageing for 7132h, the precipiatate size

appears to increase. Distribution of precipitates in the group sizes of 10.00-14.99 μm^2 and <4.99 μm^2 show a relatively high frequency reflecting that most precipitates coarsen compared to ageing times of 4944h.

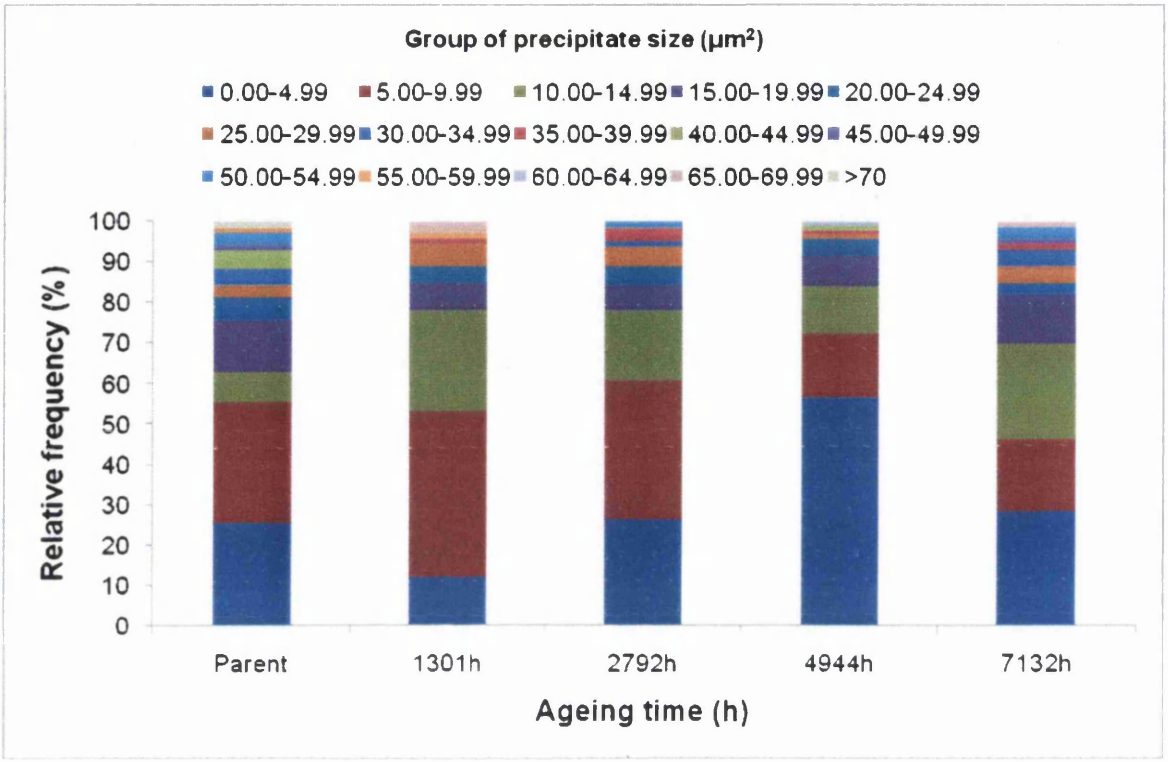

Figure 38: MX particle size distribution in E1250 steel statically aged at temperature of 550°C.

Particle size evolution for the sample aged at 575°C shows decreases as the ageing time is increasing (Figure 39). It is found that the mean second phase particle size is decreasing when the grain size is decreasing (Figure 45). Thus second phase particle might have an effect on controlling the grain size during ageing. Figure 40 show the MX particle distributions at an aging temperature of 575°C and suggest that precipitates coarsen during ageing to 2035h. However, the majority of the precipitates are distributed in the size group of finer precipitate size (<14.99μm^2) after prolonged ageing to 3489h.

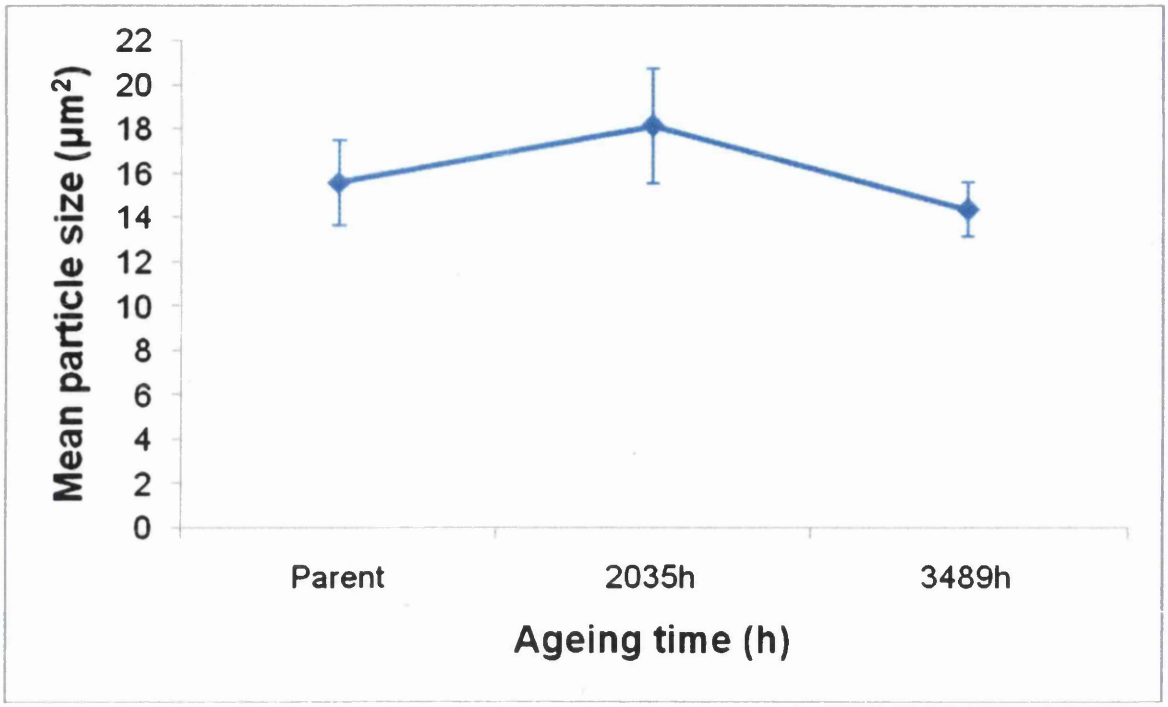

Figure 39: Change of MX particle mean size of E1250 steel during ageing at 575°C.

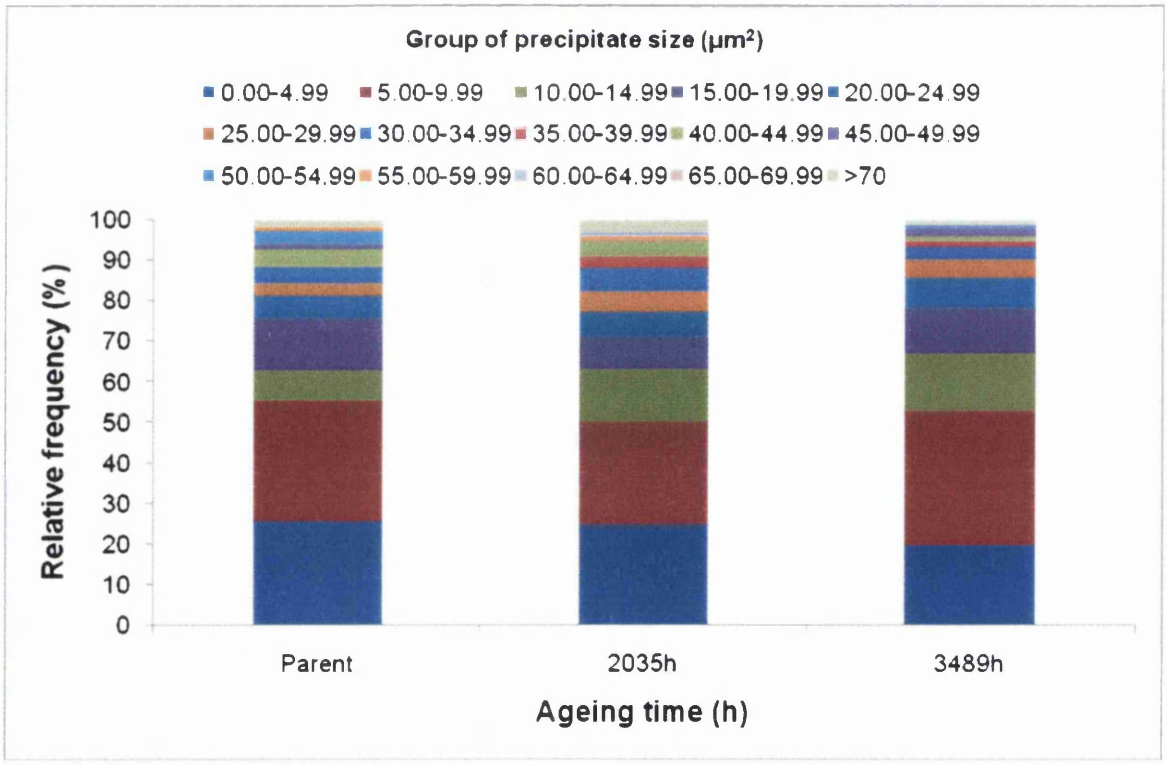

Figure 40: MX particle size distribution measurement in E1250 steel aged at temperature of 575°C.

4.3.2 Particle size measurement in the E1250-BH

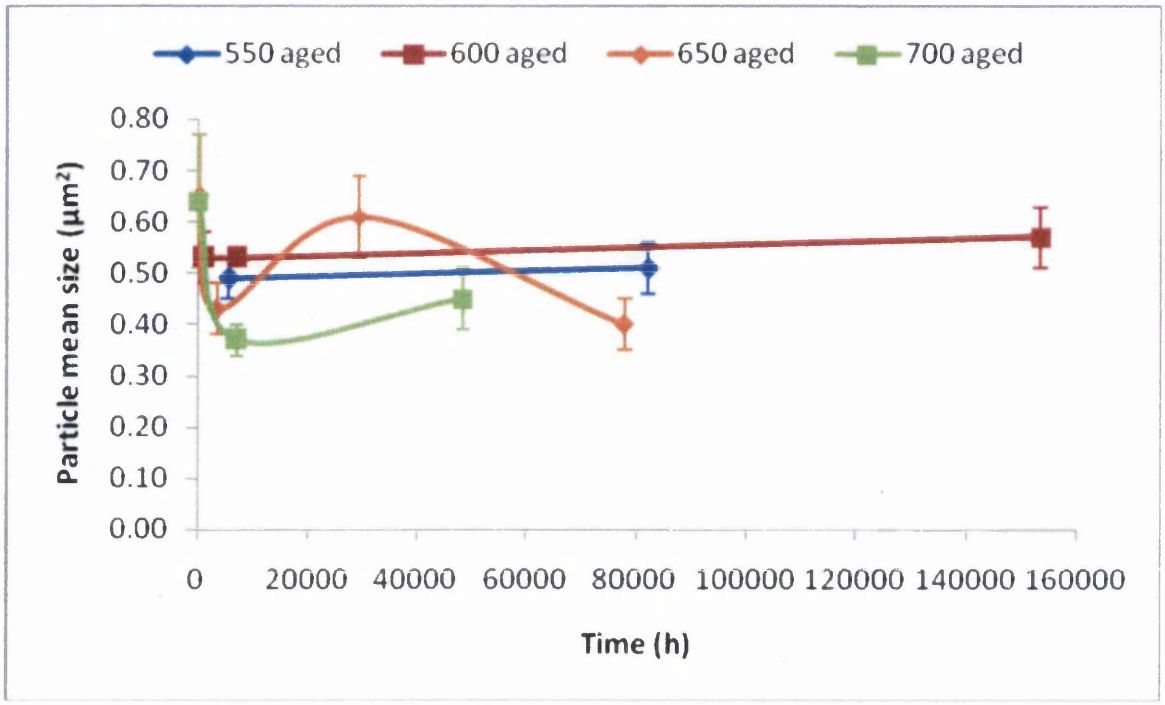

Figure 41: Change of MX particle mean size in BH-E1250 steel aged at a temperatures of 550°C, 600°C, 650°C and 700°C.

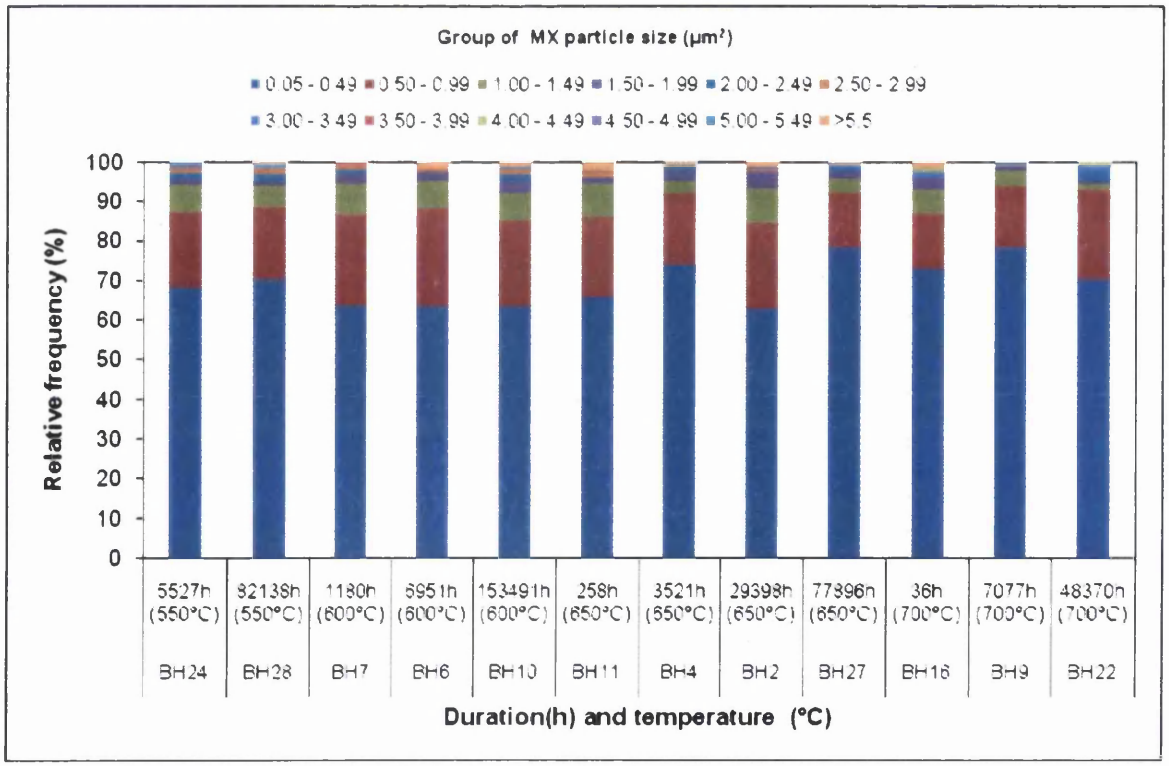

Figure 42: MX particle size distribution in BH-E1250 statically aged specimens.

During long term aging at temperatures up to 600°C, the mean particle size of MX precipitates is stable. The mean particle size of MX particles is variable when temperatures increase to 650°C. However, a decrease in MX particle size is observed during long term aging at a temperature of 700°C. In contrast, it is found that a slight increase of MX particle size is observed during exposure to 600°C. (Figure 41) Distribution of MX particle size for E1250-BH again shows that the size of these secondary precipitate are stable at aging temperature up to 600°C (Figure 42). However, mean particle sizes are fluctuating when aging at a temperature of 650°C and above. In addition, the relative frequency for the fine particle size group is not constant at an aging temperature of 650°C. Prolonged aging at a temperature of 700°C indicates some coarsening as a decrease in the relative frequency value of fine particle size group is observed.

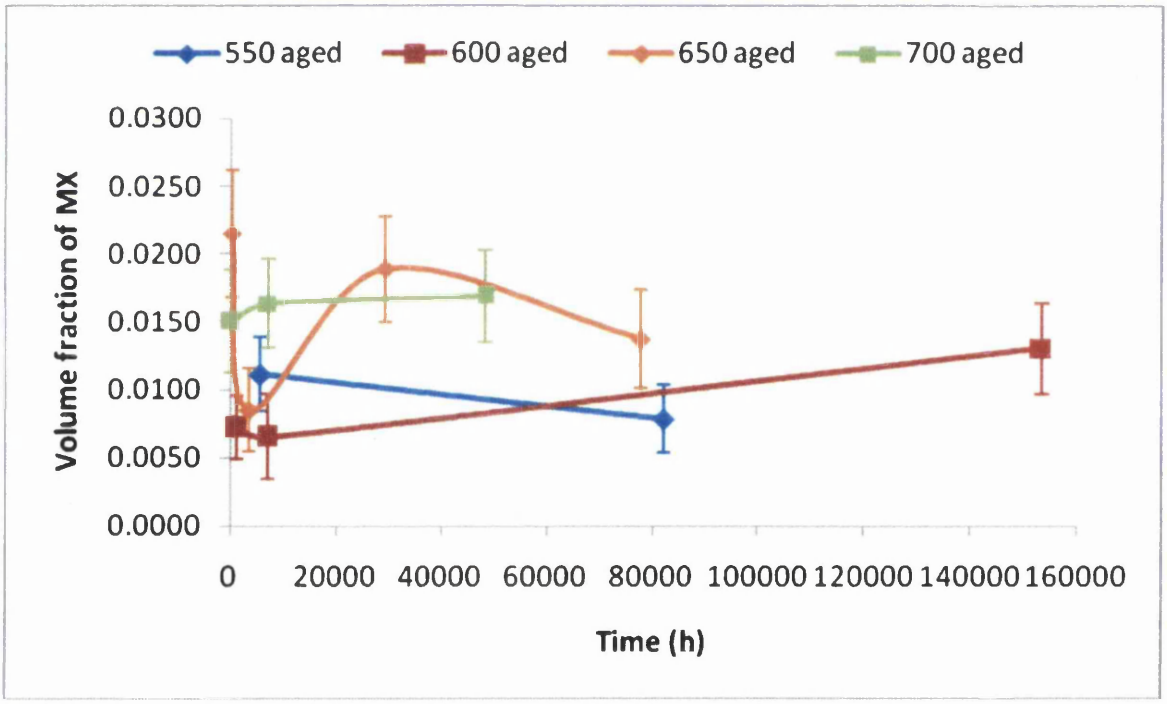

Figure 43: Volume fractions of MX precipitates for the E1250-BH samples aged at temperatures of 550°C, 600°C, 650°C and 700°C.

Volume fractions of MX are presented in Figure 43. The volume fraction of statically aged specimens is increased with an increase in aging time at a temperature of 600°C only. The magnitude of volume fractions measured show a decrease after prolonged ageing. An increase of the volume fraction for creep deformed specimens is

observed at temperatures below 600°C. The amount of MX precipitate phase is 0.8%-1.0% at temperatures of 500°C-700°C as predicted in MTDATA calculations (Figure 29a). The volume fraction calculated for MX phase presence in the steel is below the value of 0.02. Results from experimental data seem to yield lower values compared to the modelling calculations. This is not surprising since the experimental results are extracted from microstructures that are not always under equilibrium conditions at the elevated temperatures of creep exposure. Moreover, the experimental calculations are based on the 'surface fraction' only and some of the extremely fine MX particles (nano size) were not counted due to the limitations of size measurement under SEM.

4.4 Grain size analysis

SEM samples were unetched for particle size measurement due to etched sample causing severe pitting of second phase precipitate. However, to calculate grain size, etching is preferred and sometimes the times of etching need to be extended for another 30 –60s for some samples. When etching with oxalic acid, the grain boundaries are attacked and thereby a sharp boundary is created at the grain boundaries interface seen using SEM/SE (Figure 34(a)), the grain boundaries in SEM/BSE are also very sharp (Figure 34(b)).

Characterisation of grain size by an index defined by the standard charts in ASTM E112 was used to find the ASTM grain size of Esshete 1250 in the as received condition. The magnifications used for the recorded micrographs were 100x according to the ASTM standard [82].The average grain size was estimated by the chart comparison method according to ASTM standard E112. [82] This method is fast but not as accurate as other measurement methods. Due to the nature of the fine grain structure in Esshete 1250 austenitic steel (ASTM grain size of 7), this comparison method did not show a variation of grain size in multiple samples measured. The total samples for measurement were 37. Therefore, grain size measurements were then performed by Optilab image analysis software using SEM micrographs taken from the transverse sections of specimens etched with 10%w.o dilute aqueous oxalic acid. This etchant was chosen due to its ability to reveal grain boundaries of the austenitic steel. The grain sizes perpendicular to the long axis in stress-free (statically aged) material and also the creep exposed material were

obtained. All micrographs used for the measurement were taken at a fixed magnification of 250x. Approximately 150-300 grains were included in the micrograph under this magnification and it is best to have more than 100 grains for measurement according to the British standard BS1002:03. Results of mean grain area from E1250 and E1250-BH specimens were tabulated in graphs. The error bar plotted was the standard error of mean calculated from the standard deviation divided by the square root of number of the grain measured of each sample. The non-uniform of grain size has been observed on SEM electron micrographs. This caused some concern hence, grain size distribution graphs were constructed to facilitate the interpretation of the grain size evolution.

4.4.1 Grain size evolution of E1250 parent

Optilab image analysis was performed for calculating the trend grain size on this work. Figures 44 and 45 show the results of the grain size measurements following long term ageing at temperatures of 550°C and 575°C respectively, for E1250 specimens. It can be observed that a decrease in grain size is correlated with longer ageing time. The error bar shows the standard error of the measured grain area.

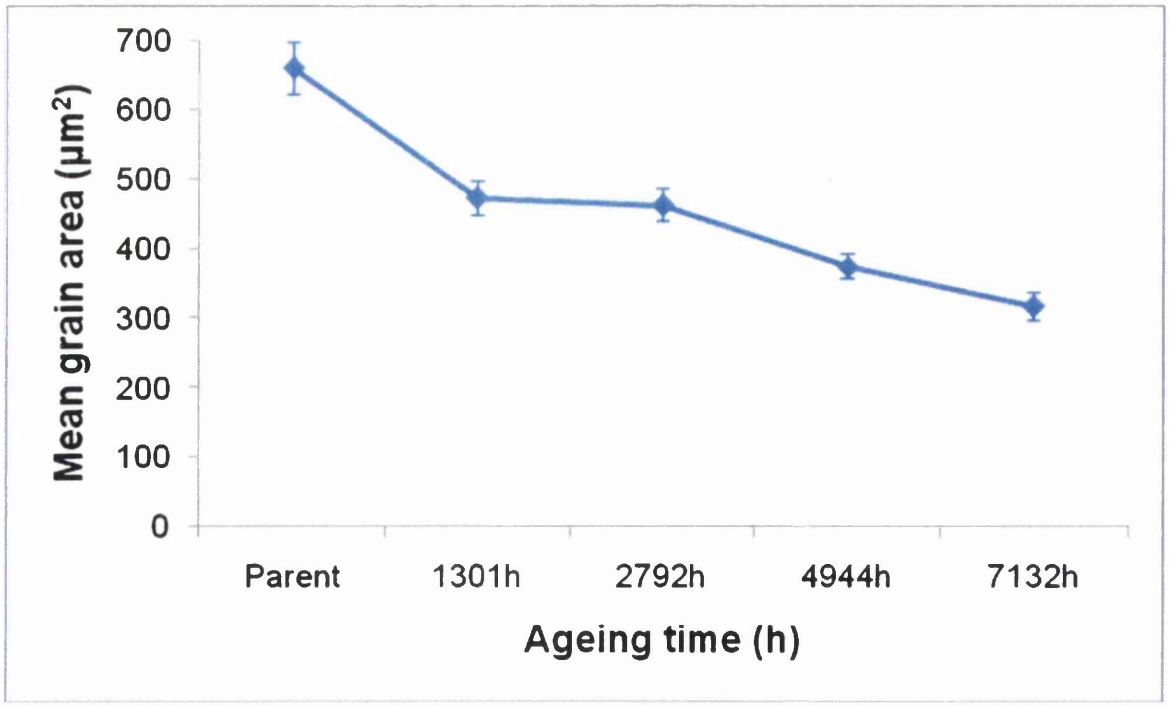

Figure 44: Grain size evolution in E1250 steel aged at a temperature of 550°C.

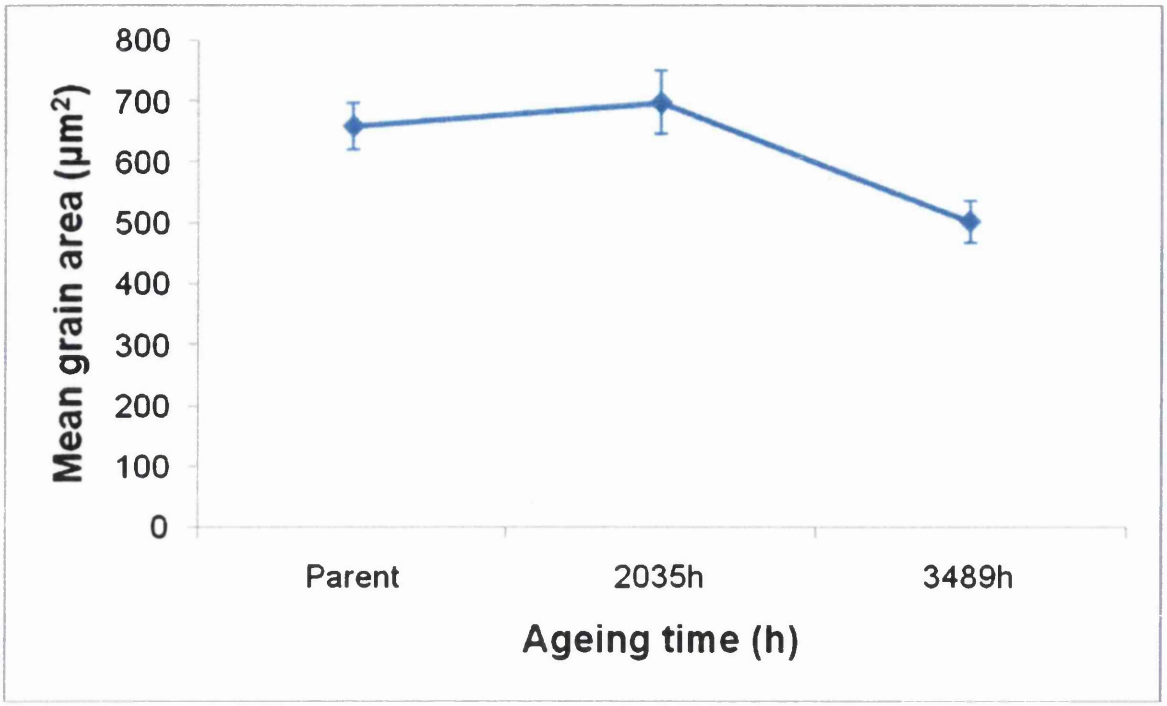

Figure 45: Grain size evolution in E1250 steel aged at a temperature of 575°C.

Grain size distributions are presented in bar chart to interpret the size evolution. Grain area distributions results in the as received E1250 parent specimen are presented in Figures 46 and 47. It was found that most of the grains are distributed in the group size of $400\mu m^2$-$599\mu m^2$ for the as received (parent) specimen, whereas in the aged specimen, the majority of the grains are distributed in the group size of less than $200\mu m^2$ for both ageing conditions. Mean grain size and distribution of the grain size obtained from both specimens indicate that grain size is reduced after prolong ageing.

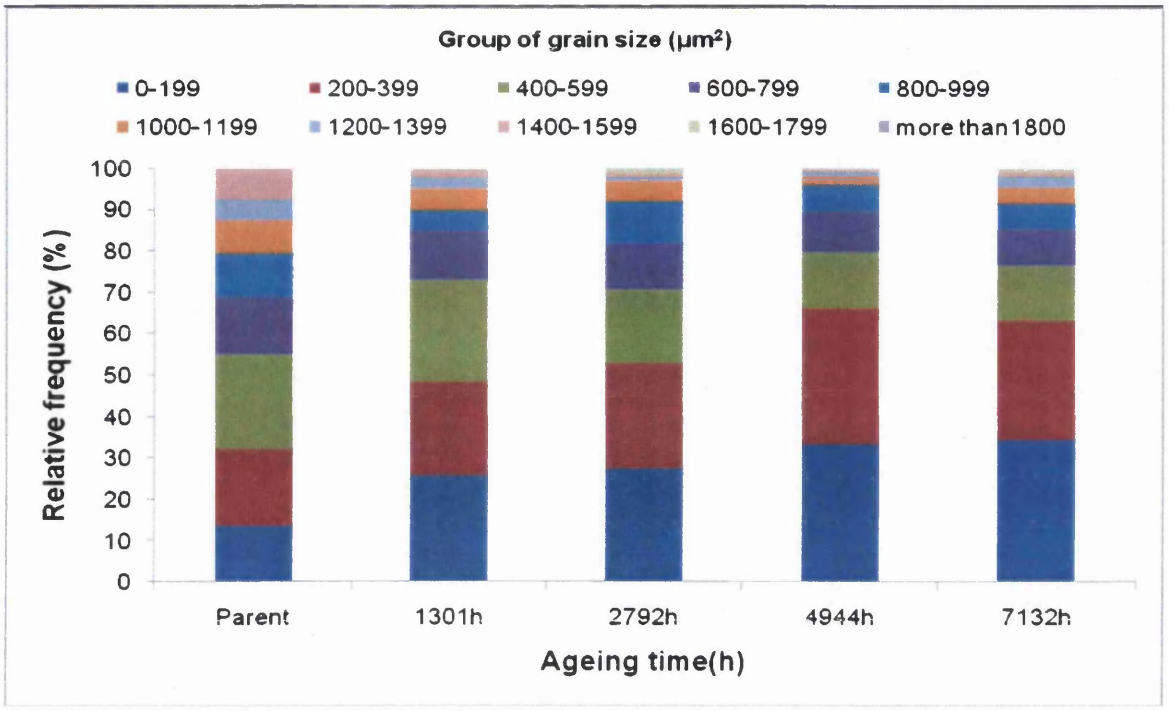

Figure 46: Grain area distribution measurements of E1250 steel aged at a temperature of 550°C.

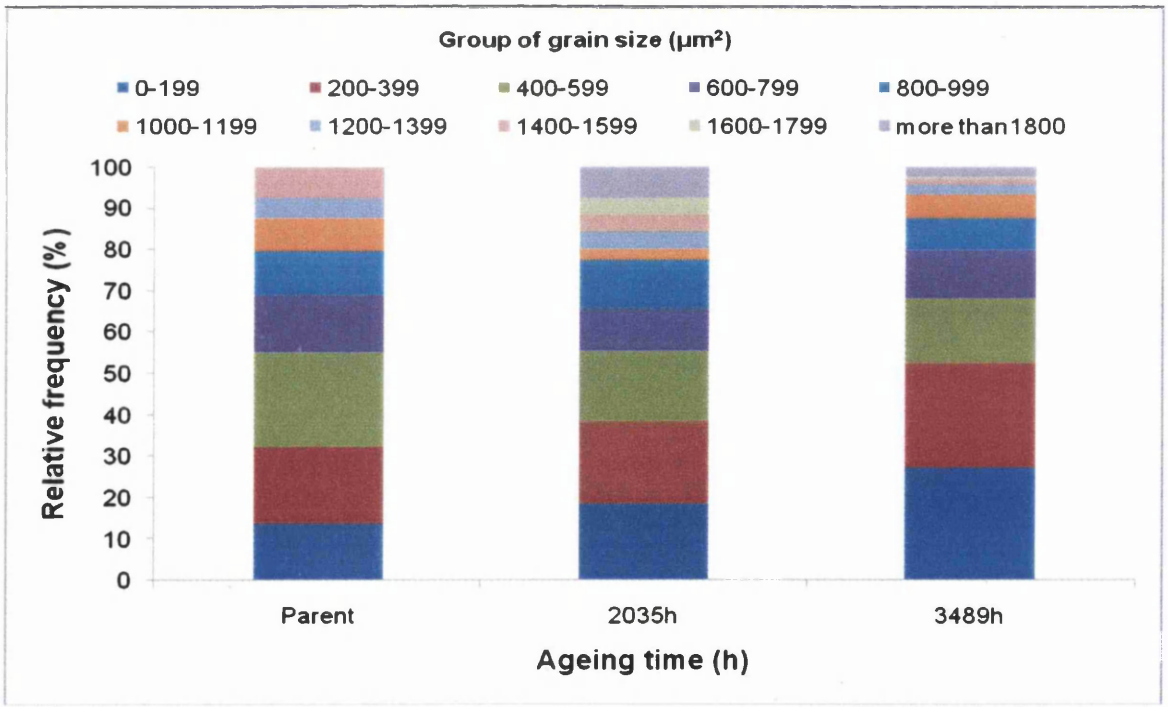

Figure 47: Grain area distribution measurements of E1250 steel aged at a temperature of 575°C.

4.4.2 Grain size evolution of the E1250-BH

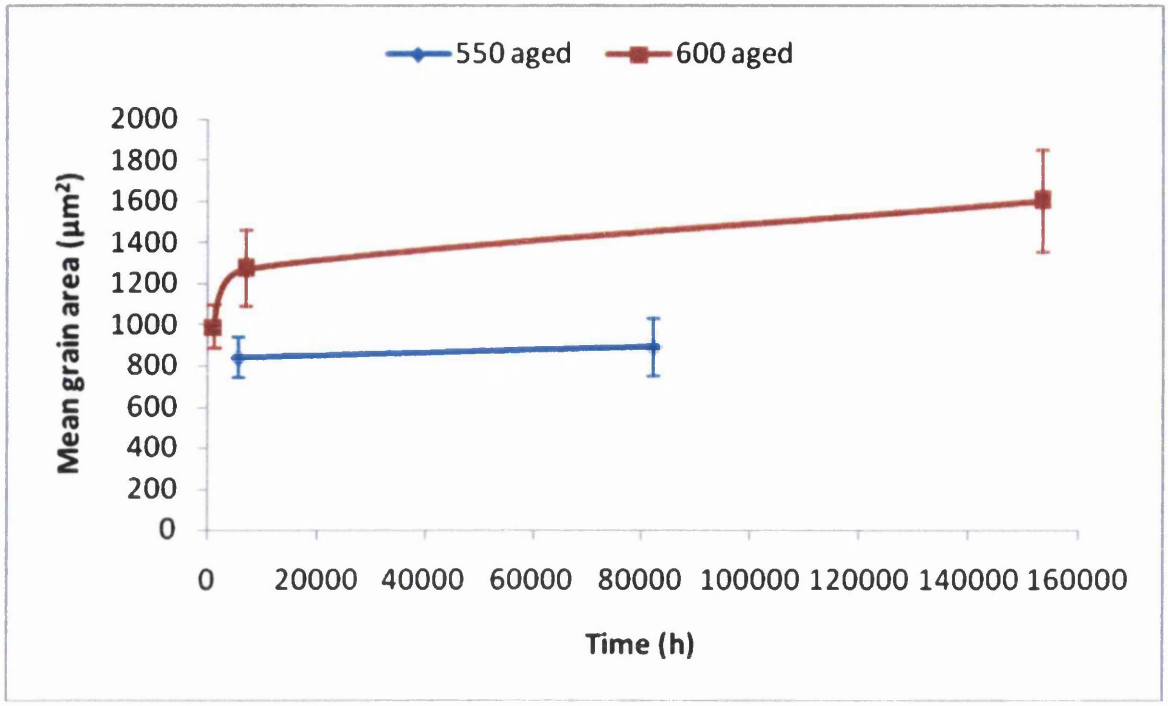

Figure 48: Grain size evolution versus ageing time in BH-E1250 steel at temperatures of 550°C and 600°C.

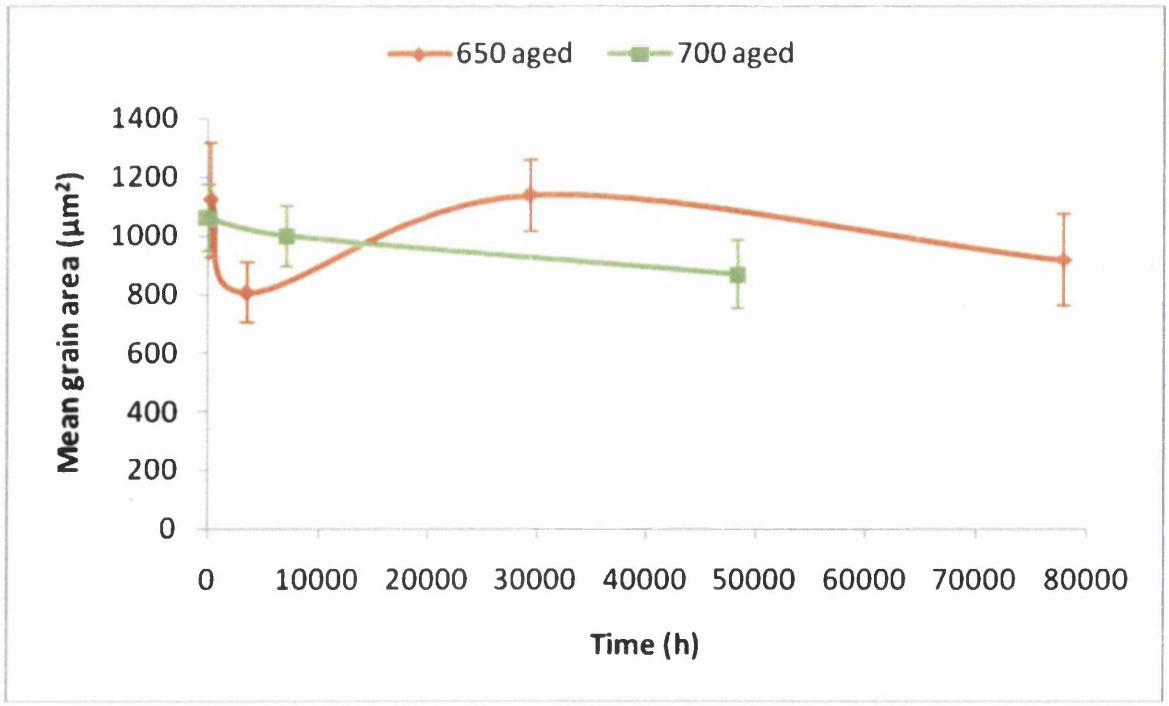

Figure 49: Grain size evolution versus ageing time for BH-E1250 steel at temperatures of 650°C and 700°C.

Grain size evolutions of statically aged samples are illustrated in Figures 48 and 49. The distributions of grain sizes for each specimen are plotted for quantitative analysis (Figure 50). The statically aged specimens show an increase in mean grain area with prolonged time up to temperature of 600°C. At ageing temperature above of 650°C, a decrease of mean grain area is observed after prolonged ageing.

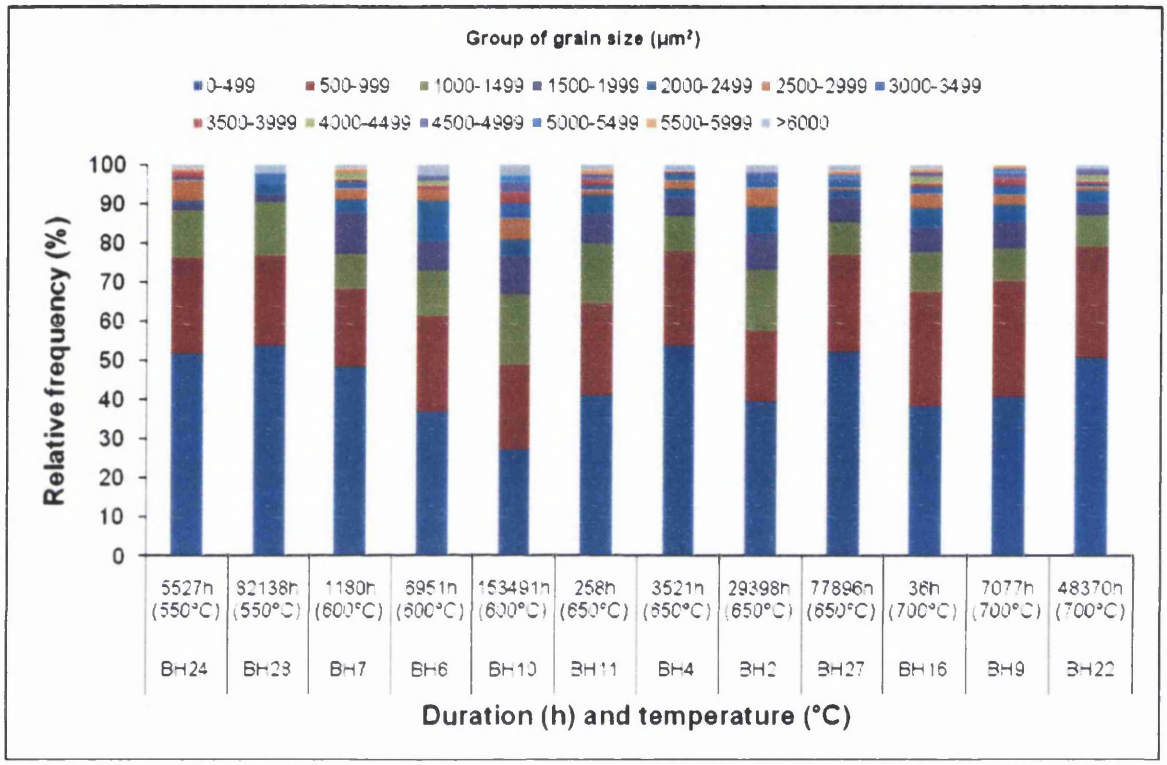

Figure 50: Grain area distributions of E1250-BH statically aged specimens at temperature of 550°C, 600°C, 650°C and 700°.

Figure 50 shows the distribution of grain size for each E1250-BH specimen under statistically aged samples, after long term ageing at temperature up to 700°C. It was found that at a temperature of 550°C, the majority (~50%) of the distribution in grain area is in the smallest size group (<500μm^2). The relative frequency does not appear to have much difference even after prolonged aging to 82138h. The relative frequency of grain size distribution is decreased when specimens are subjected to a higher aging temperature of 600°C. The relative frequency shows a decrease when the duration is increased, which mean grain sizes tend to increase at prolonged aging time at a temperature of 600°C. At a temperature of 650°C, the relative frequencies of the majority group size are not constant for all the specimens aged up to 77896h. The results in Figure 42 show a decrease of

grain size at this temperature. On the other hand, there is an increase of relative frequency for grain size distribution of the smallest group (<500μm^2) at a highest aging temperature of 700°C. Therefore, grain coarsening does not occur under during prolonged aging at temperature of 700°C.

4.5 Hardness Evolution of Esshete 1250 creep samples

Hardness test is performed according to British Standard (BS 3S 500:1996) on statically aged samples.

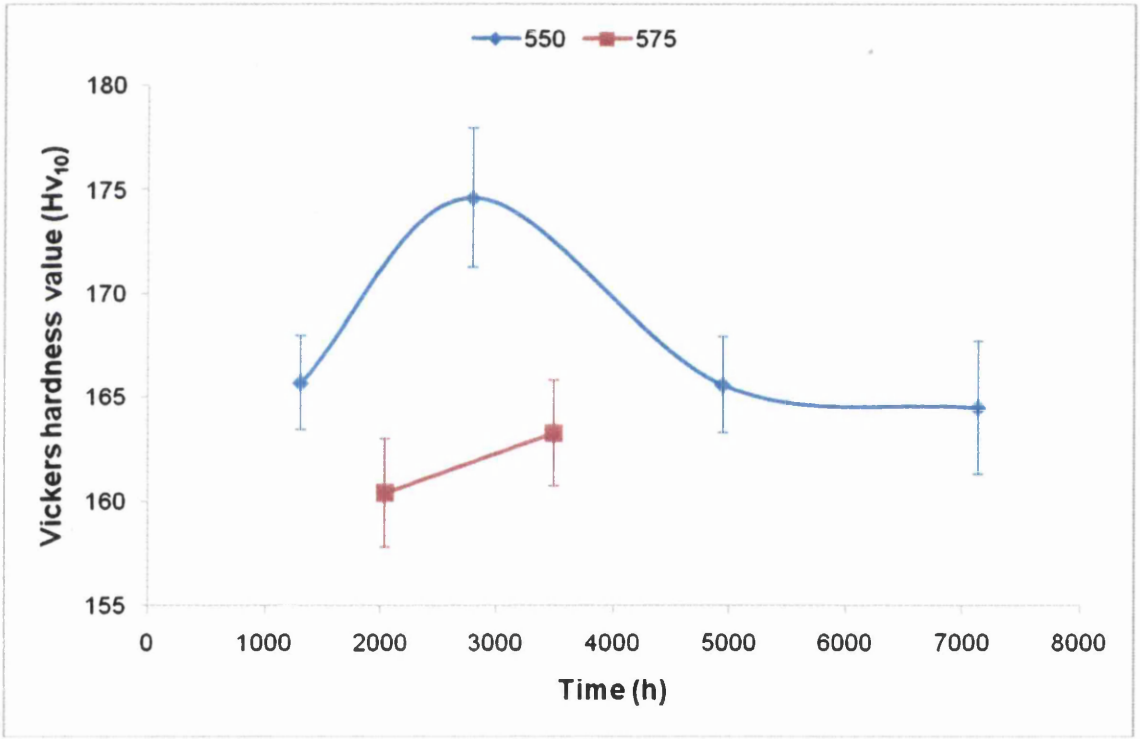

Figure 51: Vickers hardness evolution for the E1250 statically aged specimens at a temperature of 550°C.

It was found that an increase of hardness occurs during short term ageing in the E1250 specimens aged at 550°C and 575°C. However, hardness value decreased after prolonged ageing at temeprature of 550°C. (Figure 51) Mean particle size shows a decrease as time is increased. The grain size also shows decreasing trend when time is increased.

Figure 52 shows the hardness evolution of E1250-BH statically aged samples. Vickers hardness value shows a decrease as time is increased. It was observed that hardness value are higher at lower temperatures. Hardness decreased as temperature is increased. The mean particle size of MX is decreased and volume fraction of this precipitate is decreased as time is increased. Precipitate seems to have stregthening effect during long term aging.

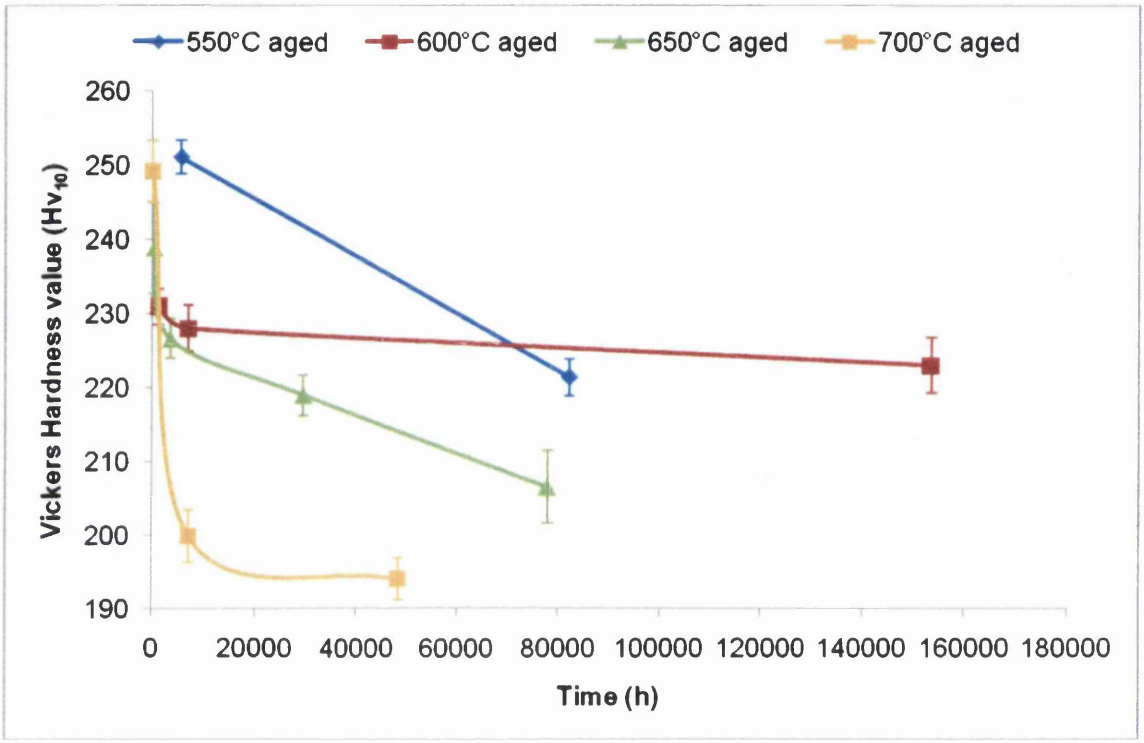

Figure 52: Vickers hardness evolution for the BH-E1250 statically aged specimens.

CHAPTER 5

5.0 EVOLUTION OF MICROSTRUCTURE DUE TO CREEP

Gauge portions of creep tested samples were used for the microstructural characterisation. The microstructures were characterised using SEM, particularly to identify the MX precipitate by EDX. The SEM samples were etched using 10w.o% dilute oxalic acid at 2V, 30-60s to reveal grain boundaries and precipitates.

5.1 Precipitation behaviour during long term service exposure

The precipitates formed during service exposure in E1250 austenitic stainless steel are of great interest. According to the MTDATA prediction (Figures 29 and 31), major phases predicted to occur over the creep exposure temperature range (550°C to 700°C) are austenite, σ-phase and MX phase. MTDATA prediction of MX phase is rich in Nb. This in agreement with the result of SEM and EDX analysis carried out on the MX secondary phase of the steel. Figure 53 show the SEM together with the EDX spectra of phases detected on one of the creep exposed sample at the creep test temperature of 550°C with rupture life of 2792h. More EDX analysis results are included in the Appendix. This work confirms the main chemical element present in the majority of the precipitates (coarse and fine) is rich in Nb. However, it is only an indication of the main

element present and not the quantity or amount of a specific chemical element present in the analysed area.

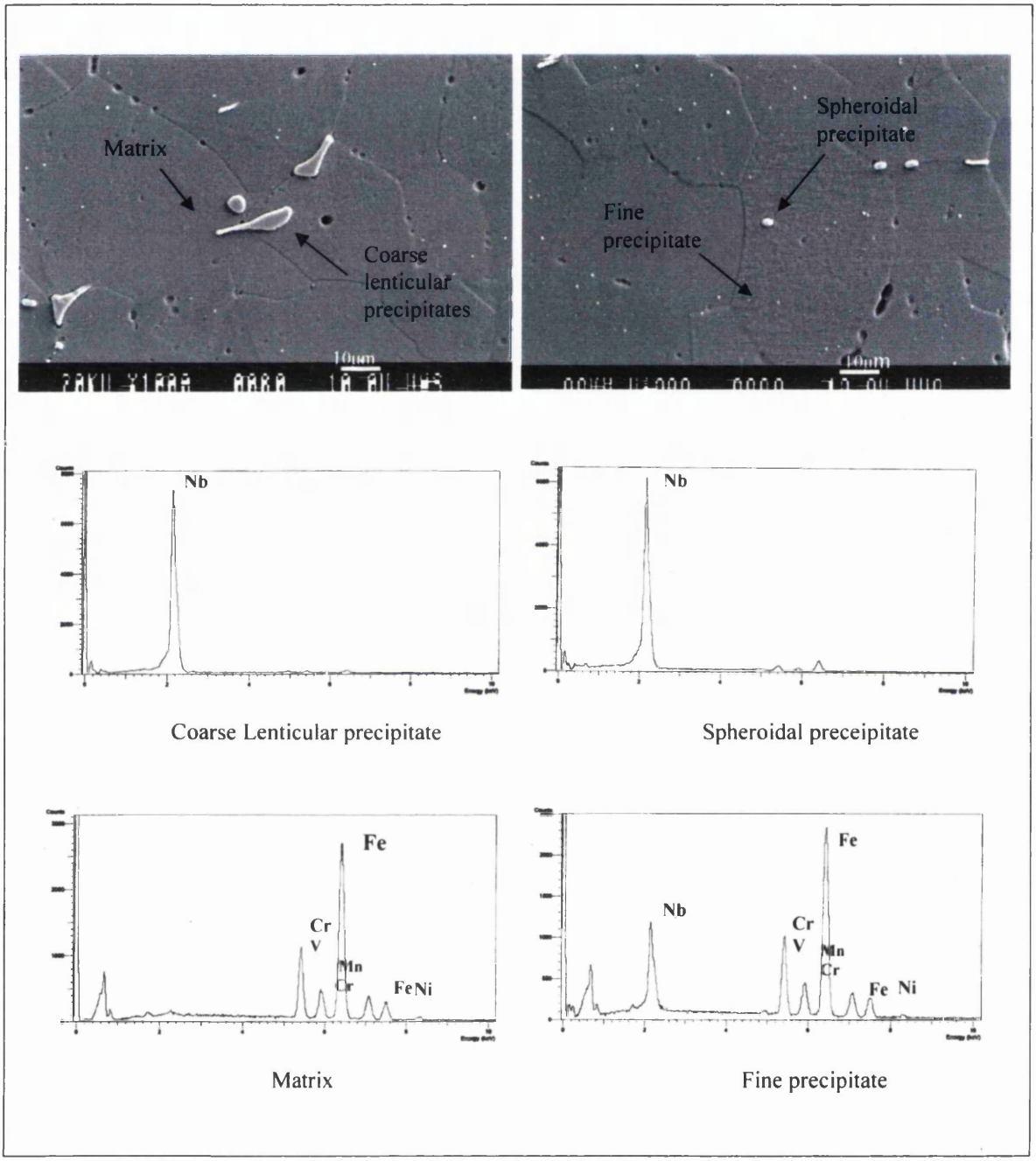

Figure 53: Secondary electron micrographs and associated EDX spot microanalysis traces in Esshete 1250 creep tested for 2792h at 550°C.

Result from the EDX spectra on the finely distributed precipitate (<1μm) does include other elements such as Fe, Ni, Mn and etc, yet Nb was also detected as well. The indication of other elements except Nb was due to the dilution effects from the

surrounding austenite matrix and might not be indicative of the exact fine precipitate composition.

The MX particle size were measured on samples exposed to creep (gauge area). The measuring method is described in detail in Chapter 3 section 3.3.4. Evolution of MX particle was plotted in graph and the distribution of the particle size was presented in bar chart. The mean MX particle sizes were increase in the E1250 parent specimen under creep exposure at a temperature of 550°C (Figure 54). However, the mean particle size decreases at a higher temperature of 575°C. These results are presented in Figure 56. At lower temperatures, creep rupture strength is enhanced by a finer particle size. However, this is not the case at a higher temperature. Other factors might affect the creep rupture strength in addition to the contribution of fine second phase particles. The distributions of precipitate size during creep at temperatures of 550°C and 575°C is presented in Figures 55 and 57 respectively. At a lower temperature of 550°C, the precipitates appear to increase in size as time increases. The mean precipitate size decreases at a higher temperature of creep exposure.

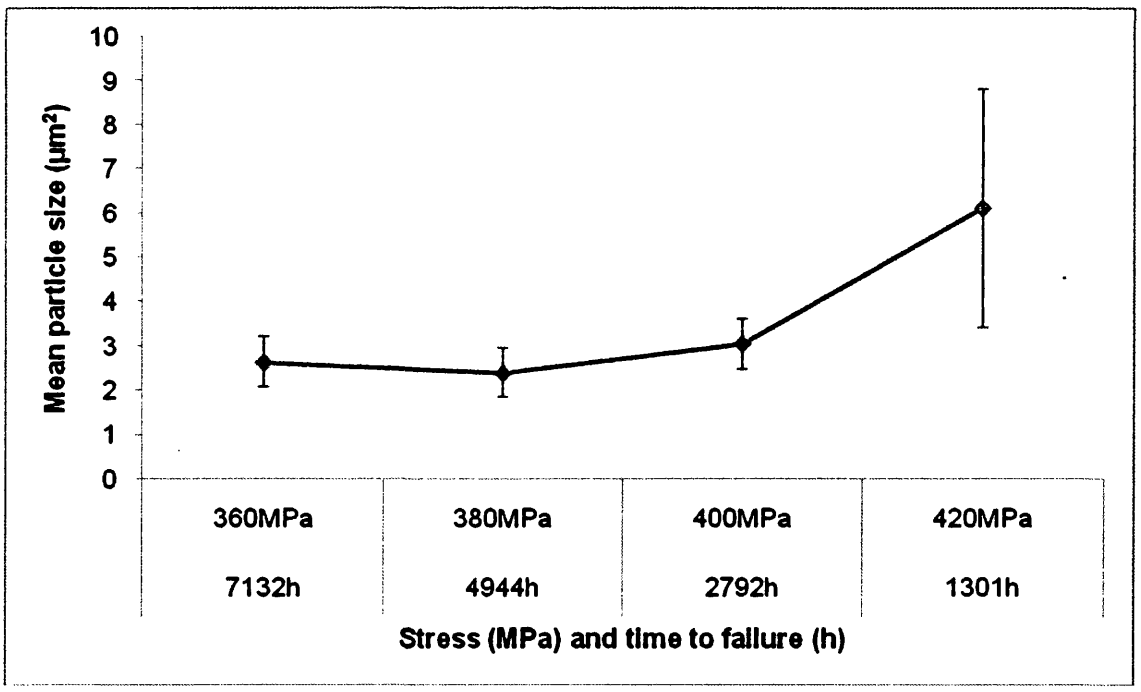

Figure 54: Change of MX particle mean size of E1250 steel during creep exposed at 550°C.

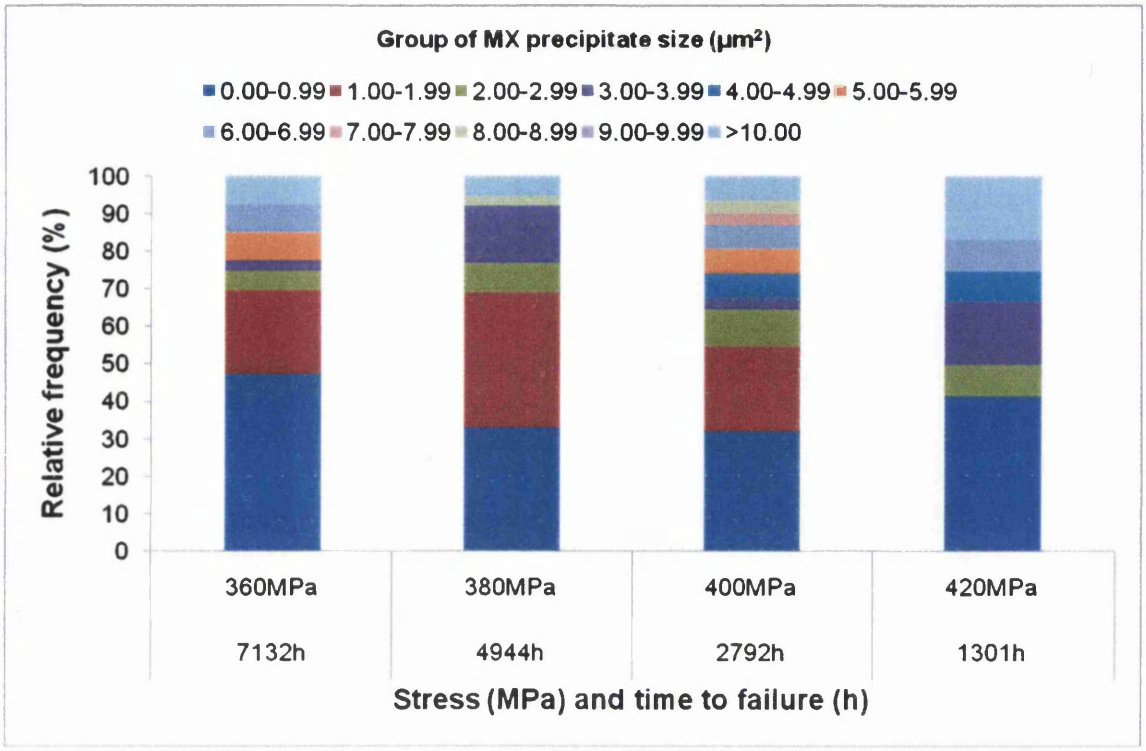

Figure 55: MX particle size distribution measurement in E1250 steel during creep exposed at temperature of 550°C.

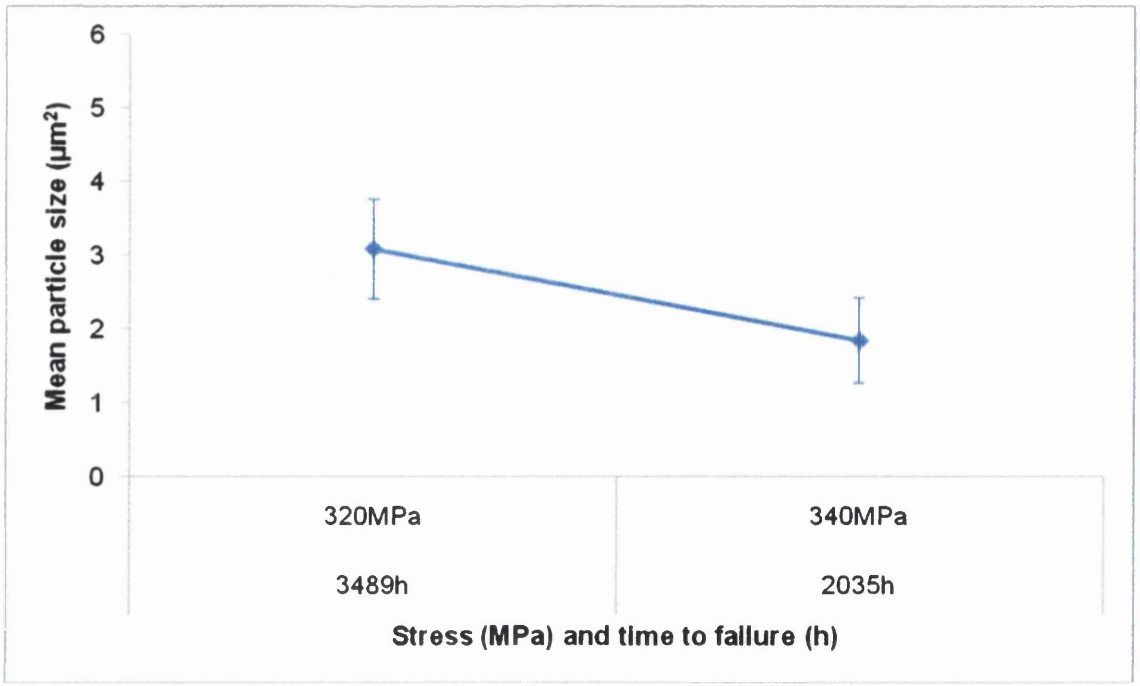

Figure 56: Change of MX particle mean size of E1250 steel during creep exposed at 575°C.

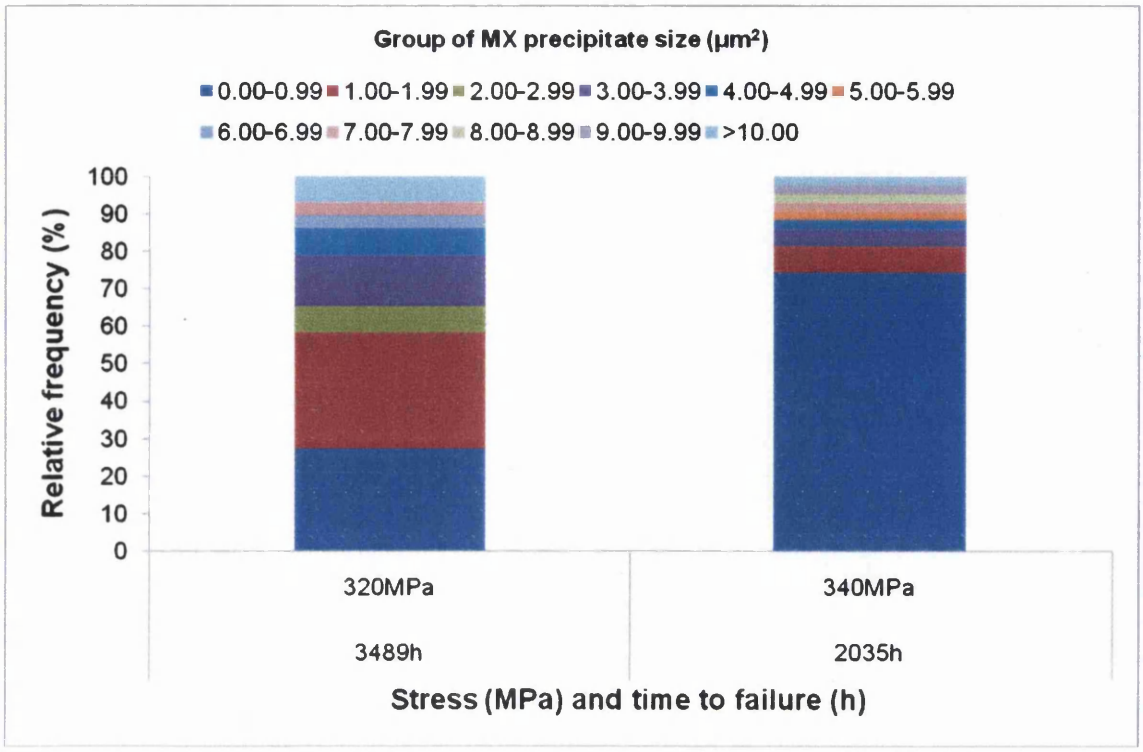

Figure 57: MX particle size distribution measurement in E1250 steel during creep exposed at temperature of 575°C.

The distribution chart for mean size of the MX precipitates for E1250-BH samples have been presented in Figure 59. Mean MX particle size was increase during creep exposure at temperature of 550°C. This is correlated with the decrease in relative frequency for the finest particle size group. The relative frequency for the fine particle size group is considered constant during creep exposure at temperature of 600°C. During creep exposure at a higher temperature of 650°C, an increasing value for the relative frequency of the fine particle size group indicates that no coarsening is observed. Prolonged creep exposure at a higher temperature of 700°C shows an increase of the relative frequency value for the fine particle size group. However, the overall relative frequency of the fine particle size group at a temperature of 700°C is lower than the value shown for temperatures below 650°C. This indicates coarse MX particle had lead to a decrease in rupture life of the specimen. Figure 60 shows volume fraction of MX particles during creep exposure at temperature of 550°C, 600°C, 650°C and 700°C. It was found that volume fraction of MX particles does not increase at temperature below 600°C. However, an increase in volume fraction was found at samples exposed to creep temperature above 650°C.

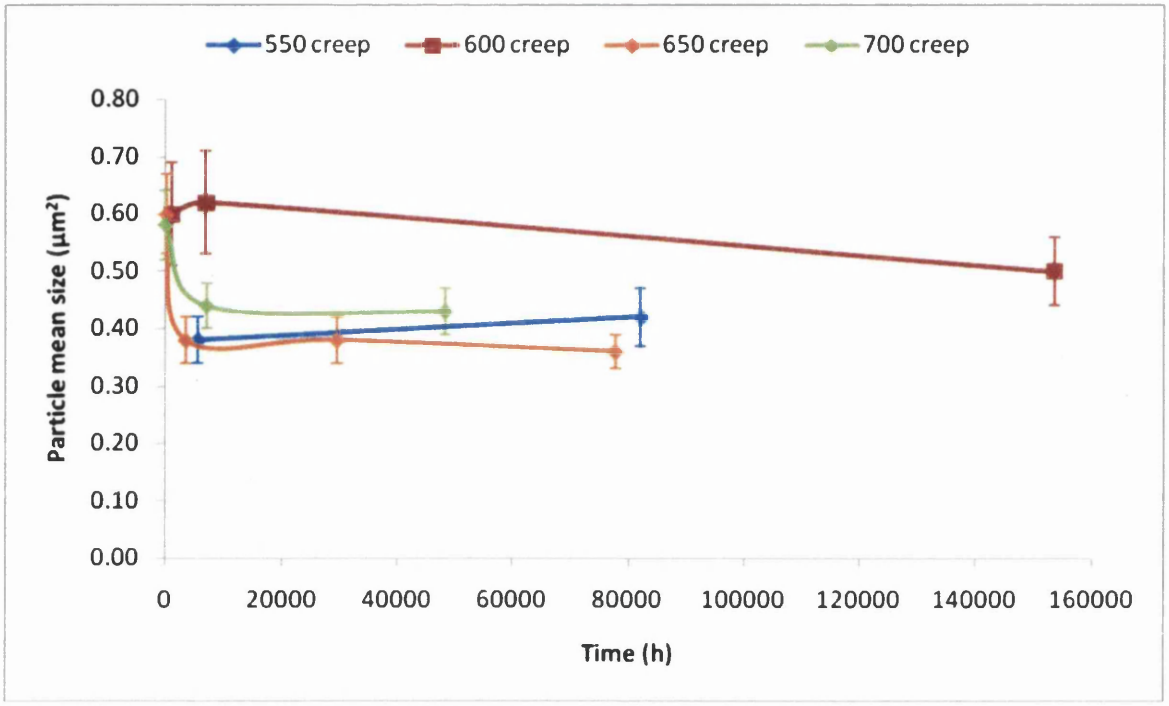

Figure 58: Change of MX particle mean size of E1250-BH steel during creep exposure at temperatures of 550°C, 600°C, 650°C and 700°C.

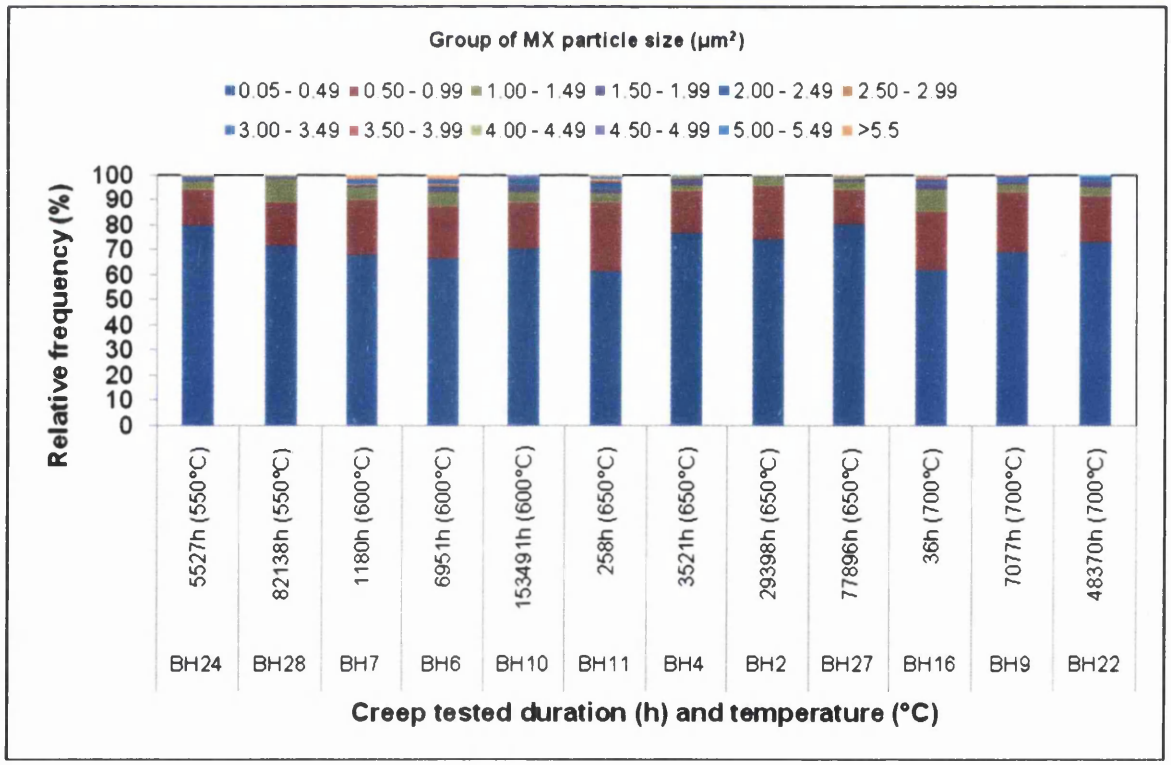

Figure 59: MX particle size distribution in E1250-BH creep deformed specimens.

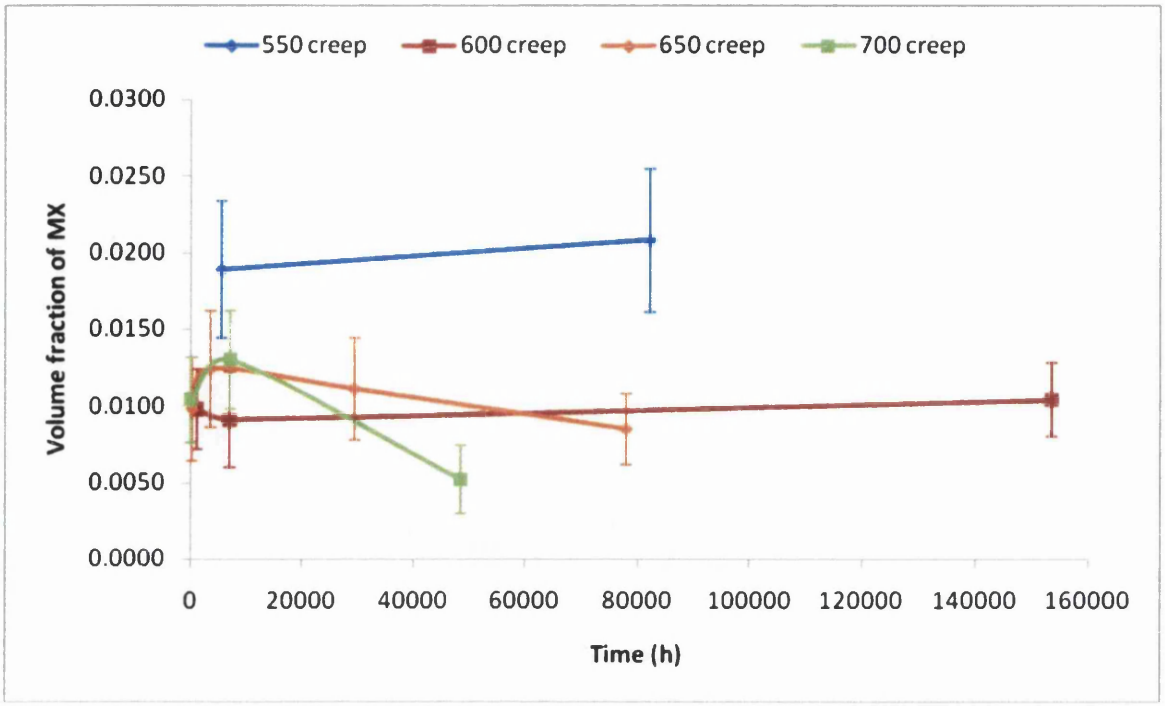

Figure 60: Volume fractions of MX precipitates for the E1250-BH aged samples creep tested at temperatures of 550°C, 600°C, 650°C and 700°C

5.2 Grain size evolution under service exposure

The SEM samples were electrolytically etched using 10w.o% dilute oxalic acid at 2V, 30-60s to reveal the grain boundaries and precipitates. The method use for grain size measurement was described in Chapter 3 section 3.3.4.

The creep exposed (gauge length area) specimens exhibit austenite grain structure with finely dispersed precipitates all over the matrix. In addition, large particles of MX phase were observed randomly precipitated throughout the matrix of each sample. The creep exposed steels exhibit a number of precipitates of varying size and distribution. According to MTDATA modelling together with EDX analysis, these are believed to be predominantly niobium carbides that are known to form when stabilised austenitic steels are subjected to high temperature (>400°C).

The mean grain area of the creep specimens of E1250 at temperatures of 550°C and 575°C was measured and the results obtained are presented in Figures 61 and 62, respectively. This indicates that the increase in temperature on creep exposed samples does not affect grain growth. Finer grain size is however enhancing creep rupture life at higher temperatures. The decrease of grain size might be due to fine precipitate formation during creep exposure and the effect of creep strengthening might also be due to this type of precipitates present.

At a constant temperature of 550°C or 575°C, it is found that the mean grain area is increased as stress level increases. The increase of grain size has resulted in a reduction of the rupture time. It is hypothesized that higher grain size will result in an increase in creep rupture strength. This is not the case for E1250 steel. It can be found that the majority of the creep exposed specimens at temperature of 550°C contain grains distributed in the group size of less than 600μm^2, as shown in Figure 63. At a higher temperature of 575°C, the majority of grain area is distributed in the group size of less than 600μm^2 as well (Figure 64).

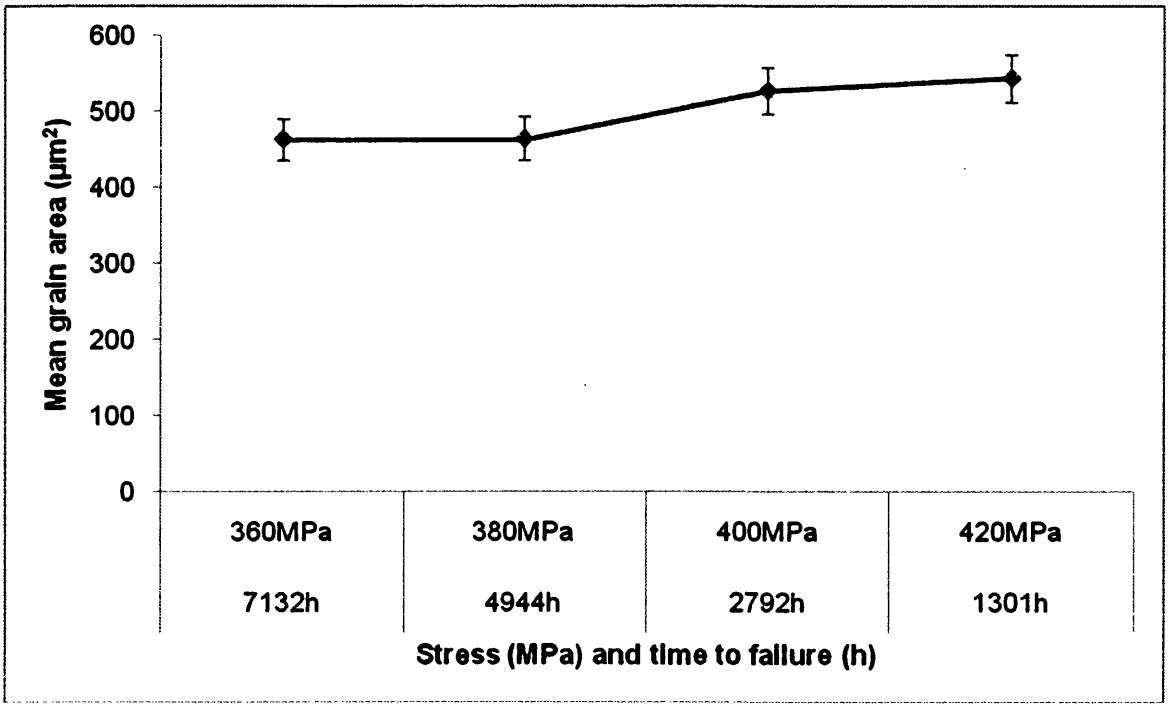

Figure 61: Grain size evolution in creep exposed E1250 steel at a temperature of 550°C.

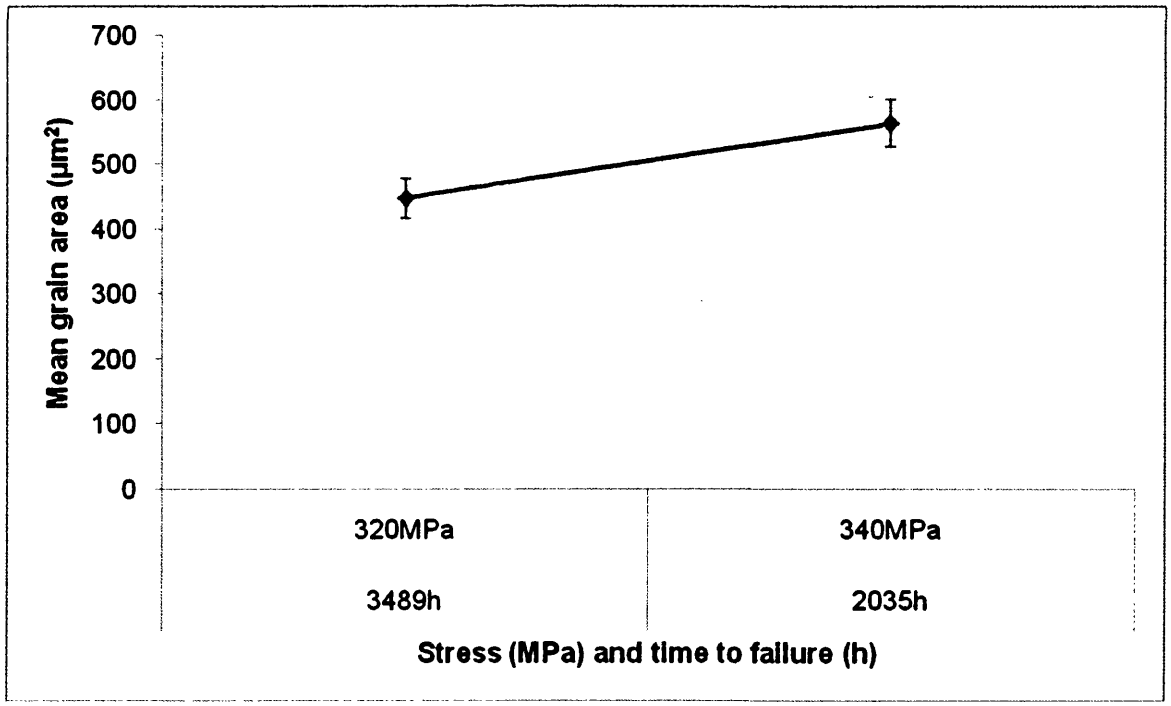

Figure 62: Grain size evolution in creep exposed E1250 steel at a temperature of 575°C.

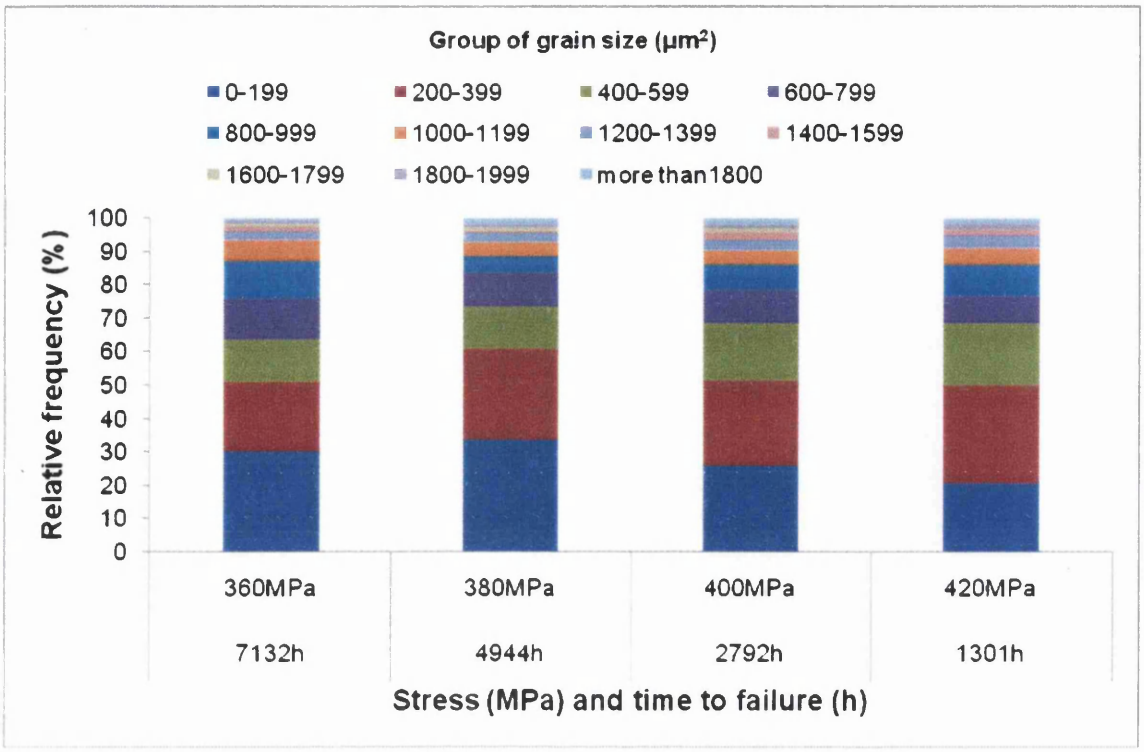

Figure 63: Grain area distribution measurements of creep exposed E1250 steel at a temperature of 550°C.

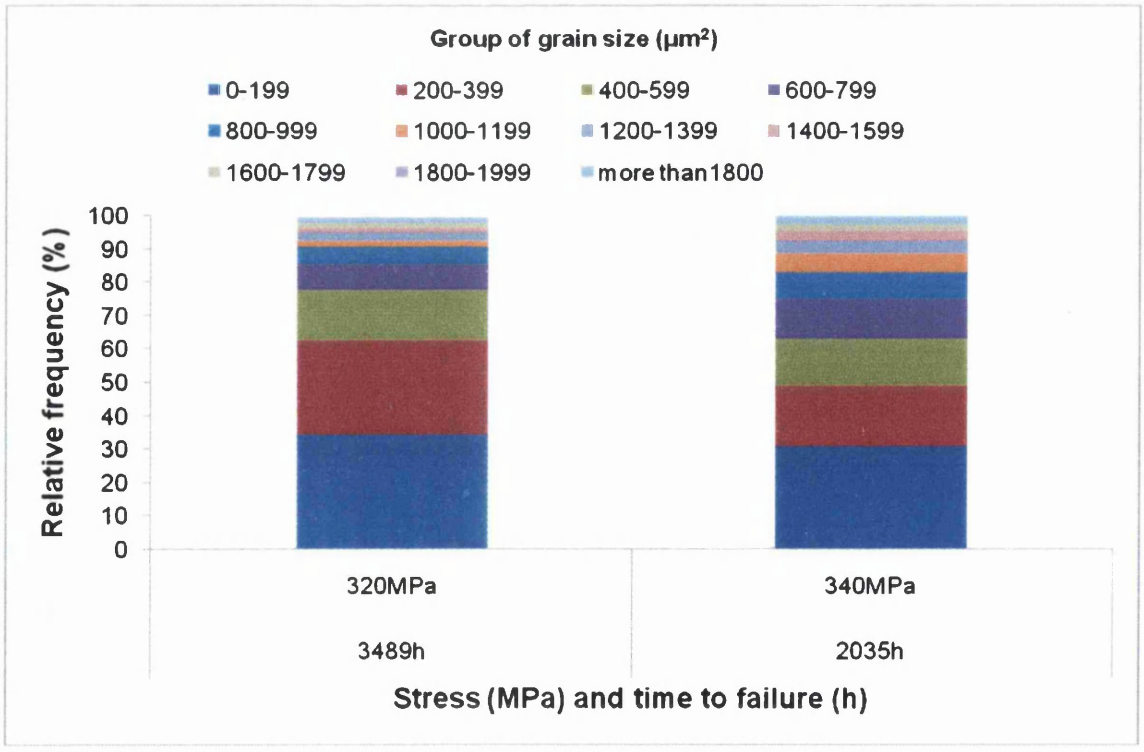

Figure 64: Grain area distribution measurements of creep exposed E1250 steel at a temperature of 550°C.

The grain size of E1250-BH samples shows a decrease during creep exposure at a temperature of 550°C. However, at a higher temperature of creep exposure of 600°C, an increase of mean grain size is observed. (Figure 65) This is followed during creep exposure at the higher temperatures of 650°C and 700°C. (Figure 66) No coarsening of grain size is found during long term high temperature creep exposure, at the temperatures studies.

The grain size distribution of creep deformed specimens is presented in Figure 67. Majority of grain size (~50%) are distributed in the group size of less than 500μm^2 at the creep temperatures of 550°C, 650°C and 700°C. Thus no tendency of grain coarsening even after prolonged exposure time is observed. However, at a temperature of 600 °C, the majority of mean grain size is found to be distributed in the group size less than 1000μm^2. Therefore, grains seem to coarsen only at temperatures of 600°C. Nevertheless, this does cause a reduction in creep rupture life.

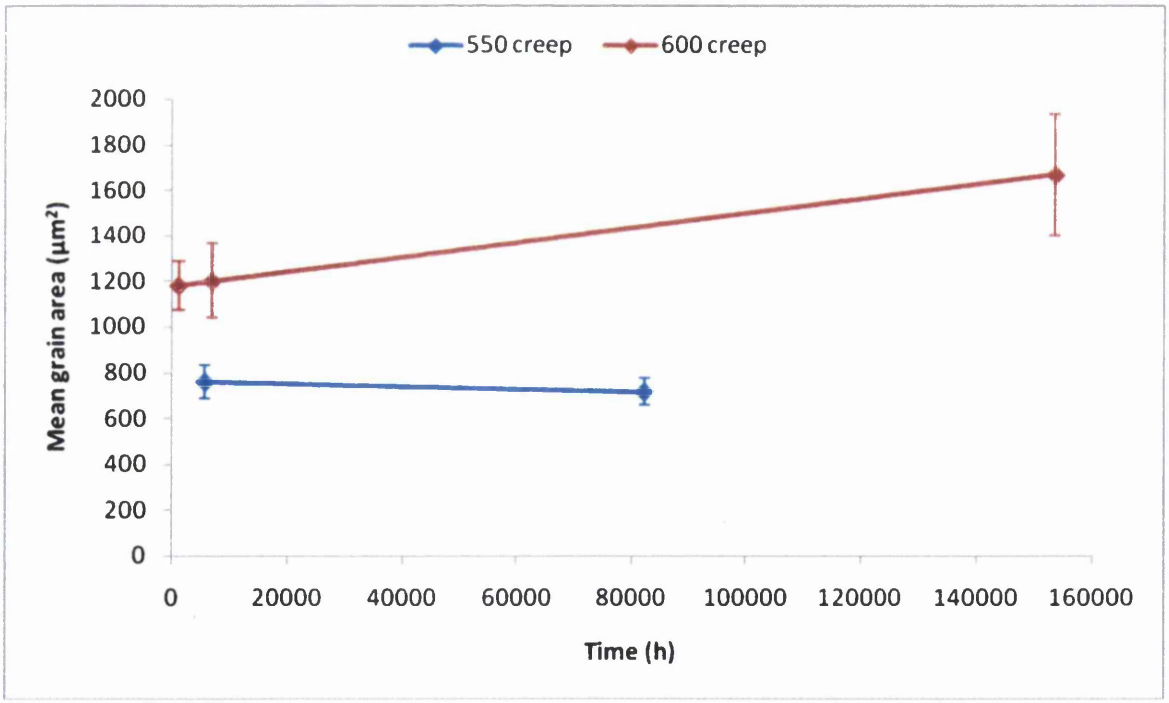

Figure 65: Grain size evolution versus creep time for BH-E1250 steel exposed to creep at temperatures of 550°C and 600°C.

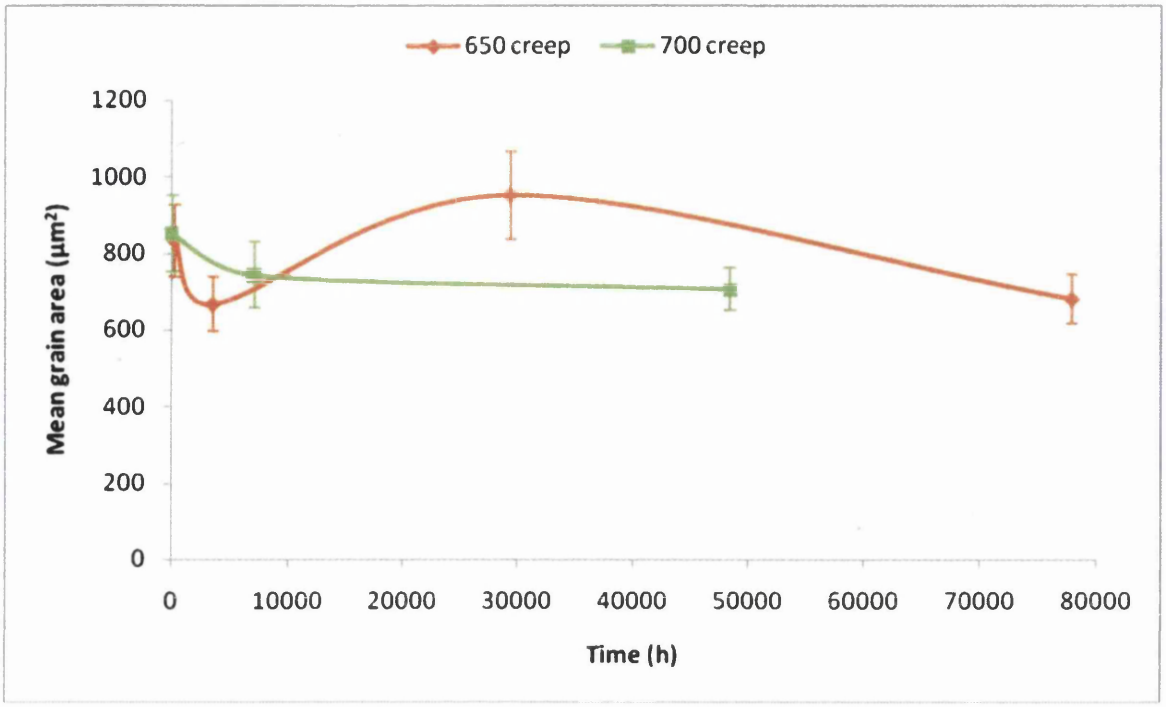

Figure 66: Grain size evolution versus creep time for E1250-BH steel exposed to creep at temperatures of 650°C and 700°C.

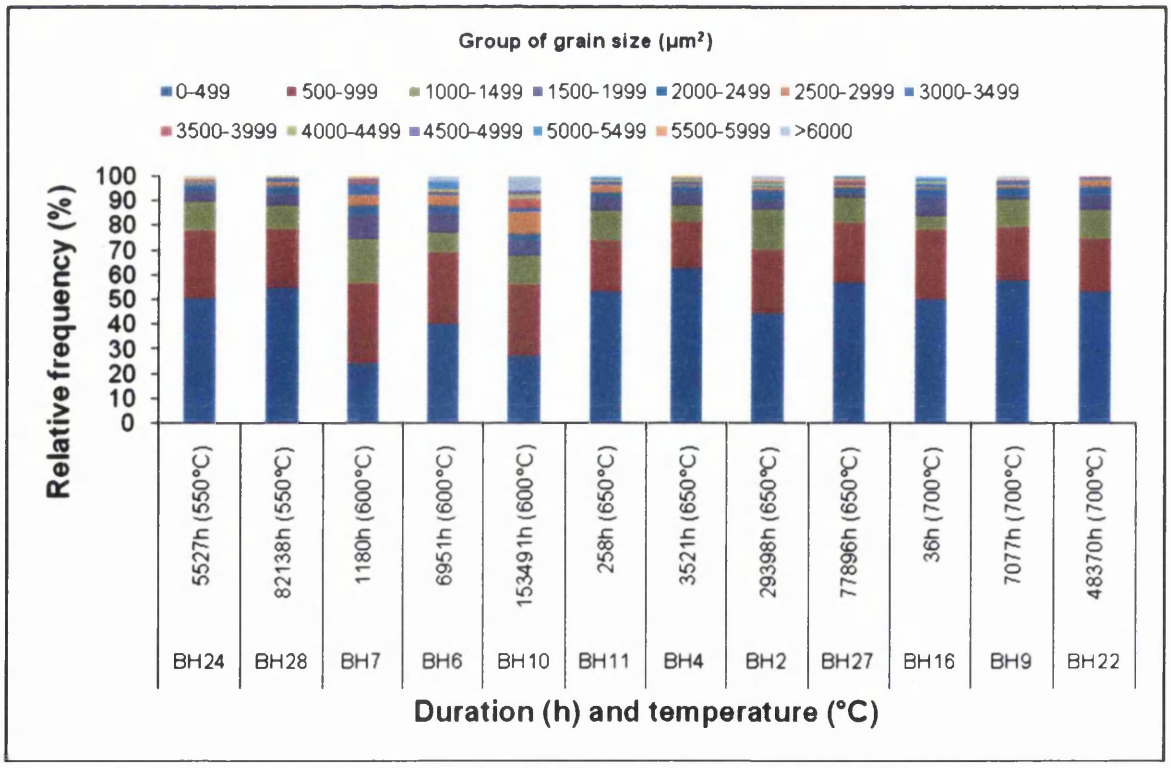

Figure 67: Grain area distributions of E1250-BH creep deformed specimens at temperatures of 550°C, 600°C, 650°C and 700°.

5.3 Hardness evolution of creep deformed material

Hardness test was performed according to the British Standard BS 3S 500:1996. [92] Figure 68 show hardness evolution of E1250 during creep exposure at temperature up to 575°C. It is found that Hv value decreased as mean grain size decreased for E1250 creep exposed samples. Hardness value also decrease as mean particle size decrease at a temeperature of 550°C. Little information could be obtained from result for creep exposed sample at a temperature of 575°C since only two specimens were provided for analysis and this is insufficient for obtaining result data. However, the obtained result on this limited samples were included for comparison.

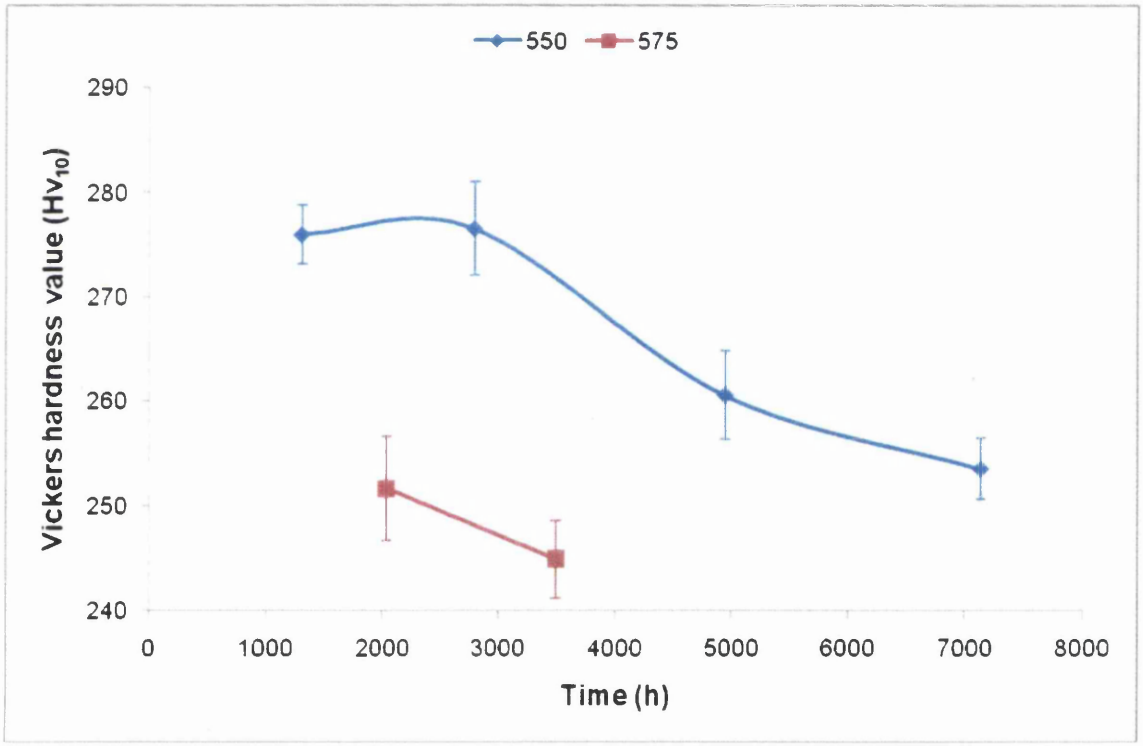

Figure 68: Vickers hardness evolution for the E1250 creep deformed specimens at temperatures of 550°C and 575°C.

The Hv value for E1250-BH creep samples were increase as time is increase. (Figure 69) However, mean grain size increase as Hv value increase at temperature below 600°C (Figure 65). Mean particle size show slightly decrease but volume fraction of MX particle was stable at the temerature of 600°C (Figures 58 and 60). Mean grain size show decreases at creep temperature above 650°C where Hv value was increased

(Figure 66). Mean particle size and volume fraction of MX particle decrease at the temperature above 650°C (Figures 58 and 60).

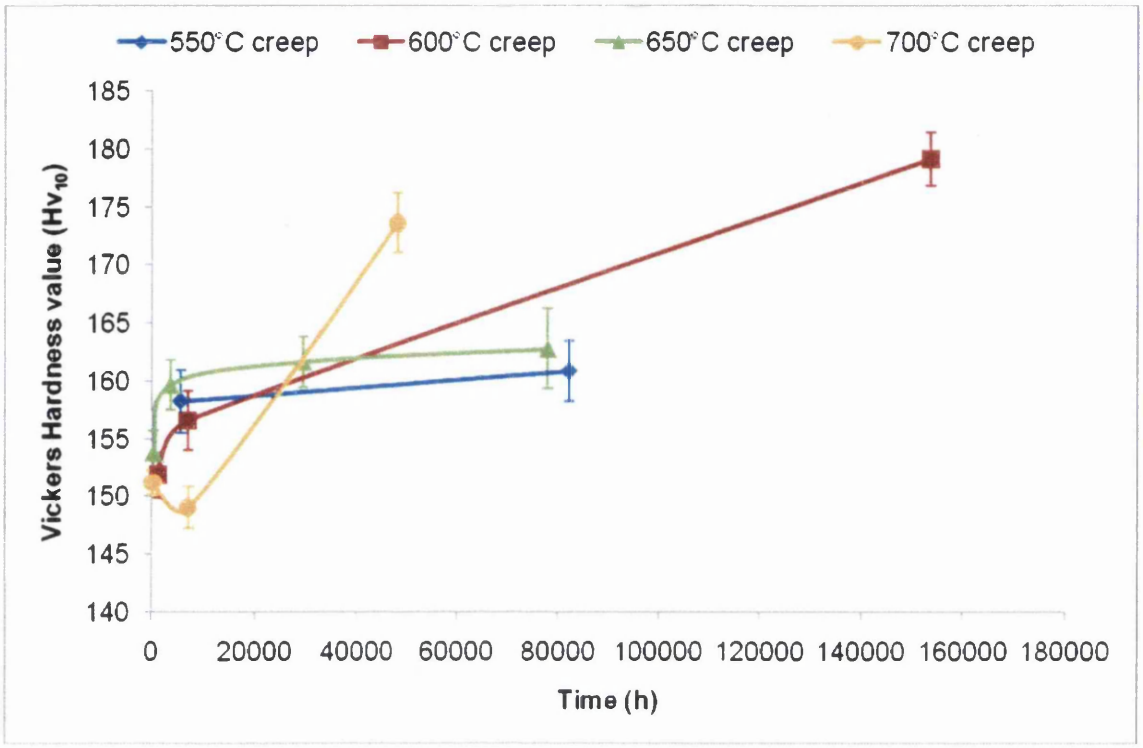

Figure 69: Vickers hardness evolution for the E1250-BH creep deformed specimens.

5.4 Creep deformation graph

The creep rupture lives obtained at various temperatures and stress levels are summarised in the form of a time-temperature Larson-Miller parameter (LMP) plot in Figures 70 and 71 according to Equation 12. The values used for the Larson-Miller constant was 20. Tables 11 and 12 give the creep data and LMP value calculated using the available data.

Table 11: Creep data for E1250 steel.

Test Ref.	Temperature (°C)	Stress (MPa)	Duration (h)	log t_f	LMP
MZM	550	360	7 132	3.85321	7065.505
MZL	550	380	4 944	3.69408	7022.038
MZK	550	400	2 792	3.44592	6954.252
MZJ	550	420	1 301	3.11428	6863.665
MZO	575	320	3 490	3.54283	7005.723
MZP	575	340	2 035	3.30856	6941.734

Table 12: Creep data for E1250-BH steel.

Test Ref.	Temperature (°C)	Stress (MPa)	Duration (h)	log t_f	LMP
BH24	550	402	5527	3.74	19543.63
BH28	550	263	82138	4.91	20508.41
BH7	600	309	1180	3.07	20145.21
BH6	600	263	6951	3.84	20817.68
BH10	600	232	153491	5.19	21991.23
BH11	650	263	258	2.41	20689.29
BH4	650	232	3521	3.55	21737.1
BH2	650	185	29398	4.47	22587.93
BH27	650	116	77896	4.89	22978.6
BH16	700	247	36	1.56	20977.52
BH9	700	108	7077	3.85	23209.48
BH22	700	70	48370	4.68	24021.8

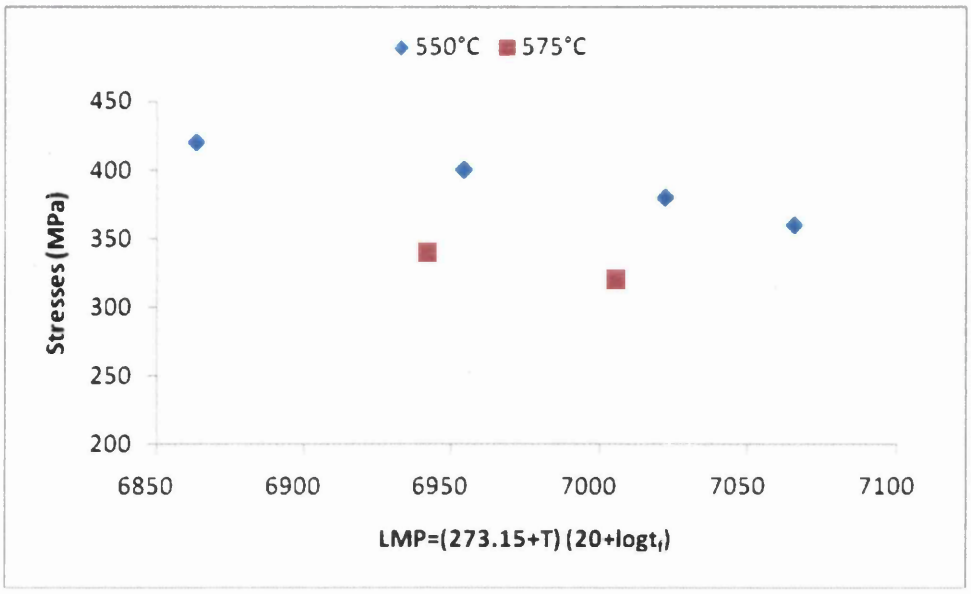

Figure 70: Rupture stress as a function of Larson-Miller Parameter (LMP) for E1250 steel.

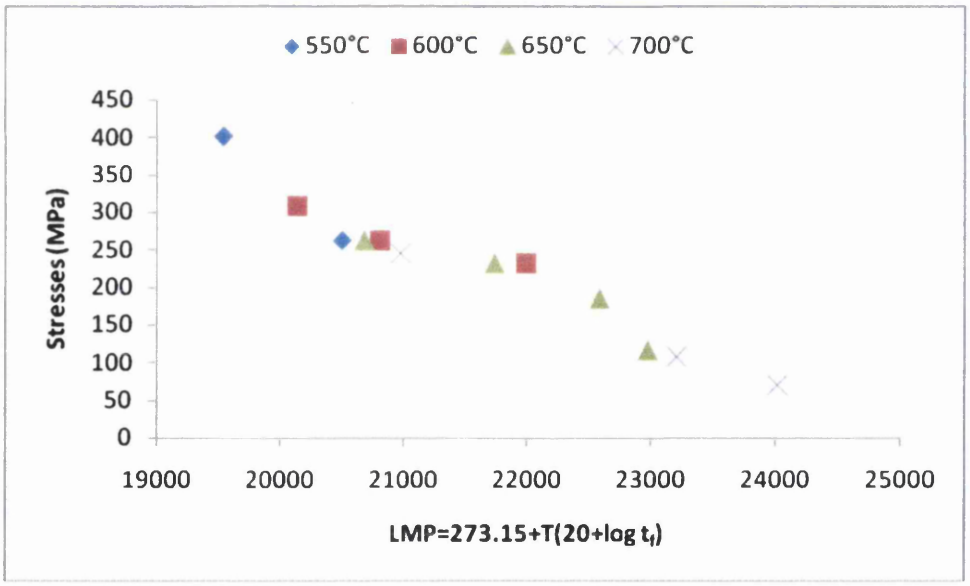

Figure 71: Rupture stress as a function of Larson-Miller Parameter (LMP) for E1250-BH steel.

The LMP decreased linearly with decrease in stress. LMP is a function of both temperature and time hence, combination of these two parameters controls the evolution of the microstructure. The microstructure of creep exposed specimens with combination of various temperatures and stresses was investigated.

CHAPTER 6

6.0 DISCUSSION

6.1 Quantifying the microstructure

Grain size in the steels is non uniform due to it exposed to high temperature for long period. Due to the fine grain structure and small precipitates are not visible in optical microscope, SEM was employed to study the microstructure of the steel. When the sample is etched with oxalic acid, the grain boundaries are attacked and thereby a sharp boundary is created at the grain boundaries interface.

All grain size measurement is performed on micrographs with 250x magnification. There is at least 80 grains are calculated from each sample for grain area analysis. Attempt had been made on using lower magnification of 200x so that to include at least 100 grains for measurement. However, due to some very fine grain was invisible under magnification of 200x, higher magnification (250x) was used for grain area analysis in this study. Figure 72 shows a typical SEM micrograph for grain area measurement work.

Micrographs were at high magnification of 500x are used for particle size measurement due to the finely distributed second phase precipitate (~1μm) of MX are observed under this magnification. The amount of detected particle in each micrograph for measurement was more than 100 particles under the 500x magnification. This is to ensure that enough amount of particle is available for the sizing analysis.

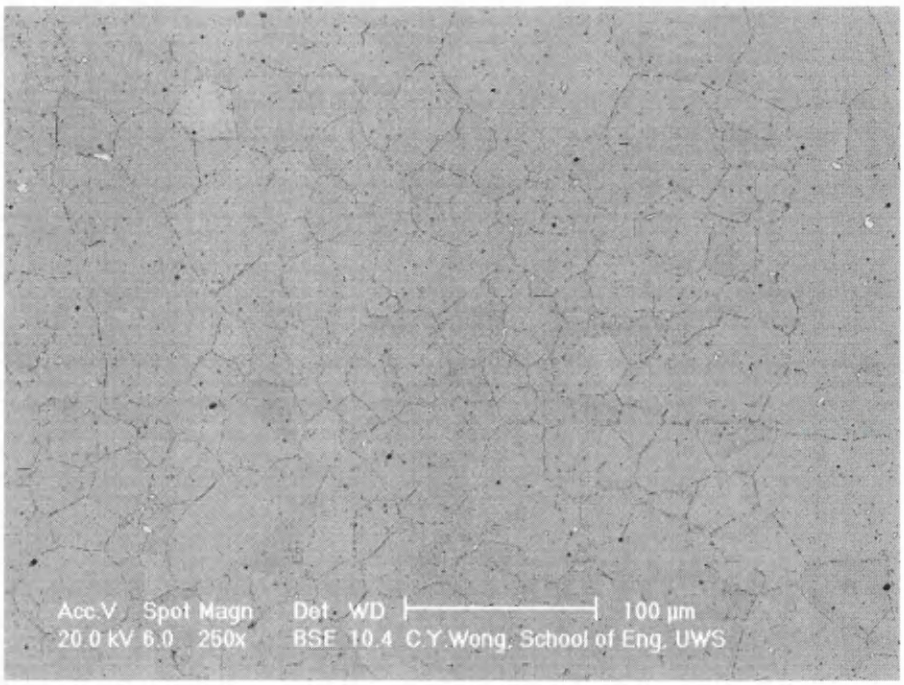

Figure 72: SEM micrographs etched with 10w.o.% dilute oxalic acid at 2V for 60s used for grain area measurement. (E1250-BH statically aged at 550°C for 82138h)

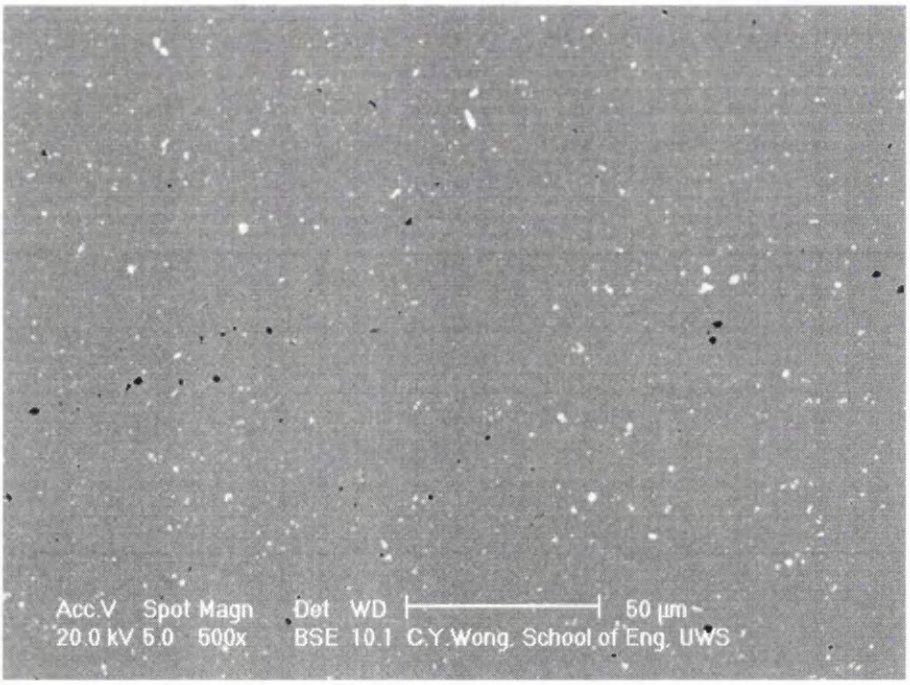

Figure 73: SEM micrograph used for precipitate size measurement. (E1250-BH creep exposed at 650°C at a stress of 116MPa, 77896h)

MX precipitate could be examined because of its particular appearance in SEM when using backscattered electrons images. MX phase contain Nb which provide a

greater atomic number than the matrix and appears brighter in SEM image. Thus, the resulting contrast on the image facilitates the identification of MX phase by using EDX and also measurement of the precipitate size using computer software (Optilab). According to MTDATA modelling, these are believed to be predominantly niobium carbides that are known to form when stabilised austenitic steels are subjected to high temperature (>400°C).

MX is a quite frequently report carbide in ferritic and austenitic stainless steels. The problem of quantifying the composition of the secondary phase of MX carbide was the sensitivity to the analysis of C and N. However, with the aid of MTDATA modelling prediction and support of the existing literature, it is reasonable to assume that the precipitate species might be indeed NbC particles.

6.2 Microstructural evolution during high temperature exposure

It is well known that in pure metals or single phase solid solution alloys, grain size markedly increases the strength thus creep resistance. This does not apply to alloyed steels containing more than one phase or multiphase. The variation of grain size however, had very small effect on creep compared to other factors in alloyed steels. In alloyed steels, especially austenitic alloys in this study, the evidence required to investigate the effect of grain size is more difficult to obtain because some precipitation often occurs during creep testing.

Degradation of the mechanical properties occurs in austenitic steels due to two principal factors: precipitation reactions that occur during prolonged exposure at elevated temperatures and environmental effects, such as corrosion or nuclear irradiation. MX, $M_{23}X_6$ and σ-phase are typical precipitates that can be found in austenitic stainless steels. These occurrences are well documented and have been reported on numerous occasions [42, 46, 65]. Carbon exists in the steel in the form of MC carbides, which offer the best creep strength. It is found that creep strength in the steel is enhanced when small, evenly distributed MC carbides are present. Unfortunately, the carbides tend to grow in size and decline in number during service at high temperatures. For a material that is prone to carbide growth creep strength could decrease rapidly with prolonged exposure.

As we can see from the grain size evolution shows decreasing trend with increase of time and temperature, while MX particle are found to have finer sizes with increased temperature and time. The increase in volume fraction of MX precipitates has been found to lead to increased rupture life at temperatures lower than 600°C. However, a decrease in volume fraction when the temperature rises to 600°C lowers the creep strength during short term aging. While a stable amount of MX over the temperature region of 600°C-650°C does maintain a stable creep strength after prolonged exposure (*Figure 60)*. At a higher temperature of 700°C, the volume fraction

of MX precipitates does not decreases after short term exposure time though it is noticeably reduced after long term exposure.

The result of the grain size measurements shows that grain size does not coarsen after prolonged ageing at high temperatures and the subsequent precipitate especially fine MX will be assumed to affect grain size evolution. One reason that could cause decrease of grain size at high temperatures (>650°C) is the retarding effect on recovery by second phase precipitates. As the dislocations pile up at grain boundaries, relaxation due to higher stress and climb takes places and spread towards grain boundaries. Dislocations density also increases with the stress applied and tend to reduce their strain energy by mutual annihilation and rearrange to form low angle boundaries and thus permitting give grain growth. However, grain size is smaller owing to the precipitates inhibiting dislocation movement and their pinning effect at grain boundaries. This is how the creep resistant steel is designed and strengthened by these precipitates. Therefore, we can conclude at this point that, grain size does not appear to have a dominant effect for the rupture life of E1250 steel but as a secondary effect by precipitate strengthening. It is observed that the values of hardness are higher in the creep exposed (gauge area) than in the statically aged samples. This might again be due to the strengthening effect caused by precipitates.

The microstructure of the E1250 samples following ageing shows annealing twins in the austenite microstructure. The primary sizes of MX precipitate are globular, nevertheless some irregular shapes are observed as coarse precipitates. It is well established that these large primary MX precipitates have formed during solidification. The MX precipitates are stable during prolonged creep testing within the temperature range of 550°C -700°C. The distribution of these particles is heterogeneous, and some clusters are observed as shown by the thin arrows indicated in the micrographs (*Appendix*). In the case of gauge samples, the precipitate morphology results are similar to those grip samples. T. Sourmail [42] has reported the formation of complex MX particles. It is clear that NbX exhibit globular morphology. MX precipitates have an FCC crystal structure.

It is important to note that the variation of the volume fraction and average size of particles in aged and creep samples might relate to the grain size evolution of the

material. There are no tendencies of coarsening of MX precipitate measured (>0.06μm^2) within the temperature range of 650°C-700°C. However, the grain size exhibits a slight decrease in these temperatures (650°C-700°C). Coarsening of MX has not been enhanced by a high diffusion path due to the fine grain size and the availability of grain boundaries. One reason might be that fine MX particles form essentially within the grains but less readily at grain boundaries. If the size of precipitates becomes finer as the temperature at which precipitation occurs is higher, extensive hardening effect is therefore associated with a critical dispersion of the precipitate. Precipitate volume fraction increases after prolonged exposed time in the grip area of the sample. Precipitates are expected to coarsen at higher temperatures. One reason that causes evident precipitate coarsening is the Ostwald Ripening effect. Small and fine particles tend to dissolve and give rise to precipitate on larger particles causing them to grow. The coarsening of precipitates associated with decreasing volume fraction of precipitates in the grip region, of temperatures of 550°C is attributed to the Ostwald Ripening effect.

Precipitation other than NbC such as $M_{23}C_6$ carbide and σ-phase are common precipitates form in stainless steel. Willoughby [32] had found that $M_{23}C_6$ was formed at grain boundaries after short term ageing times but not after prolonged ageing in the 16Cr10Niiaustenitici stainlessi steel.iIti isi claimedi thati σ-phase also precipitated during long term aging at 700°C. [32] However, this phase has very slow C and N solubility, hence carbide precipitation should happen before it. Moreover, substitutional elements suchi asi Moi usuallyi presenti ini σ-phase is very slow in austenitei andi σ-phase is incoherent with austenite thus its nucleation is difficult and the formation time is very long. [68] The SEM image of E1250-BH exposed to temperature of 700°C for 48370h show a different in microstructure after prolonged exposure time (Figure 84l). Precipitate other than NbC seems to present in the matrix during long term aging. It is suggest that future work can be focus on precipitates other than NbC which can occur during prolonged exposure to high temperature. Esshete 1250 austenitic steel provide good creep resistant property at temperature up to 650°C. MX carbide found to be the reason of enhanced creep strength during the exposure to high temperature if it is remain finely distributed. If MX precipitate does not coarsen at a temperature higher

than 600°C, then other precipitates must play a role in reducing the creep strength at higher temperature of 700°C.

6.3 Structure related to creep deformation

Creep will be impeded by fine precipitate dispersions. This is due to the nature of interaction of fine particles and dislocations. A fine particle will hinder a dislocation and force it to climb and cross-slip. Generally, the dislocation network formed by strain hardening interconnects the particles and is thereby anchored by them. To do this effectively, the particles must be stable at the service temperature and remain finely dispersed. Diffusion occurred at elevated temperatures results in precipitates becoming coarser, thus limiting the impeding effect. However, due to the coarsening of precipitates at grain boundaries, loss of their function as grain growth pinning agents is anticipated. Hence, grain size will increase under service exposure at elevated temperatures. The relatively large grain size will slow down creep deformation hence enhance creep resistant properties. However, the precipitate size is hard to obtain by SEM together with EDX due to the submicron size of fine precipitates distributed in matrix. From the micrographs obtained on this research, it can be found that relatively coarse precipitates are formed and also some finely dispersed precipitates are distributed uniformly within the matrix. The later might contribute to the creep strength of the steel.

It is important that fine MX particles are obtained and do not coarsen during high temperature and long term exposure since this will enhance creep rupture life. It is found that increased MX particle size is associated with increased aging temperature. When stress is applied, MX particle size decreases. Fine MX particles are favoured for high temperature creep, since they act as obstacles for dislocation movement and hence enhance creep strength. This also causes a secondary effect of pinning grain boundaries thus retarding grain coarsening. The distribution graph (*Figures 55, 57 and 59*) of MX particle size in creep deformed specimens indicates that particle do not coarsen as time and temperature increase. At a creep temperature of 550°C, the relative frequency for the finest MX particles size is increased as time increases (*Figure 55*). However, when the temperature is increased to 575°C, MX particles coarsen after prolonged exposure,

as the relative amount of the finest size group is significantly reduced as time increases (*Figure 57*). This coarsening might be due to a high diffusivity path occurring when the grain size is fine (*Figure 62).* A higher diffusivities path is enhanced by more grain boundaries, hence causing coarsening of MX particle at high temperatures.

Niobium rich compounds identified in all specimens observed under an SEM using backscattered electron imaging. It can be confirmed that these MX precipitates (NbC) have indeed a variety of sizes and shapes. For creep resistant properties, fine precipitates may contribute to the creep strength under severe engineering applications. However, most alloys under service at elevated temperatures would experience coarsening of secondary precipitates. Creep deformed samples of Esshete 1250 consist of coarse NbC distributions within the austenite matrix. It is known that the formation of these carbides during heat treatment process involves considerable diffusion. Precipitates forming during ageing have a composition that is close to equilibrium. However, at lower service temperatures, the steel would not be in equilibrium, and thus the microstructure will be susceptible to changes during service. Since diffusion processes are slower at lower service temperatures, as a result, the microstructure would take longer time to change and the composition of alloy carbides to achieve equilibrium. These precipitates would control grain size via a grain pinning effect, if they are not permitted to coarsen. Any changes of carbide size during service conditions depend on the equilibrium composition at aging and service temperature, as well as the duration of exposure during service conditions. Dissolution of primary carbides may occur after long term aging. However, precipitation of higher volume of finer secondary MX might take place due to dissolution of large coarse MX particles. This is also due to the coarsening theory as described by Ostwald ripening. Precipitation of fine particles may have an effect on grain refining and also contribute to creep strength.

Microstructures of creep tested samples show similar precipitation of MX over the matrix. (*Figures 85a-85l*) SEM could not reveal any precipitates other than MX during creep exposure except for microstructure exposed to the temperature above 650°C. Precipitate other than MX found to be appears within the grains (*Figures 85i and 85l*). This intergranular precipitate only occurs after prolonged time of exposure.

Prediction of creep deformation behaviour has been carried out using the improved creep equation for modelling. An attempt has been made to plot the time-temperature creep deformation using Larson-Miller parameter (LMP) for creep samples of E1250 and E1250-BH (*Figures 70 and 71*). The LMP plot shows that stress seems to have a significant effect on creep strength of material.

Creep deformation occurs by the diffusion of atoms, which is faster at higher temperatures. Since diffusion occurs most rapidly at grain boundaries, creep deformation is concentrated here. This leads to separation of the grains along their boundaries, producing an intergranular fracture surface. Fracture surfaces of creep specimens were evaluated by scanning electron microscopy. Photos of fracture specimens illustrated in *Figure 74* showing sharp necking fracture at higher temperatures. At a lower temperature of 550°C, the fracture surface is more flat and no necking was observed.

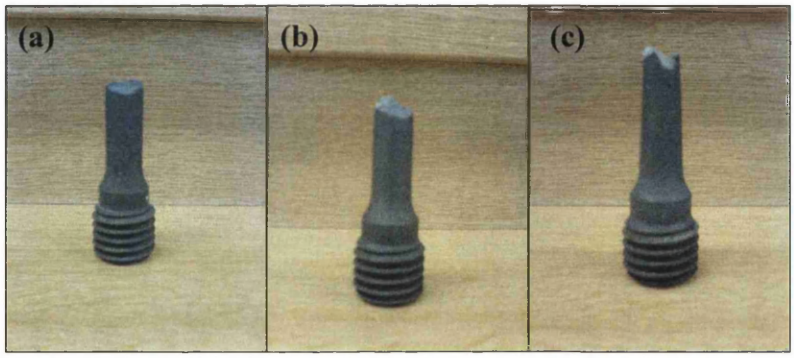

Figure 74: Fracture surface appearance at gauge portion at temperatures of (a) 550°C, (b) 600°C and (c) 650°C.

Creep failure modes as a function of temperature are shown in *Figure 75*. These three creep samples are tested at different temperatures of 550°C, 600°C and 650°C at a same stress of 263MPa. *Figure 75a* shows some reasonably smooth surfaces representing intergranular fracture. The fracture surface at higher temperature show mixed intergranular and transgranular fractures (*Figures 75b and 75c*).

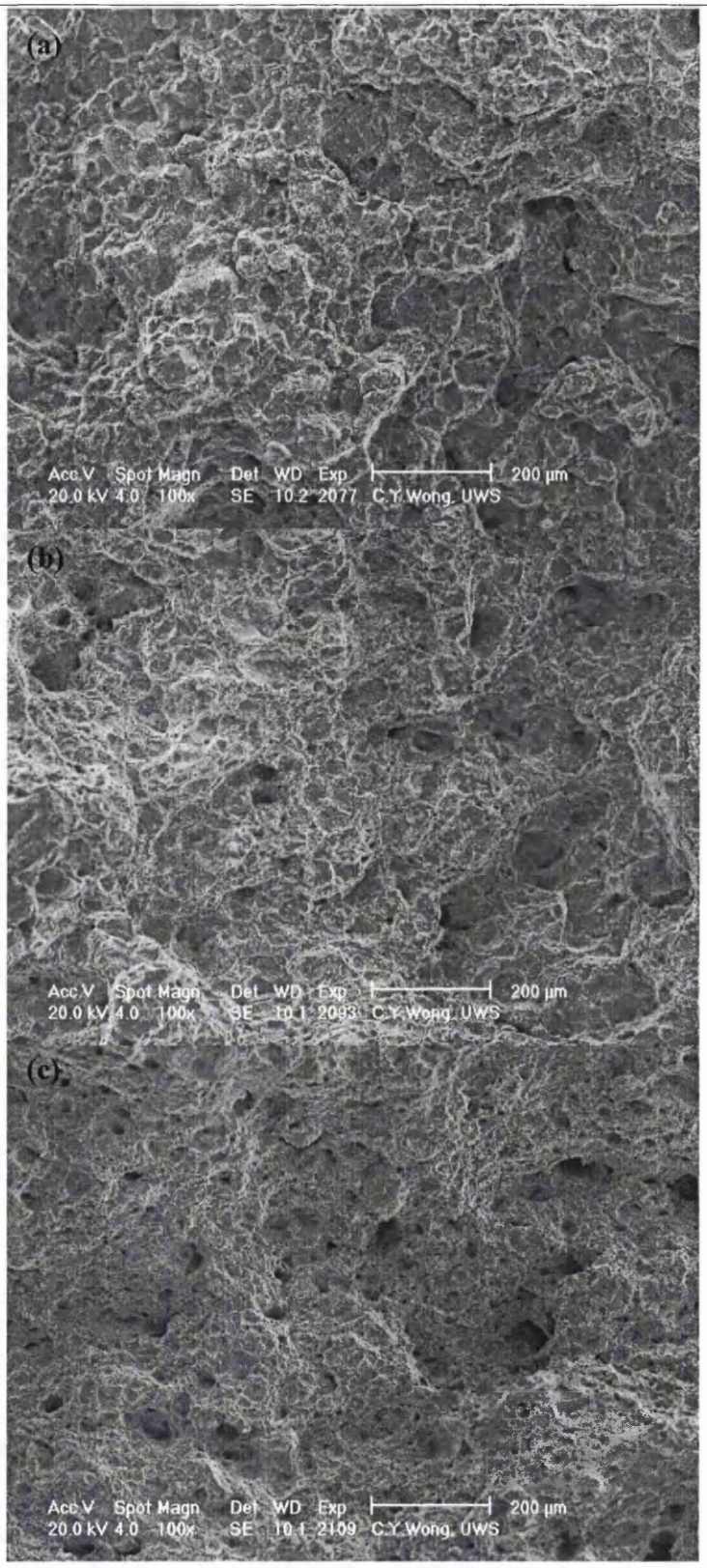

Figure 75: Rupture failure of the gauge specimen at (a) 550°C, (b) 600°C and (c) 650°C with a stress value of 263MPa.

CHAPTER 7

CONCLUSIONS

The microstructure of Esshete 1250 austenitic creep resistant steel has been characterised by scanning electron microscopy and image analysis. Attention was given to the grain size evolution, and in particular, also to the size and distribution of Nb-rich particles. As a result of this study, the following conclusions were reached:

1. Characterisation by SEM and EDX confirmed that niobium rich precipitates might be present in the form of MX compounds. As received Esshete 1250 appears to be free from significant $M_{23}X_6$ precipitation, due to Nb additions promoting the preferential formation of MX (Nb rich) precipitates. Free carbon is tied up with Nb to form stable MC, hence retarding the formation of $Cr_{23}C_6$ at grain boundaries.
2. The rupture life increases with decreasing grain size. This is correlated with the ductile fracture surface observed and grain size analysis at higher creep exposed temperatures conditions (>600°C). Grain coarsening therefore is not the main factor to sustain creep resistance at prolonged time and high temperatures conditions.
3. The stability of the precipitates found within the matrix must not be ignored. It has been observed that precipitates have not dissolved during the long-term creep exposure.
4. The effect of long term ageing does not cause any coarsening of MX precipitate.
5. The volume fraction increases over the ageing period at temperatures above 600°C. Creep strength will be affected by increasing the volume fraction of fine precipitates.

6. No tendency of grain coarsening was observed due to fine MX particle presence at prolonged creep exposure times that resulted in increased rupture life. Hence, fine MX particles might play an important role during creep deformation.

We know that creep resistant steels are more complex in their microstructure during service exposure. Precipitation of NbC is crucial for enhance the creep strength of Esshete 1250 austenitic steel. It is worth elucidating that whether these fine precipitates affect the strengthening mechanism in order to facilitate the microstructural prediction of Esshete 1250 steels during long term creep exposure. It is suggested that future work can be focused on the NbC precipitate in Esshete1250. The solubility of MX is of great interest because the proportion of each element that has to be added, in such a way as to maximise the amount the precipitation of a given product [M] [X]. Previous work had been carried out on the 18Cr10Ni austenitic steel [43, 45] and also on 20Cr25Ni alloys [24]. Since creep strength of Esshete 1250 is enhanced by finely distributed MX precipitate, it is worth to determine the correct quantities of M and X to use in order to have the best mechanical properties.

References

1. Masuyama, F., *Review - History of Power Plants and Progress in Heat Resistant Steels.* ISIJ International, 2001. **Vol. 41**(No. 6): p. 612-625.
2. R.Viswanathan, W.T.B. *Materials for Boilers in Ultra Supercritical Power Plants.* in *Proceedings of 2000 International Joint Power Generation Conference.* 2000. Miami Beach, Florida.
3. Fujita, T., *Review - Current Progress in Advanced High Cr Ferritic Steels for High-temperature Applications.* ISIJ International, 1992. **Vol. 32**(No. 2): p. 175-181.
4. H.K.D.H.Bhadeshia, *Review - Design of Ferritic Creep-resistant Steels.* ISIJ International, 2001. **Vol. 41**(No. 6): p. 626-640.
5. R.C.Hurst, ed. *Design of High Temperature Metallic Components.* 1984, Elsevier Applied Science Publishers.
6. Marshall, P. *Development of Microstructure to Optimise Mechanical Performance of Power Generation Equipment.* in *Micon 86: Optimisation of Processing, Properties, and Service Performance Through Microstructural Control.* 1988. Philadephia: American Society for Testing and Materials.
7. Maziasz, P.J. *Microstructural Stability and Control for Improved Irradiation resistance and for High-Temperature Strength of Austenitic Stainless Steels.* in *Micon 86.* 1988. Philadephia: American Society for Testing and Materials.
8. R.D.Townsend. *CEGB experience and Uk developments in materials for advanced plant.* in *International Conference on Advances in Material Technology for Fossil Power Plants.* 1987. Chicago,Illinois, USA: ASM International.
9. Viswanathan, R., et al., *Advances in material technology for fossil power plants: proceedings of an International Conference on Advances in Material Technology for Fossil Power Plants, 1-3 September 1987, Chicago, Illinois, USA.* 1987, [Cleveland, Ohio]: ASM International. xii, 654 p.
10. Davis, J.R., *Heat-resistant materials.* ASM specialty handbook. 1997, Materials Park, Ohio: ASM International.

11. Wilshire, B. and D.R.J. Owen, *Recent advances in creep and fracture of engineering materials and structures*. 1982, Swansea: Pineridge Press. [400]p.
12. T.Sourmail, H.K.D.H.B.a., *Design of Creep-resistant steels: Success & Failure of Models.* Japan Society for the Promotion of Science, Committee on Heat Resisting Materials and Alloys, 2003. **Vol. 44**: p. 299-314.
13. F.Brun, T.Y., J.D.Robson, V.Narayan, H.K.D.H.Bhadeshia and D.J.C. Mackay, *Theoretical design of ferritic creep resistant steels using neural network, kinetic, and thermodynamic models.* Materials Science and Technology, 1999. **Vol. 15**: p. 547-554.
14. Davis, J.R. and ASM International. Handbook Committee., *Stainless steels*. ASM specialty handbook. 1994, Materials Park, Ohio: ASM International. v, 577 p.
15. R.B.Scarlin, J.E.B., P.Ernst, P.J.Uggowitzer, M.O.Speidel. *Materials development for alternative rotor designs for improved fossil-fired power plants*. in *International Conference on Advances in Material Technology for Fossil Power Plants*. 1987. Chicago, Illinois, USA: ASM International.
16. H.Haneda, F.M.a. *Three years of experience with a new 12% steel in superheater*. in *International Conference on Advances in Material Technology for Fossil Power Plants*. 1987. Chicago, Illinois, USA: ASM International.
17. M.Igarashi, S.M., H.Hasegawa, K.Yamada, and F.Abe, *Creep Deformation and the Corresponding Microstructural Evolution in High Cr Ferritic Steels.* ISIJ International, 2001. **Vol. 41**: p. S101-S105.
18. M.Tamura, H.S., Y. Kato, A.Kohyama, H.Esaka and K.Shinozuka, *Relation between Creep Rupture Strength and Substructure of Heat Resistant Steel.* ISIJ International, 2002. **Vol. 42**(No. 12): p. 1444-1451.
19. Truman, H.W.K.a.R.J. *An investigation of the creep ductility of 18-12-1Nb and related steels*. in *Joint symposium on structural process in creep*. 1961. London: The Iron and Steel Institute.
20. P.J.Maziasz, R.W.S. *Modified 14Cr-16Ni stainless steels with improved creep resistence at 700°C due to tailored precipitate microstructures*. in *International Conference on Advances in Material Technology for Fossil Power Plants*. 1987. Chicago, Illinois, USA: ASM International.

21. John Hald, L.K., *Precipitate Stability in Creep Resistant Ferritic Steels-Experimental Investigations and Modelling.* ISIJ International, 2003. **Vol. 43**(No. 3): p. 420-427.

22. H.K.D.H.Bhadeshia. *Advances in the kinetic theory of carbide Precipitation.* in *Thermec 2003*. 2003: Material Science Forum.

23. Kouichi Maruyama, K.S.a.J.-i.K., *Strengthening Mechanisms of Creep Resistant Tempered Martensitic Steel.* ISIJ International, 2001. **Vol.41**(No. 6): p. 641-653.

24. F Masuyama, T Yokoyama, Y Sawaragi and T Yokoyama, *Materials for Advanced Power Engineering*, Eds D Coutsouradis et al, Kluwer Academic Publishers 1994, pp 173-181.

25. T.Sourmail, H.K.D.H.B., *Modelling simultaneous precipitation reactions in austenitic stainless steels.* Computer Coupling of Phase Diagrams and Thermochemistry, 2003. **Vol. 27**: p. 169-175.

26. Asa Gustafson, M.H., *Coarsening of precipitates in an advanced creep resistant 9% chromium steel-quatitative microscropy and simulations.* Materials Science and Engineering, 2002. **A333**: p. 279-286.

27. Villiers, F.R.N.N.a.H.L.d., *The Physics of Creep.* 1995, London: Taylor & Francis Ltd.

28. M W Spindler, S.L.S. *Creep Deformation, Rupture and Ductility of Esshete 1250.* in *Int. Conf. on Creep and Fracture in High Temperature Components-Design and Life Assessment Issues, IMechE.* 2005. London.

29. M.F.Ashby, H.J.F.a., *Deformation-Mechanism Maps: The Plasticity and Creep of Metals and Ceramics.* October 1982: Pergamon.

30. Bressers, J. and Commission of the European Communities. Joint Research Centre., *Creep and fatigue in high temperature alloys.* 1981, London: Applied Science. xii,190p.

31. Joachim Granacher, T.P. *Creep of some gas turbine materials.* in *International Conference on Advances in Material Technology for Fossil Power Plants.* 1987. Chicago, Illinois, USA: ASM International.

32. Willoughby, A.F.E.a.G., *The ageing behaviour of a Cr-Ni-Mn Austenitic Steel.* 1972, Central Electricity Reserach Laboratories. p. RD/L/R/1806.

33. Klaus Haarmann, G.P.K. *Practical experience with pipe materials suitable for use in the temperature range form 540°C to 620°C.* in *International Conference on Advances in Material Technology for Fossil Power Plants.* 1978. Chicago, Illinois, USA: ASM International.

34. R.P.Skelton, B.J.E.B. *Thermal fatigue properties of candidate materials for advanced steam plant.* in *International Conference on Advances in Material Technology for Fossil Power Plants.* 1987. Chicago, Illinois, USA: ASM International.

35. Carl E.Jaske, R.W.S. *Long-term-creep and creep-crack growth behavior of 9Cr-1mo-V-Nb steel.* in *International Conference on Advances in Material Technology for Fossil Power Plants.* 1987. Chicago, Illinois, USA: ASM International.

36. H.Haneda, F.M., S.Kaneko, T.Toyoda. *Fabrication and characteristic properties of modified 9Cr-1Mo steel for header and piping.* in *International Conference on Advances in Material Technology for Fossil Power Plants.* 1987. Chicago, Illinois, USA: ASM International.

37. Hatherly, F.J.H.a.M., *Recrystallization and Related Annealing Phenomena.* 1996: Pergamon.

38. Easterling, D.A.P.a.K.E., *Phase Transformations in Metals and Alloys.* 2nd ed. 1992: Chapman and Hall.

39. Vaclav Foldyna, J.P., and Zdenek Kubon, *Development of Advanced Chromium Steels with Respect to Microstructure and Structural Stability.* ISIJ International, 2001. **Vol. 41**(Supplement): p. S81-S85.

40. Mats Hätterstrand, M.S., Hans-Olof Andrén, *Microanalysis of two creep resistant 9-12% chromium steels.* Materials Science and Engineering, 1998. **A250**: p. 27-36.

41. Katsumi Yamada, M.I., Seiichi Muneki, Fujio Abe, *Creep Properties affected by Morphology of MX in High-Cr Ferritic Steels.* ISIJ International, 2001. **Vol. 41**: p. S116-S120.

42. Sourmail, T., *Precipitation in creep resistant austenitic stainless steels.* Materials Science & Technology, 2001. **Vol. 17**: p. 1-14.

43. Pickering, S.R.K.a.F.B. *Niobium in stainless steels.* in *Proceeding of the International Symposium Niobium 1981.* 1981.

44. Meyer, L. *History of niobium as microalloying element.* in *Proceeding of the International Symposium Niobium 2001*. 2001.

45. F.B.Pickering, ed. *The metallurgical evolution of stainless steels.* 1979, America Society of Science and The metals Society: Ohio and London.

46. J.Kallqvist, H.O.A., *Micoranalysis of a stabilised austenitic stainless steel after long term ageing.* Materials Science and Engineering, 1999. **A270**: p. 27-32.

47. John P.Shingledecker, P.J.M., Neal D.Evans, Micheal J.Pollard, *Creep behavior of a new cast austenitic alloy.* International Journal of Pressure Vessels and Piping, 2007. **84**: p. 21-28.

48. Y.Bergstrom, H.H., *Hall-Petch relationships of iron and steel.* Metal Science, 1983. **Vol. 17**: p. 341-347.

49. J.D.Hodkin, L.G.F.a.E.W.C. *Some factors affecting the creep-rupture performance of a 3%Cr-Mo-W-V steel at 550°C.* in *Joint symposium on structural process in creep.* 1961. London: The Iron and Steel Institute.

50. Kyung Seon Min, S.W.N., *Correlation between characteristics of grain boundary carbides and creep-fatigue properties in AISI 321 stainless steel.* Journal of Nuclear materials, 2003. **322**: p. 91-97.

51. M. Tanaka, J.T., R. Kato, *Effects of microstructures on the creep-rupture properties and fracture mechanisms in austenitic heat-resistant steels.* Materials Science & Engineering, 2005. **A410-411**: p. 79-84.

52. K.B. Kang, O.K., W. B. Lee, and C. G. Park, *Effect of precipitation on the Recrystallization Behavior of a Nb containing steel.* Scripta Materialia, 1997. **Vol. 36**: p. 1303-1308.

53. K.J.Irvine, J.D.M., F.B.Pickering. *Structural aspects of creep-resisting steel.* in *Joint symposium on structural processes in creep.* 1961. London: The Iron and Steel Institute.

54. Lifshitz, I.M.a.V.V.S., *The Kinetics of Precipitation form supersaturated solid solutions.* J. Phys. Chem. Solids, 1961. **Vol. 91**: p. 35-50.

55. K.Lucke, G.A., *Theory of grain growth in the presence of second phase particles.* Material Science Forum, 1992(No.94-96): p. 597-604.

56. K.Lucke, G.A.a., *Theory of Grain Growth in the Presence of Second Phase Particles.* Materials Science Forum, 1992(No. 94-96): p. 597-604.

57. Shewmon, P.G., *Transformation in metals.* 1969: McGraw-Hill Book Company.

58. Bhadeshia, J.D.R.a.H.K.D.H., *Kinetics of Precipitation in Power Plant Steels.* Calphad, 1996. **Vol. 20**(No. 4): p. 447-460.

59. Martin, J.W. and R.D. Doherty, *Stability of microstructure in metallic systems.* Cambridge solid state science series. 1976, Cambridge: Cambridge University Press. x,298p.

60. Zener, C.J., *Theory of Growth of Spherical Precipitates From Solid Solution.* Journal of Applied Physics, 1949. **Vol. 20**: p. 950.

61. Verhoeven, J.D., *Fundamentals of Physical Metallurgy.* 1975: John Wiley & Sons.

62. H.K.D.H.Bhadeshia, N.F.a., *Modelling Simultaneous Alloy Carbide Sequence in Power Plant Steels.* ISIJ International, 2002. **Vol. 42**(No. 7): p. 760-769.

63. Keisuke Yamamoto, Y.K., Fu-Gao Wei, Yashinao Mishima, *Design of Laves phase strengthened ferritic heat resisting steels in the Fe-Cr-Nb(-Ni) system.* Materials Science & Engineering A, 2002. **A329-331**: p. 249-254.

64. Izabel Fernanda Machado, A.F.P., *The occurrence of Laves phase in Fe-15%Cr-15%Ni austenitic stainless steel containing niobium.* Acta Microscopica, 2003. **vol.12**(No.1): p. 111-114.

65. A.F.Padilha, D.M.E., E.Materna-Morris, M.Rieth, M. Klimenkov, *Precipitation in AISI 316L(N) during creep tests at 550 and 600°C up to 10 years.* Journal of Nuclear Materials, 2007. **362**: p. 132-138.

66. Joonoh Moon, S.K., Jongbong Lee, Changhee Lee, *Limiting austenite grain size of TiN-containing steel considering the critical particle size.* Scripta Materialia, 2007. **56**: p. 1083-1086.

67. Pickering, F.B., *Introduction: The Metallurgy Evolution of Stainless Steel.* American Society for Metals and The Metals Society, 1979: p. 1-42.

68. D. M. E. Villanueva, F.C.P.J., R. L. Plaut and A. F. Padilha, *Comparative study on sigma phase precipitation of three types of stainless steels: austenitic, superferritic and duplex.* Materials Science and Technology, 2006. **Vol. 22**: p. 1098-1104.

69. Kruml, J.S.a.T., *Sigma Phase Equilibria and Nucleation in Fe-C-Ni Alloys at High Temperature.* Scripta Materialia, 1996. **Vol. 35**: p. 689-693.

70. Keisuke Yamamoto, Y.K., Yashinao Mishima, *Effect of matrix substructures on precipitation of the Laves phase in Fe-Cr-Nb-Ni system.* ISIJ International, 2003. **Vol.43**(No.8): p. 1253-1259.

71. Kaori Miyata, Y.S., Hirokazu Okada, Fujimitsu Masuyama, Tomomitsu Yokoyama and Nobuyoshi Komai, *Microstructural Evolution of a 12Cr-2W-Cu-V-Nb Steel during Three-year Service Exposure.* ISIJ International, 2000. **Vol. 40**(No.11): p. 1156-1163.

72. E.O.Hall, Proc. Phys. Soc, 1951. **Ser. B**(64): p. 747-753.

73. N.J.Petch, J. Iron and Steel Institute, 1953. **Vol. 174**: p. 25-28.

74. C.S.Smith, Trans. Metall. Soc. A.I.M.E, 1948. **175**: p. 15.

75. M.Militzer, A.G., E.B.Hawbolt and T.R.Meadowcroft, *Austenite Grain Growth Kinetics in Al-Killed Plain Carbon Steels.* Met. and Mater. Trans., 1996. **27A**: p. 3399-3409.

76. M.Hillert, *On the Theory of Normal and Abnormal Grain Growth.* Acta Metall, 1965. **Vol. 13**: p. 227-238.

77. L.Q.Chen, C.E.K.a., *Computer Simulation of 3-D Grain Growth Using a Phase Field Model.* Acta Materialia, 2002. **Vol.50**: p. 3057-3073.

78. Group, M.T., *MTDATA*. 1998, National Physical Laboratory: London.

79. Spindler, M., *Plant Intergrity*. 2004, British Energy: Gloucester.

80. Folkhard, E. and G. Rabensteiner, *Welding metallurgy of stainless steels*. 1988, Wien: Sringer-Verlag.

81. M.Sireesha, S.K.A., S.Sundaresan, *Metallurgical changes and mechanical behaviour during high temperature aging of welds between Alloy 800 and 316LN austenitic stainless steel.* Materials Science and Technology, 2003. **Vol. 19**: p. 1411-1417.

82. International Standard, Steel-Micrographic determination of the apparent grain size, ISO 643:2003.

83. John P. Shingledecker, Philip J. Maziasz, Neal D. Evans and Micheal J. Pollard, *Creep Behaviour of New Cast Austenitic Alloy,* International Journal of Pressure Vessels and Piping 84 (2007) 21-28.

84. Yukio Takahashi, hiroshi Shibamoto, Kazuhiko Inuoe, *Long term creep rupture behaviour of smoothed and notched bar specimen of 316 staniless steel (316FR) and their evolution,* Nuclear Engineering and Design 238 (2008) 310-321.

85. F.R.N. Naborro and H.L. de Villiers, The physics of creep, Taylor & Francis Ltd, 1995.

86. H.K.D.H.Bhadeshia, N.F.a., *Modelling precipitation of niobium carbide in austenite: multicomponent diffusion, capillarity and coarsening.* Materials Science and Technology, 2001. **Vol. 17**: p. 403-408.

87. Neubauer, B.; Wedel, U. ¯*Rest Life Estimation of Creeping Components by Means of Replicas*", Advances in Life Prediction Methods, American Society of Mechanical Engineers, New York, p. 307-314, 1983.

88. S L Spindler, *Creep Deformation Modelling of Esshete 1250 Parent,* Engineering Division Report, British Energy Generation Limited.

89. M W Spindler, *Tensile Properties of Esshete 1250 Parent and HAZ Used for Boiler Spines,* Central Engineering Support, British Energy Generation Limited.

90. Brandon, Kaplan, *Microstructural Characterization of Materials,* 2nd Edition, Wiley, 2008.

91. Leszek Wojnar, *Image Analysis Applications in Materials Engineering,* CRC Press, 1999.

92. British Standard Aerospace Series, Procedure for Insapection, testing and acceptance of steel sheet and strip. BS 3S 500:1996.

93. A.F. Padilha, D.M. Escriba, E. Materna-Morris, M. Rieth, M. Klimenkov, *Precipitation in AISI 316L(N) during creep tests at 550 and 600°C up to 10 years,* Journal of Nuclear Materials 362 (2007) 132-138.

Microstructural observation of E1250 as received samples

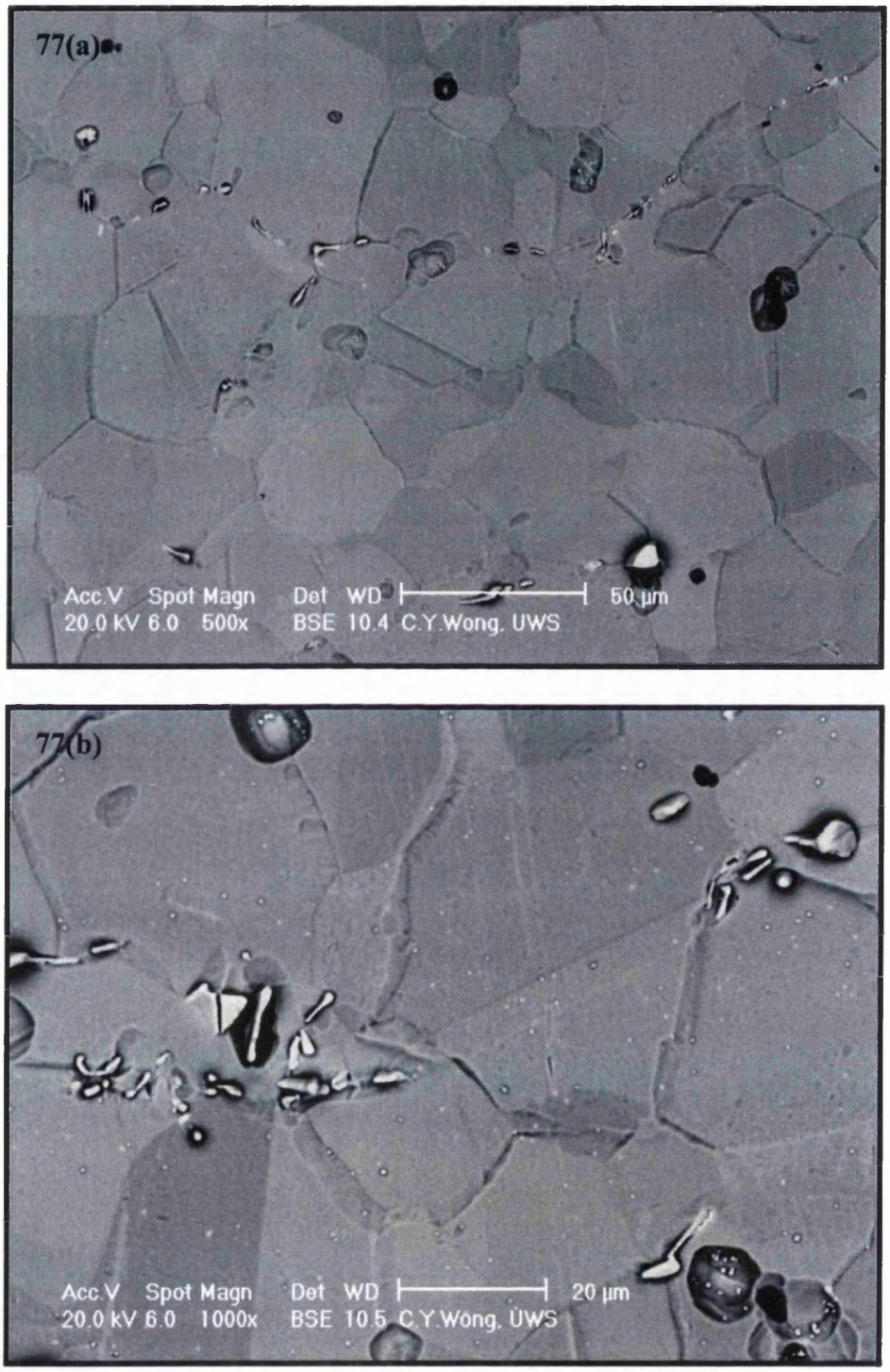

Figure 77: (a) Backscattered electron micrograph of E1250 parent metal, (b) Morphology of precipitates in the as-received E1250 following solution treatment at 1080°C for 45 mins. Both samples are etched using 10%w.o. dilute aqueous oxalic acid solution.

Microstructural observation of E1250 parent creep exposed samples

Examination of the six creep samples confirmed that the bright contrast second phase particles represent the majority of the precipitated particles, imaged on the level of SEM examination. It can be easily seen that these particles form at grain boundaries and also within the matrix (*Figures 78(a)-(f)*). The precipitates are varied in size ranging from approximately 0.5μm to 30μm, having irregular shape. It is also found that many finely dispersed particles were precipitate over the matrix.

Microstructure of the E1250 parent aged samples


78(b)
Acc.V Spot Magn Det WD Exp 20 µm
20.0 kV 5.0 1000x BSE 10.3 1228 C.Y.Wong, UWS


78(c)
Acc.V Spot Magn Det WD Exp 20 µm
20.0 kV 5.0 1000x BSE 10.4 1242 C.Y.Wong, UWS


78(d)
Acc.V Spot Magn Det WD Exp 20 µm
20.0 kV 5.0 1000x BSE 10.3 1232 C.Y.Wong, UWS

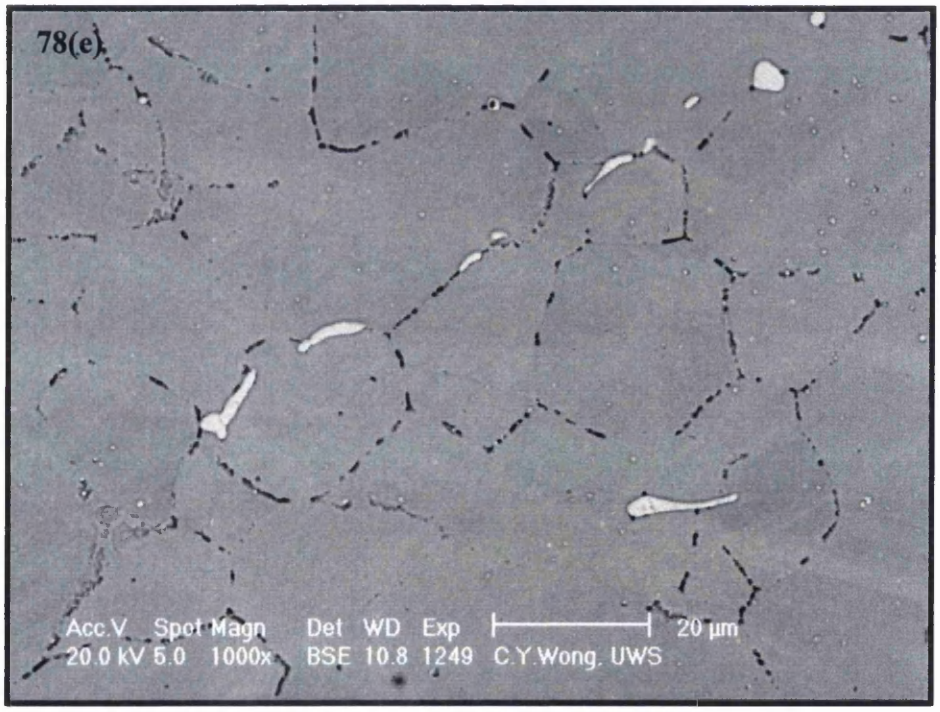
78(e)
Acc.V Spot Magn Det WD Exp 20 µm
20.0 kV 5.0 1000x BSE 10.8 1249 C.Y.Wong, UWS

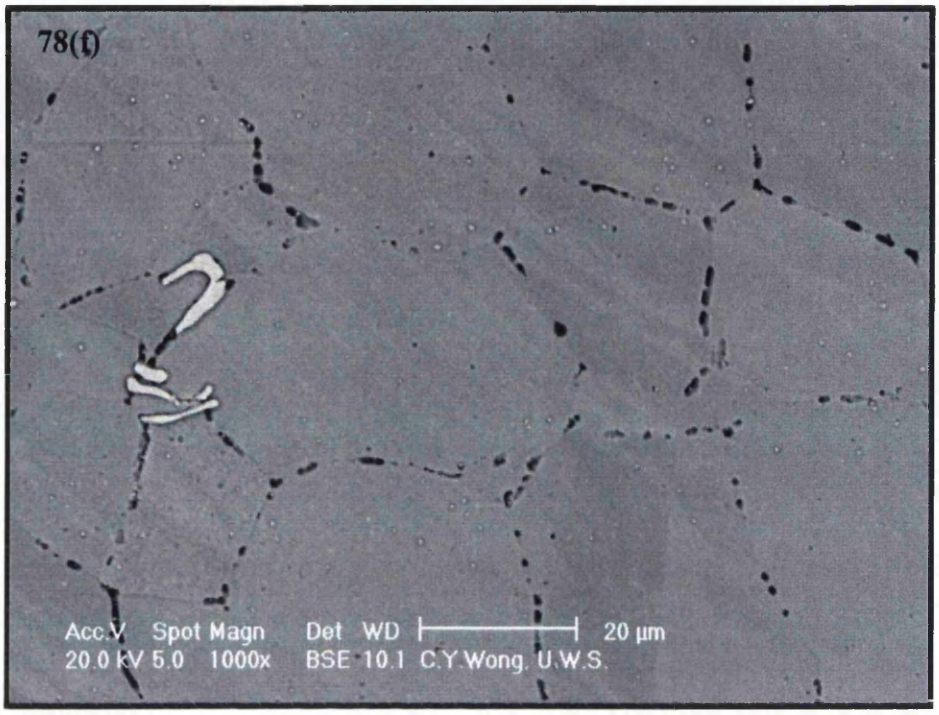

Figure 78: SEM micrographs of E1250 parent creep exposed samples extracted from the grip area. Samples were exposed at 550°C for a) 7132h, b) 4944h, c) 2792h, d) 1301h and samples exposed at 575°C for e) 3489h, f) 2435h.

5.3.2 Microstructure underneath the fracture surface

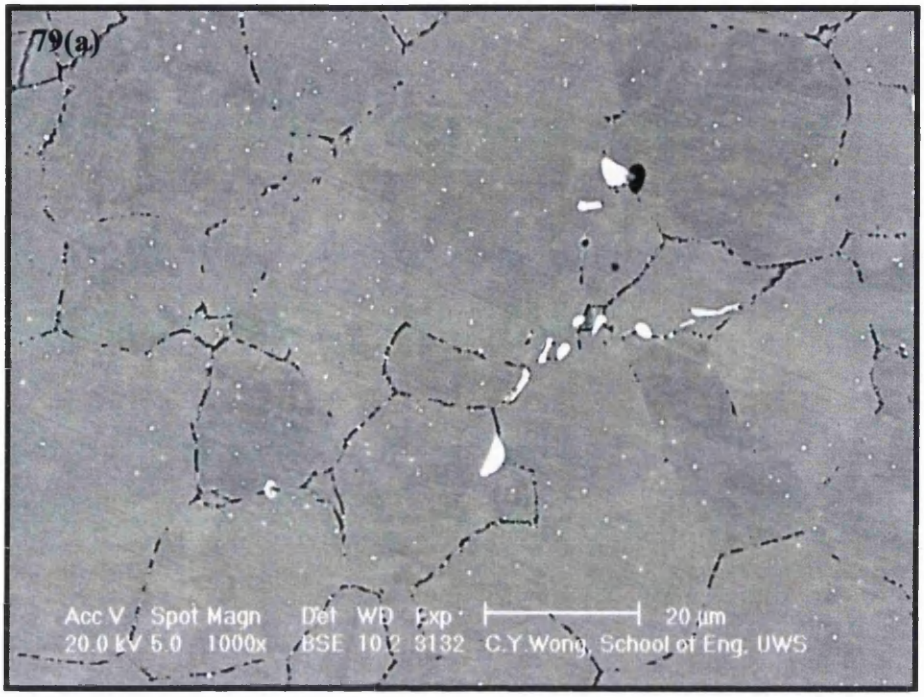

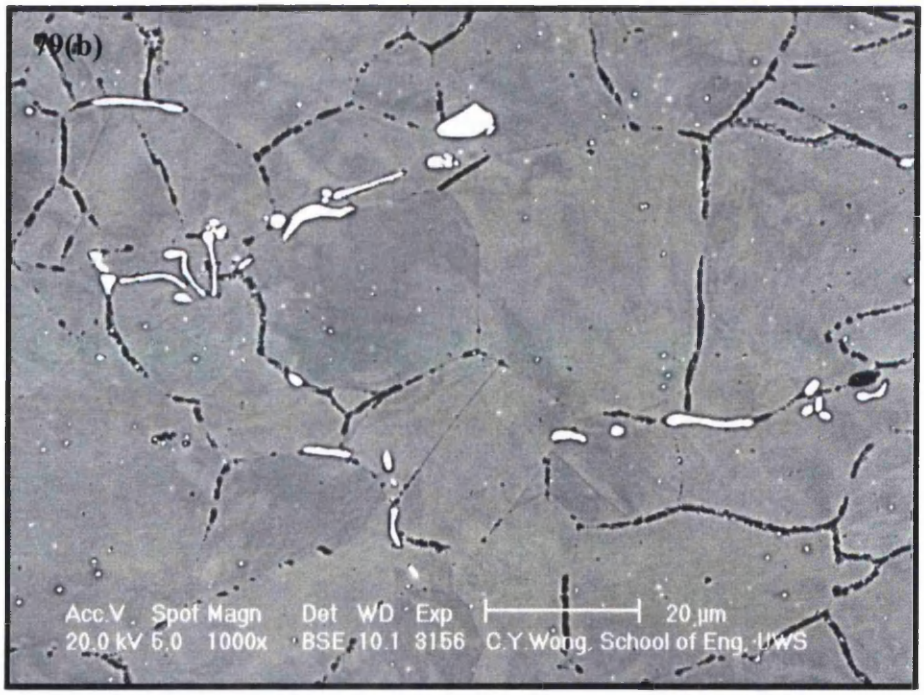

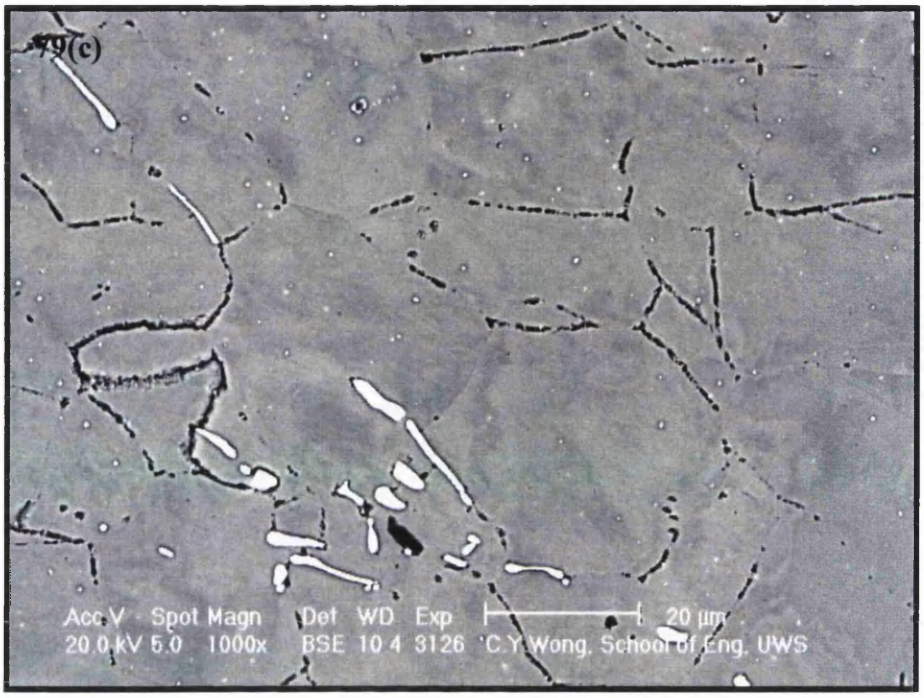
79(c)
Acc.V Spot Magn Det WD Exp 20 µm
20.0 kV 5.0 1000x BSE 10.4 3126 C.Y.Wong, School of Eng, UWS


79(d)
Acc.V Spot Magn Det WD Exp 20 µm
20.0 kV 5.0 1000x BSE 10.1 3149 C.Y.Wong, School of Eng, UWS

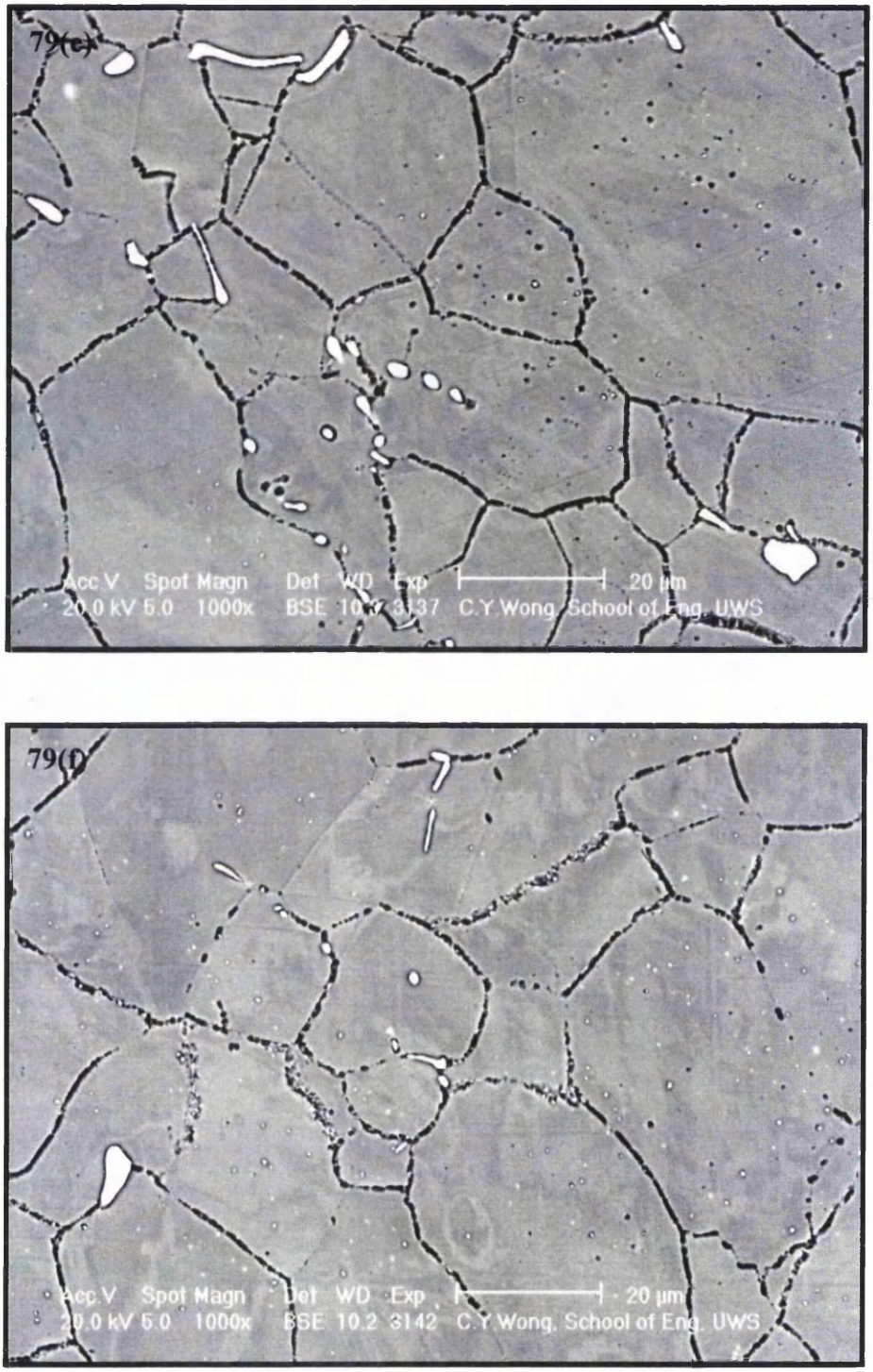

Figure 79: SEM micrographs of E1250 creep samples extracted from underneath the fracture area. Creep samples were exposed at 550°C under for a) 7132h, b) 4944h, c) 2792h, d) 1301h and creep samples exposed at 575°C for e) 3489h, f) 2035h.

SEM imaging of fracture surfaces

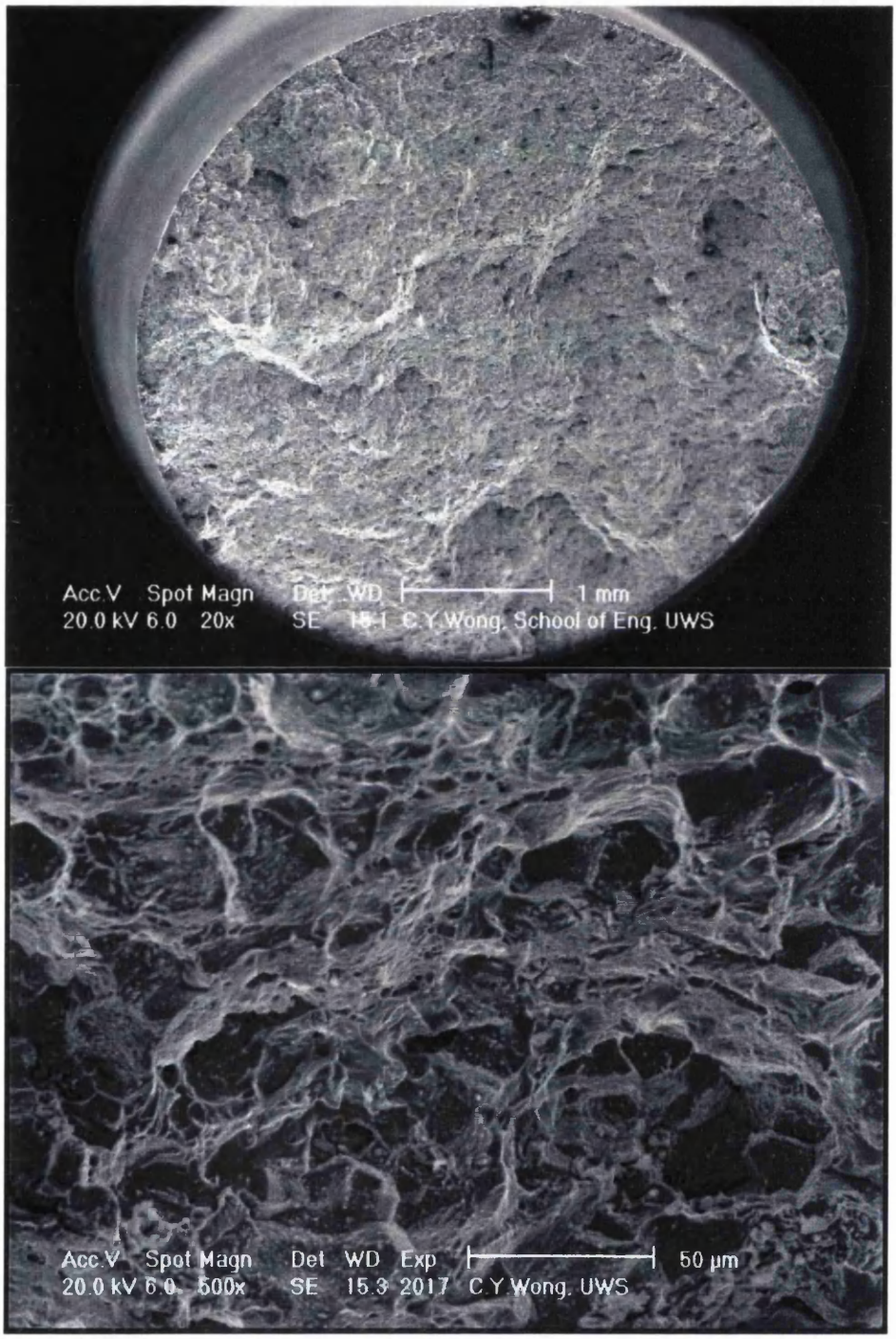

Figure 80 (a) SEM micrographs of the creep fracture of P3 sample after rupture life of 7132h.

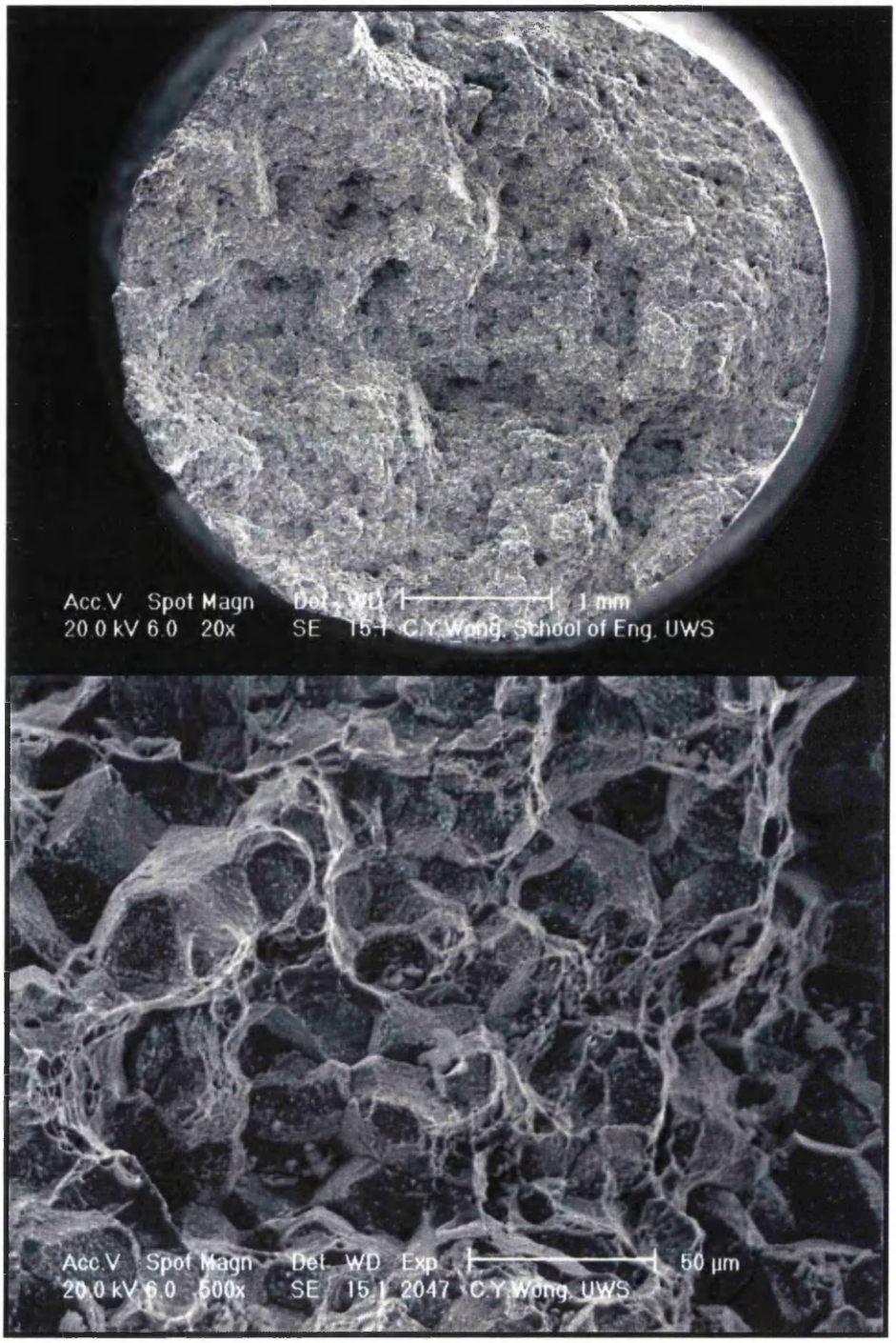

Figure 80 (b) SEM micrographs of the creep fracture of P8 sample after rupture life of 4944h.

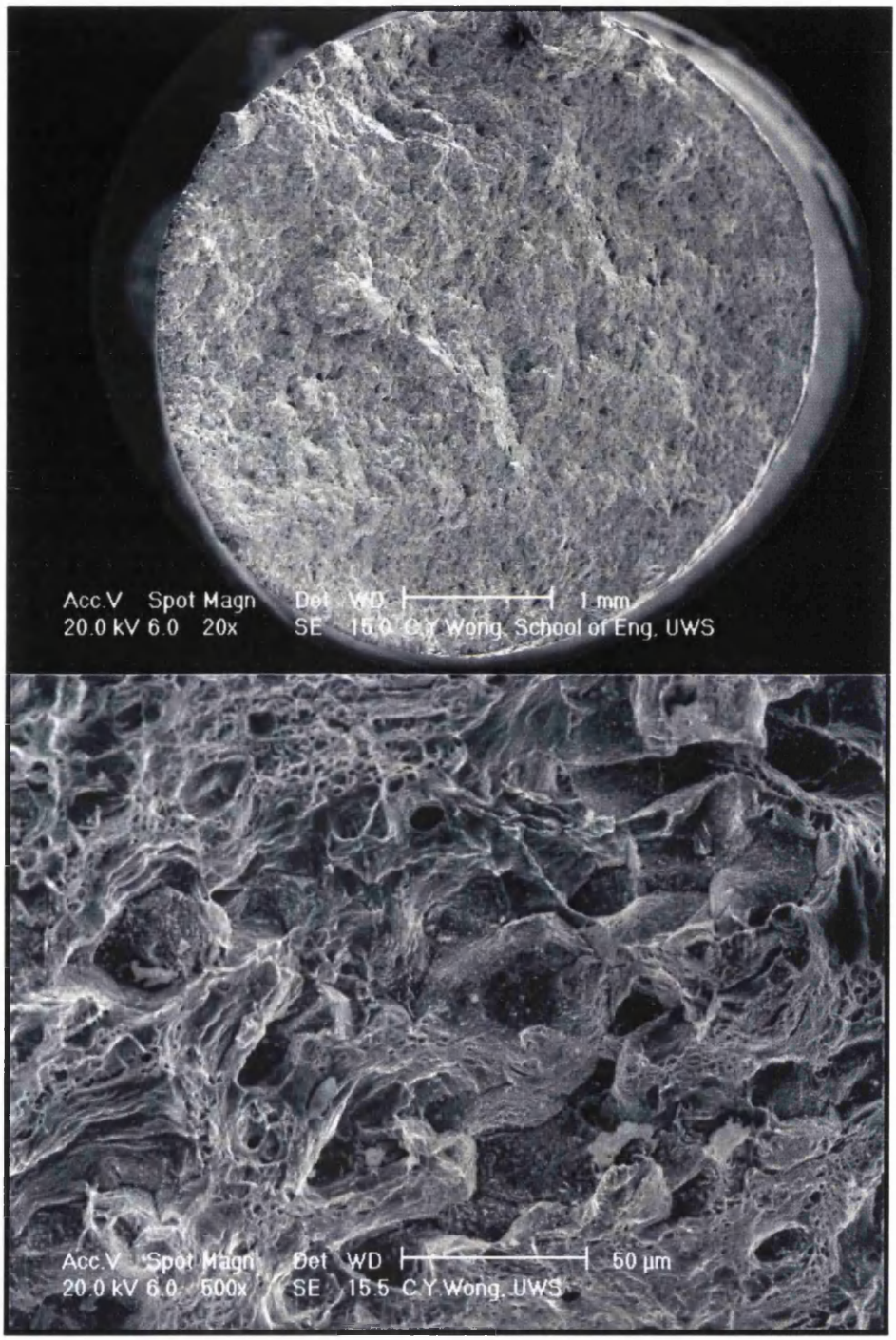

Figure 80 (c) SEM micrographs of the creep fracture of P2 sample after rupture life of 2792h.

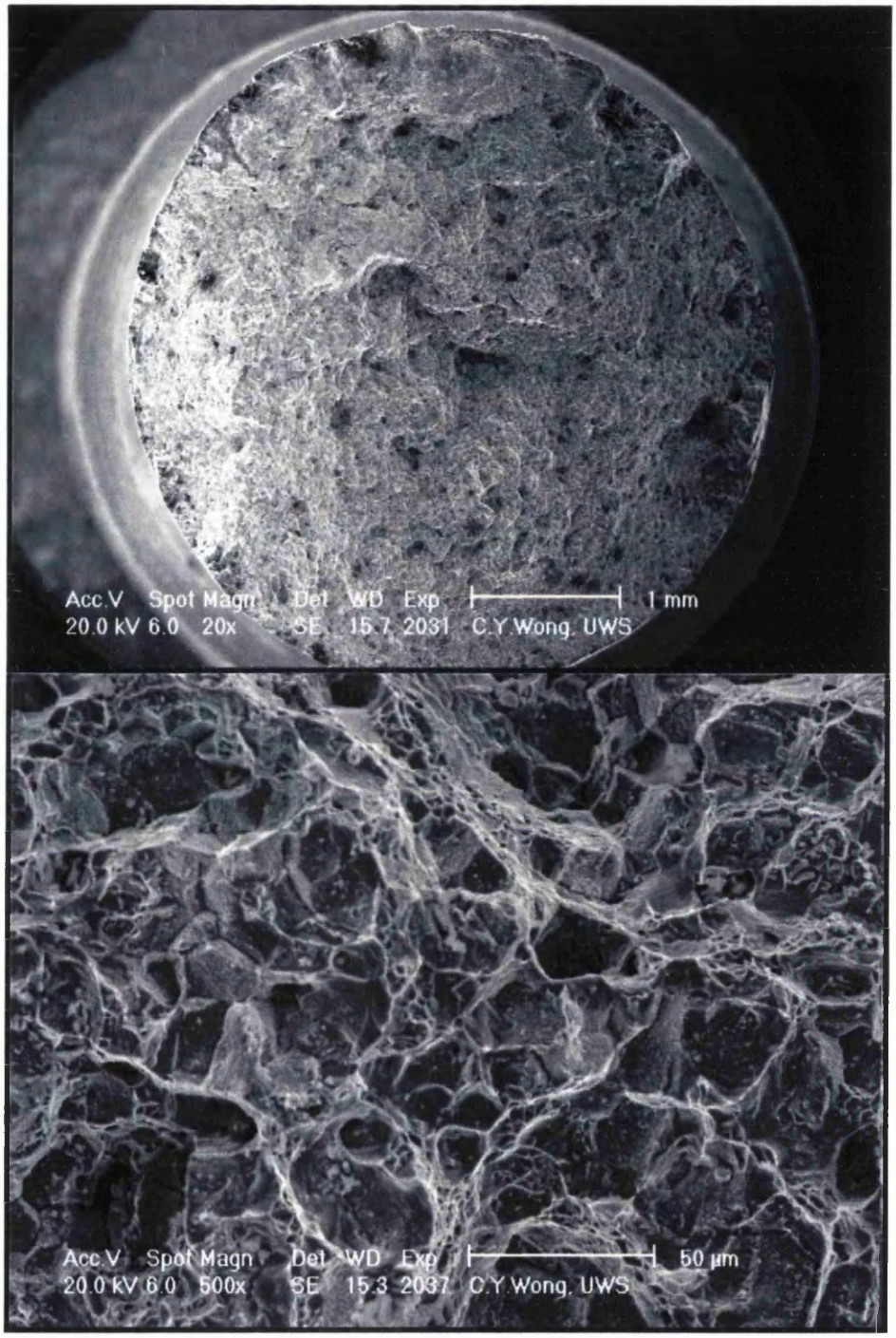

Figure 80 (d) SEM micrographs of the creep fracture of P7 sample after rupture life of 1301h.

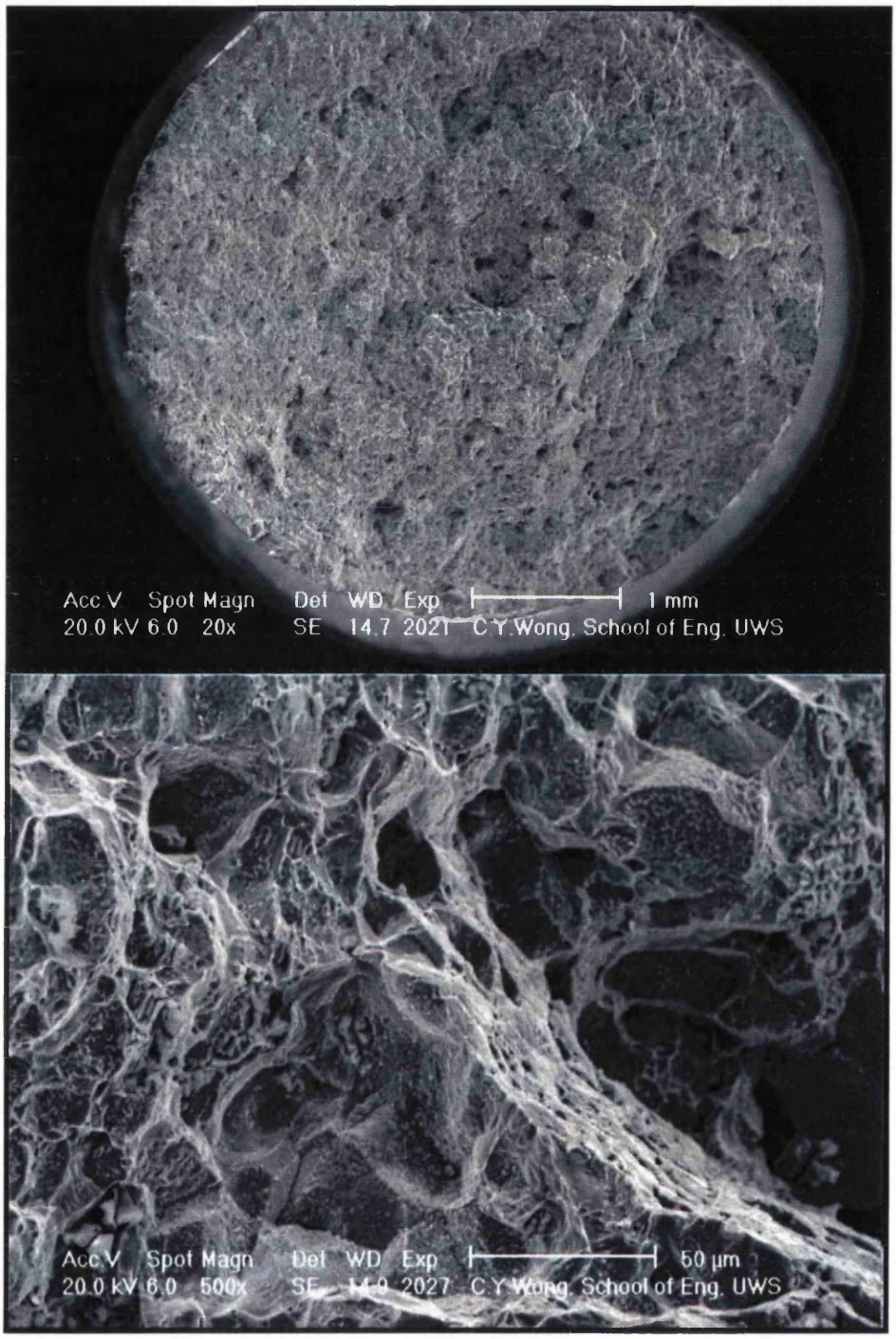

Figure 80 (e) SEM micrographs of the creep fracture of P4 sample after rupture life of 3489h.

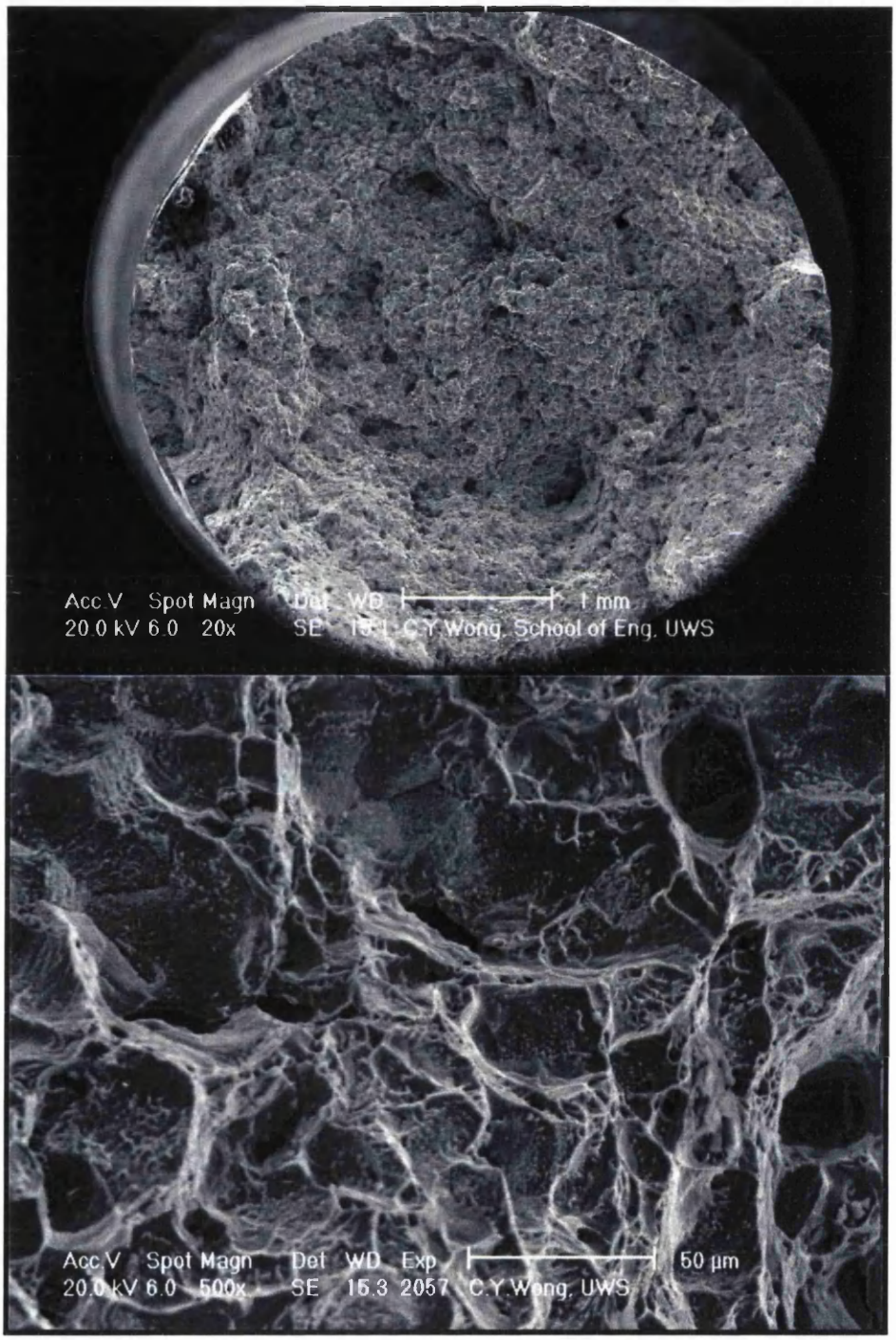

Figure 80 (f) SEM micrographs of the creep fracture of P10 sample after rupture life of 2035h.

Microstructural observation of Esshete 1250 BH creep exposed samples

SEM backscattered micrographs were recorded for all specimens which were etched using dilute aqueous oxalic acid. The material had an austenitic matrix in which MX precipitates are embedded in the matrix but there were also present at grain boundaries. Figures 81-84 shows statically aged samples while figures 85(a)-85(l) shows the gauge area (creep samples) of the steels studied at the different temperatures and stresses employed.

5.4.1 Microstructure of the 12 BH aged samples

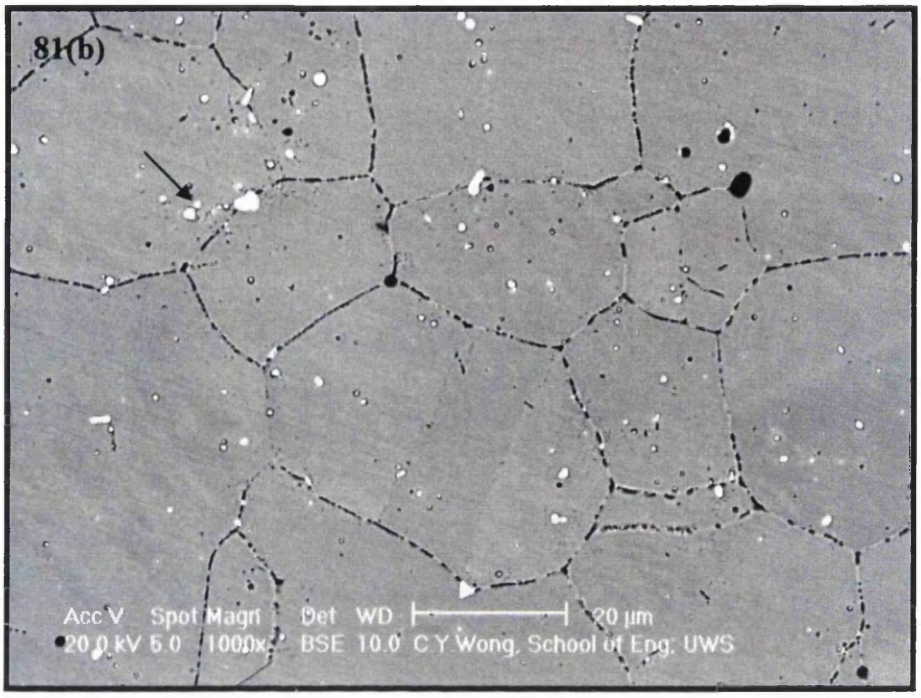

Figure 88: Backscattered SEM micrographs of specimens aged at 550°C (a) BH24 for 5527h, (b) BH28 for 82138h.

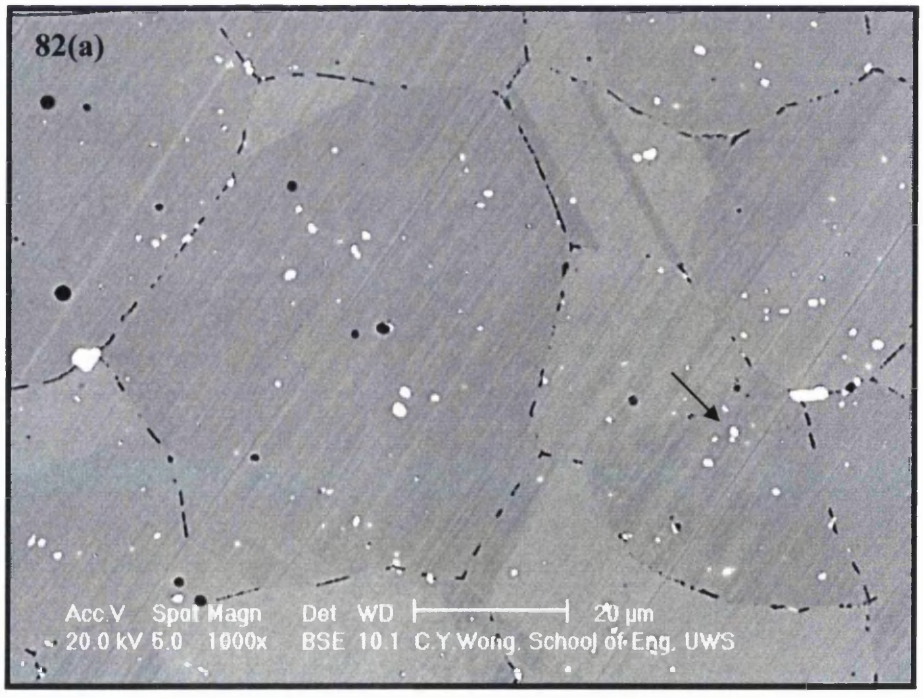

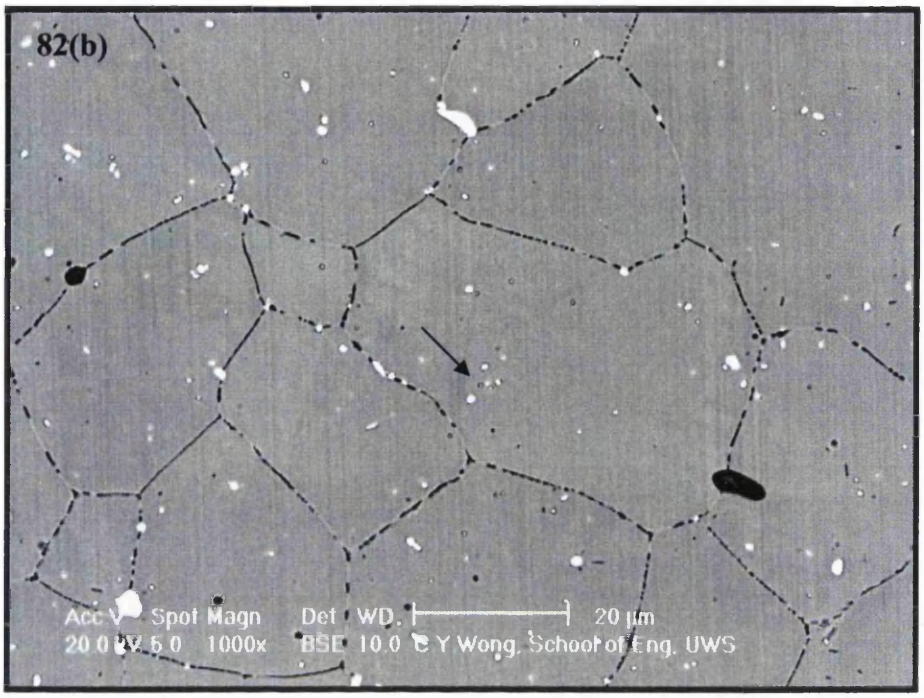

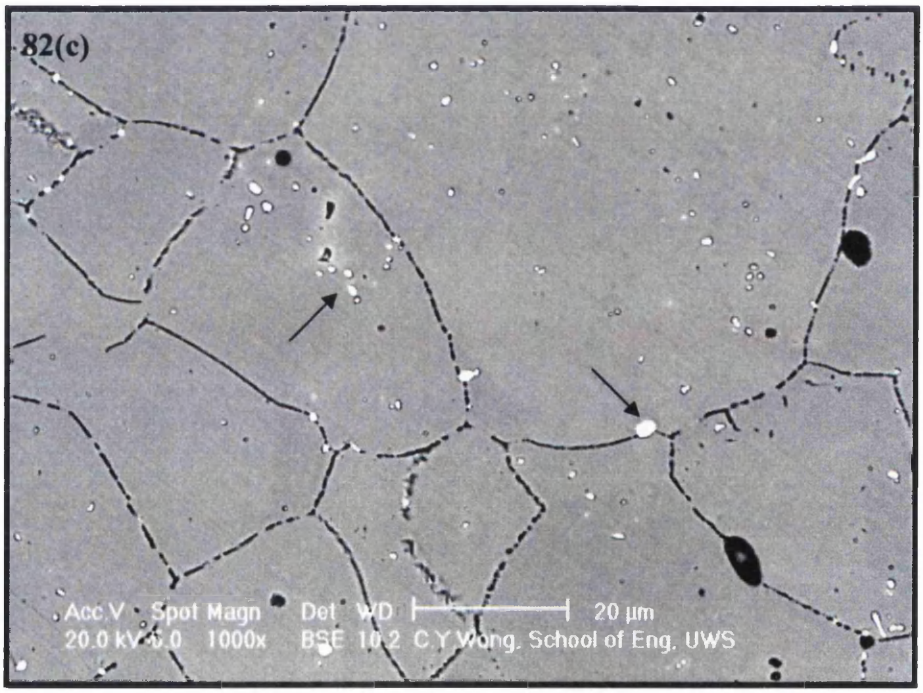

Figure 82: Backscattered SEM micrographs of specimens aged at 600°C (a) BH7 for 1179.5h, (b) BH6 for 6951h, and (c) BH10 for 153491h.

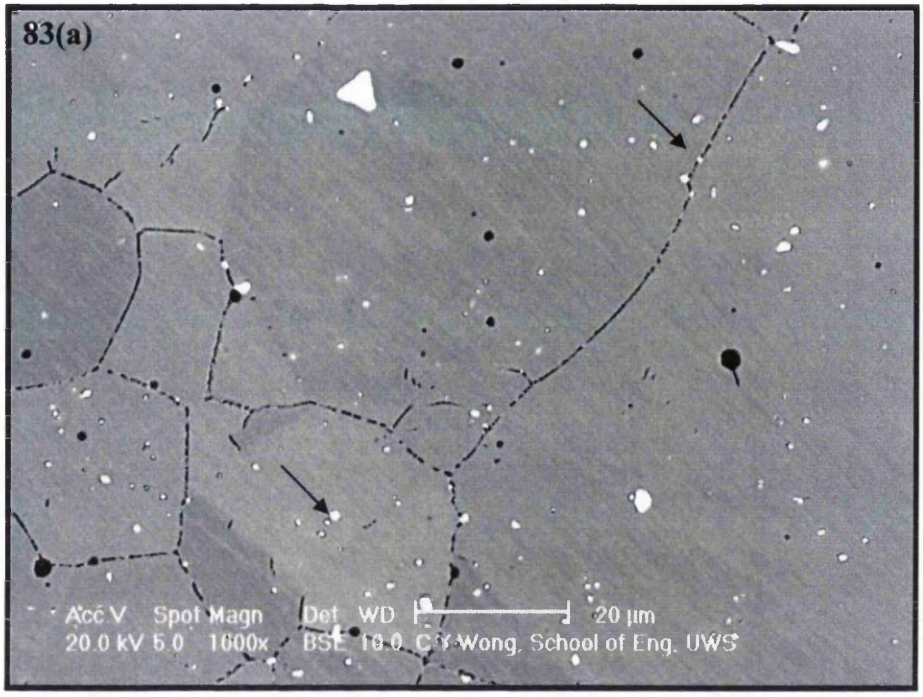
83(a)
Acc.V Spot Magn Det WD 20 µm
20.0 kV 5.0 1000x BSE 10.0 C Y Wong, School of Eng. UWS

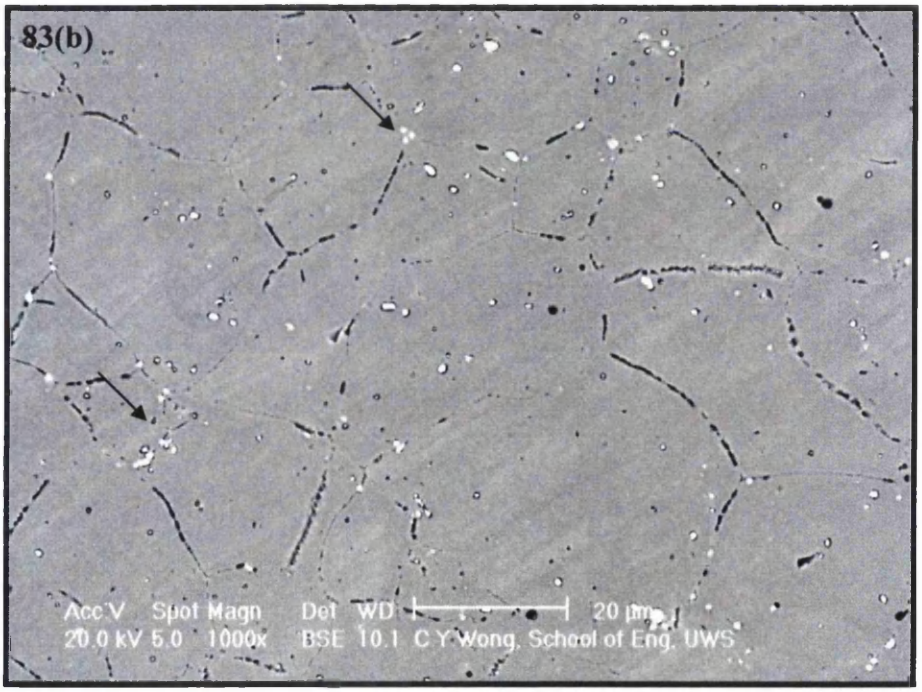
83(b)
Acc.V Spot Magn Det WD 20 µm
20.0 kV 5.0 1000x BSE 10.1 C Y Wong, School of Eng. UWS

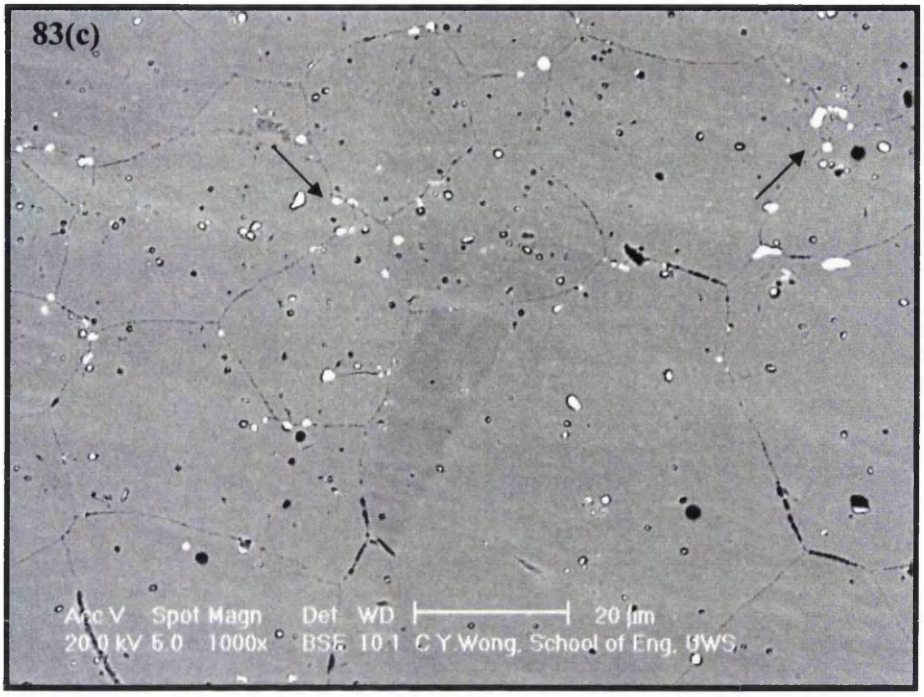

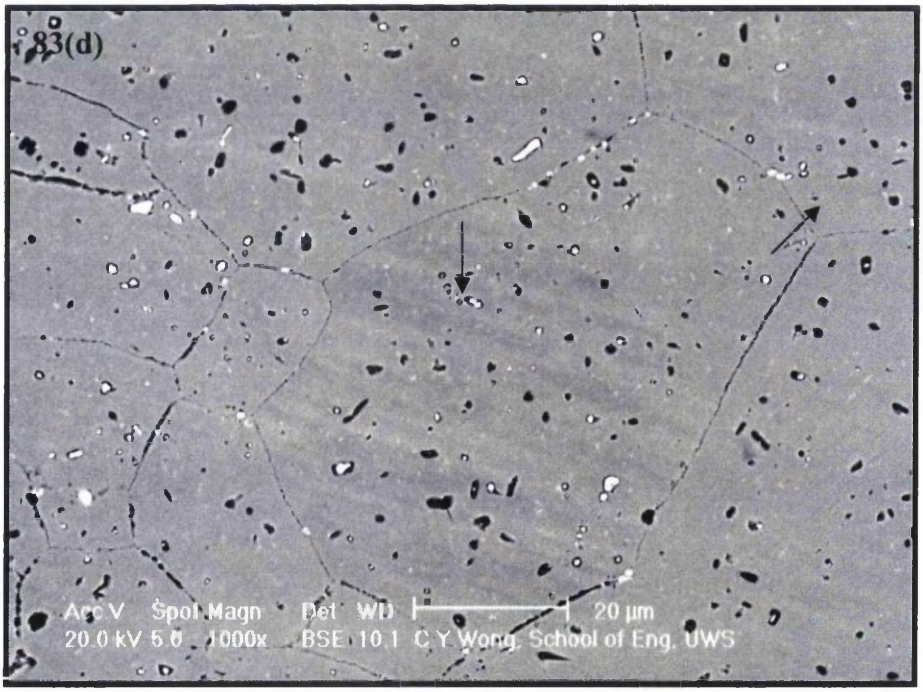

Figure 83: Backscattered SEM micrographs of specimens aged at 650°C (a) BH11 for 257.75h, (b) BH4 for 35221h, (c) BH2 for 29398h, and (d) BH27 for 77896h.

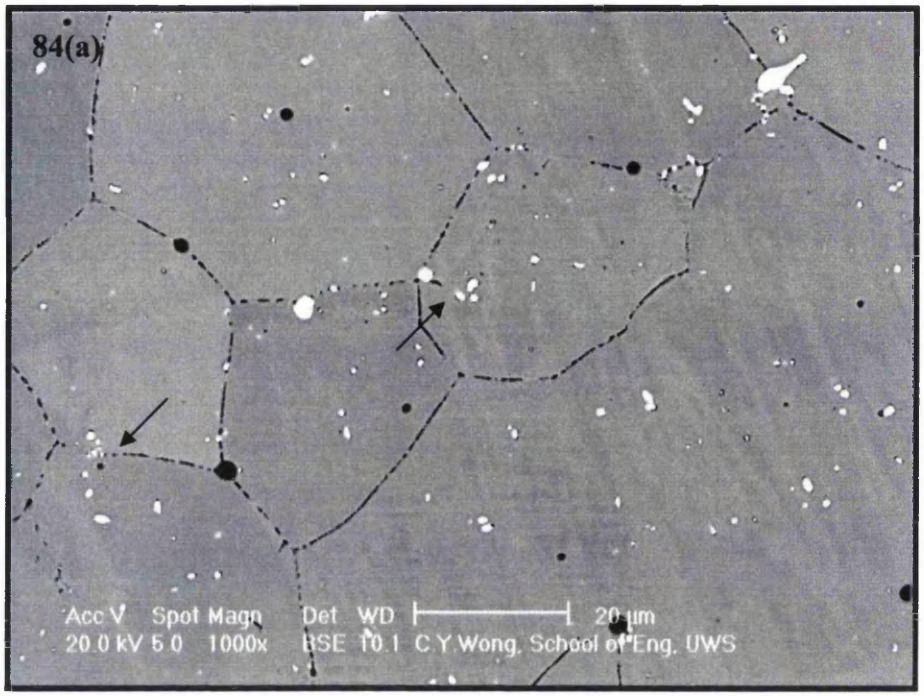
84(a)
Acc.V Spot Magn Det WD 20 µm
20.0 kV 5.0 1000x BSE 10.1 C.Y.Wong, School of Eng. UWS

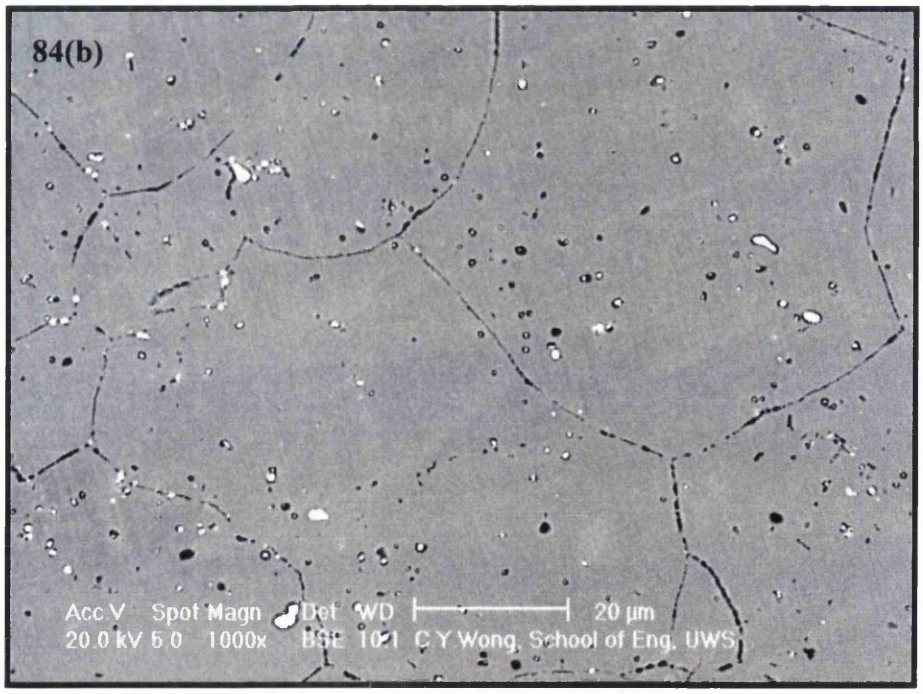
84(b)
Acc.V Spot Magn Det WD 20 µm
20.0 kV 5.0 1000x BSE 10.1 C.Y.Wong, School of Eng. UWS

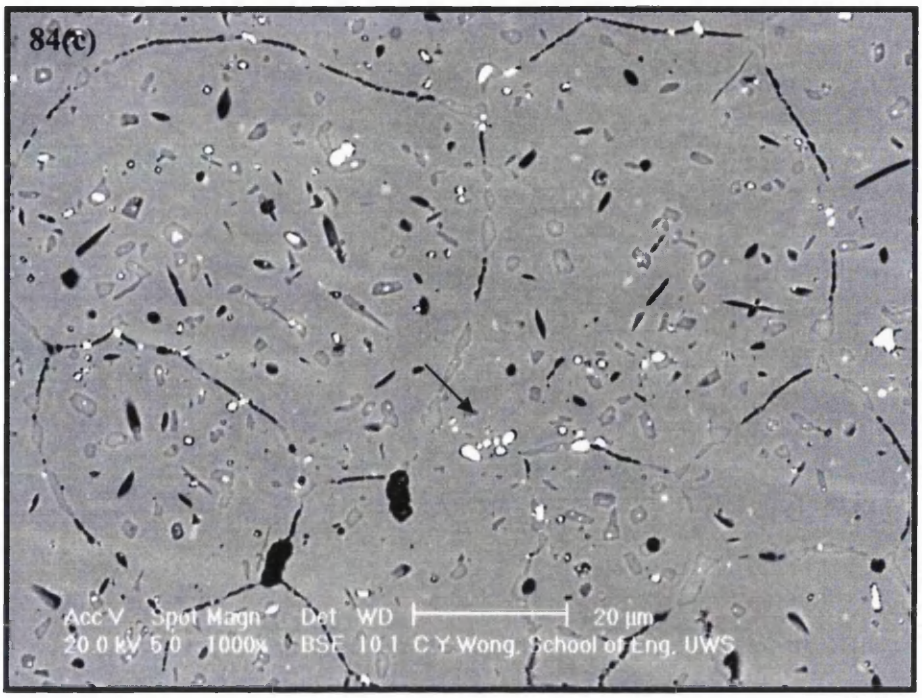

Figure 84: Backscattered SEM micrograph of specimens aged at 700°C (a) BH16 for 35.5h, (b) BH9 for 7077h, and (c) BH22 for 48370h.

Microstructure underneath the fracture surface

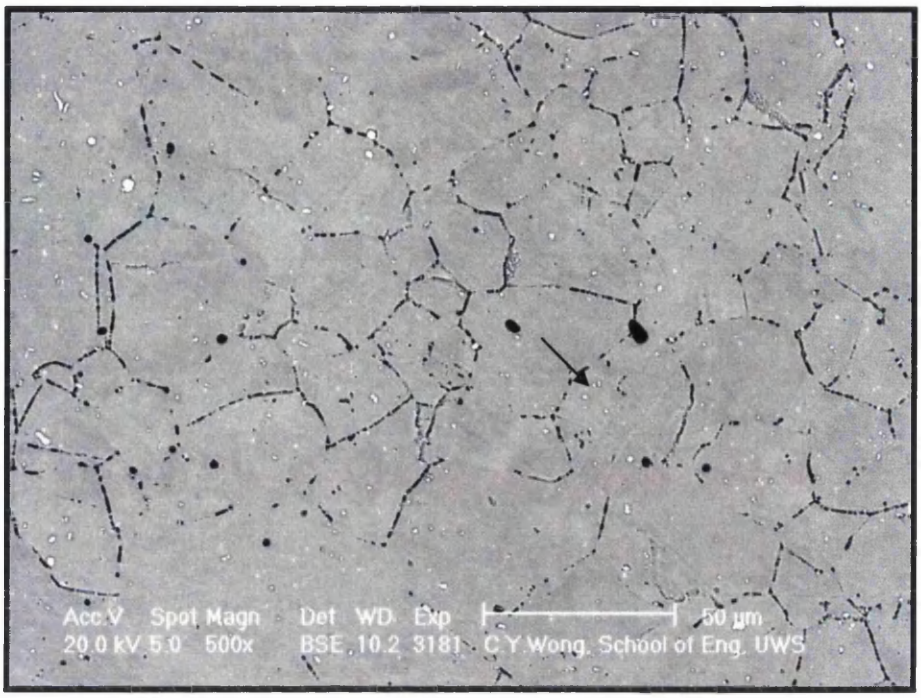

Figure 85(a): SEM micrograph of the microstructure adjacent to the fracture surface for BH24. The sample was initially creep tested at a temperature of 550°C and at a stress of 402MPa. (5527h)

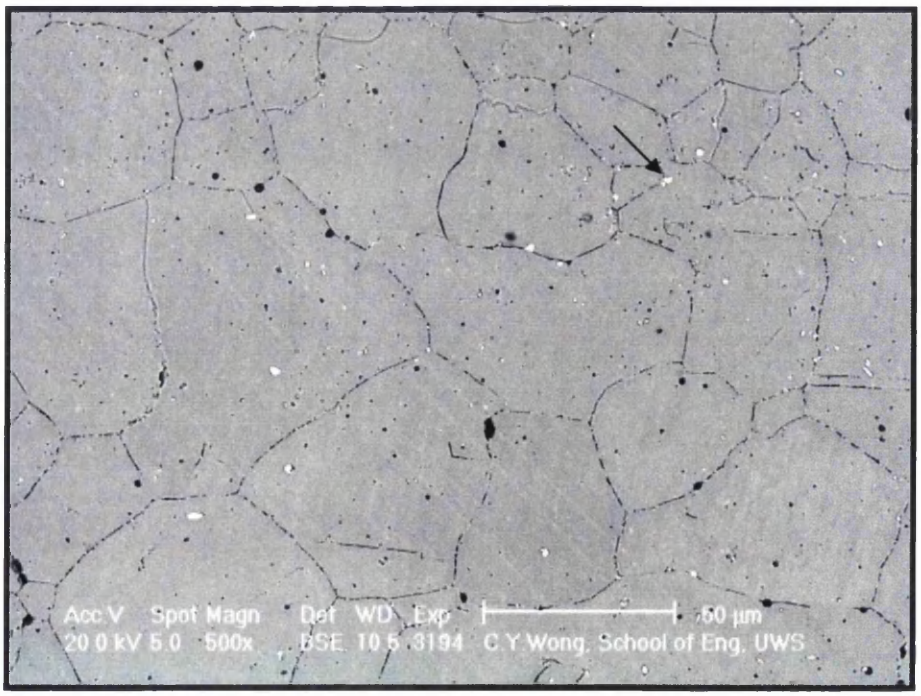

Figure 85(b): SEM micrograph of the microstructure adjacent to the fracture surface for BH28. The sample was initially creep tested at a temperature of 550°C and at a stress of 263MPa. (82138h)

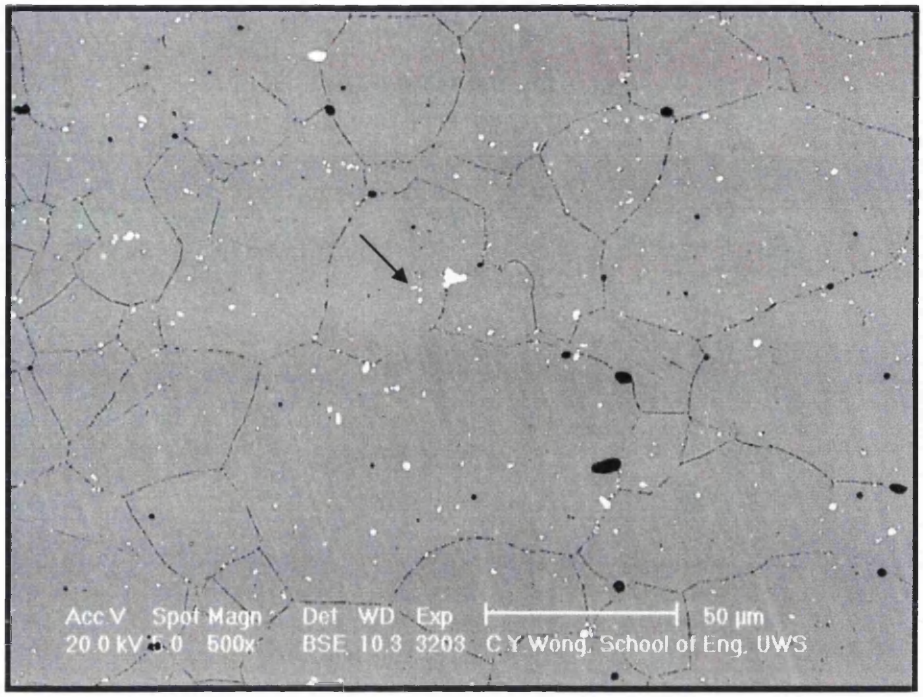

Figure 85(c): SEM micrograph of the microstructure adjacent to the fracture surface for BH7. The sample was initially creep tested at a temperature of 600°C and at a stress of 309MPa. (1179h)

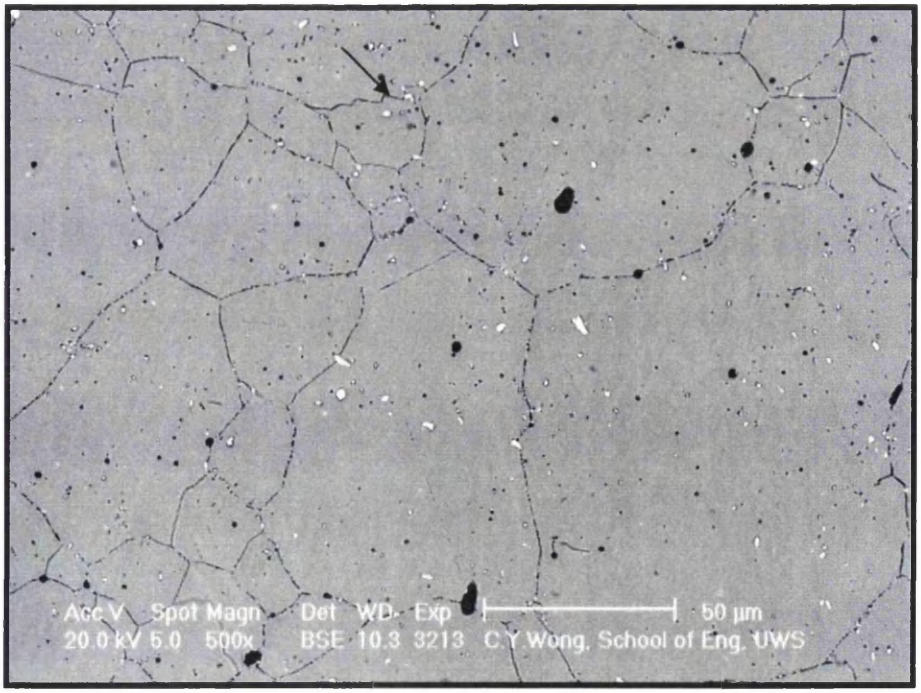

Figure 85(d): SEM micrograph of the microstructure adjacent to the fracture surface for BH6. The sample was initially creep tested at a temperature of 600°C and at a stress of 263MPa. (6951h)

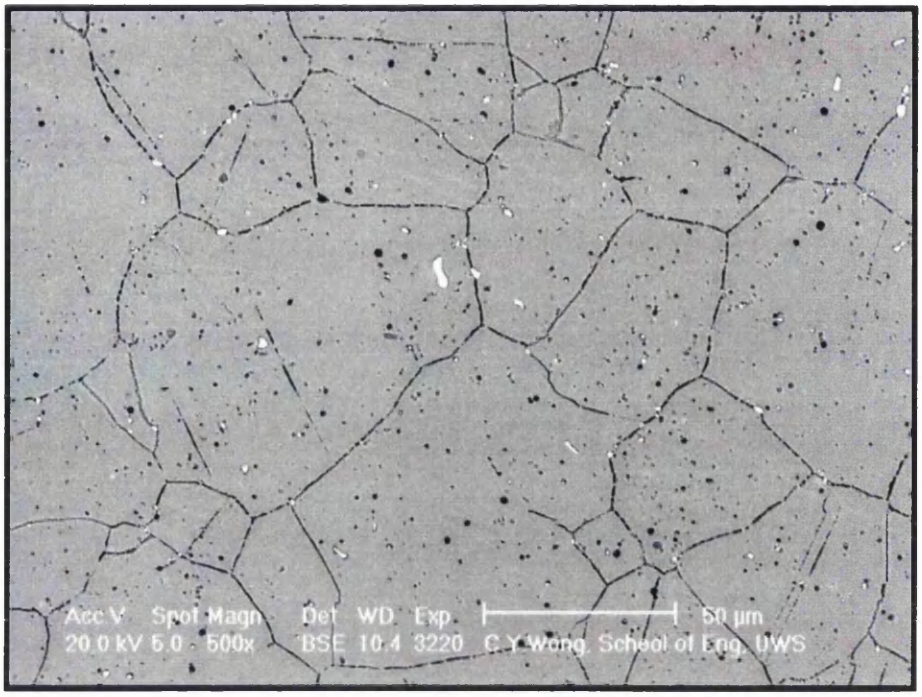

Figure 85(e): SEM micrograph of the microstructure adjacent to the fracture surface for BH10. The sample was initially creep tested at a temperature of 600°C and at a stress of 232MPa. (153491h)

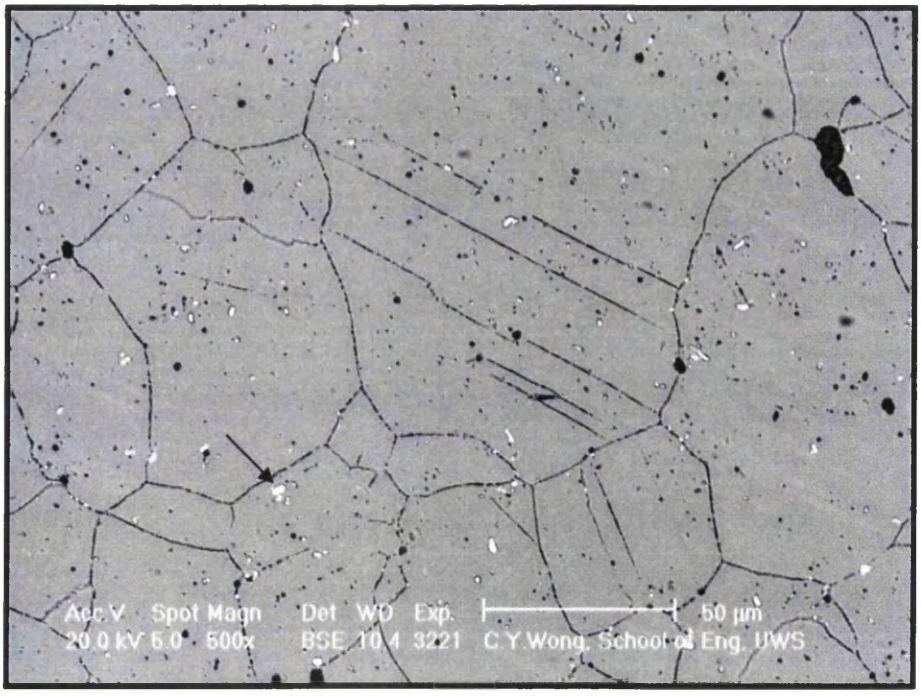

Figure 85(f): SEM micrograph of the microstructure adjacent to the fracture surface for BH11. The sample was initially creep tested at a temperature of 650°C and at a stress of 263MPa. (258h)

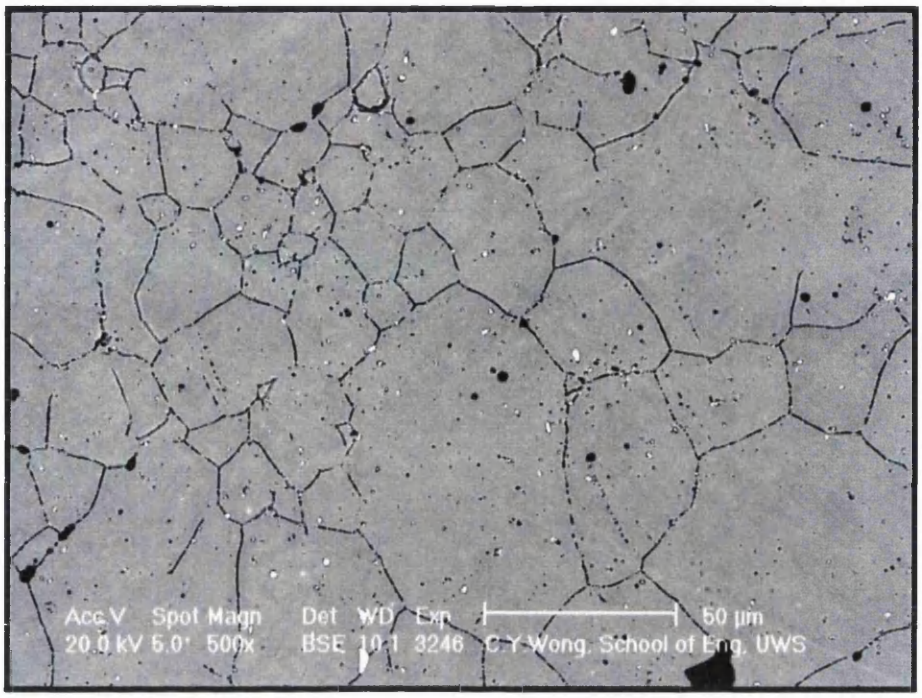

Figure 85(g): SEM micrograph of the microstructure adjacent to the fracture surface for BH4. The sample was initially creep tested at a temperature of 650°C and at a stress of 232MPa. (3521h)

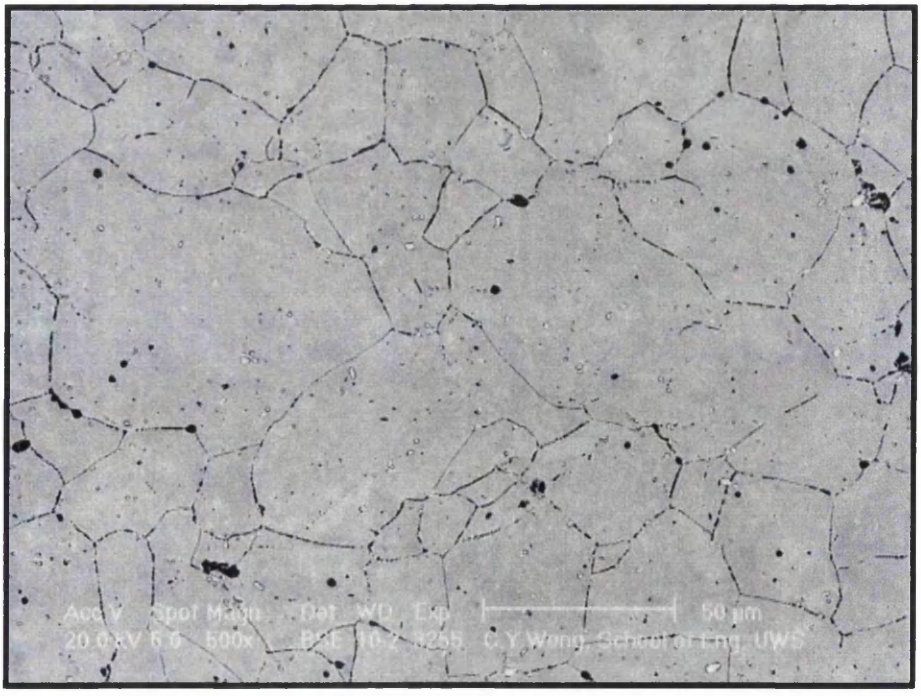

Figure 85(h): SEM micrograph of the microstructure adjacent to the fracture surface for BH2. The sample was initially creep tested at a temperature of 650°C and at a stress of 185MPa. (29398h)

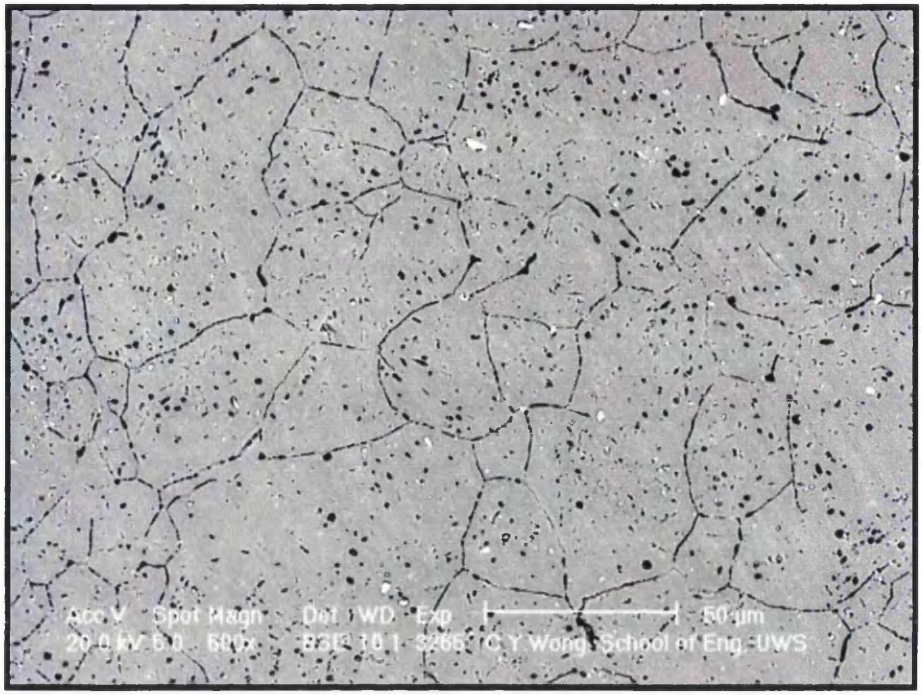

Figure 85(i): SEM micrograph of the microstructure adjacent to the fracture surface for BH27. The sample was initially creep tested at a temperature of 650°C and at a stress of 116MPa. (77896h)

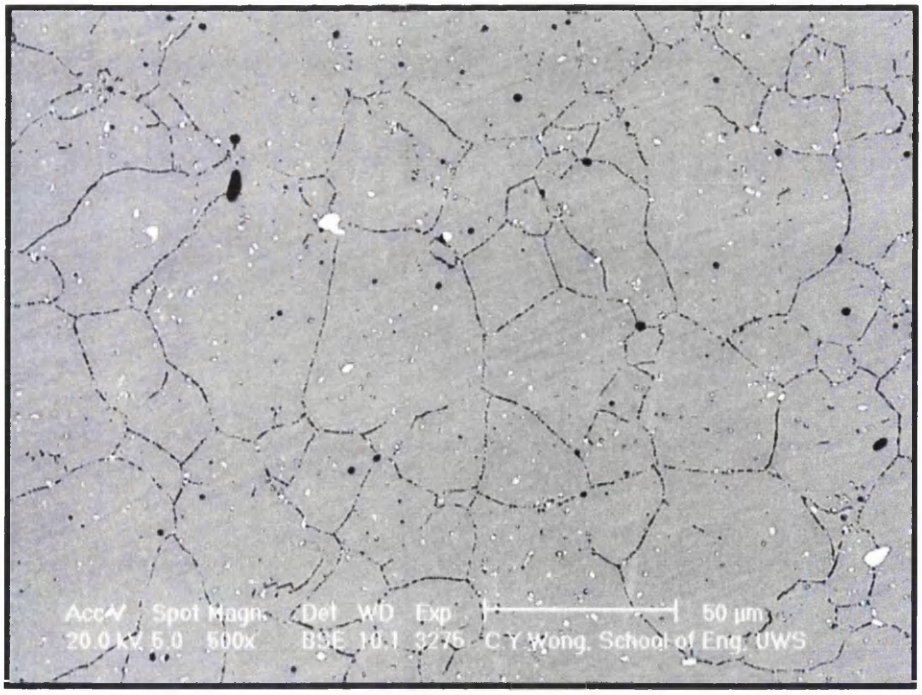

Figure 85(j): SEM micrograph of the microstructure adjacent to the fracture surface for BH16. The sample was initially creep tested at a temperature of 700°C and at a stress of 247MPa. (35h)

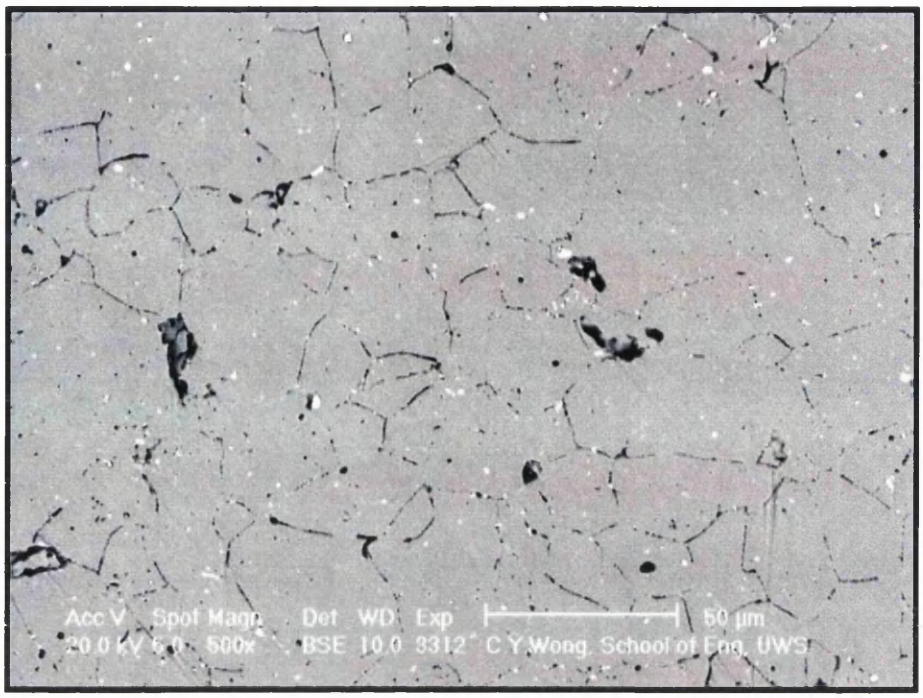

Figure 85(k): SEM micrograph of the microstructure adjacent to the fracture surface for BH9. The sample was initially creep tested at a temperature of 700°C and at a stress of 108MPa. (7077h)

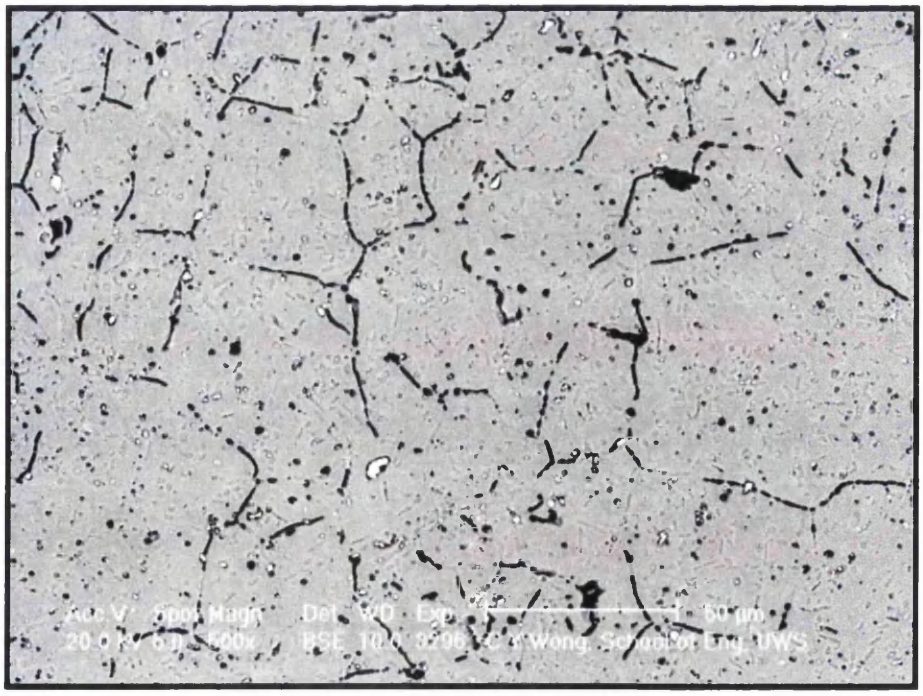

Figure 85(l): SEM micrograph of the microstructure adjacent to the fracture surface for BH22. The sample was initially creep tested at a temperature of 700°C and at a stress of 70MPa. (48370h)

Microstructure of the fracture surface

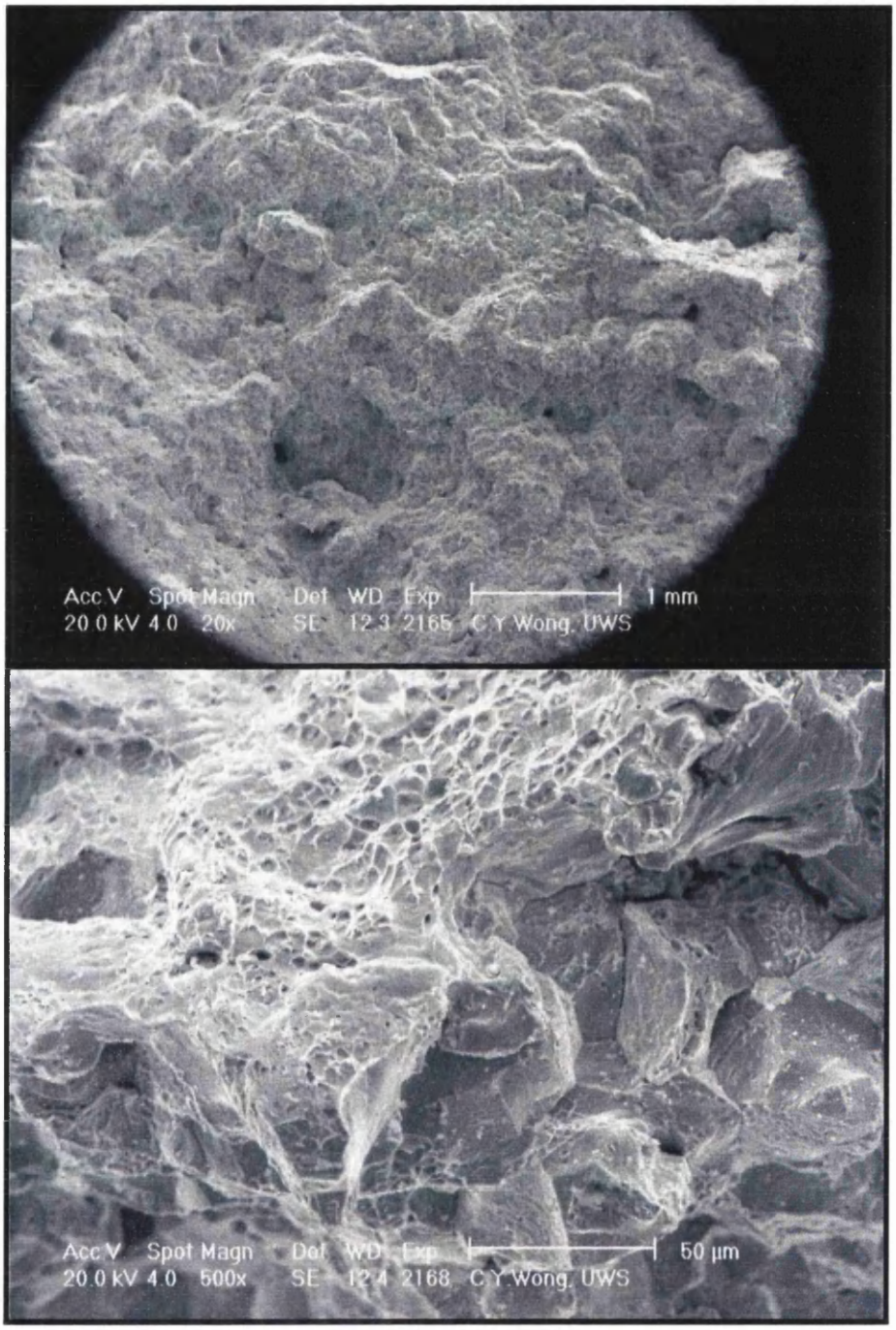

Figure 86(a): SEM micrographs of the creep fracture area for BH24 sample after rupture life of 5527h.

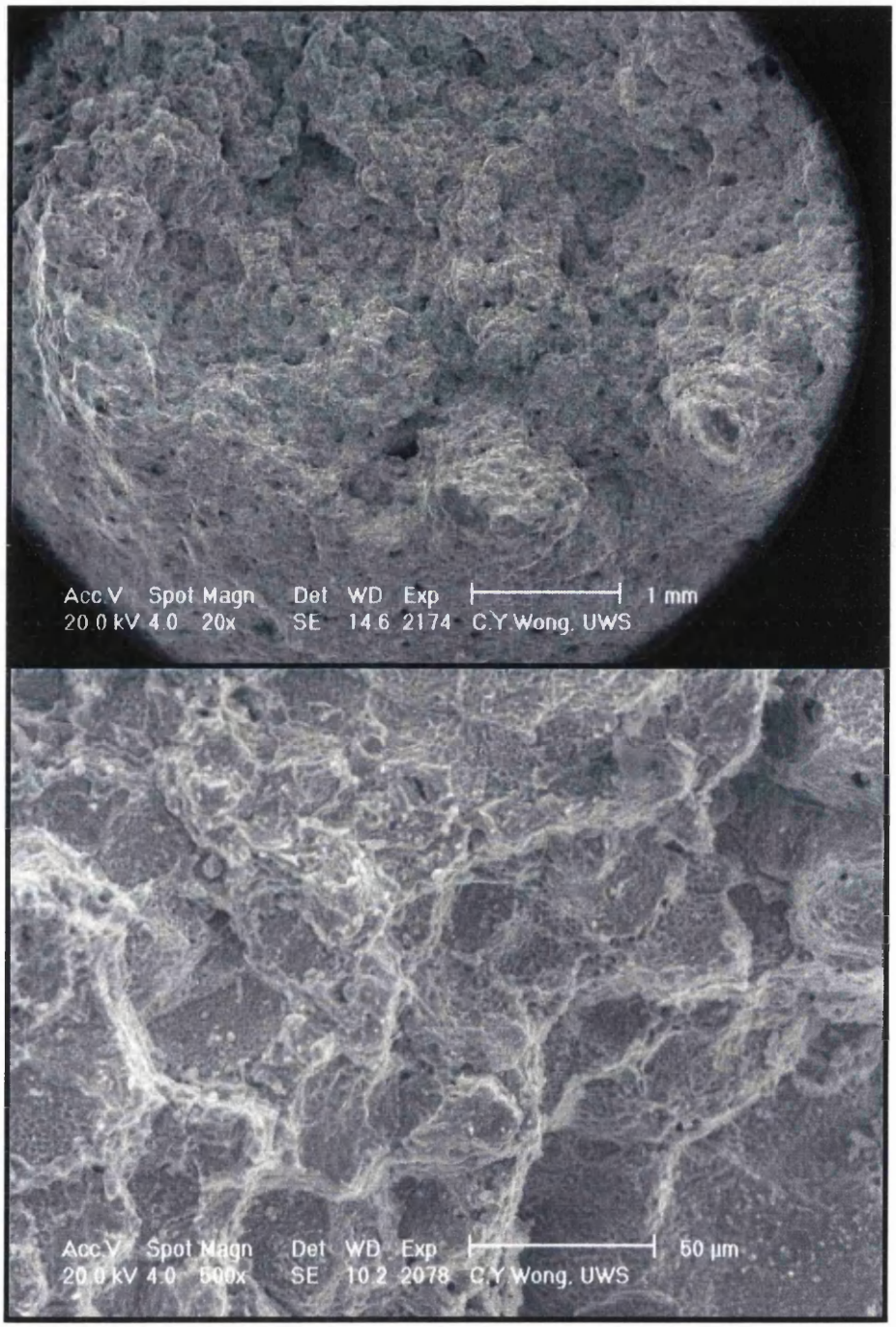

Figure 86(b): SEM micrographs of the creep fracture area for BH28 sample after rupture life of 82138h.

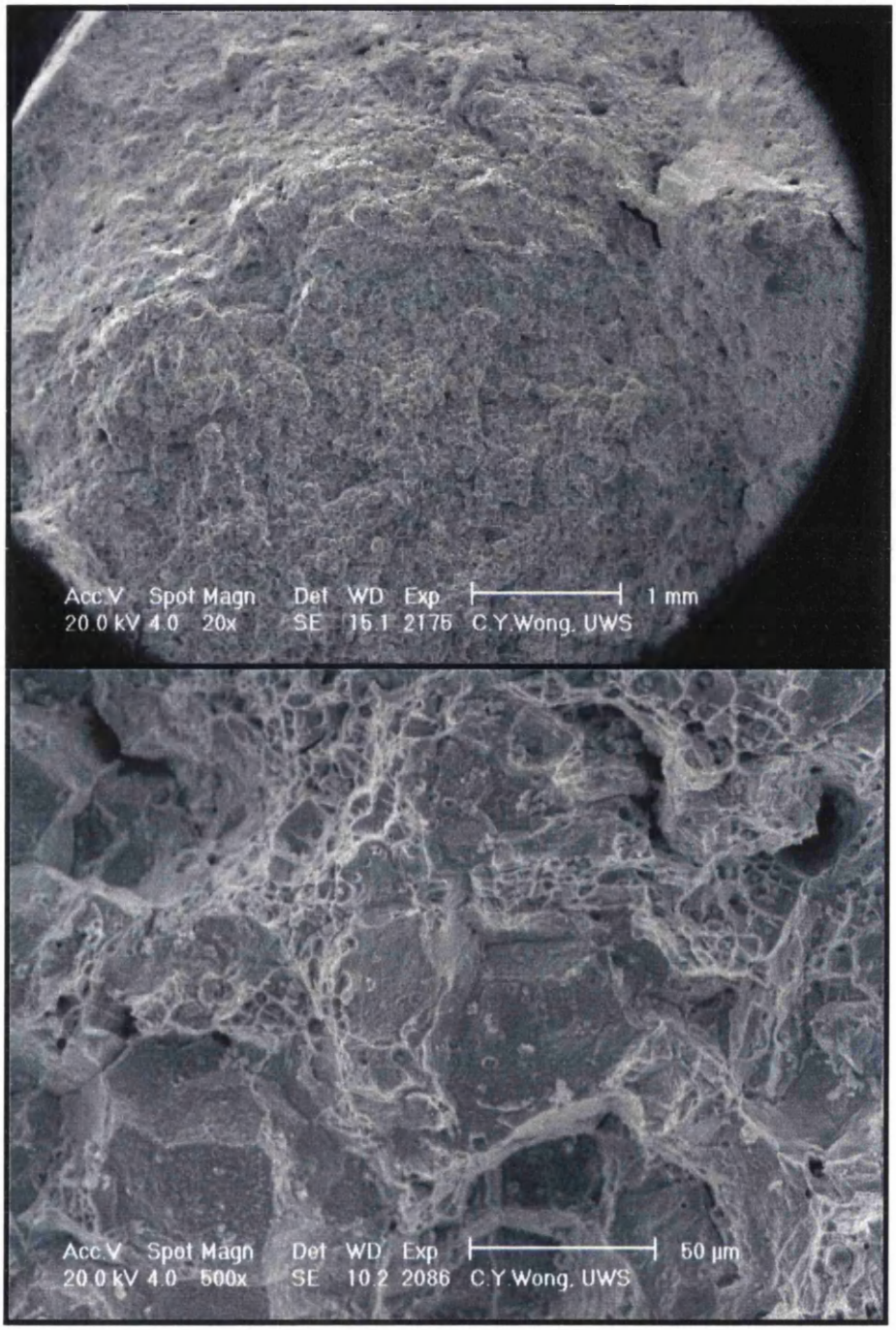

Figure 86 (c): SEM micrographs of the creep fracture area for BH7 sample after rupture life of 1179h.

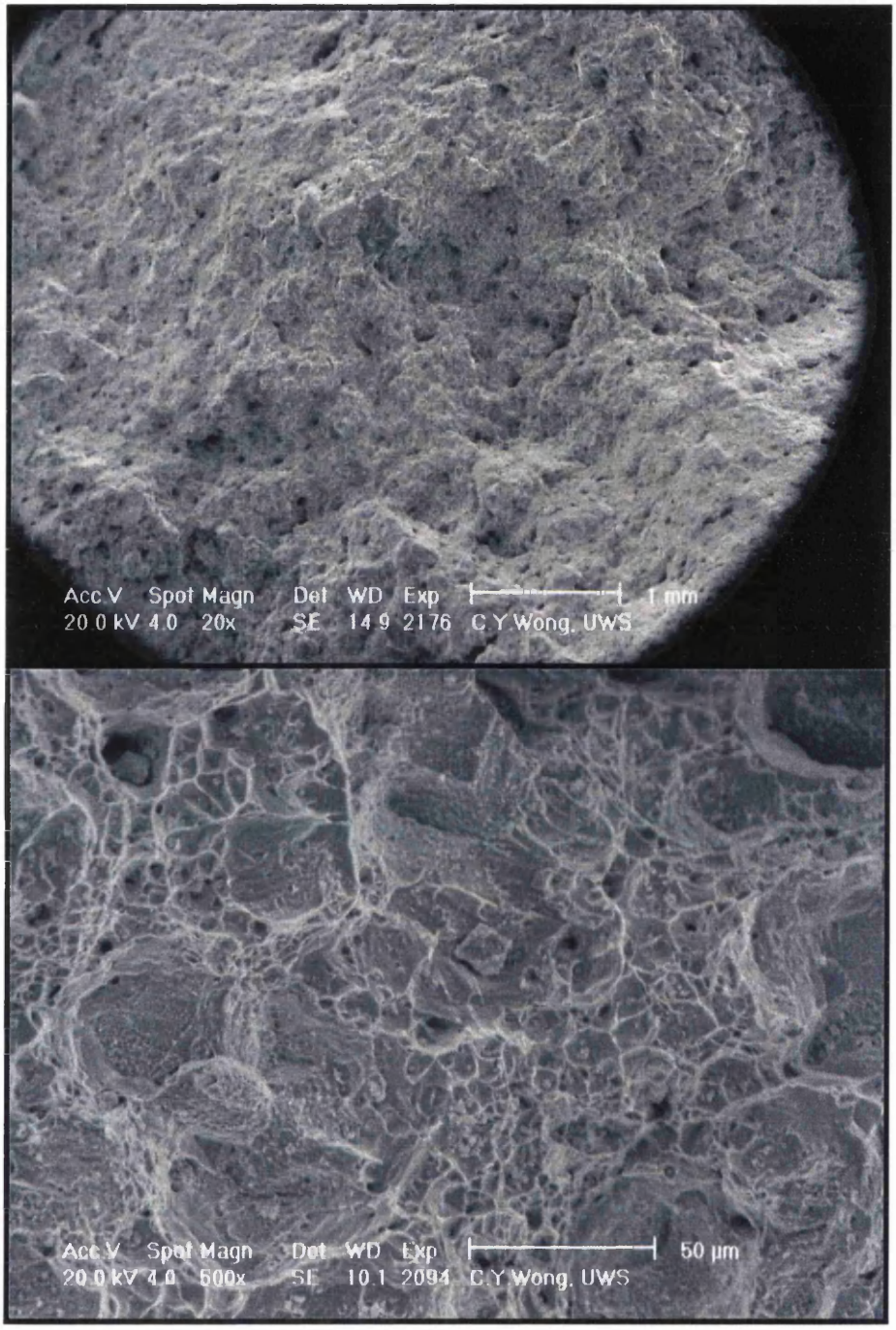

Figure 86 (d): SEM micrographs of the creep fracture area for BH6 sample after rupture life of 6951h.

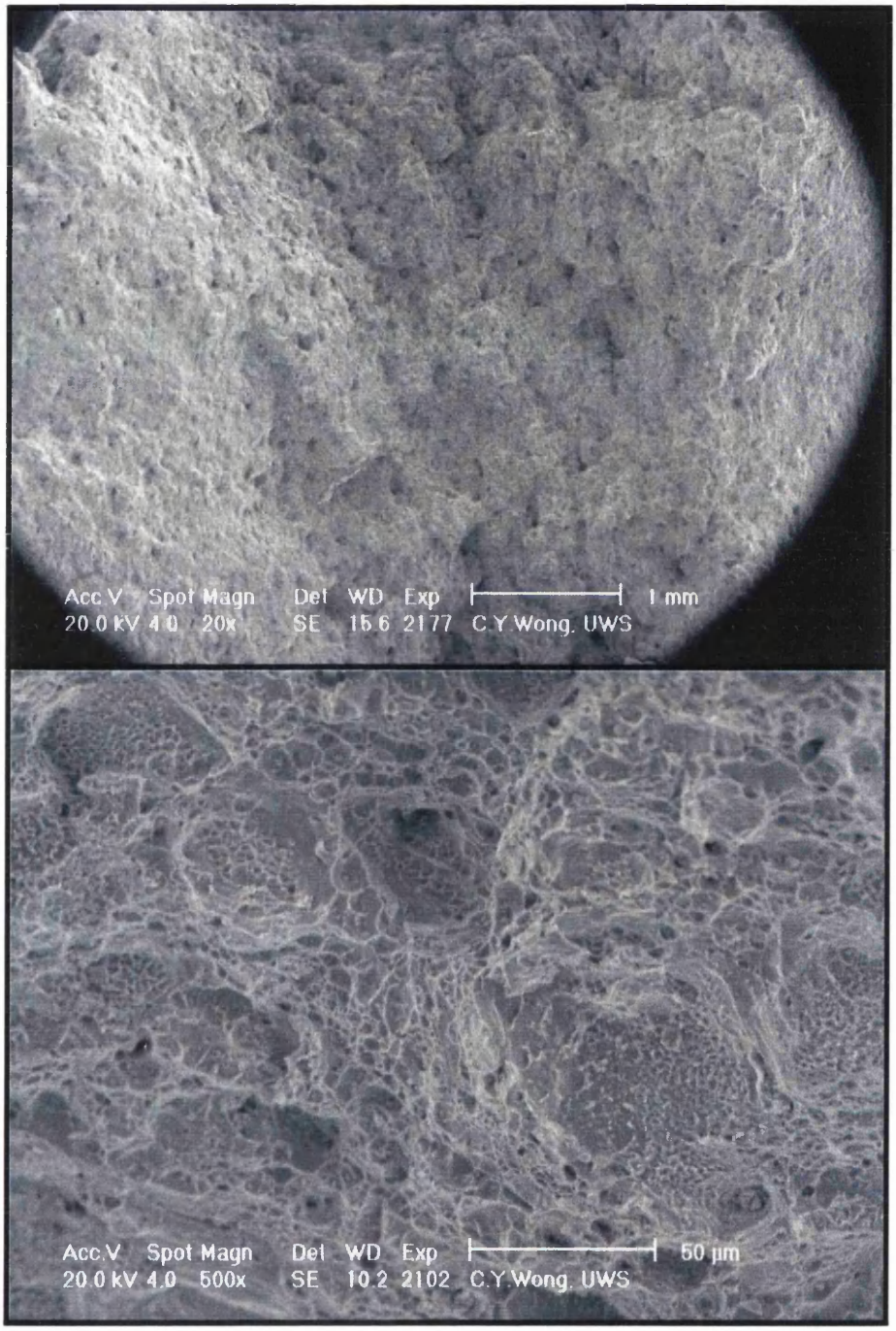

Figure 86 (e): SEM micrographs of the creep fracture area for BH10 sample after rupture life of 153491h.

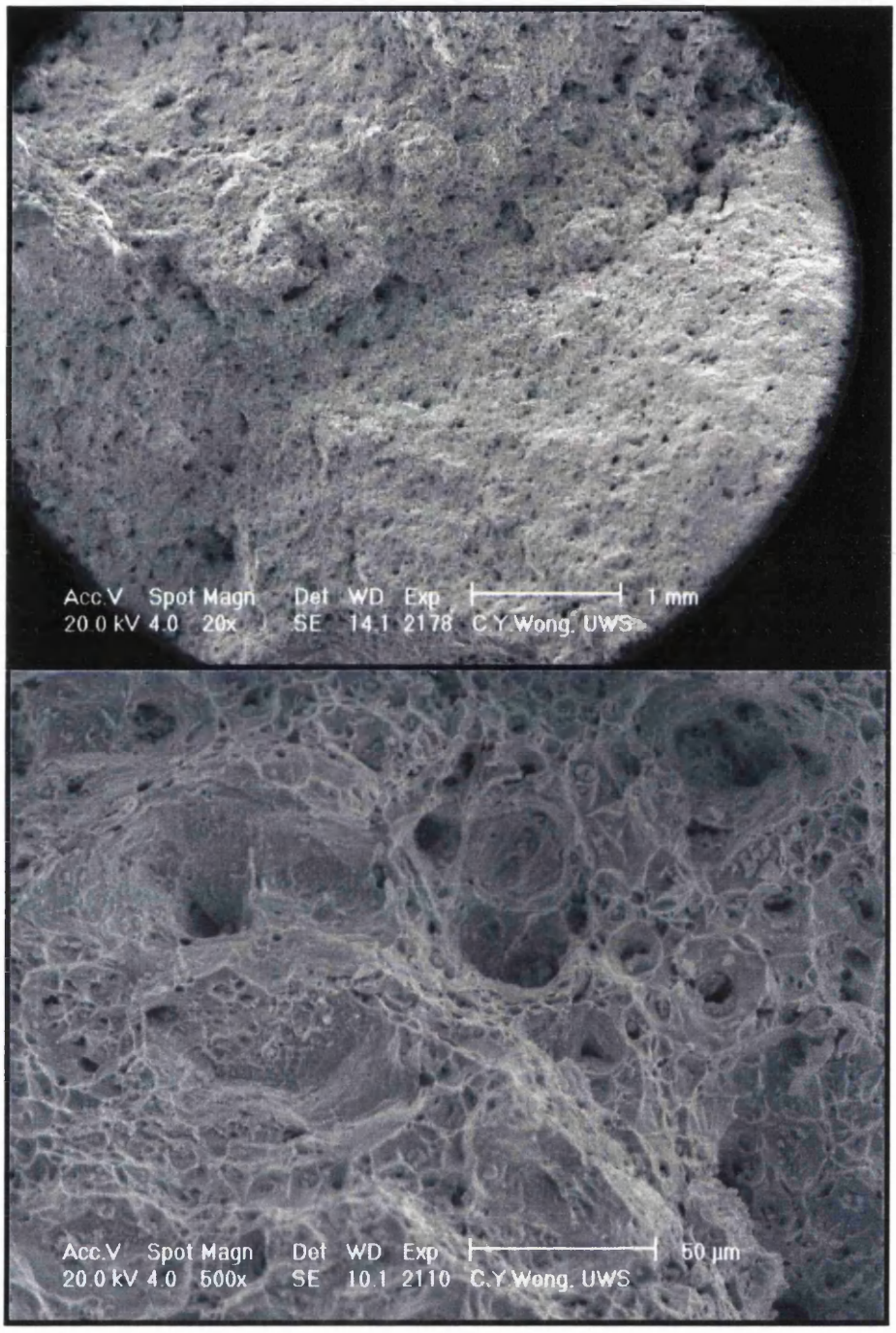

Figure 86 (f): SEM micrographs of the creep fracture area for BH11 sample after rupture life of 258h.

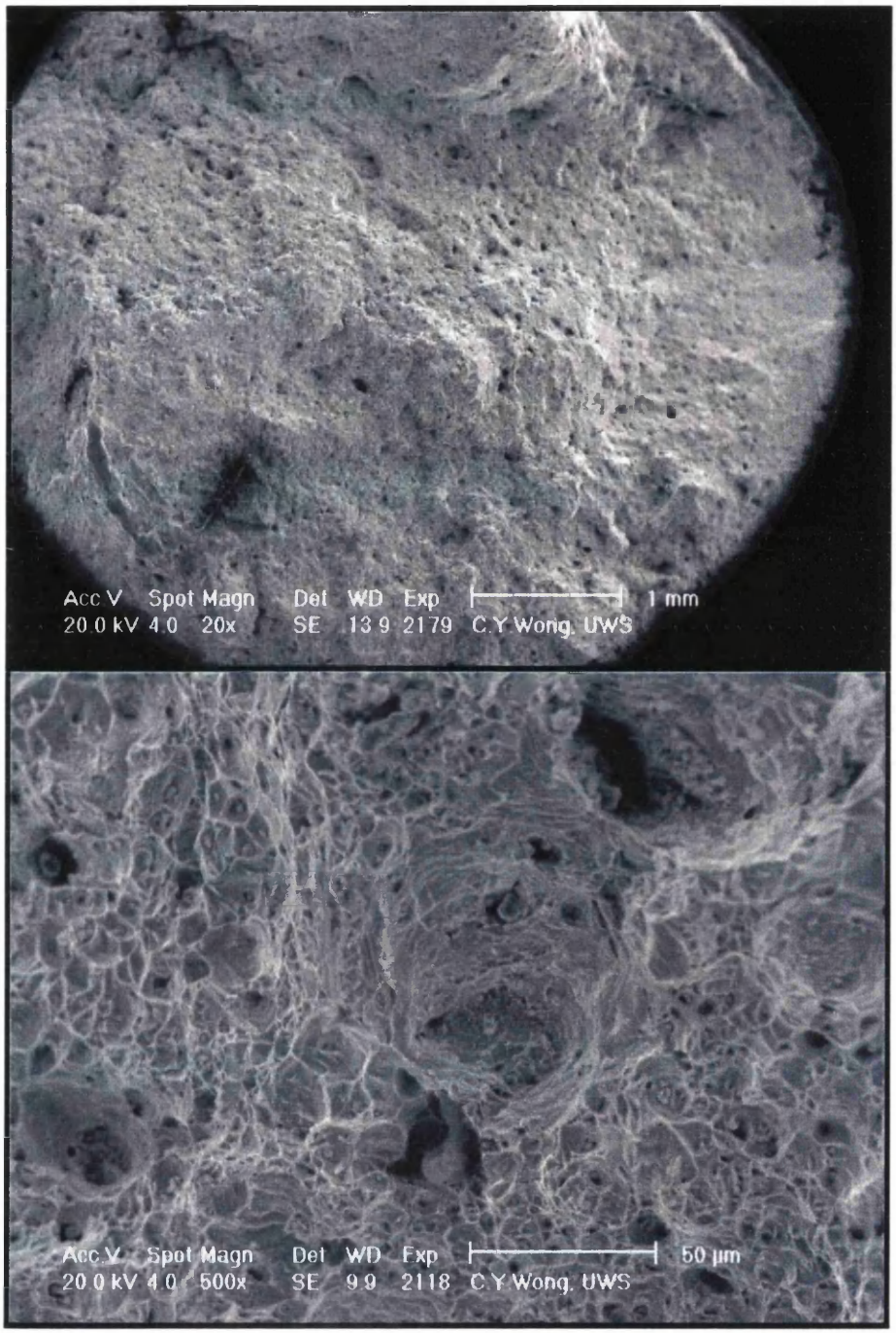

Figure 86 (g): SEM micrographs of the creep fracture area for BH4 sample after rupture life of 3521h.

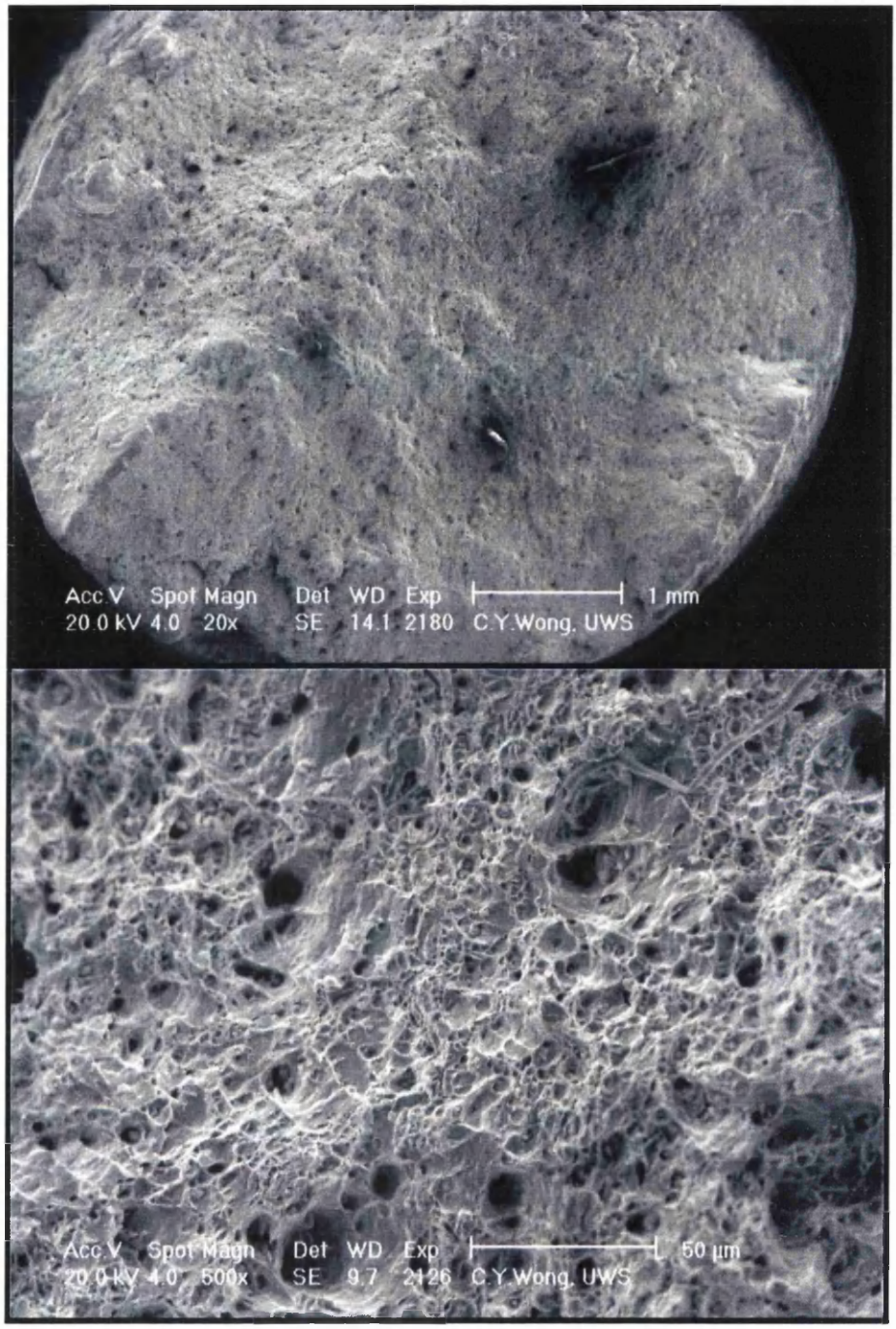

Figure 86 (h): SEM micrographs of the creep fracture area for BH2 sample after rupture life of 29398h.

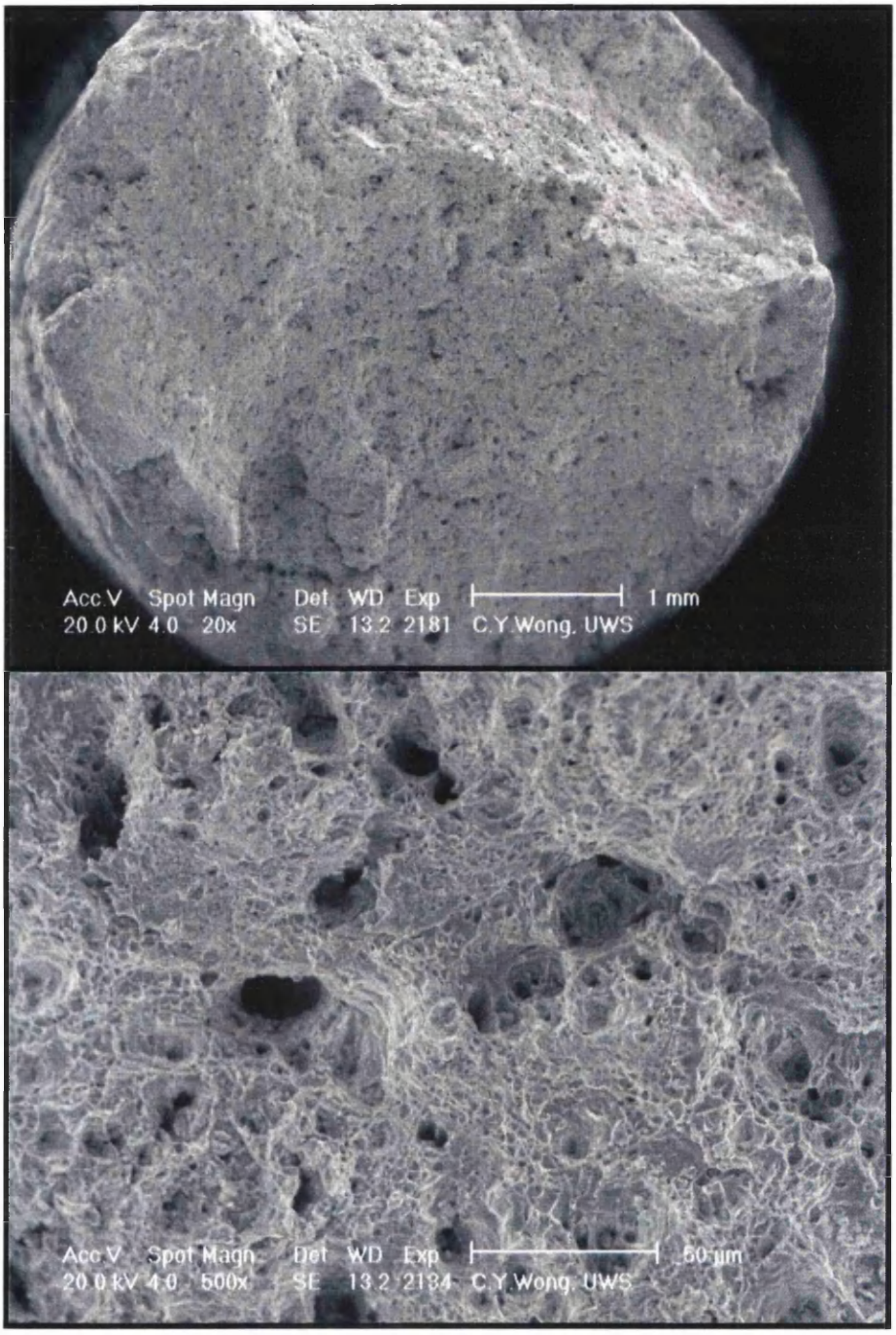

Figure 86 (i): SEM micrographs of the creep fracture area for BH27 sample after rupture life of 77896h.

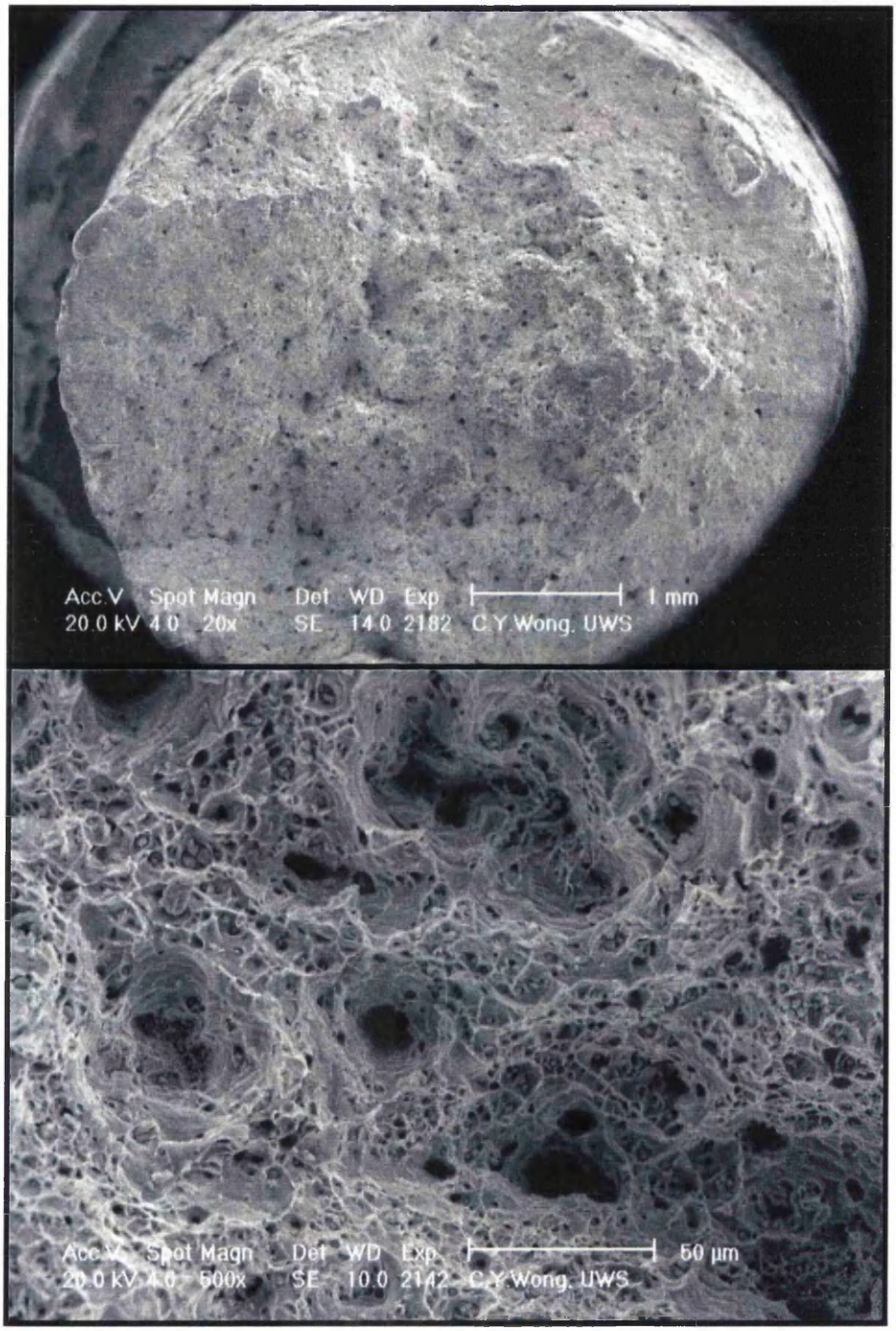

Figure 86 (j): SEM micrographs of the creep fracture area for BH16 sample after rupture life of 35h.

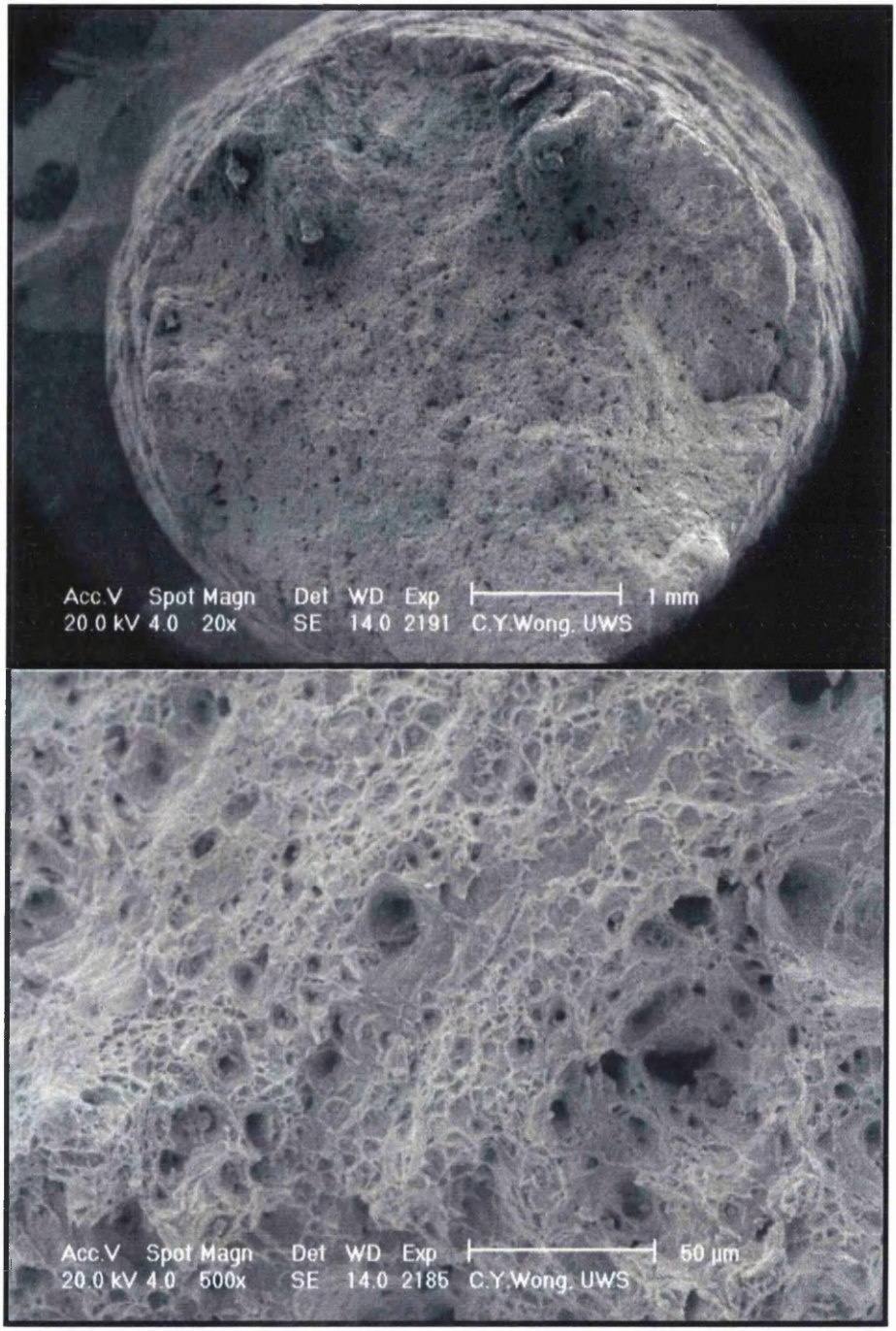

Figure 86(k): SEM micrographs of the creep fracture area for BH9 sample after rupture life of 7077h.

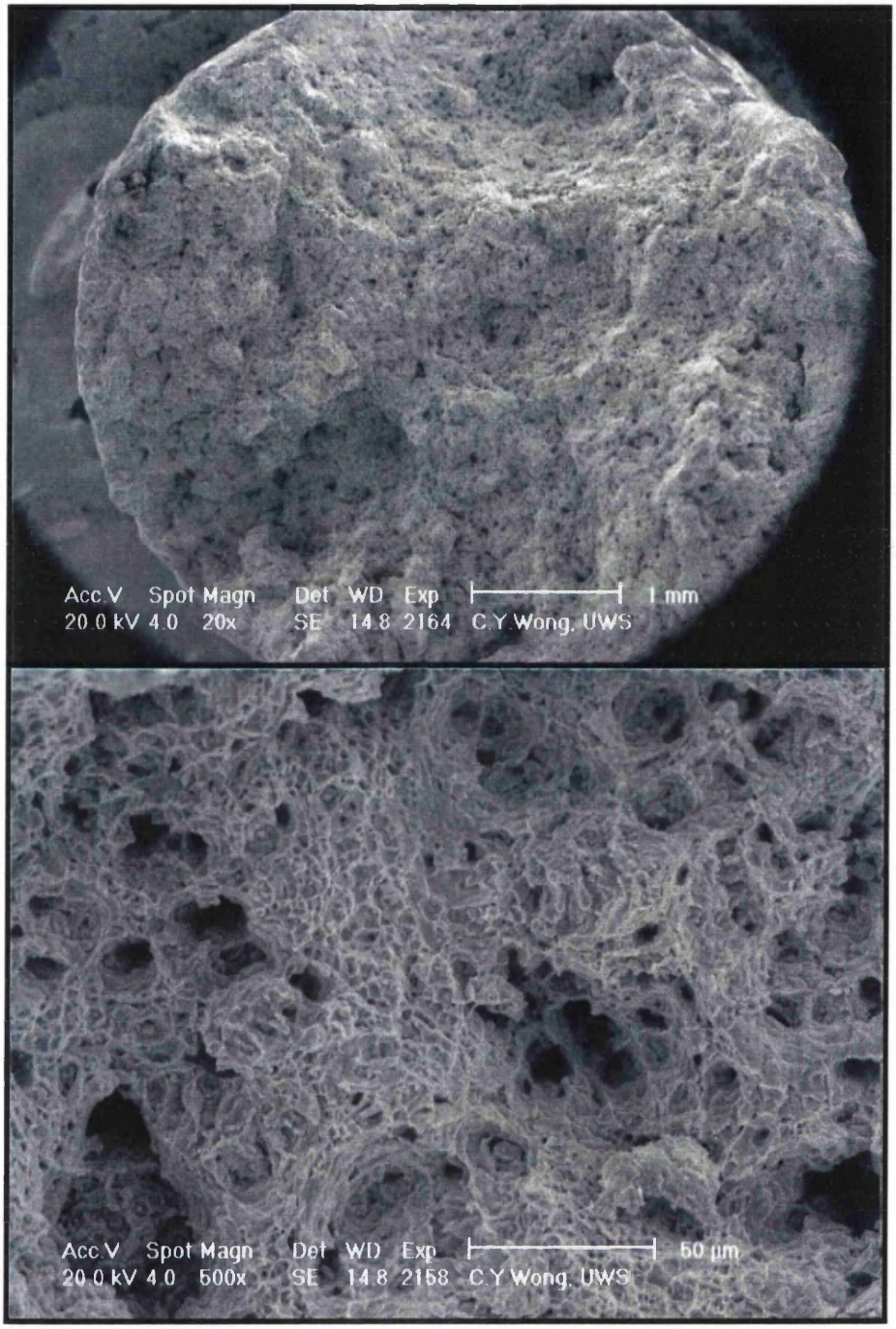

Figure 86 (l): SEM micrographs of the creep fracture area for BH22 sample after rupture life of 48370h.

EDX analysis for Esshete 1250

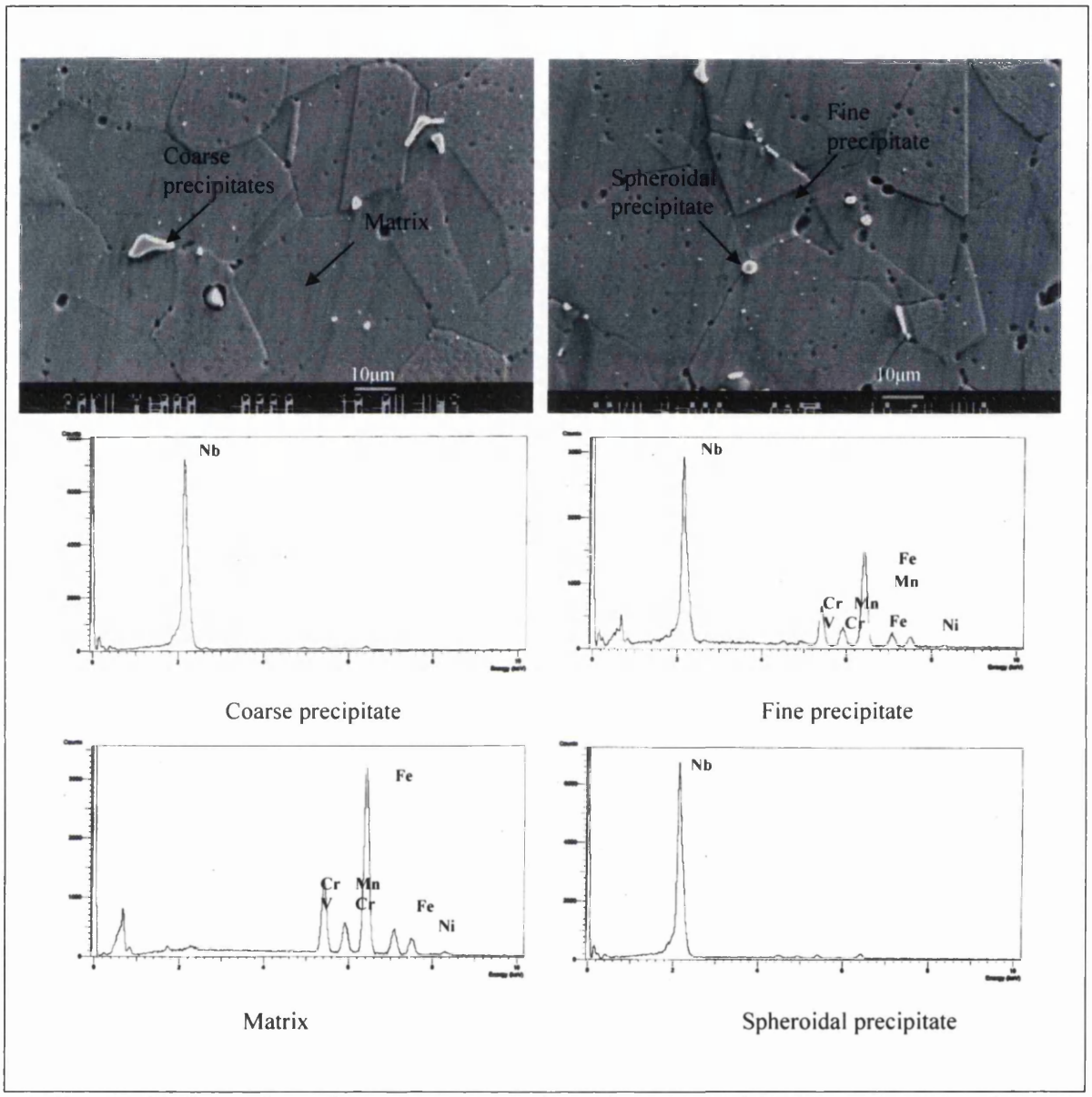

Figure 87: Secondary electron micrographs and associated EDX spot microanalysis traces in Esshete 1250 parent sample creep tested for 1301h at 550°C.

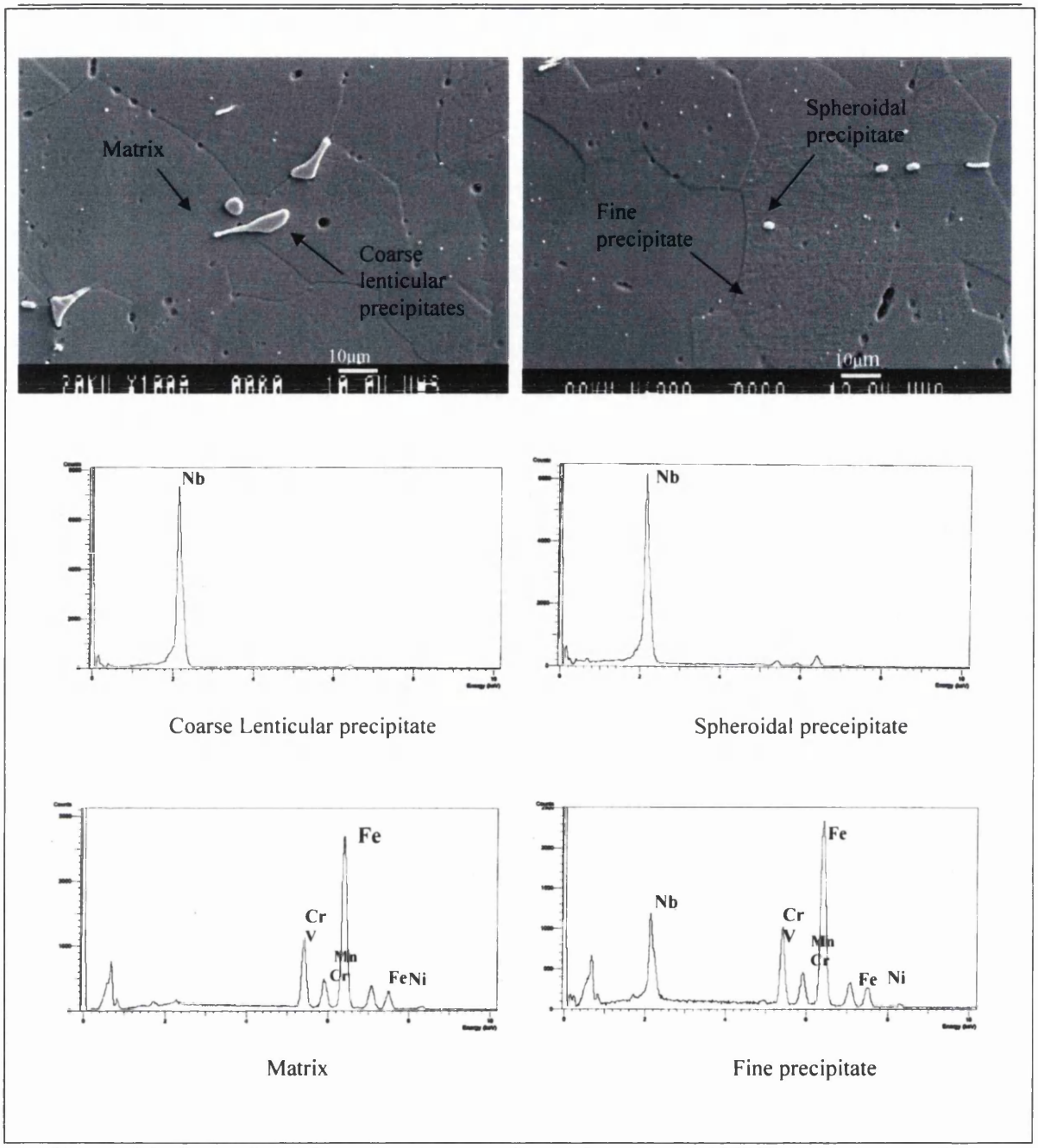

Figure 88: Secondary electron micrographs and associated EDX spot microanalysis traces in Esshete 1250 parent sample creep tested for 2792h at 550°C.

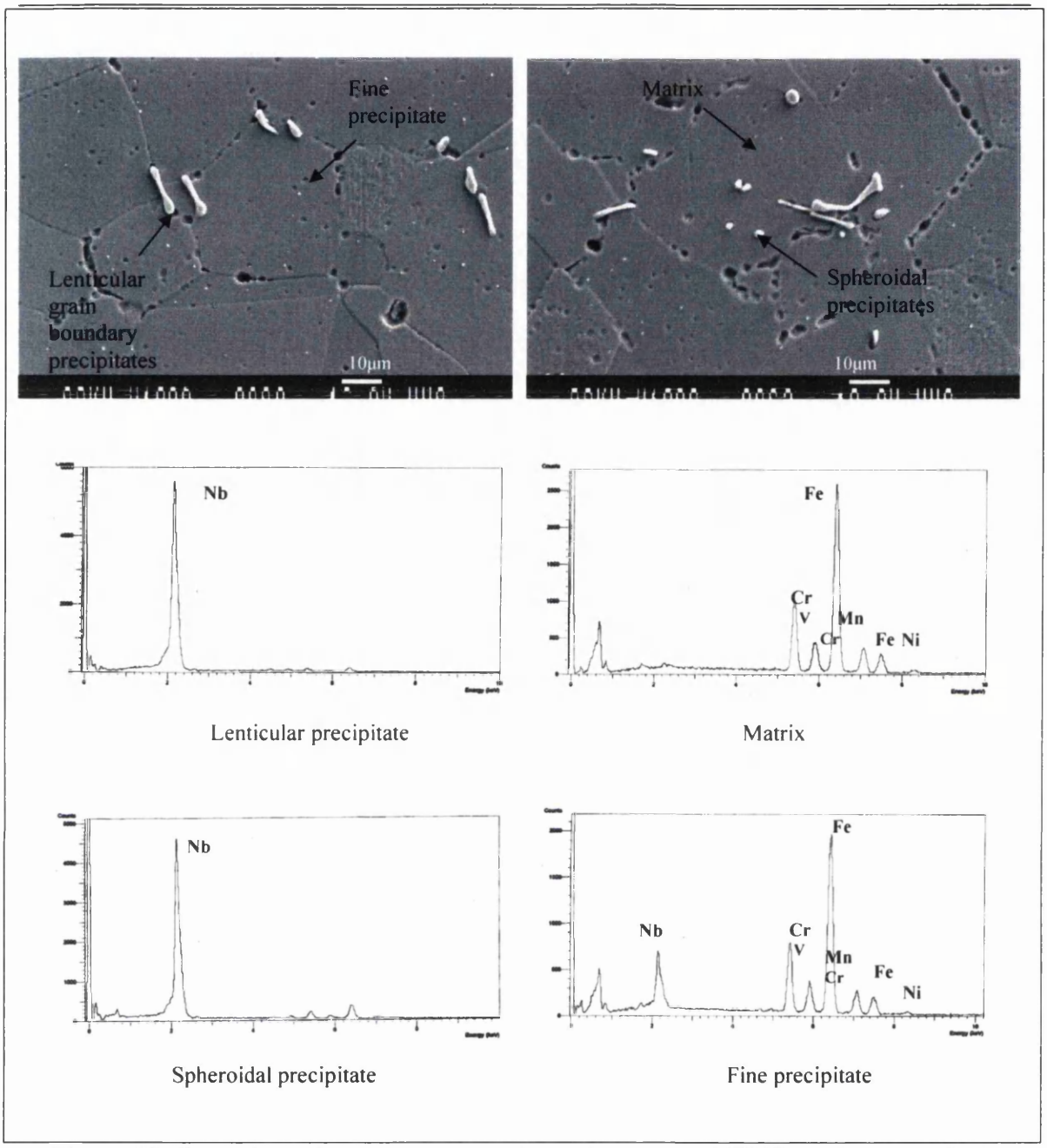

Figure 89: Secondary electron micrographs and associated EDX spot microanalysis traces in Esshete 1250 parent sample creep tested for 4944h at 550°C.

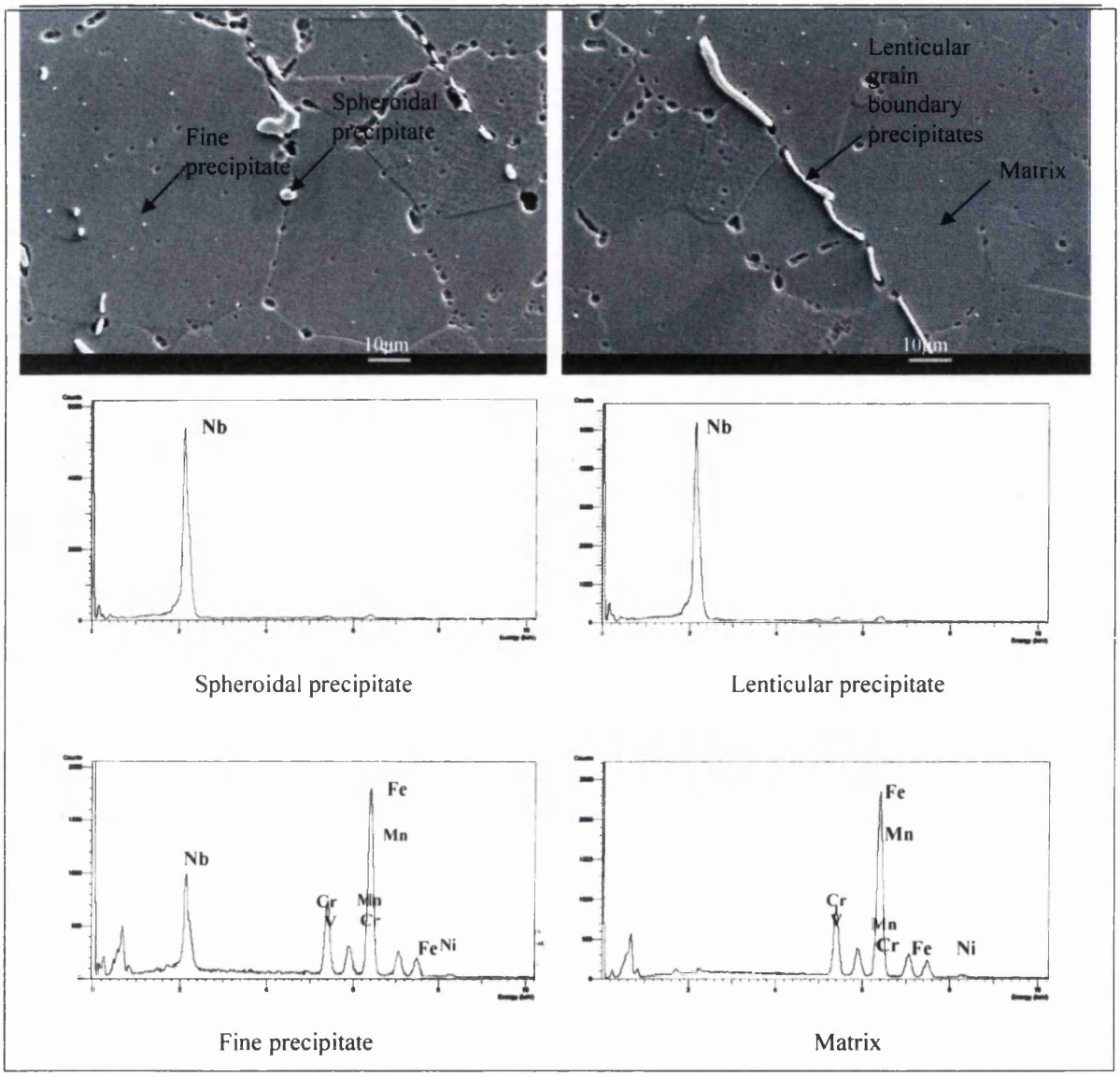

Figure 90: Secondary electron micrographs and associated EDX spot microanalysis traces in Esshete 1250 parent sample creep tested for 7132h at 550°C.

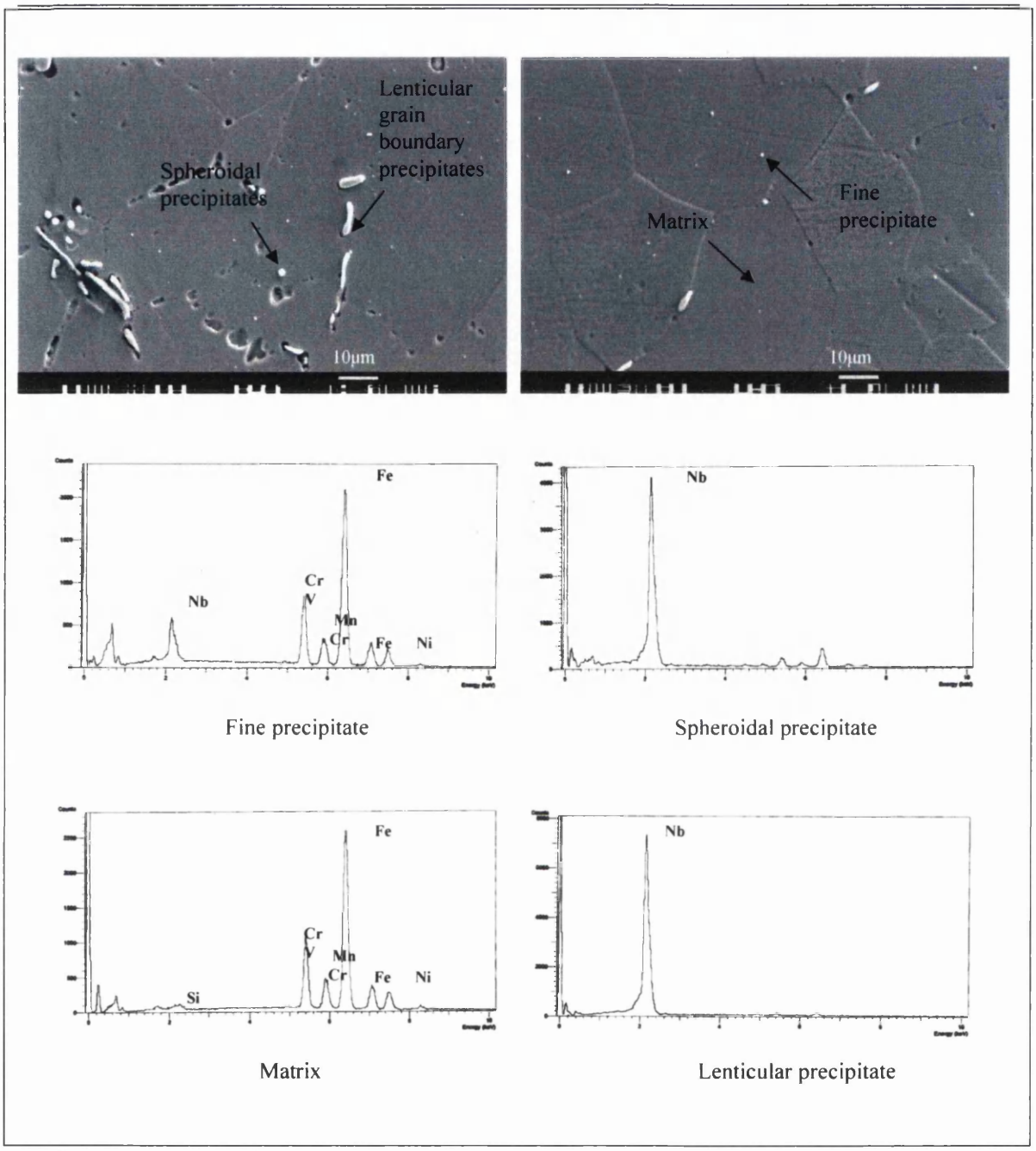

Figure 91: Secondary electron micrographs and associated EDX spot microanalysis traces in Esshete 1250 parent sample creep tested for 2035h at 575°C.

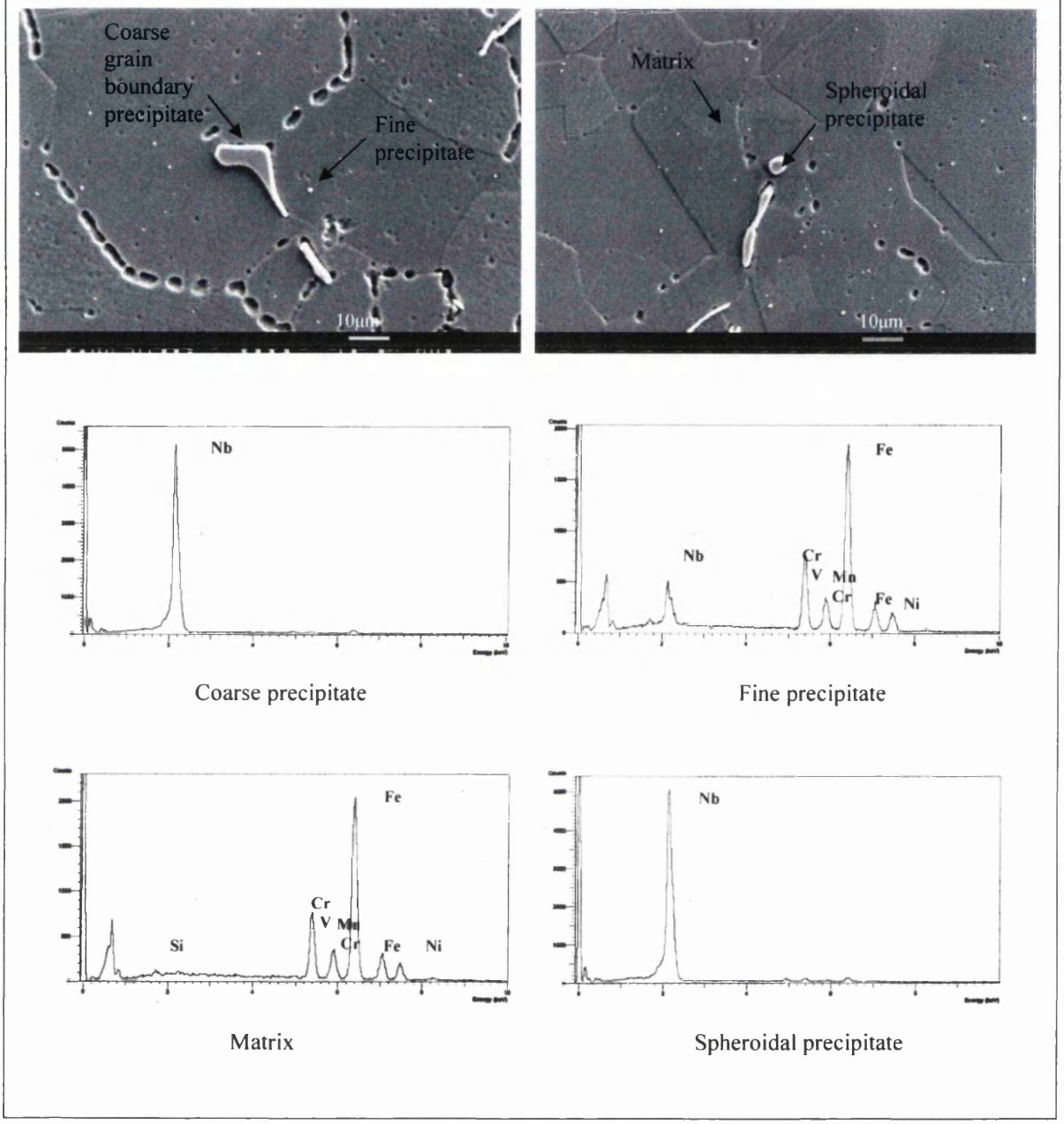

Figure 92: Secondary electron micrographs and associated EDX spot microanalysis traces in Esshete 1250 parent sample creep tested for 3489h at 575°C.